Thermal Energy Storage for Industrial Applications

ME55035: MSc Thesis

Pauline Gelling

TUDelft

ARCADIS

Thermal Energy Storage for Industrial Applications

by

Pauline Gelling

Student Name	Student Number
Pauline Gelling	4546512

Supervisor:	Prof. Dr. K. (Kamel) Hooman
	Ir. J. (Jelmer) Westra *(Arcadis)*
Thesis committee:	Prof. Dr. ir. K. (Kamel) Hooman
	Dr. ir. R. (René) Delfos
	Dr. ir. E. (Emanuele) Zanetti
	Ir. J. (Jelmer) Westra *(Arcadis)*
Project Duration:	April, 2023 - March, 2024
Faculty:	Mechanical Engineering, Delft

Cover: Arcadis

TUDelft

Preface

It is my great pleasure to present this thesis, the result of a roller coaster with quite a few loopings. This thesis is conducted as the last hurdle of the Master Mechanical Engineering and is intended to contribute to a greener future. I would like to thank some people who have supported me during this process.

First and foremost, I would like to thank Professor Kamel Hooman for his guidance throughout my thesis. You guided me with the calmness required to not get sick during those loopings and end the roller coaster with a smile on my face.

Next, I would also like to thank Arcadis for the opportunity to conduct my thesis at their organization. Jelmer Westra, thank you for your guidance and for giving me a broader view on engineering. Jaap Nies and Bram Kersten, thank you for the brief, but always valuable remarks.

Furthermore, I would like to thank all the people who are more worth than every thesis could ever be: my family and friends. Thank you for distracting me from my thesis and motivate me to finish it. Papa, thank you for being my sparring partner. Tim, thank you for your patience.

While reflecting on the process of studying at the TU Delft I can say with certainty that I have learned a lot. With a backpack full of memories, knowledge, friends, recipes, and insights I am ready for the next steps.

Pauline Gelling
Delft, March 2024

Abstract

The growing consumption of fossil energy resources increases greenhouse gas emissions (GHG). To meet the industry sector's target of reducing GHG emissions by 49% in 2030, relative to the levels in 1990, there is a need for energy storage (Government, 2019). Energy storage offers a potential solution to enhance the utilization of renewable energy, by addressing the intermittent nature of these sources. This study includes a conceptual design for three Thermal Energy Storage (TES) materials, steel slag, phase change salt, and molten salt, able to generate steam in the industry (4-20 bar). Moreover, this study attempts to contribute to faster commercialization of the phase change materials, by aiming to contribute to a thermal conductivity improvement method. The thermal conductivity limits the discharging and charging ranges nowadays.

The concept designs are based on a fluctuating steam demand pattern provided by Arcadis. Two storing modes are extracted, a stand-alone thermal energy source which can meet a 12-hour steam demand and an energy source intended for peak shaving. Based on literature, the storage configurations, with the associated key parameters are extracted, for each material, to attain an estimation of the dimensions and losses. Due to the inflexibility of literature on phase change salt, a semi-empirical model is developed. With this model, the temperature of the heat transfer fluid (HTF) temperature at the outlet of the storage can be calculated based on various input parameters. The input parameters include the type of phase change salt, type of HTF, mass flow rate of the HTF, and the dimensions of the storage. The HTF outlet temperature in combination with the mass flow determines the discharge power. Based on the output of the TES, an economically optimized design, of a shell and tube steam generator, using AspenEDR software, is conducted.

The results for the stand-alone case showed almost similar volumes for the steel slag and phase change salt. The molten salt storage solution was larger based on the requirement of two tanks, a hot and a cold one. Furthermore, phase change salts resulted in the highest total stored energy, which is a measure of the inability to completely discharge the phase change storage in combination with a maximum temperature drop of the HTF outlet temperature. An increase in the thermal conductivity of the phase change salt can reduce this problem. Another advantage is the possibility of using any HTF for charging and discharging the phase change salt. Due to diffusion inside the TES upon partly charging and discharging, steel slag and phase change salt seemed not suitable for peak shaving.

Next, the focus is on increasing the thermal conductivity of the phase change salt. A readily available, stainless steel, wire mesh implemented in the phase change salt, at the shell side of a shell and tube storage, already yields a 10% increase in overall discharging performance (Opolot et al., 2023). A graphite coating, applied on the mesh, could enhance the corrosion resistance, thereby enabling the the use of a higher conductive steel, such as carbon steel. Furthermore, could a graphite coating increase the overall thermal performance, by generating highly conductive pathways parallel to the mesh (HEDH & Hooman, 2023). A suitable graphite coating is obtained by exploring graphite coatings in various application areas. Together with the requirement of this coating, the first choices are made regarding the components of the coating. In addition, various experimental results are conducted to determine a potential coating composition and application method.

Results showed that a graphite coating consisting of graphite, Polyvinylidene Fluoride (PVDF) and N-Methylpyrrolidone (NMP), applied with the use of a dip coater, followed by drying, could be attached to the carbon steel with a thickness of 2 mm in four layers. The influence of the graphite coating is estimated with the use of a resistance model.

Further research should focus on quantitatively determining the influence of the graphite coating application in combination with the evaluation of the corrosion resistance of the coating.

Contents

List of Figures

List of Tables

x

Nomenclature

Abbreviations

Abbreviation	Definition
AR	Aspect Ratio
CAPEX	Capital Expenditure
CFRP	Carbon Fiber Reinforced Plastics
CSP	Concentrated Solar Power
COP	Coefficient of Performance
CVD	Chemical Vapor Deposition
ECTFE	Ethylene and Chlorotrifluoroethylene
EDR	Exchanger Design and Rating
EG	Expanded Graphite
ETFE	Ethylene and Tetrafluoroethylene
FEP	Fluorinated Ethylene and Propylene
FTIR	Fourier Transform Infrared Spectroscopy
GHG	Greenhouse Gas
GIC	Graphite Intercalation Compounds
HDPE	High-density Polyethylene
HOGF	Highly Oriented Graphite Film
HTF	Heat Transfer Fluid
HVAF	High Velocity Air-Fuel
HVOF	High Velocity Oxy-Fuel
kW	Kilowatt
kWh	Kilowatt-hour
HEX	Heat Exchanger
IEA	International Energy Agency
LFA	Laser Flash Analyser
LMTD	Log Mean Temperature Difference
MAO	Micro Arc Oxidation
MF	Melamine-Formaldehyde
MVP	Mechanical Vapour Recompression
MW	Megawatt
MWh	Megawatt-hour
NMP	N-methylpyrrolidone
PCM	Phase Change Material
PCTFE	Polychlorotrifluoroethylene
PEO	Plasma Electrolytic Oxidation
PFA	Perfluoroalkoxy Alkane
PTFE	Polytetrafluoroethylene
PVD	Physical Vapor Deposition
PVDF	Polyvinylidene Fluoride
StT	Shell to Tube
SEM	Scanning Electron Microscope
TEMA	Tubular Exchange Manufacturers Association
TES	Thermal Energy Storage
TPS	Transient Plane Source
TVR	Thermal Vapour Recompression
XRD	X-Ray Diffraction

Symbols

Symbol	Definition	Unit
a	Surface area per unit bed volume	[m^{-1}]
A	Surface	[m^2]
AR	Aspect ratio	[-]
C	Volumetric heat capacity	[kJ/m^{3}K]
c_p	Specific heat capacity	[kJ/kgK]
d	diameter	[m]
$d_{1\rightarrow 2}$	Distance between two discs	[m]
ΔG	Gibb's free energy	[J/mol]
E	Energy	[J] or [kWh]
D_e	Equivalent diameter	[m]
E_{cell}	Cell potential	[V]
f	Friction factor	[-]
F	Faraday's constant	[J/Vmol]
$F_{1\rightarrow 2}$	Shape factor	[-]
G	Mass flux	[kg/m^{2}s]
g	Gravitational acceleration	[m/s^2]
Gr	Grashoff number	[-]
H	Height	[m]
h	Heat transfer coefficient	[kJ/kgK]
h_i	Interfacial conductance	[W/m^{2}K]
h_0	Film thickness	[m]
I_0	Current amplitude	[-]
k	Thermal conductivity	[W/mK]
K	Permeability	[m^2]
L	Length	[m]
$\dot{m}$	Mass flow	[kg/s]
m	Mass	[kg]
n	Number of mole	[-]
Nu	Nusselt number	[-]
P	Power	[W]
p	Pressure	[Pa]
P_T	Tube pitch	[-]
Pr	Prandtl number	[-]
Q	Heat	[J] or [kWh]
$\dot{Q}$	Heat flow	[W]
r	radius	[m]
R	Thermal resistance	[m^{2}K/W]
Ra	Rayleigh number	[-]
Re	Reynolds number	[-]
t	Time	[s]
T	Temperature	[K]
th	Thickness	[m]
T_0	Amplitude of temperature change	[-]
U	Overall heat transfer coefficient	[W/m^{2}K]
u	Withdrawal speed	[m/s]
v	Velocity	[m/s]
v_∞	Fluid surface velocity	[m/s]
$\dot{V}$	Volumetric flow	[m^3/s]
w	Axial Fluid velocity	[m/s]
W	Work	[J]
z	Axial coordinate	[m]
α	Thermal diffusivity	[m^2/s]

Symbol	Definition	Unit
β	Thermal expansion	[K^{-1}]
γ	Surface tension	[J/m^2]
δ	Distance shell and lower tube	[m]
ϵ	Porosity	[-]
$\epsilon_{surface}$	Surface emissivity	[-]
η	Efficiency	[-]
μ	Viscosity	[Pa s]
ω	Angular velocity	[s^{-1}]
ϕ	Phase	[-]
ϕ_c	Capacity effectiveness	[-]
ρ	Density	[kg/m^3]
τ	Half period	[-]

Sub- and superscripts

Symbol	Definition
amb	Ambient
c	Cold
$char$	Charge
$cond$	Conduction
$conv$	Convection
$crit$	Critical
dis	Discharge
eff	Effective
ext	External
f	Fluid
h	Hot
in	Inlet
ins	Insulation
l	Left
lam	Laminar
lat	Latent
lo	Lower end
liq	Liquid
lm	Log mean
m	Middle
mat	Material
max	Maximum
out	Outlet
p	Particle
pp	Pulsed Power
r	Right
rad	Radiation
req	Required
s	Solid
ss	Stainless Steel
T	Tank
t	Thickness
tot	Total
$turb$	Turbulent
up	Upper end
v	Volumetric
w	Tank wall

1

Introduction

This thesis is established based on the results of the literature report conducted prior to this study. The conclusions of the literature report, which gives the introduction to this thesis, were the following.

The growing consumption of fossil energy resources increases greenhouse gas (GHG) emissions. The subsequent rise in GHG emissions contributes to climate change and its associated impacts on the environment and human societies. To meet the industry sector's target, set by the Dutch government, of reducing GHG emissions by 49% by 2030, relative to 1990 levels, there is a need for energy storage (Government, 2019). Industrial energy consumption accounts for approximately 40% of the current global total final consumption, predominantly reliant on fossil fuels, notably coal. It stands as the second-largest emitting sector following power generation. As the global economy and population continue to expand, the demand for materials and goods escalates, underscoring the significance of comprehending the technologies and strategies capable of facilitating the sustainable production, utilization, and disposal of essential commodities (IEA, 2022). Energy storage offers a potential solution to enhance the utilization of renewable energy within industrial settings. It provides a viable solution to address the intermittent nature of renewable energy sources, allowing for their efficient utilization and reducing reliance on fossil fuels. Moreover, the volatility of fossil fuel prices serves as an additional incentive to reduce reliance on fossil energy sources.

Concentrating on thermal energy storage for steam generation opens up opportunities for multiple sectors, making it a versatile solution. This is because steam generation is one of the common processes within industry. Steam generation in the food industry typically occurs within the range of 4 to 20 bar, corresponding to phase change temperatures of 143.6 to 212.4°C, respectively. Specific to the food industry, the steam demand depends on the batch processes and varies heavily within hours. The heavily fluctuating demand is now often accompanied by the use of fossil fuels in boilers. Research aiming at enhancing the sustainability of boiler usage has led to the adoption of electric boilers or biomass-based boilers. The goal is to research the ability to solely use renewable energy and electric boilers by implementing thermal energy storage to deal with the intermittency of the energy source. The requirement for these thermal storage materials is that they must be capable of delivering energy at temperatures, based on the required steam pressures, between 143.6 and 212.4°C.

Thermal energy storage can be categorized into three types: sensible, latent, and thermochemical storage. The energy density and complexity increase from sensible to latent to thermochemical storage. The maturity of these storage technologies follows the opposite trend. Thermochemical storage is further divided into sorption-based and reaction-based systems. Among these, sorption-based systems are more mature but are not capable of discharging at the desired temperatures. On the other hand, reaction-based thermochemical storage options can achieve the required temperatures, but their maturity level is currently insufficient for practical implementation. As a result, the thermochemical storage option is ruled out.

Sensible storage harnesses the temperature rise of a material to store energy. In contrast, latent energy storage involves a phase change, utilizing the latent heat associated with the transition to store energy. Materials employed for latent energy storage are often termed phase change materials (PCMs). For both thermal energy storage types, sensible and latent, the material itself should have the following desirable properties in Table 1.1.

Thermo-physical properties	Chemical properties	Mechanical properties	Environmental properties	Economic
High thermal conductivity	Chemical stability	Mechanical stability	Low manufacturing energy	Cheap
High energy density (volumetric and gravimetric)	Good charging and discharging ability	Low thermal expansion coefficient	Low carbon footprint	Availability
High heat capacity	Non-toxic	Fracture toughness		Cost of manufacturing
Thermal reliability and stability	Non-explosive	Compressive strength		
Low thermal expansion coefficient	Low corrosion potential w.r.t. heat transfer fluid			
	Compatible with construction material			

Table 1.1: Desirable properties thermal storage materials

Nevertheless, there are differences between sensible and latent energy storage. In the case of sensible storage, an additional factor to consider is the temperature range in which the operation is feasible, as it determines the suitability of a material for a specific application. It also defines the amount of energy, together with the specific heat of the material, that can be stored. On the other hand, latent heat storage, which involves a phase change, relies on both the temperature where the phase change occurs and the latent heat of reaction as crucial parameters to be considered.

Within both categories, certain media may not meet the temperature requirements for effective energy storage and are consequently eliminated. The material groups under consideration, are the following:

Sensible	Latent
Mineral oils	Hydroxides
Molten salts	Metals and alloys
Liquid metals	Salts
Earth materials	Eutectics
Concrete	
Brick	
Metals and alloys	

The characteristics and specific advantages and disadvantages of the categories can be found in the literature study.

In general, sensible storage has as its main advantage the low cost of materials, except for liquid metals and thermal oils, and simplicity of use. Moreover, the majority of sensible storage materials exhibit stability at high temperatures. However, the temperature decrease and thereby the power decrease during discharging is a drawback for sensible storage.

When comparing sensible and latent heat, in general, the latent storage density is around 50 to 100 times higher. Another advantage of latent storage is the more or less constant temperature during discharging. The main drawback of latent heat storage is the poor thermal conductivity of the inorganic salts and hydroxides. In contrast to salts, the metal and alloys have a high thermal conductivity. However, the metals and alloys are generally expensive. All the included categories of latent heat storage are prone to corrosion when in contact with the container material and this is a major drawback.

The literature review concentrated on identifying appropriate materials for storing thermal energy within the necessary temperature range. This thesis will center on assessing the implementation of the thermal energy storage solution. The subject of this research was suggested by Arcadis and is conducted at the Technical University Delft. This results in the following research question:

"**How might thermal energy storage be realized within the food industry?**"

This research question will be addressed through the following sub-questions:

- What is the typical steam demand profile observed in the food industry? And how could thermal energy storage be applied?
- Which thermal storage materials show promise for integration within the food industry?
- Which storage method is most relevant for each material, and want are the corresponding key parameters?
- To what dimensions does this lead for thermal energy storage systems?
- How is the discharged energy converted into steam for the respective materials?
- What approaches can be adopted to accelerate the market readiness of phase change salts?
- What are the effects of implementing these potential improvements?

These questions will be answered throughout this report.

Next, the case description on which the dimensions of the thermal energy storage are based will be outlined.

2

Case description

The literature review outlines the imperative for energy storage in a broad context and describes the developments for a more specific category: thermal energy storage. Additionally, it describes the various types and material choices available. Subsequently, this research narrows its focus to the specific application of thermal energy storage within the food industry, considering the challenges posed by fluctuating steam demand and exploring potential solutions. A problem description is provided in this chapter which includes the fluctuating steam demand and concludes on the amount of energy which needs to be stored.

Arcadis has provided data of typical steam demand in the food industry. This data shows the steam demand for every hour of a year in kg/hr, Figure 2.1. Some general information about this data is presented in Table 2.1.
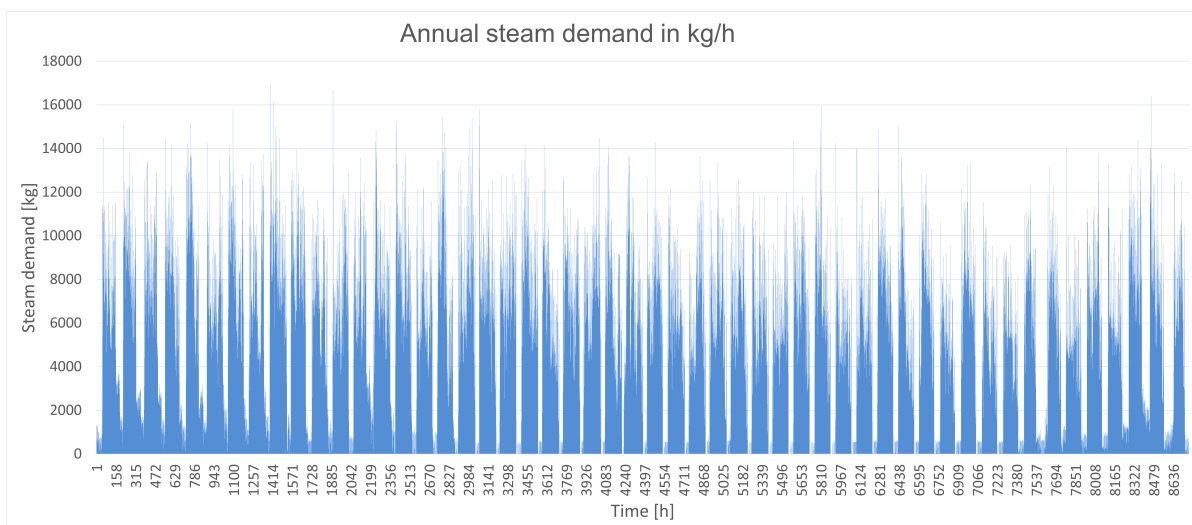
Figure 2.1: Case study annual steam demand.

Characteristic	Value
Steam pressure	11 bar
Steam temperature	184.06 °C
Mean steam demand	5,428 kg/hr
Maximum steam demand	16,960 kg/hr
Total annual demand	47,546,640 kg/yr
Feed water enthalpy	435 kJ/kg ($\approx$104°C)
Steam enthalpy	2,780.6 kJ/kg

Table 2.1: Characteristics of steam demand case

To better understand the general pattern, the data is examined more closely. A typical steam demand reduction can be seen during two days of the week, which clearly is the weekend. In order to see a typical pattern during the week a general week is presented in Figure 2.2. The term general week is used since the steam demand in this particular week is the closest to the mean steam demand over all weeks.
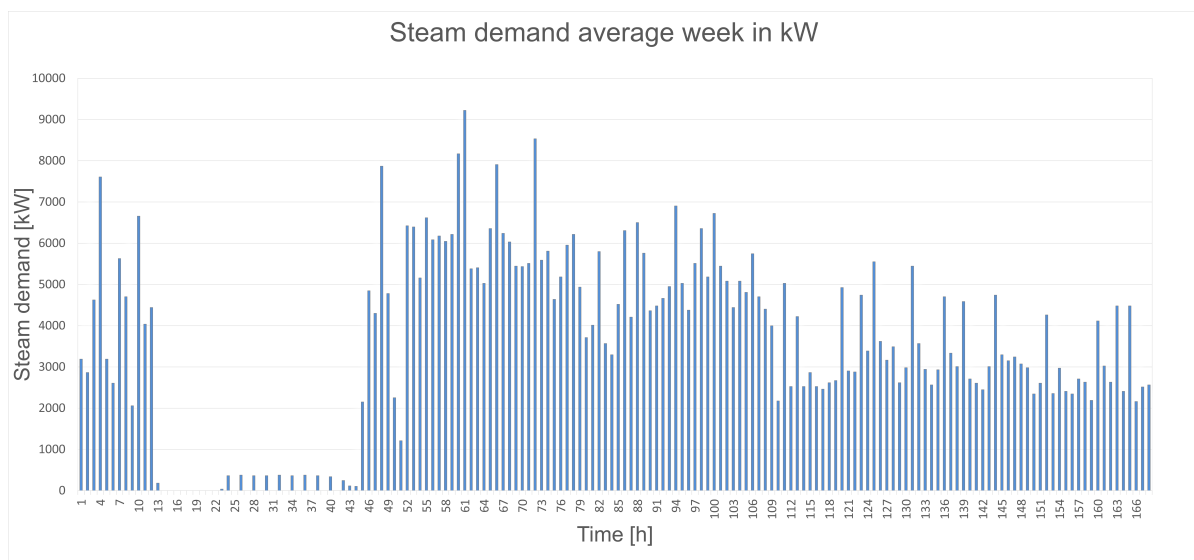
Figure 2.2: Fluctuating steam demand in kWh/h for one, average, week

During this study, the emphasis lies in understanding and designing the mechanisms of energy storage rather than delving into the origin of the stored energy. For example, will it be (re)charged by excess energy or due to solar panels is not part of this study. However, to find a useful application, the scenarios that could possibly find application within the food industry have been determined based on broad lines of energy supply types. This resulted in two scenarios:

- A stand-alone energy supply. This energy source can be recharged in times of excess energy or by waste heat recovery, for example. In some cases, for example, when using waste heat of a process, it will be useful to have two alternating storage tanks. The first storage will contribute by providing energy for a process and the parallel tank can be charged by the waste heat of another process.
- A storage type that will handle peaks in energy demand. A constant energy source is assumed. Here, the storage will discharge during peaks above this constant demand and recharge during lower energy demand. Herein, an added value is that the equipment within the processes does not have to be able to handle the peaks and can therefore be smaller.

These two scenarios are projected on the data which is provided.

It is presumed that the energy for charging is supplied through resistive heating. This could be optimized in the future by using a heat pump, for example. The Coefficient of Performance (COP) for resistive heating is 1. The COP is a measure of delivered thermal energy with respect to the consumed electric energy. Heat pumps enable the option to deal with higher to COP's. Higher temperature heat pumps, however, show a decrease in COP with respect to lower temperature heat pumps.

2.1. Scenarios
2.1.1. Stand alone
In the stand alone scenario, the determination of required energy storage is based on both the duration and magnitude of steam demand within these hours. Nevertheless, this storage system must have the capacity to function as an independent energy source during peak hours. To optimize the design without undue large scale, the peak hours are strategically selected based on the characteristics of a typical week. After consultation with Arcadis and considering the feasibility of employing the aforementioned two-tank configuration throughout the entire 24-hour day, it has been decided that the storage system should be capable of generating energy for a duration of 12 hours. This choice is debatable sd other choices could have been made too.

The highest energy demand in consecutive 12 hours for a general week is equal to 120,680 kg steam with a minimum of 7,720 kg/hr and a maximum of 14,160 kg/hr. The total storage is equal to 78,609.6 kWh

2.1.2. Peak shaving
Peak shaving diverges from the standalone scenario in that it operates under the assumption of a standard boiler capacity, with the storage system exclusively addressing the peaks in demand. When there is a low energy demand, the storage system will be charged by the energy that is not needed for the boiler. The determination of the appropriate boiler capacity involves summing the surpluses and shortages when considering the assumed boiler capacity. The assumed capacity is deemed accurate when the net sum approximates zero. This stems from the nature of peak shaving, where surpluses are utilized to offset shortages.

The advantages of peak shaving are mainly based on the use of smaller equipment in combination with a more constant rate. A constant rate could increase the efficiency of the equipment.

Peak shaving is valuable for a fluctuating demand. To prevent the storage from exclusively charging during weekends, all hours with a demand below a certain threshold, 1 kWh in a specific hour, are filtered out. For the average week, assuming a boiler capacity of 4.4 MW, the cumulative sum of deficits and surpluses amounts to 7.9 MWh. The value of 4.4 MW is manually found by changing the boiler capacity with 0.1 kW every time and finding the lowest value of the sum. To contextualize, the 7.9 MWh constitutes 1.3% of the total energy demand for that week. When choosing this type of storage, optimizing this value is required. To generate an overview of the surpluses and deficits Figure 2.3 is shown. What should be noted is that a negative deficit is equal to a surplus in the figure.
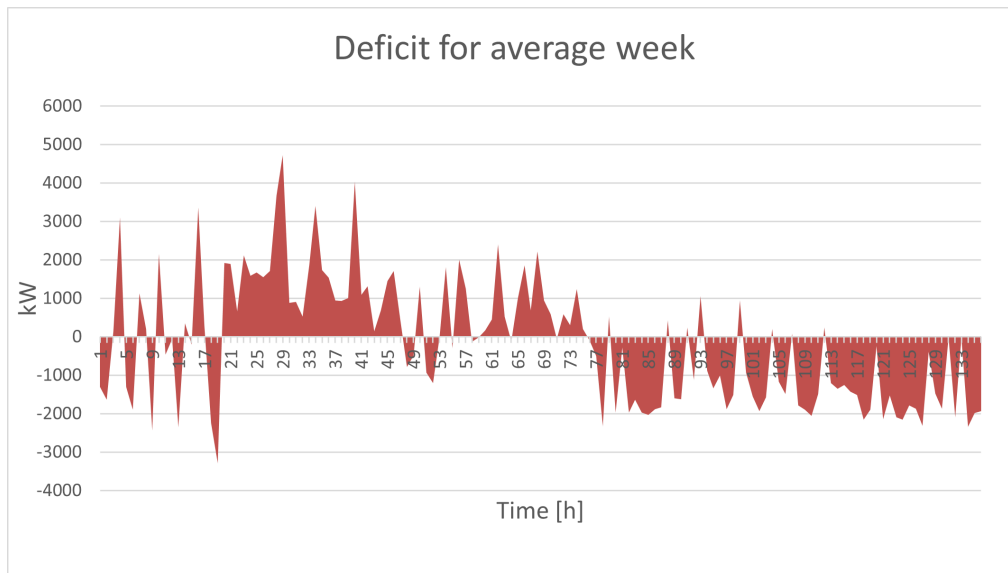
Figure 2.3: Deficit for every hour when assuming constant steam boiler capacity of 4.4MW for the average week.

Moreover, the determination of the storage size should be predicted on the cumulative deficits or cumulative surpluses, as illustrated in Figure 2.4. It is essential to note that, in this context, the storage is presumed to be half full initially. This assumption entails a trial-and-error process, ensuring that the negative surplus in Figure 2.4 aligns with twice the initial assumption. In the present case, this initial assumption is 20 MWh for a tank initially at half capacity, corresponding to the negative surplus peak of approximately 40 MWh.
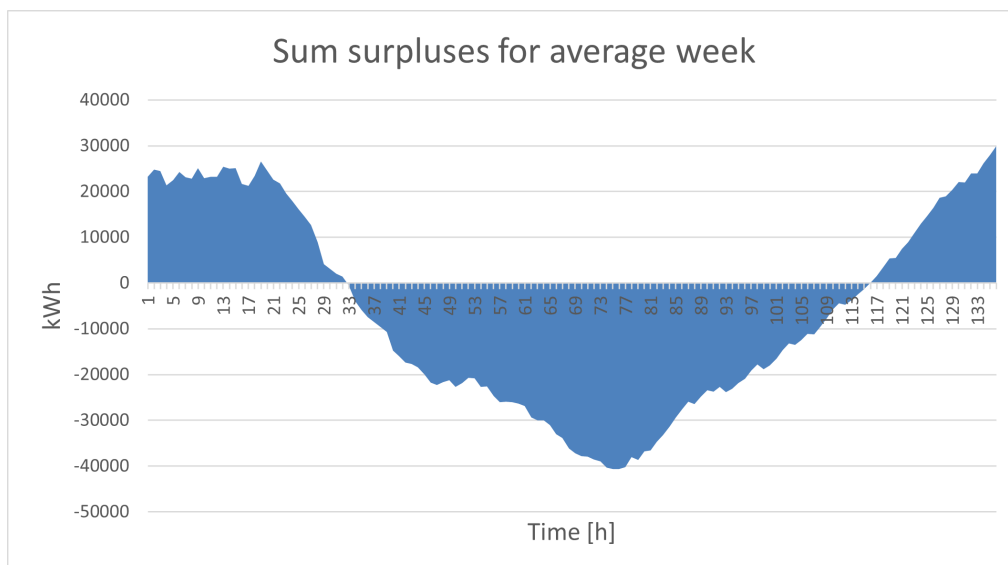
Figure 2.4: Sum surplus (with assumed boiler capacity of 4.4 MW) for one, average, week.

2.1.3. Annual reference

In order to explore the feasibility of these approaches on the data for the whole year, this set-up is tested for all the data. For the stand-alone case, this resulted in a storage of 98 MWh. For the peak shaving case, Figure 2.5, shows storage capacities of around 120 MWh. This is even with a larger standard boiler capacity of 5MW. Based on these annual values, the peak shaving case results in a larger storage which is not expected. This is due to the long consecutive deficits in the steam demand case. Using a backup boiler, which is also used during peak demand nowadays, can be a feasible solution. However, within this research, the focus will be on the general week.
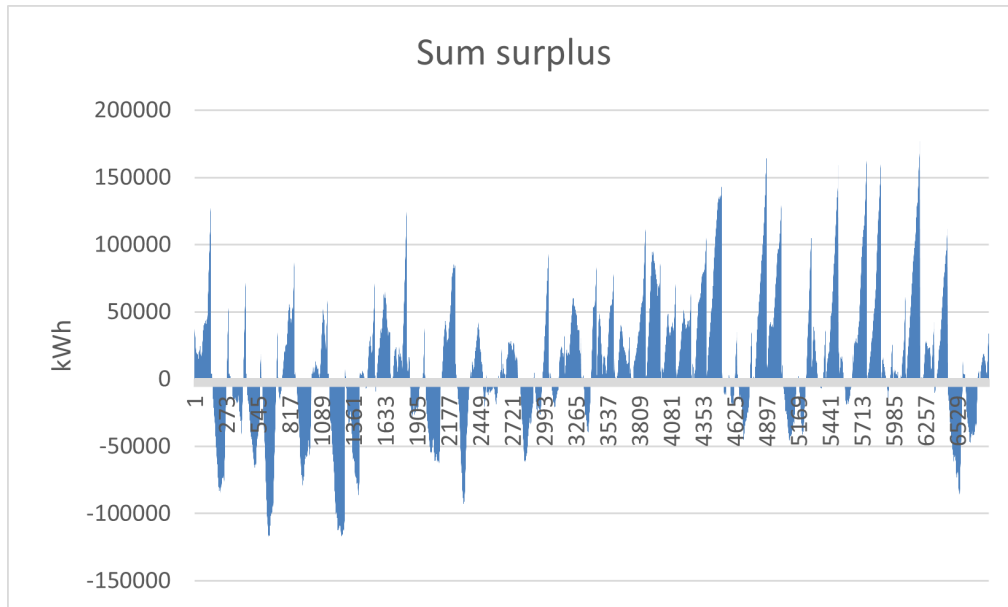
Figure 2.5: Sum surplus on annual basis.

3

Choices

In this Chapter, the selection of thermal energy storage materials for the subsequent phase of the research will be determined. The potential materials capable of generating steam between 4 and 20 bar have been extracted from the literature study. The 20 bar, was considered limiting, as many thermal storage materials, including organic phase change materials, are unable to discharge at these temperatures.

Reviewing the list of potential materials, there are essentially three storage methods represented: liquid sensible, solid sensible, and phase change materials undergoing a phase transition between solid and liquid. It has been decided, in consultation with Arcadis, that it is worthwhile to select and further develop one material from each category. Latent storage, which includes phase change materials, is less deployed than sensible storage materials. However, to harness the numerous advantages offered by latent storage, this study seeks to find possibilities for integrating such media within the food industry. In conclusion, the more established sensible, liquid and solid, storage technologies will be adapted for application in the food industry, and additional enhancements will be explored through the incorporation of phase change materials.

3.1. Choices storage materials

3.1.1. Sensible storage choice

Based on the literature research, it is evident that there are still several potential sensible storage materials available for consideration.

Liquid

For the liquid sensible storage materials, three possibilities are present: thermal oil, molten salt, and liquid metal. The high temperature of the lower boundary for the use of liquid metal, which is the melting temperature of metals, combined with the limiting temperature of most well-known thermal oils makes the molten salts the most interesting candidate. In addition, molten salts are recognized as the most mature thermal storage technology among the existing liquid sensible materials. Therefore, it has been decided to include this material in the subsequent phase of research.

Solid

In the case of solid sensible storage materials, presented in the first column of Table 3.1, further exploration is required due to the availability of multiple options, leading to a more detailed analysis of the material characteristics. First, a ranking is performed based on the mean ρc_p, which represents the volumetric energy density in kJ/m^{3}K. These values are extracted from the literature for each material. Secondly, a ranking to assess the thermal conductivity of the remaining materials is applied, which is a measure of how fast the storage is able to charge or discharge.

	Mean specific heat, c_p [kJ/kgK]	Mean density, ρ [kg/m^3]	$\rho * c_p$ [kJ/m^{3}K]	First ranking	Mean thermal conductivity, k [W/mK]	Second ranking	Total ranking
Sand	0,89	1600	1424	8	0,89	7	8
Gravel	1,84	2050	3772	2	1,84	2	2
Rock	1,035	2605	2696,2	6	1,035	5	5
Brick	1,17	2400	2808	5	1,17	4	4
Concrete	0,915	2500	2287,5	7	0,915	6	7
Ceramic	0,75	4540	3405	3	0,75	8	5
Cast iron	0,6985	7350	5134	1	69,85	1	1
Steel slag	0,88	3430	3008,1	4	1,46	3	3

Table 3.1: Properties extracted from literature for the selected storage materials

In Table 3.1 the results of this method are presented. In the final column, the overall ranking is determined by the mean of the previous two rankings, with each ranking carrying equal weight. By employing these sequential selection steps, the most promising sensible storage materials have been identified for the next phase of investigation. The three materials that are the most promising include cast iron, gravel, and steel slag. It should be noted that cast iron represents a material group of steels and alloys. From the materials left, all three have advantages and disadvantages.

Gravel and slag have almost similar properties. Cast iron has better storage performance. However, this cast iron can result in a higher price due to the high cost and density of these materials. The high price of materials is not directly defining the high price of the storage, since the cost of the whole system is more important than the cost of the material itself. Therefore, the cast iron is not yet excluded.

However, multiple researchers have paid attention to the use of slag since multiple-sided advantages are present. First of all, this slag is a waste product of industry and is therefore of particular interest according to the price and environment. Within the research of Calderón-Vásquez et al., 2021, it is concluded that in this case copper slag, is indeed competitive compared to molten salt technology based on high temperature usage and reduced capital cost. In the Netherlands, significant amounts of this material find application in construction. It serves various purposes such as providing a base for roads or as fill material to elevate dykes, noise barriers, and landfill sites. However, a report has been released which indicates that when steel slag interacts with rainwater or groundwater, harmful substances present in the slag dissolve into the water, leading to the release of a wide range of heavy metals. This resulting contaminated water, characterized by an exceptionally high pH level, poses environmental risks by contaminating the soil and surface water (Broekman, 2023). Finding application of slag material in thermal energy storage has thus multiple benefits. Consequently, it is concluded that besides molten salts, the slag of iron, or another slag type originating from a metal or alloy, is included in further research based on the possibility of reusing waste in combination with good thermal properties.

3.1.2. Latent storage choice
The latent storage materials are categorized into material groups based on the options extracted from the literature. This classification is employed due to the wide range of materials encompassed within each group. For instance, alloys can exist in various compositions of elements, and within these compositions, the weight percentages of elements may also differ, leading to an extensive array of possibilities.

Nevertheless, to concentrate on a particular material or material group, a more detailed examination of the phase change temperature is undertaken. To be able to use metals and alloys as phase change material, temperatures of 340-1084°C should be reached in order to melt the material. Higher temperatures lead unavoidably to greater losses. Therefore, the focus of this thesis will not be on using metals and alloys as phase change materials. Salts, salt eutectics and hydroxides are still left. Hydroxides and salt eutectics are a subcategory of salts. To conclude, the phase change salts are included in further research.

4

Design

4.1. Structure of Chapter 4

In this chapter, the design of thermal storage systems, for the three chosen materials, will be outlined through the following sequential steps, shown in Figure 4.1:

1. Explanation material
2. Examples of the specific storage material solutions will be analysed in literature
3. Derivation of the storage method, such as packed bed, fluidized bed, shell and tube, etc., based on the insights gained from literature. Thereafter, examining the key parameters which are essential for the effective design of the storage system
4. Determination of the optimal value of these key storage parameters
5. Utilization of these optimal values to ascertain the dimensions of the storage system
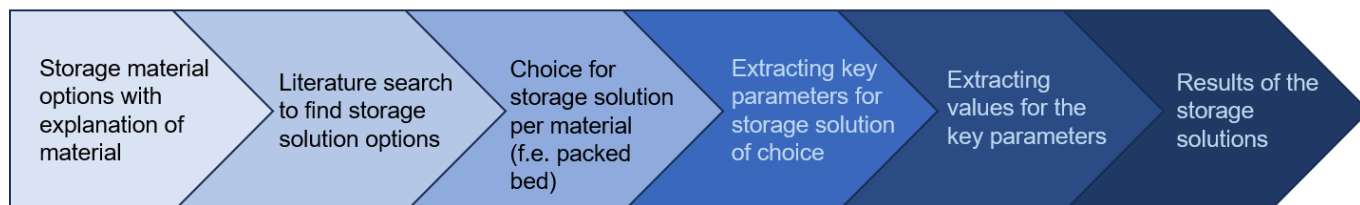
Figure 4.1: Overview chapter 4.

4.2. Slag
4.2.1. Explanation material
During the production of iron and steel, waste in large amounts is produced which is called slag. This material, known as metallurgical industry slag, is primarily generated during the iron ore melting process, resulting in the production of approximately 10-20% slag per ton of steel. A part of the waste is considered as useful by-product and is recycled. The other part is seen as waste and can have negative influences on the environment. Consequently, using slag as storage medium solves problems in the iron and steel sector concerning waste management. Slag predominantly consists of oxides. These oxides include aluminium, calcium, silicon, iron, and magnesium. Upon cooling, the slag transforms into a material with ceramic properties. This material exhibits either an amorphous or crystalline structure, depending on the rate of cooling (Ortega-Fernández et al., 2015) (Gutierrez et al., 2016). The steel slag can be crushed or grounded into different sizes (Roslan et al., 2016). A picture of steel slag is shown in Figure 4.2.

Figure 4.2: Example representation of slag (Calderón-Vásquez et al., 2021)

Ortega et al. (2015) concluded, in 2015, that using slag is a promising thermal energy storage material. The thermal stability up to, at least, 1000 °C in combination with the good compatibility with air as heat transfer fluid, did not reveal any corrosion after 500 hours of tests. These were some of the main positive findings besides the good thermo-physical properties.

Steel slag is, as said before, utilized for internal recycling within the steel industry. Other application areas are road construction, cement production, the construction sector, and civil engineering (W. Gao et al., 2023).

4.2.2. Literature

Following an extensive review of the literature on the utilization of slag as a medium for thermal energy storage within a packed bed, three articles were identified, which collectively establish a framework for the pursuit of initial outcomes in this domain. Primarily, a summary outlining the objectives of each article will be presented followed by the results.

In the first article, published in 2015 by Ortega et al. (2015), electric arc furnace slag is reviewed as a new thermal storage medium within a packed bed system. Therefore, the stability, both thermal and chemical, and the influence of temperature on the physical properties are assessed. In addition, a configuration of a storage system based on air as the heat transfer fluid is proposed in this article. The studied slags include EAF slag 1 and EAF slag 2. However, since they showed almost similar properties, EAF slag 1 is used as storage material in the proposed configuration, where the slag is computationally modelled as a function of ΔT_{tol}, which represents the maximum outlet fluid temperature difference. This temperature differential of the HTF is calculated as the disparity between the HTF outlet temperature over time and the initial outlet HTF temperature. Based on the ΔT_{tol}, three different operation modes are modelled, since certain processes may face operational constraints if the outlet temperature of the storage system decreases excessively. An example is an electricity production steam turbine. For the fluid temperatures, the basis on which the ΔT_{tol} is projected is for the hot fluid temperature of 1073K and the cold fluid temperature of 873K.

The first mode represents the temperature tolerance allowed for electricity production steam turbine, $\Delta T_{tol}=\pm 5$K. The second operation mode allows a larger temperature difference of $\Delta T_{tol}=\pm 20$K. This tolerance is appropriate for different heat demanding processes. The last one is based on a mixed tolerance, $\Delta T_{tol}=+20$K for charging and $\Delta T_{tol}=-5$K for discharging.

The model description is a porous media formulation, based on the Ergun equation. The packed bed is treated as a whole, a continuous porous material. A close random sphere packing arrangement, with a void fraction of $\epsilon=0.37$, is assumed. This results in a transient problem for the heat transfer with both phases not in thermal equilibrium. Therefore, a two-phase model is used. Both phases are coupled only by the heat transfer, with a constant heat transfer coefficient. To determine this coefficient, the Nusselt correlations for Re_p>15 are used.

$$Nu = 2 + 1.1 Re_p^{0.6} Pr^{1/3} \tag{4.1}$$

The thermal conductivity of both phases is determined based on a model of Wakao and Kaguei, 1983. Within this model, isentropic behaviour in both directions, axial and radial, is assumed.

Furthermore the total energy input (charge) and stored energy (discharge) are evaluated according to

$$E_{input/stored} = \int_{t_c/t_d} \dot{m} c_p(T)(T_{out} - T_{in})\, dt \tag{4.2}$$

The convective heat transfer coefficient of the outer wall in contact with atmospheric air, h, is estimated at 7W/m^{2}K and this resulted in

$$P_{wall}^{loss} = \int_{area} h(T_{ext} - T_f)\, dA \tag{4.3}$$

And losses due to the fan use

$$E_{pumping} = \int_{t_c+t_d} \frac{\dot{m}}{\rho} \Delta p\, dt \tag{4.4}$$

The overall efficiency is defined as,

$$\eta = \frac{E_{stored}}{E_{input} + E_{pumping}} \tag{4.5}$$

Within this formula for the efficiency, the energy of the fluid within the acceptable range for each mode is considered useful energy. This results in the fact that losses are only based on pumping energy and losses through the wall.

The results showed that the first mode, with the restriction on temperature difference of $\pm 5K$, showed a huge decrease of 75% of useful storage volume after 10 cycles. This is due to the fact a large amount of the thermocline zone is excluded due to the temperature restrictions. The other modes showed a more stationary state after some cycles. Therefore, in the results, only the first mode is split into cycles.

Parameter	Mode 1, cycle 1	Mode 1, cycle 3	Mode 1, cycle 10	Mode 2	Mode 3
E_{input} [kWh]	95.5	51.2	26.1	58.4	40.2
E_{stored} [kWh]	70.2	46.7	25.0	56.4	38.8
Lateral losses [kWh]	1.31	1.17	0.55	1.39	0.91
Pumping losses [kWh]	0.93	0.55	0.29	0.66	0.46
Efficiency [-]	0.58	0.70	0.80	0.95	0.95

Table 4.1: Results from research of (Ortega-Fernández et al., 2015)

The second article aims to find the optimal heat recovery system for an electrical arc furnace of a steel making plant by using the waste material of this plant, the slag, in a packed bed (Ortega-Fernández & Rodríguez-Aseguinolaza, 2019). The large heat release needs to be captured in a relatively short period. This therefore results in high pressure drops. To obtain a continuous heat supply, a double storage tank is designed to overcome the batch operation limitation of the furnace. This means that if one tank is in charging mode, the other tank is in discharge mode, this process is shown in Figure 4.3. Multiple particle diameters and aspect ratios are addressed in this study.
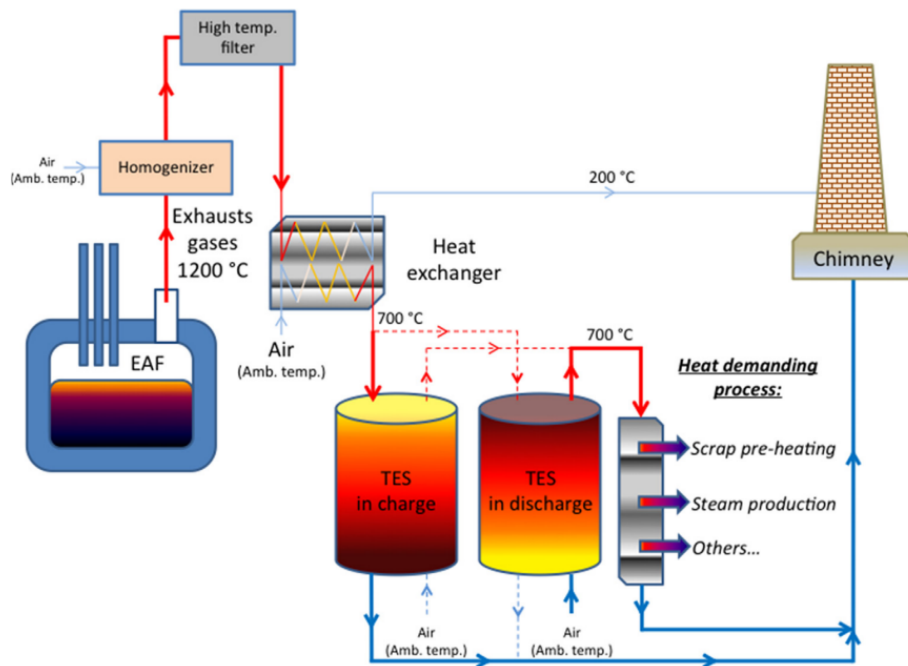
Figure 4.3: Overview system of Ortega-Fernández and Rodríguez-Aseguinolaza (2019)

The casting process of one cycle takes 60 minutes in total. However, the charging period within this configuration is 45 minutes with air at 700°C, since 15 minutes are required for other parts of the process. Discharging should take 60 minutes to target continuous heat supply for the other processes in which the energy from the thermal energy storage is used.

Similar to the previous article, the packed bed is treated as a continuous porous medium. However, more in-depth insights are provided about the model itself. The pressure drop is stated as

$$\frac{\Delta p}{H} = \frac{150\mu}{d_p^2}\frac{(1-\epsilon)^2}{\epsilon^3}v_\infty + \frac{1.75\rho_f}{d_p}\frac{(1-\epsilon)}{\epsilon^3}v_\infty^2 \tag{4.6}$$

And the fluid and solid energy conservation as

$$\epsilon\rho_f c_{p,f}\left(\frac{dT_f}{dt} + v_\infty\frac{dT_f}{dx}\right) = k_f\left(\frac{d^2T_f}{dx^2}\right) + h_p a_p(T_s - T_f) - h_{loss}a_w(T_f - T_{amb}) \tag{4.7}$$

$$(1-\epsilon)\rho_s c_{p,s}\left(\frac{dT_s}{dt}\right) = k_s\left(\frac{d^2T_s}{dx^2}\right) + h_p a_p(T_f - T_s) \tag{4.8}$$

h_p is the heat transfer coefficient between both phases and this is the coupling parameter between the two equations. This heat transfer coefficient is retrieved from the Nusselt correlations, dependent on Re<15 of Re>15.

A more extensive determination of the heat loss coefficient is provided with respect to the previous article. However, the definition of the energy charge, and discharge are similar. Nevertheless, there exists a disparity in the definition of the efficiencies:

$$\eta = \frac{E_{dis}}{E_{char}} \tag{4.9}$$

where the only losses are due to thermal losses through the wall. Furthermore, the material efficiency is defined as

$$\eta_{mat} = \frac{E_{dis}}{E_{max}} \tag{4.10}$$

where the E_{max} is defined as the total energy the packed bed can store when a temperature increase of 200 to 700 °C is established. 200°C is based on the steam generation temperature plus a pinch temperature of approximately 15°C.

This resulted, for different numbers of casting (cycles), in a total (dis)charged energy, pumping energy, cycle and material efficiencies, presented in Table 4.2.

	1 casting cycle	2 casting cycles	3 casting cycles
Charged energy [kWh]	1419	1382	1445
Discharged energy [kWh]	893	928	930
Pumping energy [kWh]	46	29	17
Cycle efficiency [-]	62.9	67.1	64.4
Material efficiency [-]	85	88.4	88.6

Table 4.2: Results from research of Ortega-Fernández and Rodríguez-Aseguinolaza (2019)

The third study evaluated the viability of employing copper slag as a storage medium in scenarios where Concentrated Solar Power (CSP) serves as the charging energy source (Calderón-Vásquez et al., 2021). This process is illustrated in the paper and can be seen in Figure 4.4.
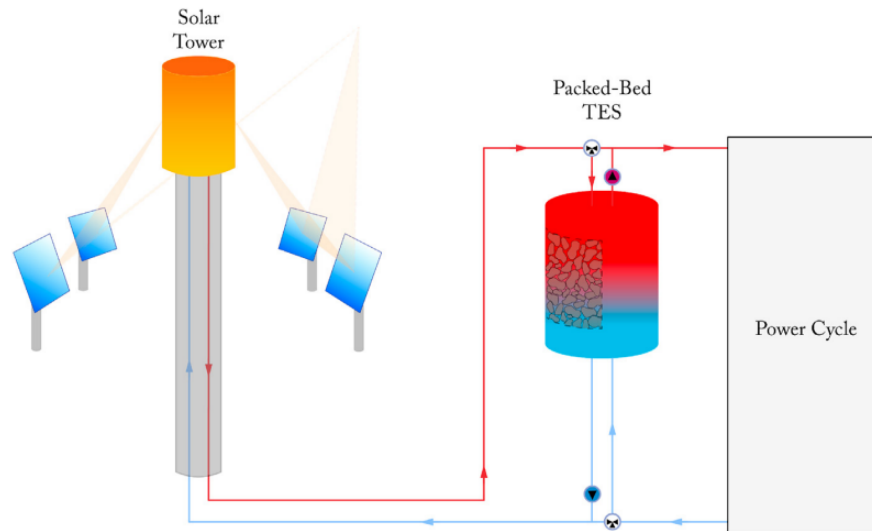
Figure 4.4: Representation of the system within the research of Calderón-Vásquez et al. (2021)

A heat transfer model was developed in order to predict the cyclic behavior of the storage and assess the impact of the dimensions on the storage. Within this research, the approach is somewhat different. The charging time, temperature of the HTF (air) and mass flux have been fixed. The aspect ratio and volume are varied and the influence on the heat transfer is evaluated. The energy balances are defined as

$$\epsilon \rho_f c_{p,f} \frac{\delta T_f}{\delta t} + \epsilon \rho_f c_{p,f} w \frac{\delta T_f}{\delta z} = h_v(T_s - T_f) + \frac{U_T(\pi d_T)}{A_T}(T_\infty - T_f) \tag{4.11}$$

$$(1 - \epsilon)\rho_s c_{p,s} \frac{\delta T_s}{\delta t} = h_v(T_f - T_s) + k_{s,eff} \frac{\delta^2 T_s}{\delta z^2} \tag{4.12}$$

where $k_{s,eff}$ is defined as

$$k_{s,eff} = \epsilon k_f + (1 - \epsilon)k_s \tag{4.13}$$

and the heat transfer coefficient, which couples the two equations is defined as

$$h_v = (G/d)^{0.76} \tag{4.14}$$

The pressure drop, energy charge and discharge and efficiency is defined similar to the second article. This results for different AR and volumes in the following round trip efficiency and charged energy densities are presented in Table 4.3.

	AR=1 & 0.5m^3	AR=2 & 0.5m^3	AR=1 & 2.5m^3	AR=2 & 2.5m^3
Round-trip efficiency [-]	85	77	80	78
Charge density [kWh/m^3]	130	85	83	53

Table 4.3: Results from research of Calderón-Vásquez et al. (2021)

Conclusions from previous literature cases

Observations across the three cases show a commonality: each employs a packed bed storage configuration, with air serving as the designated heat transfer fluid. In all cases the charging and discharging occurs in opposite directions. Moreover, the similarities between the three cases will be addressed based on the material properties and void fraction. These are:

- The void fraction in the three cases is ~ 0.4
- The slag properties, that were present in all three cases, of EAF slag 1 include

  - ρ = 3430 kg/m^3
  - c$_p$ = 865 J/kgK
  - k = 1.47 W/mK

However, other different system parameters and results are presented in Table 4.4.

	System 1	System 2	System 3
Volume tank [m^3]	1	3	0.5-2.5
Aspect ratio	2	0.5/1/2/4	1/2
Diameter pebbles [cm]	1	0.5/1/2	1.7
Mass flow [kg/s]	0.1	0.43-2.65	0.036-0.17
Temperature hot fluid [K]	1073	973	923
Temperature cold fluid [K]	873	293	293
Charging time [min]	-	45	480
Energy density discharge [kWh/m^3]	38.8-46.7	297.7-310	45-118
Fluid flow [kg/s]	0.1	0.43-2.65	0.036-0.17

Table 4.4: Comparison between three literature cases

The efficiencies of the systems are determined differently. This makes the efficiencies not comparable. Therefore, these are not included in the comparison table.

What can furthermore be learned from the three cases, is that if the outlet temperature tolerances are too tight, the useful storage volume decreases rapidly. However, as Ortega et al. (2015) stated, the tolerances for heat demanding processes are less tight than the electricity production steam turbine and therefore this works in the favor of this research. Moreover, what can be learned from the second article, is that if the charging and discharging are required to be fast, the energy losses based on the pumping increase enormously, which is an unfavourable effect. In addition, the two-tank solution for using waste heat is another interesting application, found in the second article. The third article shows the effect of the different aspect ratios and volume and this will be further investigated in the next step, the storage method and key parameters. Moreover, the third article demonstrates the effects of employing CSP as a charging medium, which could be of significant interest when utilizing this particular type of energy source.

Furthermore, the heat transfer equations utilized in the referenced papers serve as the foundation for determining the dimensions, losses, and heat transfer aspects in this research.

4.2.3. Storage method and key parameters
The storage method will involve a packed bed system, characterized by the following key parameters that can be derived for such a configuration:

- Temperature of the packed bed when fully charged
- Temperature tolerance HTF
- Aspect ratio
- Diameter slag pebbles
- Mass flux

In addition, the cycling behaviour and temperature development of the HTF upon discharging are determined. This will lead to a required volume and configuration of the packed bed.

4.2.4. Value key parameters
To gain insights into the optimal value of the key parameters, parametric studies are searched within literature. A parametric study involves a systematic variation of multiple model parameters, enabling the automated execution of one or several analyses for each unique combination of parameters within the system ("Defining a parameter study", n.d.). Within these cases, all the other parameters are set and the influence of one parameter ought to be found.

Temperature
As said before, the maximum operating temperature of slag is around 1000°C. When temperatures above 400°C were present, some mass gain was observed in the first cycles. This is assumed to be caused by oxidation of the slag. However, in consequent cycles, the mass gain decreased to less than 0.5wt%. This value is low enough to assume thermal stability (Calderón-Vásquez et al., 2021). Literature which includes experimental results, is focused on the application area in which the discharged energy is used. For example, the parametric study of Ortega et al. (2017). This study is focused on using temperatures of 20-700°C since it is oriented to the next generation CSP electricity production. To be able to use the results obtained and prevent the required use of high grade steel materials, the maximum temperature is set to 700°C in this study.

Aspect ratio
The aspect ratio of a packed bed is defined as the ratio between the length of the tank and the diameter,

$$AR = \frac{L}{d_T} \tag{4.15}$$

Ortega et al. (2017) performed a parametric study in order to find the optimal aspect ratio for a packed bed with slag material. With a fixed mass flow rate, the aspect ratio 2 showed promising results. This is based on Figure 4.5_l, in which can be seen that increasing the aspect ratio from 0.5 to 5, a 30% increase in energy stored is achieved. However, what also can be noted is that the efficiency does not increase substantially after reaching the aspect ratio of 2. In Figure 4.5_r the efficiency is presented. What should be noted is that this is the efficiency of the first cycle. Subsequent cycles can obtain efficiencies up to 95% which will be explained later. To conclude, based on the results of this parametric study in combination with the mechanical complexity of tanks with a higher length, the aspect ratio of 2 is chosen to be optimal.
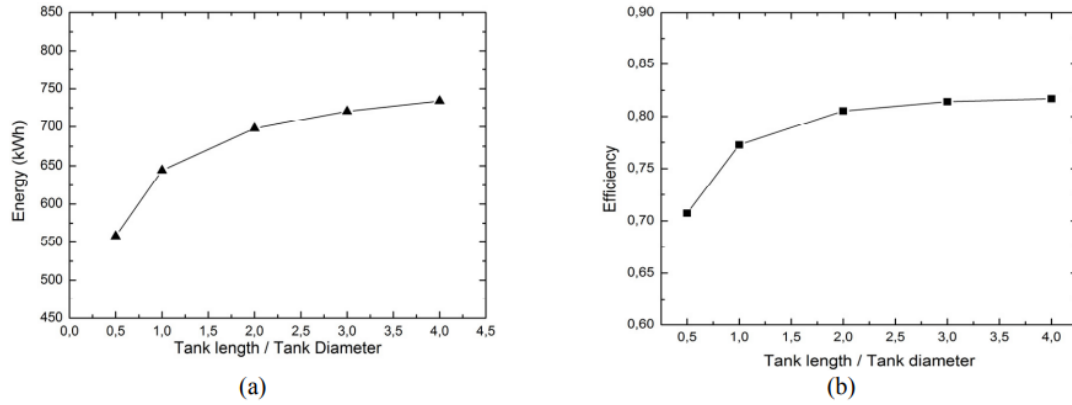
Figure 4.5: Discharged energy in kWh (left) and efficiency (right) for different AR with the use of mass flow 0.3 kg/s (Ortega et al., 2017)

Particle diameter

The influence of the HTF mass flow rate and particle diameter is assessed as a combination within the study of Ortega et al. (2017). An aspect ratio of 2 is considered. The results can be seen in Figure 4.6.
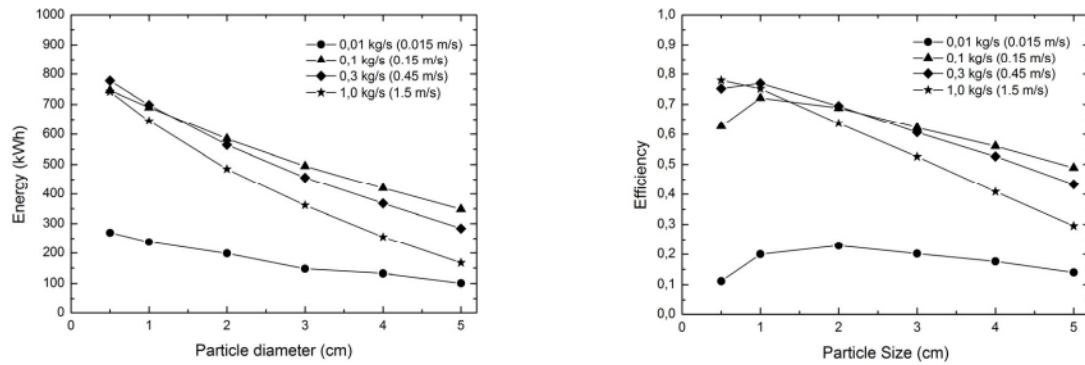
Figure 4.6: Parametric analysis of mass flow rate and particle diameter on discharge energy (left) and efficiency (right) (Ortega et al., 2017).

It can be concluded from this figure that, independent of the mass flow rate, a larger particle diameter results in a smaller amount of stored energy and a decrease in energy efficiency. In addition, in the right Figure, the energy efficiency in can be found for different particle sizes. In this paper, the efficiency is defined as:

$$\eta = \frac{E_{dis}}{E_{char} + E_{pump}} \tag{4.16}$$

The efficiency drops for the smallest diameter of 0.5 cm. This can be explained by the increase in the pressure drop induced by the packed bed. The above conclusions lead to an optimal particle diameter of about 1 cm.

Velocity HTF

Next, the influence of different flow velocities of the HTF was analysed. The flow rates in Figure 4.6 varied between very laminar to very turbulent. First, it can be concluded that the lowest mass flow rate (0.01 kg/s) gives by far the lowest discharged energy and efficiency. This can be explained by the dominance of conduction and radiation as heat transfer mechanisms at low velocities. Conduction between the solid particles in the axial direction is the main cause of an increase of the temperature stratification region. At higher speeds, convection as a heat transfer mechanism will have a greater influence which has a positive effect.

Nevertheless, the highest mass flow rate (1 kg/s), also gives lower discharged energy and efficiency at some particle diameters. This is because the pebbles are unable to release or absorb energy at this rate. For smaller particle diameters, this has an even smaller influence, shown in the left figure, since the thermo-physical properties, such as thermal conductivity, have less influence for smaller diameters.

Furthermore, the influence of the particle diameter on the outlet temperature of the HTF is assessed in Figure 4.7.
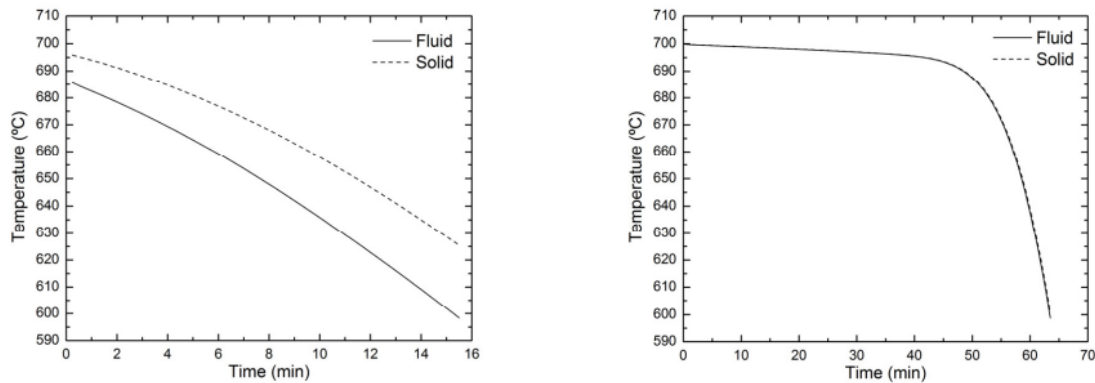
Figure 4.7: Temperature of solid and fluid during discharge. Diameter pebbles 5 cm (left) and diameter pebbles 0.5 cm (right) (Ortega et al., 2017).

From this, as expected, it can be concluded that with a larger particle diameter, Figure 4.7$_l$, the temperature of the HTF at the outlet is not equal to the temperature of the solid. With a smaller particle diameter, Figure 4.7$_r$, the outlet temperature is equal to the temperature of the solid. However, these results had an HTF mass flow rate of 1 kg/s. Therefore, it could be interesting to see these results for lower mass flow rates. Furthermore, it is also important to see the effects of the outlet HTF temperature as function of discharging time.

Temperature development upon discharging

Ortega-Fernández and Rodríguez-Aseguinolaza (2019) have shown the temperature progression of the HTF during discharge in Figure 4.8. The tolerances of the HTF outlet temperature determine the discharging time. For example. if the tolerances are 20°C, the discharging will stop earlier than when having a tolerance of 40°C, shown in Figure 4.8. It shows that during about 85% of the time, the outlet temperature equals about 700 ºC. After that, the temperature decreases rapidly to about 660 ºC after which discharging is stopped. A side note to this figure is the short discharge time of about 1 hour.
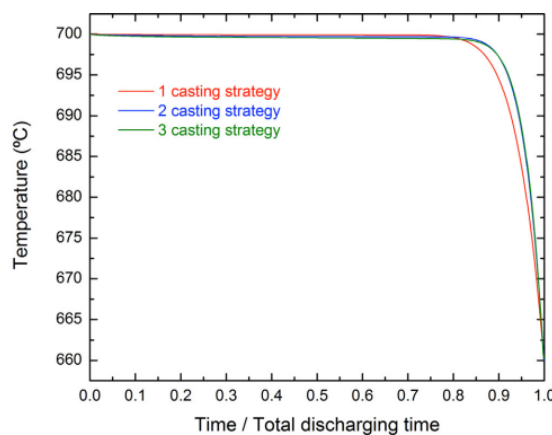
Figure 4.8: Output HTF (air) temperature during discharging time (Ortega-Fernández & Rodríguez-Aseguinolaza, 2019)

According to Figure 4.7b and 4.8, the adverse effect of diffusion inside the particles, which causes an adverse, larger thermocline region, is neglected upon discharging since the particle diameter will be 1 cm which is closer to Figure 4.8b. An almost horizontal temperature evolution of the HTF outlet temperature is obtained upon discharging. This is also assumed for longer discharging times.

First cycle versus last cycle

Another important aspect during packed bed charging and discharging is the difference between the first and Nth cycle. This phenomenon can be seen, for example, in Figure 4.9 from the research of Hänchen et al. (2011). It shows that after a number of cycles, the temperature distribution inside the packed converges and reaches a steady-state dependent on the charging and discharging strategy.

Hänchen et al. (2011), showed the evolution of the output temperature of the HTF, at the end of a charging period, from the 1st to the 20th cycle in Figure 4.9_l. The output temperature, at column height 3m, increases as several cycles have passed. The strategy within this research is to charge and discharge for 6 hours every cycle. The changing energy balance over several cycles can be seen in Figure 4.9_r. At the start, energy losses in the form of sensible heat are present, which represents the energy that cannot be extracted upon discharging. The exit losses, which represent the energy losses according to the temperature increase of the HTF presented in Figure 4.9_l, are present after a number of cycles and become constant. This is, in other words, hot HTF which cannot transfer its energy to the storage. The wall losses will also become constant as the packed bed will reach a constant temperature gradient during charging and discharging. The pumping losses are small in the case of Hänchen et al. (2011) and therefore not shown. The efficiency increases in the first cycles till it converges and the mean temperature after charging increases from the 1st to the 20th cycle.
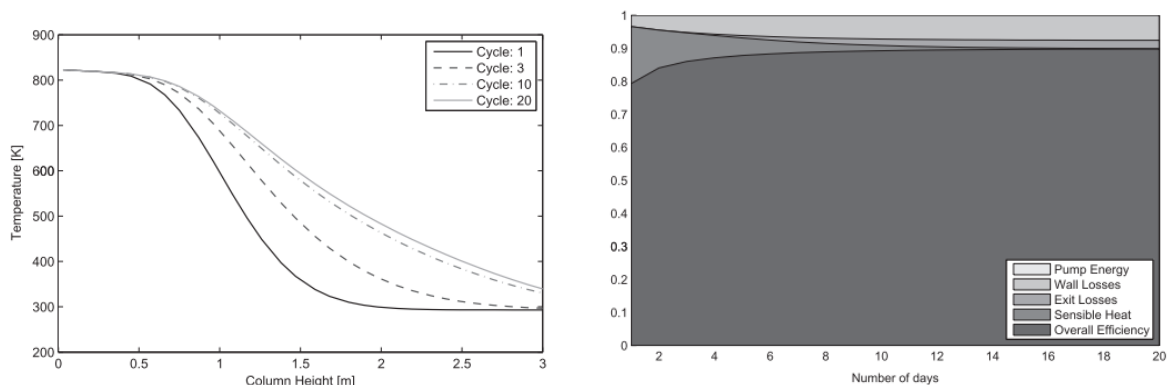
Figure 4.9: Temperature distribution of fluid across height of the storage system at the end of charging period for a series of 6h charge and 6h discharge cycles (left) and the energy balance for day 1-20 (right)(Hänchen et al., 2011)

Another strategy could be to stop charging and/or discharging based on a temperature difference of the HTF outlet temperature. This effect is shown in Figure 4.10. What is observed is that the temperature of the packed bed decreases over the length upon charging cycles. This is due to the limit on the HTF outlet temperature difference. That means the temperature is reached in an earlier stage compared to the first charge due to residual heat. Due to this limit are the charging times shorter and is the energy charged decreasing till the steady-state case.
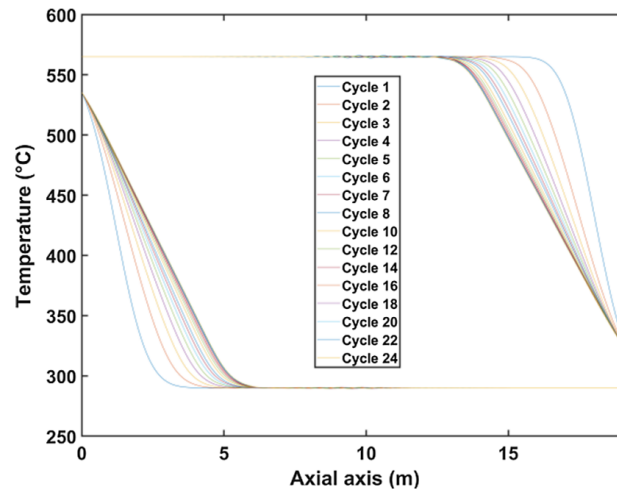
Figure 4.10: PCM (dis)charge strategy based on outlet HTF temperature (Cabello Núñez et al., 2019)

The third strategy, as depicted in Figure 4.11, utilizes waste heat for storage. The observed pattern reveals a charging process until an almost linear temperature is attained. This occurs because the surplus waste heat is abundant, allowing for some spillage without significant consequences. As a result, a more uniform temperature can be achieved.
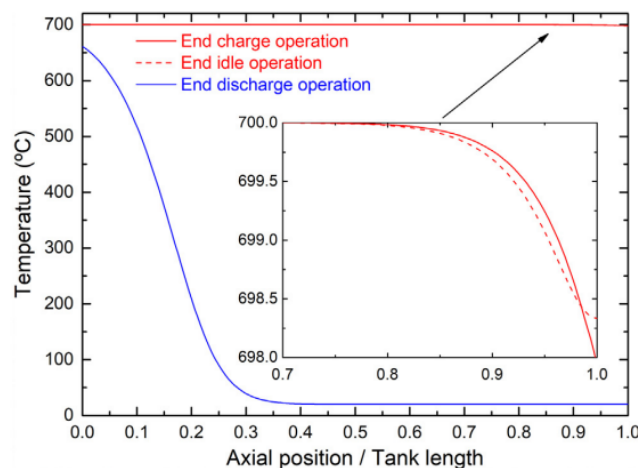
Figure 4.11: PCM charge strategy based on fully charging (Ortega-Fernández & Rodríguez-Aseguinolaza, 2019)

Thus three strategies for charging could be chosen according to the three articles:

• Strategy 1: Constant time and energy input for every cycle
• Strategy 2: Maximum HTF outlet temperature tolerance
• Strategy 3: Stop when fully charged

Strategy 1 and 2 will result in a packed bed that is not able to fully load or unload. The proportion of the packed bed volume, in percentage, to which this applies is estimated from experimental results. This percentage is extracted by defining the percentage of the stratification zone from a charging or discharging temperature profile with respect to the optimal temperature profile. The optimal temperature profile will be a uniform temperature profile throughout the whole column. For now, a pattern similar to Figure 4.10 is adopted. This is because the storage will not be charged by waste heat and therefore is strategy 3 not plausible. Strategy 1 is based on the idea of charging based on a time limit. However, in this case, this can be adjusted by heating with a higher flow velocity of the HTF for example. Thus, approximately 12.5% of the storage cannot be used. This percentage is based on Figure 4.10.

4.2.5. Dimensions and operating parameters

Stand alone energy supply
To develop the design for the packed bed thermal storage, the following consecutive steps are under-taken.

First, an estimate of the storage dimensions is obtained in order to evaluate if the velocities of the heat transfer fluid are within the limits of the research of Ortega-Fernández and Rodríguez-Aseguinolaza (2019) and to estimate the losses. These losses result in a larger storage since the steam demand is the parameter which determines how large the storage should be and in all cases should the storage be able to generate this demand.

With the use of the following equation, the first estimate of the mass of the slag is determined, based on a temperature difference of 500°C (200-700).

$$m_{slag} = \frac{Q_{req,tot}}{\Delta T c_p} \tag{4.17}$$

This results in a volume according to

$$V_{slag} = \frac{m_{slag}}{\rho_{slag}} \tag{4.18}$$

Together with the void fraction, this results in a first estimate of the tank volume

$$V_{tank} = \frac{V_{slag}}{1 - \epsilon} \tag{4.19}$$

In combination with the aspect ratio of 2 this results in a certain length and diameter of the tank and an inlet area. Based on this inlet area the HTF velocities upon discharging can be determined. Charging heat transfer velocities can be determined at a later stage since this does not include the fluctuating pattern.

With the assumption that the HTF leaves the packed bed with a temperature of 700 °C, the velocities of the heat transfer fluid can be determined, which is shown in Table 4.5.

This is based on the following equations

$$\dot{m}_{HTF} = \frac{Q_{req,1hour}}{\Delta T c_p} \tag{4.20}$$

The velocity is based on

$$v_{HTF} = \frac{\dot{m}_{HTF}}{A_{inlet} * \rho_{HTF}} \tag{4.21}$$

Hour	Required energy [kW]	$\dot{m}_{HTF}$ in kg/s	v_{HTF} in [m/s]
1	6618	12.53	0.793
2	6084	11.52	0.729
3	6175	11.70	0.740
4	6045	11.45	0.725
5	6214	11.77	0.745
6	8168	15.47	0.979
7	9224	17.47	1.106
8	5380	10.19	0.645
9	5407	10.24	0.648
10	5029	9.52	0.603
11	6358	12.04	0.762
12	7908	14.98	0.948

Table 4.5: Steam demand in kW with accompanying mass flow and velocity of the HTF discharge.

Reaching back to the results of the parametric study of Ortega et al. (2015), the velocities of the air at 0.45 m/s showed excellent results. When unloading at velocities of 1.5 m/s, the stored energy and efficiency dropped. The mean velocity in the above case is 0.79 m/s with a maximum of 1.106 m/s and a minimum of 0.603 m/s. However, these 12 hours were the peak hours of the week.

The losses within this packed bed are based on the equation used in Ortega-Fernández and Rodríguez-Aseguinolaza (2019). They stated that the evaluation of the thermal losses is a complex issue. In addition, insulation in real systems could be advanced enough to have quasi-adiabatic TES tank insulation. However, they determined a simplified TES insulation strategy which is modeled in their research. This allows satisfactory energy calculation and leads to simple implementation in the model. They only included the lateral wall in order to determine the losses from the packed bed to the environment. Furthermore, the coefficient which includes the heat transfer from the fluid to the tank, h_w is determined based on the approximation given by Beek (1962). This approximation states that h_w is equal to 0.8*h_p. h_p is the particle heat transfer coefficient. This value of 0.8 will probably originate from the fact that heat transfer from air colliding with the slag pebbles will have better heat transfer than air which flows along a wall.

Furthermore, in the insulation layer only conductive heat transfer is evaluated. In addition, the convective heat transfer between the outer wall and the environment is assumed to be convection due to free steam of air at a temperature of 20°C. The overall heat transfer coefficient for determining the losses can be calculated as

$$h_{loss} = \frac{1}{\frac{1}{h_w} + \frac{d_t}{2k_{ins}}ln(\frac{d_{ext}}{d_t}) + \frac{d_t}{d_{ext}}\frac{1}{h_{ext}}} \tag{4.22}$$

with h_w the tank wall heat transfer coefficient [W/m^{2}K], d_t diameter tank in m, k_{ins} thermal conductivity of the insulation layer in W/mK d_{ext} diameter tank with insulation and h_{ext} the external tank heat transfer coefficient in W/m^{2}K.

As mentioned before, h_w is equal to 0.8*h_p. The latter, h_p originates from the following Nusselt correlation:

$$Nu = \frac{h_p d_p}{k_f} = 2 + 1.1Re_p^{0.6}Pr^{1/3} \tag{4.23}$$

This equation is selected for Reynolds numbers above or equal to 15.
If the Reynolds number is lower than 15, the following Nusselt correlation should be used:

$$Nu = \frac{h_p d_p}{k_f} = 1.26[\frac{1 - (1 - \epsilon)^{5/3}}{W}](Re_p Pr)^{1/3} \tag{4.24}$$

Where W corresponds to Equation 4.25.

$$W = 2 - 3(1 - \epsilon)^{1/3} + 3(1 - \epsilon)^{5/3} - 2(1 - \epsilon)^2 \tag{4.25}$$

Re_p and Pr are based on

$$Re_p = \frac{v_\infty \rho_f d_p}{\mu} \tag{4.26}$$

$$Pr = c_p \mu k^{-1} \tag{4.27}$$

What should be noted is that in a packed bed, the velocity at the inlet of the packed bed determines the Reynolds number.

Next, h$_{ext}$ is originating from

$$Nu_H = \frac{h_{ext} d_T}{k_f} = 0.6 + \frac{0.387 Ra_H^{1/6}}{[1 + (\frac{0.492}{Pr})^{9/16}]^{8/27}} \tag{4.28}$$

$$Ra_H = g * \rho_f \beta (T_{ext} - Tamb) H^3 \mu^{-1} \alpha^{-1} \tag{4.29}$$

This equation for Nu$_H$ describes the free convection process in a vertical plate. This is applicable to a vertical cylinder if the following condition is satisfied

$$\frac{d_{ext}}{H} = \frac{35}{Gr_H^{0.25}} \tag{4.30}$$

$$Gr_H = \rho^2 \beta (T_{ext} - T_{amb}) * H^3 \mu^{-2} \tag{4.31}$$

The total heat loss is then equal to

$$Q_{loss} = \int_{t_{start}}^{t_{end}} (h_{loss} * T_{mean} 2\pi r * L) dt \tag{4.32}$$

For the pumping power, first the pressure drop should be calculated. Different expressions for the pressure drop are present in literature. However, Hänchen et al. (2011), Calderón-Vásquez et al. (2021) and Ortega-Fernández and Rodríguez-Aseguinolaza (2019) use the Ergun equation. This equation is valid for a wide range of laminar and turbulent flows up to 1$\leq$ Re$\leq$ 10^4. The Ergun equation is

$$\Delta p = \frac{H_t G^2}{\rho_f d} (1.75(\frac{1-\epsilon}{\epsilon^3}) + 150 \frac{(1-\epsilon)^2}{\epsilon^3} \frac{\mu_f}{Gd}) \tag{4.33}$$

The work consumed by the pump or fan will be expressed as

$$E_{pump} = \int_{t_{start}}^{t_{end}} \frac{A_T G}{\rho_f} \Delta p \, dt \tag{4.34}$$

The heat losses as well as the sensible losses explained before, need to be added to the initial energy which needs to be stored. This results in a larger storage volume and therefore the heat transfer velocities decrease.

4.2.6. Conclusion dimensions

To conclude, the dimensions and characteristics are as follows for the stand alone case:

- Stored energy 117 MWh
- Length 12.0 m
- Diameter 6.0 m
- Volume 343 m^3
- Mass 741*10^3 kg
- Effective storage density 229 kWh/m^3 and 0.11 kWh/kg
- Heat loss in 12 hours 351 kWh
- Pump loss upon discharging in 12 hours 3.6 MWh

What should be noted is that the assumption is made that all the energy of the air which is heated can be used till the air is again cooled to 200°C. It is not possible to generate steam at temperatures lower than approximately 10-15°C above the required steam temperature. The air of 200°C will be reused in the storage.

The useful energy storage density, both based on volume and weight, is determined based on the energy which is required for the 12-hour storage ($\approx$80 MWh).

The flow sheet of this process in combination with the process description can be found in Appendix A.

Peak shaving

For the peak shaving case, the maximum energy supply within an hour is 4823,7kW. This is lower than all the hours for the stand alone case. However, the storage will also be smaller. Therefore, the analysing step for the flow velocities should still be performed regarding Figure 4.6 and the subsequent conclusions.

Based on the introduction to peak shaving, there appears to be potential to employ this approach for achieving smaller equipment. Examining the data suggests that this could result in storage that is approximately 50% smaller than the stand-alone case. Not accounted for in this analysis is the issue that, when the tank is half charged, diffusion will occur, causing the thermocline region to expand and leading to an average temperature throughout the packed bed which is lower than the maximum temperature. This average temperature negatively impacts the discharge performance of the storage system. Figure 4.6 showed this impact. For the lowest mass flow rate, 0.01 kg/s, is the extracted energy as well as the efficiency drastically decreased. The reason is that conduction and radiation between the particles influence and control the thermocline region within the storage tank (Cabello Núñez et al., 2019). The main cause of the temperature stratification is due to the thermal conductivity of the slag material in the axial direction. The efficiency drops from around 75% to 20%.

This implies that incomplete (dis)charging or slow (dis)charging of the packed bed has a detrimental effect on the operation of the packed bed. Therefore, a reevaluation of the previously determined 40MWh in Section 2.1.2 is warranted, where the aim should be in completely discharging the thermal storage all at once. This ideal situation, depicted in Figure 4.12 illustrates an average boiler capacity with a sinusoidal representation of surplus and deficit. Over successive time steps, the thermal energy storage could be fully charged and discharged accordingly.
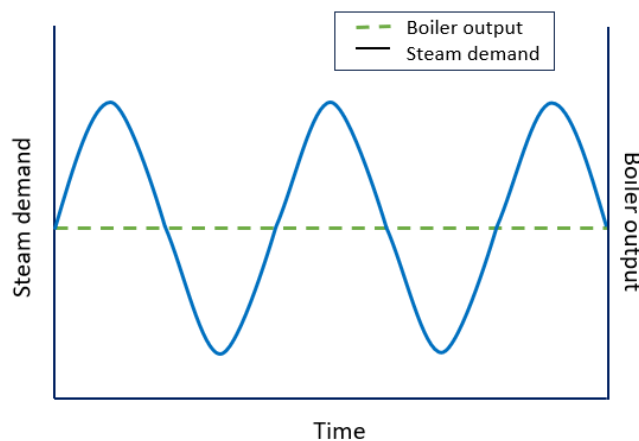
Figure 4.12: Ideal steam demand pattern for peak shaving

However, the ideal case is not present in the data provided by Arcadis. Therefore, first, a boiler steam generation, adjusted hourly, needs to be determined. This is done by taking the average of the steam demand in 5 consecutive hours and rounding this value to the nearest multiple of 500, with unit kWh. This results in the boiler estimate in kWh/h in Figure 4.13. This is done for the 'average week'. In a normal week, 168 hours should be present. However, since the weekend is excluded, fewer hours are visible in the graph. This is followed by the evaluation of surplus and deficit for every hour.
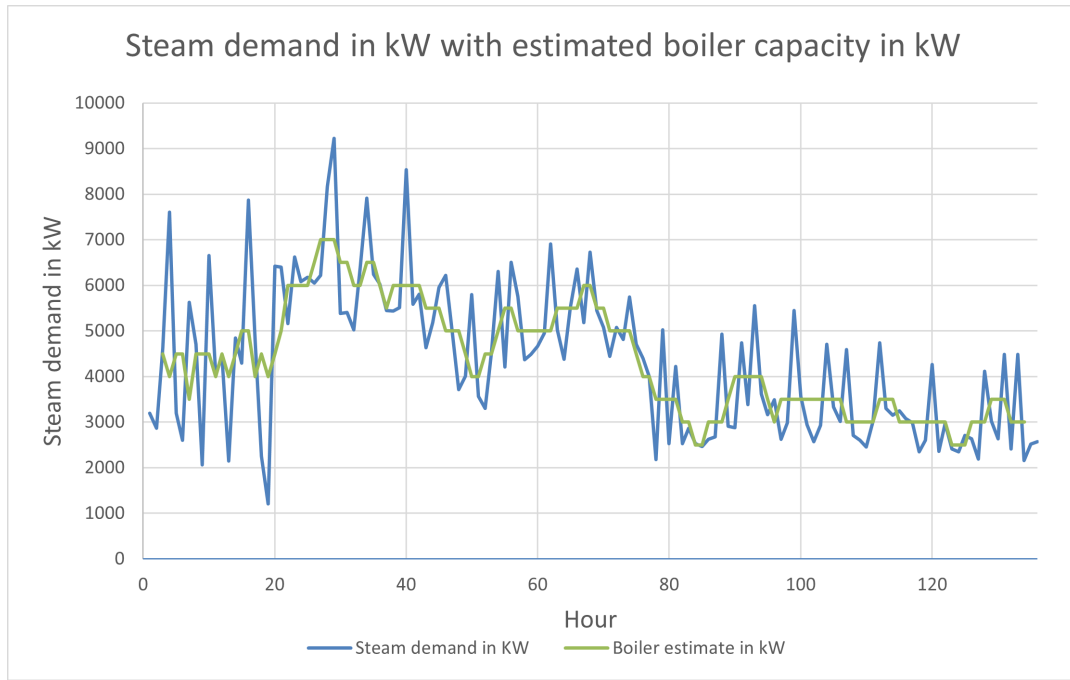
Figure 4.13: Steam demand in kW with estimated boiler capacity in kW for the average week

Next, an assumption on the start capacity of the thermal storage is made. From this start capacity are the deficits and surpluses added. This is adjusted till no negative value for the thermal storage capacity is observed. In other words, the storage can cover each peak.

$$\sum_{t_{start}}^{t_{end}} \text{start capacity} + \text{surpluses or deficits}(t) \geq 0 \tag{4.35}$$

The maximum capacity is represented by the maximum value over all hours.

$$max(\text{capacity}(t)) = max(\text{start capacity} + \text{surpluses or deficits}(t)) \tag{4.36}$$

This is around 6 MWh. However, to have a margin, is the thermal storage set at a value of 7 MWh. What should be noted is that it is hard to determine the energy content at the start of the week in comparison to the maximum capacity since it is a continuous process without a clear pattern. In this case is the thermal storage at the start filled for 70%. This is followed by evaluating the fill level of the thermal storage for every hour, presented in Figure 4.14.
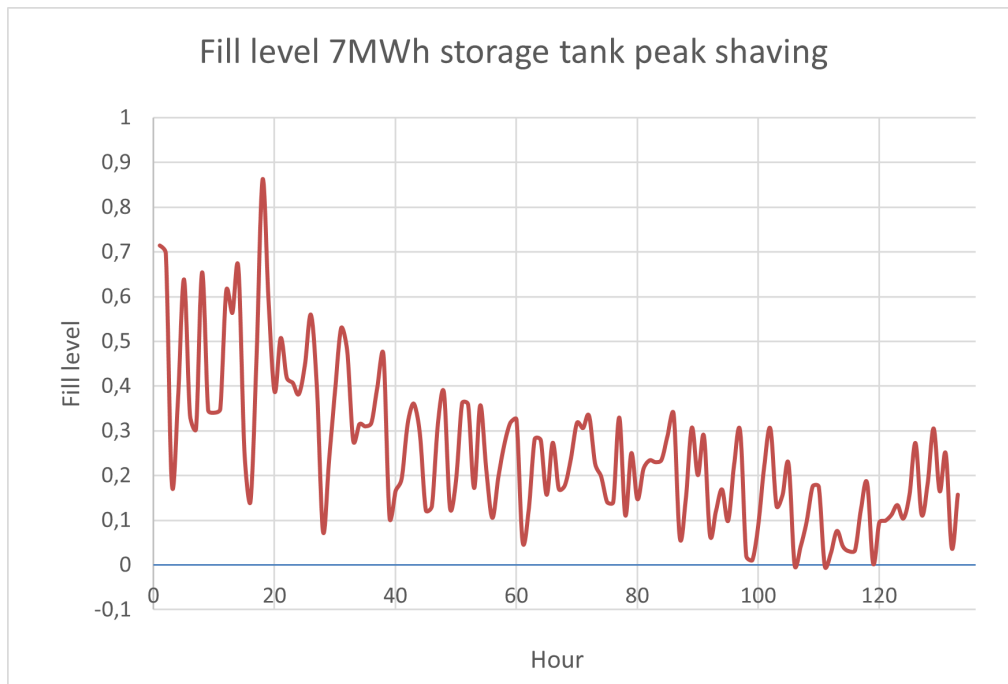
Figure 4.14: Fill level as function of time for 7 MWh storage tank for peak shaving

What should be learned from this graph is that using the thermal storage as peak shaving in order to decrease the capacity of the boiler is not feasible since the fill level does not show a complete charge or discharge pattern. The thermal stratification decreases the efficiency of the boiler drastically. Thus, peak shaving with slag material will not be feasible.

If the energy storage would be based on waste heat recovery, the perspective on above conclusions would change. The decreased efficiency of the storage could still increase the overall performance of the system in that case, so thermal storage could still be feasible.

4.3. Phase change salt

4.3.1. Explanation material

Phase change materials used in thermal energy storage, change their phase in order to store energy. The energy stored during the phase change is known as latent heat. Besides the storage of latent heat, additional heat can be stored in the sensible form before and after the phase change. According to the literature review, in the temperature region of this thesis, salts are the type of materials most commonly used as phase change material. The first step in designing a storage for this configuration is deciding on the proper type of salt with the right phase change temperature. However, choosing the right phase change temperature is dependent on the next step, converting the energy into the phase change from water into steam at 11 bar. Higher phase change temperatures make it easier to perform this conversion step, but it introduces the trade-off between increased losses and additional challenges, for example, heightened corrosion. Therefore, first, the focus is on a more in-depth research into the different phase change salts and corresponding characteristics. Then, on the basis of literature, the most robust and well known type of storage method can be found. Regarding this type of storage, the key parameters are extracted. If an approach similar to the steel slag was executed, this was followed by the optimal values of these key parameters. However, a parametrization with the correct values for the key parameters is not achievable since it is dependent on too many different variables. For instance, a parametrization for a specific tube size paired with a phase change salt may not be applicable when dealing with salts exhibiting different thermophysical characteristics, including density, thermal conductivity, and specific heat, or when considering varied tube diameters. Consequently, the introduction of a semi-empirical model becomes necessary to conclude on the dimensions based on assumed salt type and HTF.

Despite the implementation of the semi-empirical model, the assessment of key parameters remains crucial to evaluate their impacts and can be found below.
The choices regarding the type of phase change salt which can be used are enormous. Salts which are considered in this study, due to the phase change temperature, are nitrate, carbonate, sulphate, fluorides, chlorides and eutectic salts. All these categories belong to the inorganic materials. To decide on the salt type, as explained in the literature study previous to this research, desirable properties for the salt type are (Kenisarin, 2010) (Wei et al., 2018) (S. A. Mohamed et al., 2017):

- Appropriate phase change temperature for the application
- High density
- High latent heat
- High thermal conductivity
- High specific heat capacity
- Physical and chemical stability
- Small volume changes upon melting
- Low vapour pressure
- Chemical stability
- Non-toxic, non-flammable
- No supercooling
- Congruent melting
- Sufficient nucleation and crystallization rates
- Abundant, available, cheap

Eutectic mixtures often have multiple advantages over the usage of a single salt. The first one is the ability to generate a higher range of phase change temperatures upon deciding on the weight or mass ratio of the different salts. The second one is regarding the higher energy storage densities which can be achieved at the same phase change temperature in comparison to a single salt. The last one is the price aspect. Upon mixing, high and low price salts can be mixed while approximately the same phase change temperature is achieved.

In multiple reports enumerations of high temperature phase change salts are provided. For example in the report of Q. Li et al. (2019), three tables are provided with some typically used pure salts, commercial salts and some binary and ternary salts for a phase change temperature range between 200 and 100°C. Another example is within the research of Wei et al. (2018).

However, what is concluded is that the information available about the thermophysical properties of phase change salts in literature is incomplete and inconsistent. This is addressed by Q. Li et al. (2019) to the lack of a consolidated measurement standard. Thus, they conclude that selecting a salt for a specific application and compare this to other salts is not easy.

Commercial phase change salts are available via https://www.pcmproducts.net and are provided with information about phase change temperature, density, latent/volumetric/specific heat capacity, thermal conductivity and maximum operating temperature. This company is able to provide high temperature phase change salt with a phase change temperature between 104 and 885 °C.

4.3.2. Literature

To be able to successfully utilize a PCM, two main elements are required: the PCM itself and the encapsulation for this phase change material, which provides a desired heat transfer surface. A common type of encapsulation is macro-encapsulation, this type includes different geometries. For example packed beds, shell and tubes or flat plates (Q. Li et al., 2019). Examples of these configurations are shown in Figure 4.15.
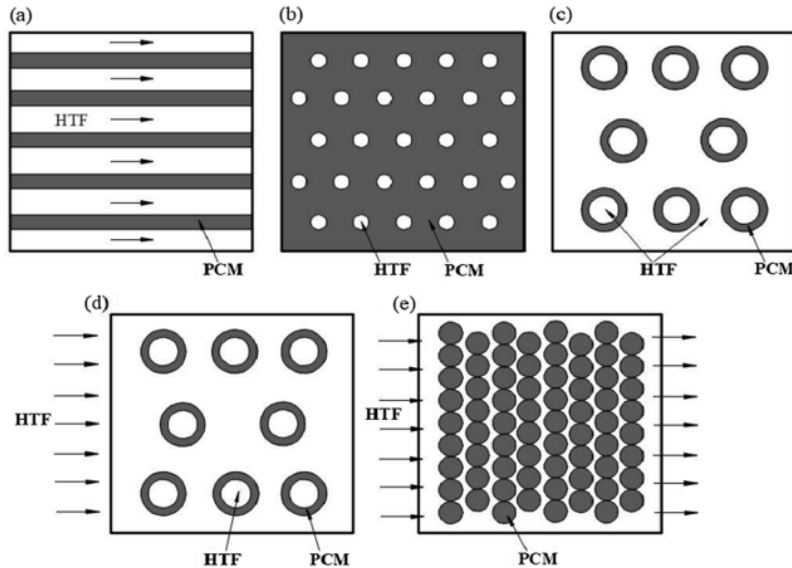
Figure 4.15: Different type of PCM storage devices. a) flat plate b) shell and tube c) shell and tube parallel flow d) shell and tube cross flow e) packed bed (Q. Li et al., 2019)

Z. Han et al. (2022) concluded that shell and tube configuration accounts for more than 70% of the studies and is therefore the most researched and popular device for commercial applications. According to Agyenim et al. (2010), this is due to the simplicity of the design of a shell and tube device accompanied by minimal heat loss. Therefore, this type of encapsulation is chosen. It should be noted that with respect to the slag material, the heat transfer surface is now dependent on the number and type of tubes.

Multiple studies have attempted to model the heat transfer behavior of the shell and tube arrangement filled with phase change salts. However, many studies in the past used models based on organic materials instead of the inorganic salts (Z. Han et al., 2022). Another shortcoming in some studies is the exclusion of the natural convection effect (Y.-B. Tao et al., 2014). Y. Tao et al. (2017), revealed the impact of natural convection on charging and discharging and concluded that especially during charging this effect is significant. The effect of natural convection on discharging could, however, be ignored.

During charging and discharging a moving liquid-solid boundary is present (Q. Li et al., 2019). Natural convection leads to the non-uniform distribution of the solid liquid interface. This results in acceleration of the PCM melting rate (G.-S. Han et al., 2017). Different configurations were tested with numerical modelling to investigate the effect of natural convection on charging. These included a horizontal configuration, a vertical configuration, PCM in the tube, PCM in the shell, HTF inlet at the top, HTF inlet at the bottom. All with identical heat transfer area. The results showed that almost all configurations showed improvements with the inclusion of natural convection. The effect was greater in the horizontal model with the PCM on the shell side than on the tube side. When comparing the different heat transfer fluid inlets, the vertical, PCM in the shell side, model with the HTF inlet at the bottom showed the best results. Vertical and horizontal configuration showed no real difference in this configuration. Furthermore, when the HTF inlet is at the top, the influence of natural convection is not significant (G.-S. Han et al., 2017).

In conclusion, according to the previous results, it can be assumed that the charging is typically faster than the discharging since natural convection is present. The configuration where the natural convection does not play a significant role is when the HTF inlet is at the top. All the other configurations showed, to some extent, faster charging times upon including natural convection. The next step will be to dive into a experimental validated research in order to find the key parameters for a shell and tube latent heat storage system.

4.3.3. Storage method and key parameters

Within the shell and tube configuration, generally the HTF flows in the tubes and the shell is filled with the PCM. The operating parameters that can be varied within a shell and tube device in order to influence the thermal performance are according to Q. Li et al. (2019), Seddegh et al. (2017), and Trp et al. (2006):

- Diameter and length of tube and shell
- Horizontal or vertical storage
- Number of tubes
- Mass flow rate
- Inlet temperature

Based on the above, it was chosen to design the latent heat storage device as a shell and tube heat storage where the PCM is inside the shell and the HTF in the tube(s). The optimal configuration of this device will be further investigated. The choice of whether to use horizontal or vertical storage is obtained first.

Besides, some researchers also focus on the eccentricity of the tube inside a shell. Eccentricity is the measure of how far a geometric shape's center deviates from its ideal or expected position. However, based on the assumption that a single tube in a shell would not be suitable based on the heat transfer surface area, and thus multiple tubes will be present, is this eccentricity research not included as a key parameter.

4.3.4. Value key parameters

Similar to the previous section about steel slag, optimal values of key parameters are found in this section. However, what should be noted is that in the previous section, a parametrization was presented of the system which is similar to the designed system in this thesis. Within this section, different type of phase change salts, heat transfer fluids, and temperatures are used in determination of the optimal value of a single parameter. Therefore, these results are only considered valuable after an experimental test with the parametrization of these values. Therefore, the semi-empircal model will be presented after this section.

Horizontal versus vertical

Mehta et al. (2019) stated that the geometric orientation of the container, with respect to gravity, plays a significant role in determining the heat transfer mechanism. This orientation influences the movement of the solid-liquid interface and thereby influences the thermal characteristics of the charging, melting, and discharging, solidification, process. Prior to their own research, based on literature, they concluded that in a vertical cylinder the melting front moves from the HTF tube in the radial direction as it proceeds from the upper to the lower part of the storage unit along axial direction. This can be seen in Figure 4.16.
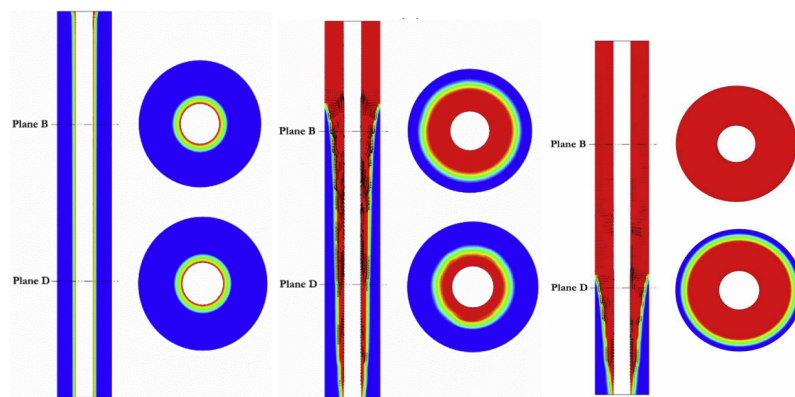
Figure 4.16: Vertical configuration at 30 min (left), 180 min (middle), and 300 min (right). Red represents liquid fraction 1.0 and blue represents liquid fraction 0.

They confirm the importance of the HTF inlet temperature as well as the negligible effect of heat transfer velocity. The related non-dimensional numbers are respectively the Stefan number and the Reynolds number. The Stefan number is correlated with the effect of the HTF inlet temperature and the Reynolds number on the HTF fluid velocity.

For the horizontal configuration the upper half of the PCM is melted first due to natural convection. The lower part of the tube takes more time to melt. This phenomenon can be seen in Figure 4.17
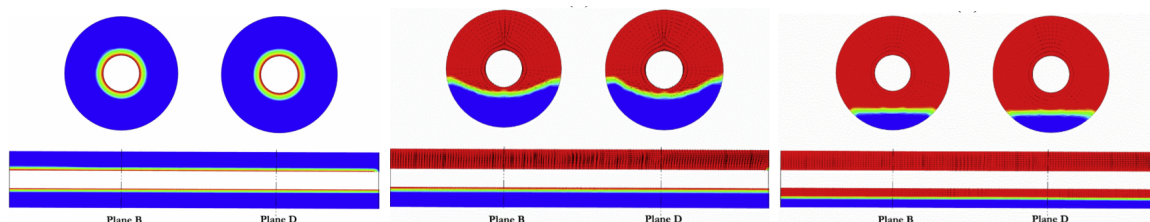
Figure 4.17: Horizontal configuration at 30 min (left), 180 min (middle), and 300 min (right). Red represents liquid fraction 1.0 and blue represents liquid fraction 0.

For the melting, charging, part of the storage unit, the horizontal configuration showed faster melting rates due to the natural convection for the whole column. Especially the upper part is melted fast since natural convection will result in the front moving upwards.

The vertical configuration showed slower melting rates. In figure 4.16c and 4.17c the liquid fraction, after the last measurement at 300 min, is shown for both horizontal and vertical. First of all, a difference in plane B and D can be noted. This is caused by the way natural convection influences the melting. What can be concluded is that for the vertical set-up the liquid front moves radially outwards as well as axial upwards.

For the horizontal set-up, the difference between B and D is almost negligible. Furthermore, it is concluded that the horizontal set-up takes 25% less time in order to melt half of the PCM. In contrast, the difference in time to melt the whole column is less than 5%. This is due to the fact that natural convection is especially important in the second part of the process, after the conduction dominated part. This influence decreases when more fluid PCM is present. Concluding, the horizontal set-up is the choice within partial loading operations. For the solidification process, both configurations showed less differences. Furthermore, they analyzed the differences in melting time with respect to the HTF inlet temperature.

	HTF 75°C Horizontal	HTF 75°C Vertical	HTF 85 °C Horizontal	HTF 85 °C Vertical
Melting time 50%	150 min	200 min	85 min	115 min
Melting time 100%	460 min	480 mim	306 min	324 min
Melting time plane B	165 min	100 min	75 min	40 min
Melting time plane D	165 min	340 min	75 min	180 min

Table 4.6: Three cases (Mehta et al., 2019)

Since low discharging rates are a problem within phase change salts, the horizontal configuration is the type of choice. This is due to the ability to discharge faster if it is partially discharged.

Shell to tube ratio
Shell to tube ratio and the number of tubes are closely linked, especially in this scenario where the shell and tube function both function as heat storage and heat exchanger. However, in order to be consistent, first separate research for both these parameters is done.

Within the study of Seddegh et al. (2017), different R_o/R_i were tested. They maintained the outer shell radius in order to minimize the mass change of the PCM. The R_o was 0.0512 m in all the configurations and the R_i ranged between 0.00635 and 0.01905. The test configuration had the PCM in the shell side and one tube in the middle. What could be concluded is that based on the charging time, discharging time, stored energy and average stored energy a ratio of 5.4 is optimal for this configuration.

To reach this conclusion, experimental tests were executed. The temperature of the HTF and the shell to tube ratio were varied. The tests involved a single tube within a shell filled with PCM. Within these tests, the HTF flow rate was kept constant at 10 L/min. First of all, all the configurations combined with different inlet temperatures of the HTF, higher temperature lead to higher energy storage densities. What they concluded is that 60-65% of this effect is a result of an increase in sensible heat storage and 35-40% is due to an increase in latent heat storage. This means that at 70°C, melting is incomplete. The higher storage densities are visible in Figure 4.18$_{lo}$.

However, the geometrical influences were the same for both temperatures. The first conclusion regarding the geometrical parameter is that if the radius ratio increases, the charging and discharging time increases. This is shown in Figure 4.18$_{up}$. In addition, for both temperatures, the increase of charging time increases drastically when the radius ratio is >5.4. Furthermore, shown in Figure 4.18$_{lo}$, the stored energy increases insignificant. However, the radius ratio <5.4 shows a sharp decrease in stored energy. In Figure 4.18$_{lo}$ is also shown that the average energy storage rate decreases for higher radius ratios. However, they concluded that the decrease in energy storage rate was higher when increasing from 5.4 to 8.1 than from 2.7 to 5.4 in percentage. Therefore, by balancing all the above conclusions, an optimal radius ratio of around 5.4 is ideal.
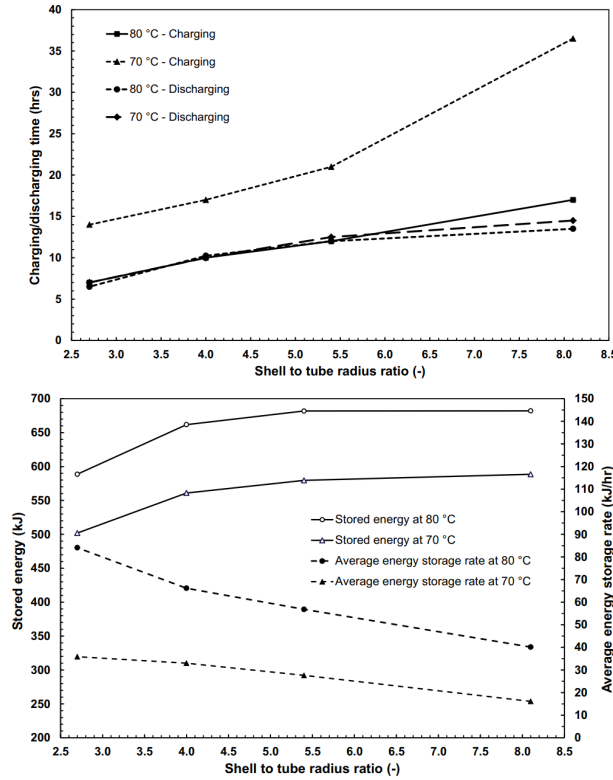
Figure 4.18: Charging and discharging time in hours for different shell to tube ratios (upper end). Stored energy in kJ for different shell to tube ratios (lower end). Both figures for 70°C and 80°C.

Number of tubes

Park et al. (2020), attempted to find the optimal number and arrangement of tubes in a horizontal shell and tube latent thermal storage configuration based on computational fluid dynamic simulations for eight configurations. This research focuses on melting performance. The PCM is n-eicosane with a melting temperature of 309.15K. The HTF is not defined, since the HTF is simulated as a tube wall with a constant temperature of 353.15K. Park et al. (2020) divided the melting process into three parts. The initial part is conduction dominated, the second is natural convection dominated and in the last one is the melting rate slowed down. The last part has a strong influence on determining the melting time. First of all, an increase in the number of tubes enhanced the initial state melting rate. This is due to the increase in heat transfer area. The melted area, according to Park et al. (2020), for the first conduction dominated part, is equal to:

$$A_{melt} = 2N\pi r' r_i + N\pi r'^2 \tag{4.37}$$

N number of tubes, r' is the radius of the melting front and r_i is the radius of the tube for each case.

The first term is a constant, based on the definition of the problem within this research, $2\pi N r_i$=constant together with the conduction dominated melting front, resulting in an almost constant r'. However, the second term expresses the influence of the number of tubes on the melted PCM area.

In the second phase, which represents the third part of melting according to the three parts presented above, the effect of natural convection decreases the slope of the liquid fraction for every configuration. This phase starts when the melt reaches the lowest part of the tube located at the lowest position within the tube. For the tube arrangement where the δ, which denotes the distance from the bottom of the shell to the lowest tube, is the smallest, the slope of the curve decreases at a later time..

What can be concluded is that the correlation between melting time and the number of tubes is not strong. However, what did show a strong correlation with the melting time was the tube arrangement. The tube arrangement, Figure 4.19$_l$ showed the optimal reduction in melting time. When assessing the energy density, eight tubes showed the highest value (4.19$_r$). This is because the total storage volume can decrease with an increase in number of tubes.
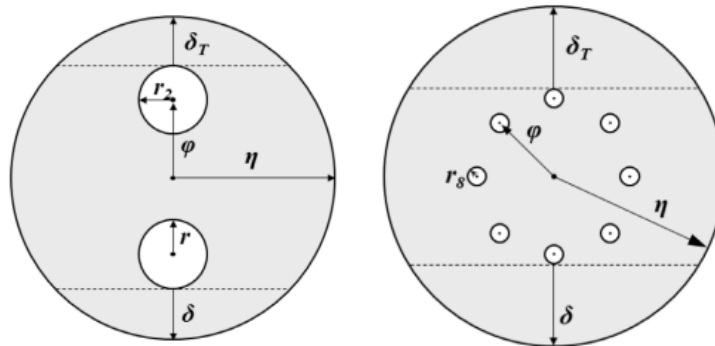
Figure 4.19: Optimal tube configuration according to (Park et al., 2020) for the shortes charging time (left) and highest energy density (right).

However, upon discharging other phenomenons will be observed, since discharging mainly depends on conduction. Therefore, the authors suggested performing similar research upon discharging. However, it is assumed, that since it is dependent on conduction, the heat transfer surface area is the most important factor.

Temperature difference
Temperature difference is a driving force for charging and discharging within the latent storage unit. In this subsection, the influence of temperature difference on the different phases of the charging period is analysed. To examine the impact of an elevated HTF temperature during charging or a reduced HTF temperature during discharging, literature is explored where natural convection is not considered. Natural convection mainly affects charging storage rather than discharging, as mentioned earlier.

Within the research of Y.-B. Tao et al. (2014) the numerical model was a self-developed model based on the enthalpy method. The model was experimentally validated. In order to evaluate the effect of the heat transfer fluid temperature, the velocity, inside radius and outside radius were kept constant and were respectively 15 m/s, 12.5mm and 25mm. The melting temperature of the PCM was 1040K. The effect of the HTF temperature is shown in Figure 4.20. What is first noticed is that the melting process is split into three parts. The first is the part of sensible storage, where the material heats up, the second is the phase change and the third is another part of sensible storage. The first and third phases can be identified by the horizontal line in Figure 4.20$_m$ and the second phase is the curved line between them. The HTF temperature impact on all phases is as follows:

- Phase 1: Due to the higher temperature difference between PCM and HTF, the heat transfer rate is increased. This results in a decrease of the duration of this phase.
- Phase 2: A temperature increase results for this phase in an augmentation of the slope of the melting fraction curve, which means a higher melting rate.
- Phase 3: Since the goal was to fully melt the PCM and not find the influence on the sensible storage, the influence on this stage is not mentioned.

The overall melting time influenced by the temperature is shown in Figure 4.20$_l$ and shows, as expected, a decrease in time for a higher HTF temperature. Figure 4.20$_r$ shows the influence on the heat storage rate. What should be noted is that a larger temperature difference gives a higher heat storage rate in the second phase.
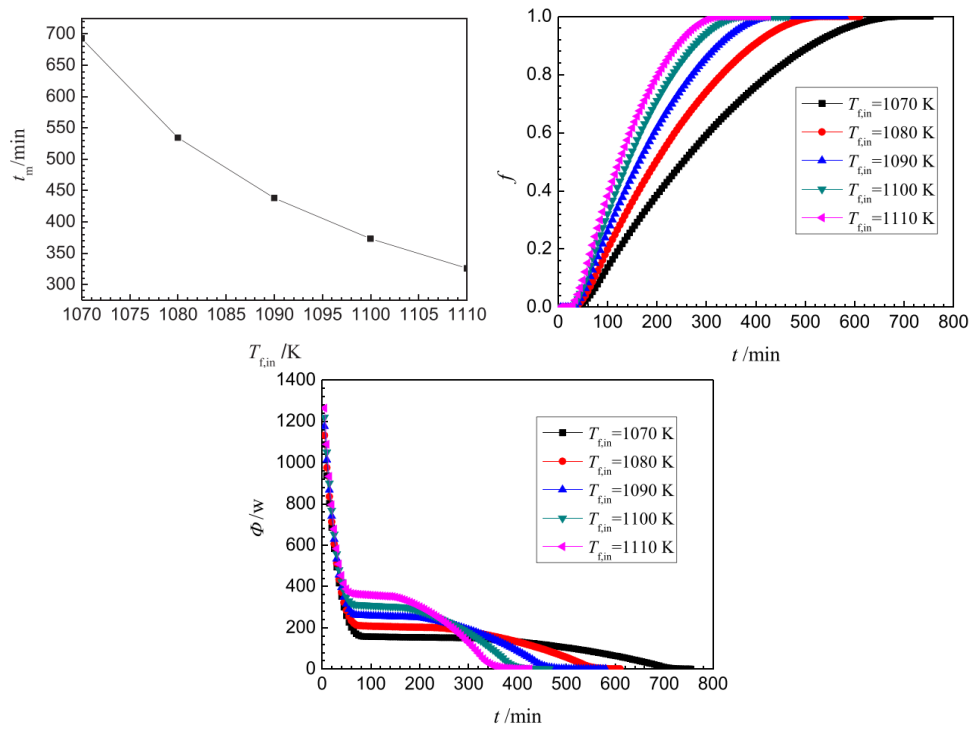
Figure 4.20: Melting time as function of HTF inlet temperature (left). Melt fraction as function of time for different HTF inlet temperatures (middle). Heat storage rate as function of different HTF inlet temperatures (right). (Y.-B. Tao et al., 2014)

In Figure 4.21 the influence of the HTF inlet temperature on the solid-liquid interface distribution, at time 180 min, is shown. The vertical axis signifies the position of the solid-liquid interface relative to the inner tube surface. The horizontal axis defines the length of the tube. Based on this data a slope of the interface is determined. For temperatures from 1070 to 1110K, this slope increases respectively from $4.7*10^{-3}$ for 1070K to $6.9*10^{-3}$ for 110K. Raising the HTF inlet temperature leads to a greater disparity in the distribution of the solid-liquid interface and influences the melting rate of the PCM.
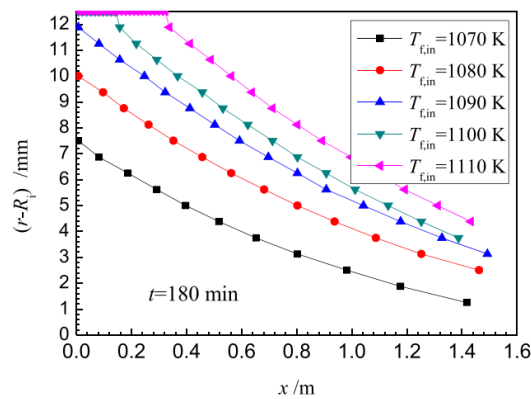
Figure 4.21: Solid-Liquid interface location as function of length at 180 min for different HTF inlet temperatures (Y.-B. Tao et al., 2014).

Heat Transfer Fluid velocity

Increased heat transfer velocities leads to a higher Reynolds number. Several articles note that, in the majority of cases, heightened heat transfer velocities do not correlate with increased stored energy. However, a lot of the research into this phenomenon is focused on organic PCMs. And these organic, paraffin, PCMs typically do not have the same thermal conductivities as phase change salts. Paraffin has a thermal conductivity around 0.3W/mK in comparison to 0.5-0.6W/mK for phase change salts considered in this thesis. Therefore, further investigation into this phenomenon in combination with the right thermal conductivity is executed below.

Fang et al. (2020) experimentally showed the influence of Reynolds number on storage density for a range, 0.21-20 W/mK, of thermal conductivities. Within this research, a cooling demand was required and the stored energy was compared to a stratified water storage. The Q_{eff} is determined as the stored energy within the ranges of the usable temperature of the HTF. This temperature is equal to $T_{dis,eff}$ and the effective energy is equal to:

$$Q_{eff} = \Sigma_{t=0}^{t=t_{T_{dis,out}=T_{dis,eff}}} \dot{m} c_{p,w}(T_{dis,in} - T_{dis,out})\Delta t \qquad (4.38)$$

The total storage capacity of this device is determined as the stored energy when the outlet HTF is equal to the inlet HTF temperature, i.e. no energy is stored anymore:

$$Q_{total} = \Sigma_{t=0}^{t=t_{T_{dis,out}=T_{dis,in}}} \dot{m} c_{p,w}(T_{dis,in} - T_{dis,out})\Delta t \qquad (4.39)$$

In addition, results are displayed as capacity effectiveness, ϕ_c as a function of the Reynolds number. The capacity effectiveness is calculated as

$$\phi_c = \frac{Q_{eff}}{Q_{total}} \qquad (4.40)$$
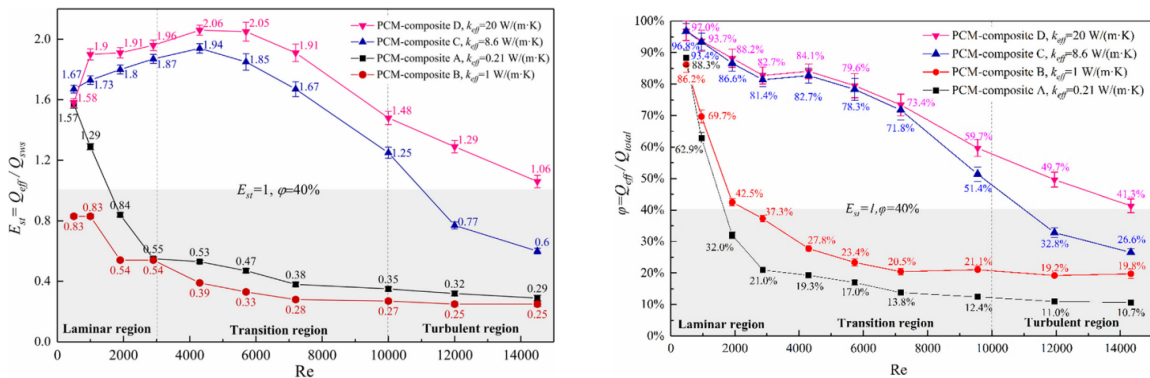
Figure 4.22: Stored energy as function of Reynolds number for different thermal conductivities (left). Variation of capacity effectiveness as function of Reynolds number for different thermal conductivities (right) (Fang et al., 2020).

What can be observed from Figure 4.22 is multiple sided. First of all, for the two lower thermal conductivities (0.21 and 1 W/mK), both graphs show a decrease for higher Reynolds numbers. Secondly, the two higher thermal conductivities show first an increase and above a certain value, Re=4000, and also a decrease in the E_{st}. For the ϕ_c, only a decrease is observed.

Another case where the evaluation of HTF velocity is conducted involves a configuration depicted in Figure 4.23, which closely resembles the expected setup in this thesis. In this configuration, the thermal energy used to charge the storage device is simulated as thermal energy from a solar collector (P. Zhang et al., 2016). During the charging process, the temperature of the HTF will therefore gradually increase. Starting from ambient temperature and reaching the desired target temperature of 250°C. When charging the thermal storage with a solar collector, the temperature of the HTF will gradually increase due to the slow heating of the HTF. Conversely, during the discharging phase, the inlet temperature of the HTF remains constant at 105°C.
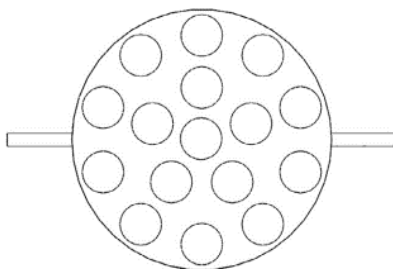
Figure 4.23: Horizontal cross-section of PCM configuration with PCM the tubes and (P. Zhang et al., 2016)

The effect of the HTF velocity on charging and discharging time is experimentally investigated. The different HTF velocities are 0.0788, 0.1046, 0.1223 and 0.1402 kg/s.

Charging
According to the results in Figure 4.24, which represent the charging, it is found that the increase in temperature of the HTF and the PCM are both very slow. This is due to the low power of the heating system, 3kW. What further can be noted is that, due to the HTF inlet at the top, the temperatures of the thermocouples located at the top of the storage system are always warmer than the bottom. Furthermore, two plateaus can be seen in the Figure. This is due to two phase changes. The first is a solid-solid phase change and the second is the solid-liquid phase change. After the second phase change, there is an increase in slope of the line. This is due to the natural convection influence, which accelerates the melting process. The target of 250°C is not achieved, as can be seen, due to the heat loss of the storage tank and circulation pipe. The charging process is ended, when the PCM inside the tank no longer varies in temperature. The charging times are:

- Velocity 0.0788 kg/s = 59360 s
- Velocity 0.1046 kg/s = 58750 s
- Velocity 0.1223 kg/s = 59500 s
- Velocity 0.1402 kg/s = 60290 s

This shows no significant influence of the HTF velocity on the charging times. Furthermore, influence of the natural convection is observed despite the HTF inlet at the top. This contradicts the results that no real influence is observed upon natural convection when the HTF inlet is at the top (G.-S. Han et al., 2017), concluded in Subsection 4.3.1. The difference with this set-up in contrast to this research is the non-constant temperature of the HTF. Therefore, during charging higher heat transfer rates can are expected.
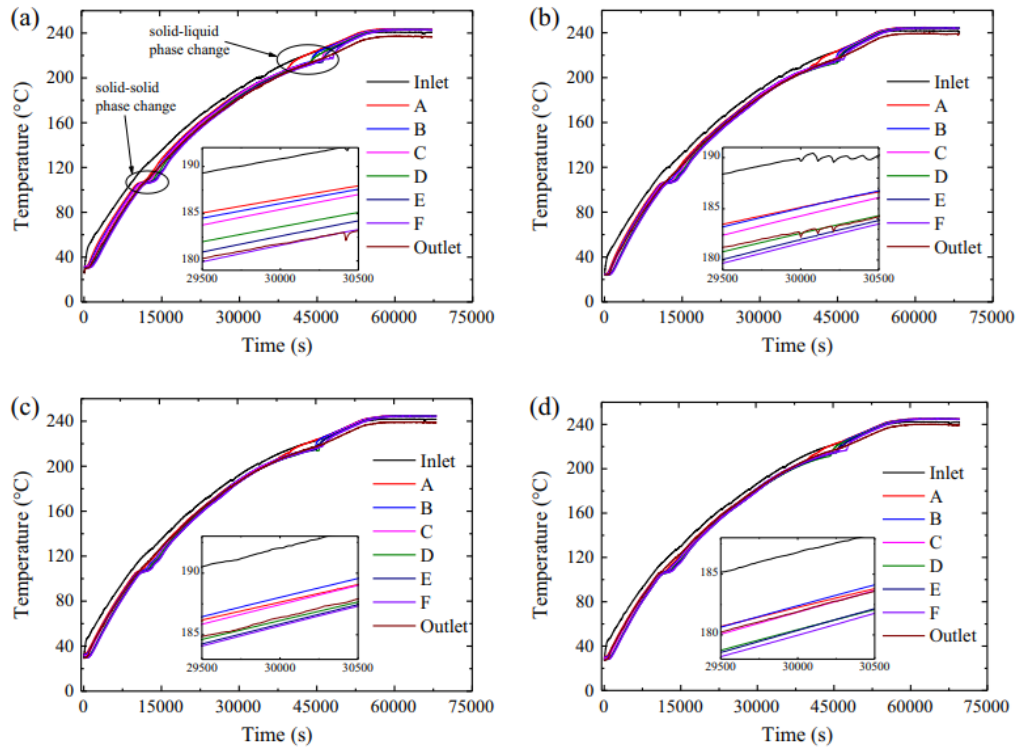
Figure 4.24: Temperature of the PCM during charging at different locations within the storage for as function of time for different HTF mass flow rates (P. Zhang et al., 2016) a) 0.0788 kg/s. b) 0.1046kg/s. c) 0.1223 kg/s. d) 0.1402 kg/s.

Discharging

For the discharging, shown in Figure 4.25, the HTF inlet temperature is, besides some initial fluctuations, at a constant temperature of 105°C. As expected, PCM near the tube wall shows a decrease in temperature first. Furthermore, due to the difference in temperature of PCM in the shell is natural convection present and does the temperature of the PCM drops quickly. Thus, even a lower thermal conductivity of the PCM in the fluid phase showed still a quick temperature drop due to natural convection. However, during the subsequent phases after the quick temperature drop, the percentage of liquid fraction decreases and therefore also the influence of natural convection.

As expected, the PCM discharging times are much lower than the charging times due to the constant temperature of the HTF inlet.

- Velocity 0.0788 kg/s = 9940 s
- Velocity 0.0951 kg/s = 9130 s
- Velocity 0.1252 kg/s = 6940 s
- Velocity 0.1387 kg/s = 5390 s

As can be observed, the HTF velocity does have an influence on the discharging time within this case. Larger HTF velocities decrease the discharging time significantly. Furthermore, also here is a contradictory result in comparison to the conclusion in Subsection 4.3.1., namely that there exist some influence of natural convection during discharging.
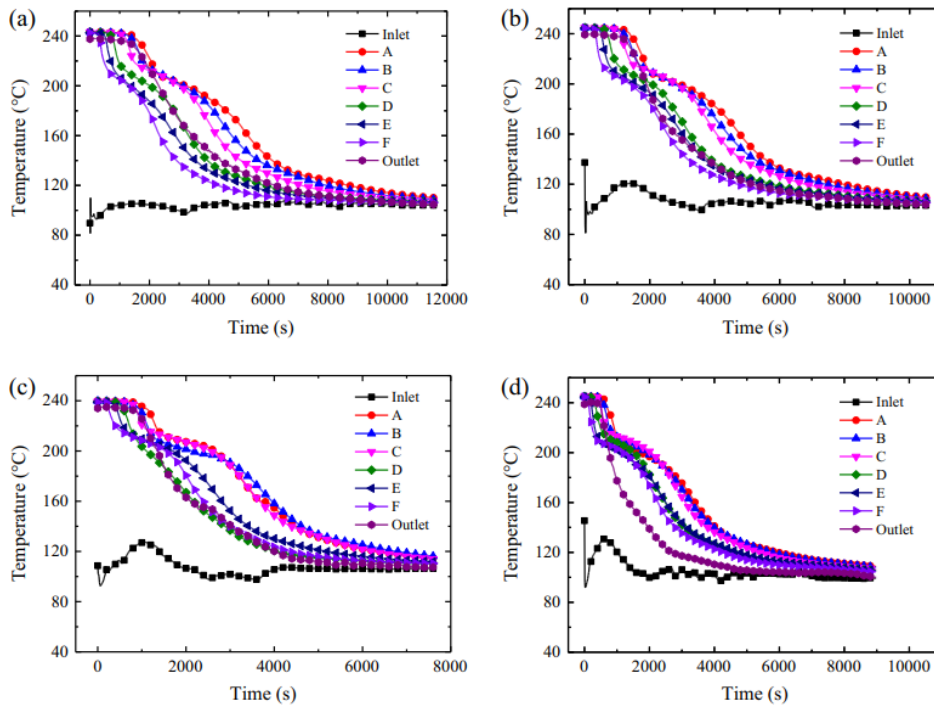
Figure 4.25: Temperature of the PCM during discharging at different locations within the storage as function of time for different HTF mass flow rates (P. Zhang et al., 2016) a) 0.0788kg/s. b) 0.0951 kg/s. c) 0.1252 kg/s. d) 0.1387 kg/s.

What can be noted from the Figures is that, in general, the temperature of the HTF follows more or less the temperature of the PCM. Nevertheless, at the highest velocity, 0.1402kg/s, a different pattern is observed with a faster decrease in temperature of the HTF, which can be seen in Figure 4.25d. This concludes that at higher velocities, the HTF outlet can be maintained at a high temperature for a shorter period of time. The duration of time of maintaining the temperature above 160°C is for the different cases temperature of the HTF inlet.

- Velocity 0.0788 kg/s = 3460 s
- Velocity 0.0951 kg/s = 2790 s
- Velocity 0.1252 kg/s = 2120 s
- Velocity 0.1387 kg/s = 1380 s

The mean power of the different charging configurations are almost similar and are around 1.6 kW. For discharging the mean power ranges between 7 and 14 kW. However, the energy efficiency is around 72% for all configurations.

What can be learned from this configuration is that when applying higher velocities, higher discharging power can be obtained. The real influence of higher velocities on the charging power is not yet determined, since in this case, the HTF inlet temperature is not constant. Also, higher velocities mean a quicker decrease in the outlet temperature of the HTF which is not desirable in this research. Furthermore, this research states that the natural convection during discharging is of influence. However, other papers explain that this influence is higher during charging. In addition, this configuration is also not similar to the configuration used in this thesis, since the PCM is in the tubes and the HTF in the shell.

4.3.5. Semi-emperical model
A semi-empirical model combines theoretical principles with empirical data to provide a comprehensive understanding of a system or phenomenon. The goal of this semi-empirical model is to see the influence of the geometry of the PCM thermal storage on the exit temperature in combination with the mass flow of the HTF. These together determine the discharge power. A semi-empirical model is necessary due to the limited and inflexible availability of experimental research results in the literature. Numerical results in literature are often based on the enthalpy method. The enthalpy method is employed to address the dynamic boundary issue encountered in solid-liquid phase transition processes (Y. Tao et al., 2017) (Y. Tao et al., 2012). However, based on the knowledge that during discharge the heat on the salt side is mainly based on conduction, the semi-empirical model will be an easily adjustable model which is able to generate quick and thereby powerful results.

The semi-empirical model is at first based on the research of Sodhi et al. (2021). This is due to the following reasons:

- Experimental data on outlet HTF temperature and salt temperature at different positions in the thermal storage system present in the paper
- Horizontal configuration
- Multi-tube configuration
- Salt with, in comparison to other literature, a relatively high melting temperature (305.1°C)

The primary focus of this model will center on discharging the thermal storage system for two main reasons. Firstly, in phase change systems, the discharge process typically exhibits a slower rate compared to the charging process, as concluded earlier. Consequently, the limitation is primarily observed during discharge. Secondly, the discharging phase also presents a critical constraint for the industrial implementation of phase change salts. If the system fails to discharge at the required power, it becomes impractical to implement. In contrast, the charging process is contingent upon the energy source and available power, which are not addressed in this thesis and thus are not considered limiting factors.

The storage configuration, shell and tube, is shown in Figure 4.26. The shell is filled with the phase change salt and in the tubes is air used as HTF. This device is small, the length of the configuration shown in Figure 4.26$_r$, is 0.75 m. The goal is to be able to generate such figures for higher temperatures, larger devices, and different HTFs, especially focusing on the outlet temperature and volume of the HTF shown in Figure 4.27.
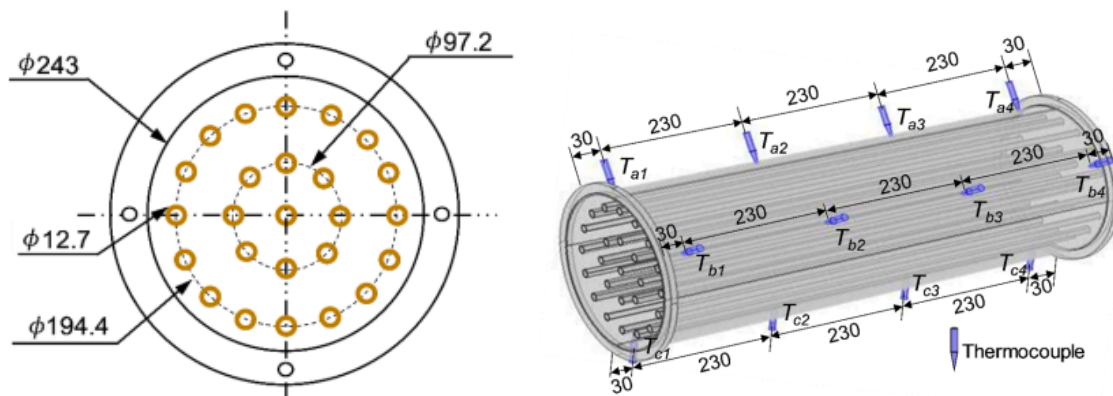
Figure 4.26: Cross section shell and tube configuration (left). Representation shell and tube configuration with corresponding sizes in mm (right). (Sodhi et al., 2021)
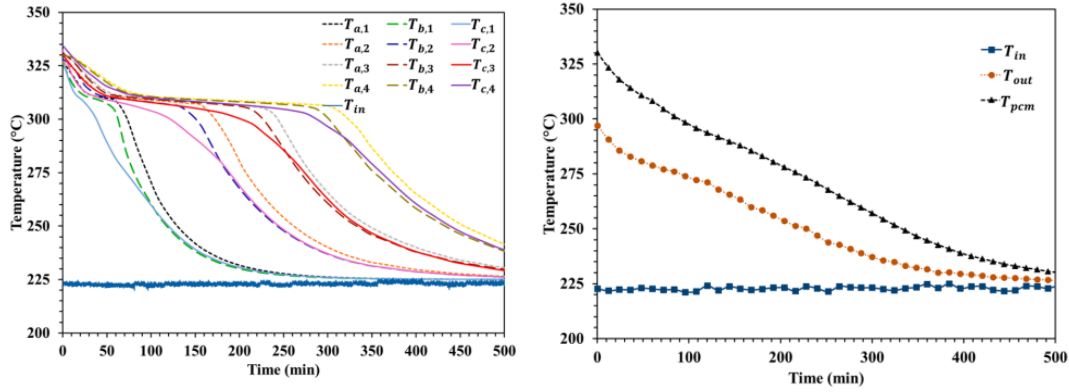
Figure 4.27: Temperature within the storage configuration based at different locations in the tube (shown in Figure 4.26) (left). Mean temperature HTF inlet, HTF outlet and phase change salt during the discharge (right) (Sodhi et al., 2021)

The semi-empirical model is developed using a single tube of the aforementioned configuration. This choice stems from the premise that if it works for one tube this will enable scaling to different tube sizes and multiple tubes. This one tube will function as an average of all locations of the configuration. The diameter of the salt per tube is calculated from the total area of the cross section of the unit shown in Figure 4.26 divided by 25. This is 0.0486m.

The geometrical input parameters are as follows:

- Length of storage 0.75 m
- Number of tubes 25
- Tube diameter $12.7*10^{-3}$ m
- Volumetric flow 73 m^3/h
- Wall thickness tube $1.2*10^{-3}$ m
- Max diameter salt $48.6*10^{-3}$ m
- Amount of salt 61 kg

One tube is divided into four sections with equal length to be able to confirm the behaviour of the salt shown in Figure 4.27a. The heat transfer surface area is equal to

$$A_{heattransfer} = \pi * d_{tube,in} * l_{\text{one segment}} \tag{4.41}$$

The heat transfer is based on three resistances with accompanied heat transfer coefficients. h_{conv} is the heat transfer coefficient from flowing air to the tube, h_{cond1} is the conduction through the tube wall, h_{cond2} is the heat transfer coefficient from the salt to the tube. This will give the overall heat transfer coefficient h_c,

$$h_c = \frac{1}{\frac{1}{h_{conv}} + \frac{1}{h_{cond1}} + \frac{1}{h_{cond2}}} \tag{4.42}$$

The heat transfer coefficient, h_{cond1}, is equal for the whole length of the heat transfer tube and equal to

$$h_{cond1} = \frac{k_{ss}}{t_{tube}} \tag{4.43}$$

with k_{ss}, the thermal conductivity of stainless steel, 14.2 W/mK.

h_{cond1} is fluctuating. Upon discharging, the heat transfer in the salt is mainly dependent on conduction. Even if the liquid and solid salt both have a low thermal conductivity, around 0.5 W/mK, the assumption is made that the liquid salt is able to transfer the heat due to the movement of the salt, convection, and that this will not be a limiting heat transfer coefficient. On the other hand, will the solidification increase the resistance to heat transfer. The determination of increasing resistance is done later.

The convective heat transfer coefficient, h_{conv}, is dependent on the flow regime within the tube. The flow regime is dependent on the Reynolds number. The Reynolds number within the paper which is used for the semi-empirical model is equal to approximately 2315. The regions in a pipe are determined as follows:

- Re<2,300 laminar flow
- 2,300<Re<4,000 transition region
- Re>4,000 turbulent

Therefore, the flow is in a transition regime. Furthermore, when a flow enters a pipe, also effects are present due to the entrance of a flow in a tube. Entrance effects are present till the entrance length is over. This entrance length is determined based on a balance between the following two equations (Bergman, 2011) (Cengel & Cimbala, 2013)

$$L_{h,lam} = 0.0575 Re_d d \tag{4.44}$$

$$L_{h,turb} = 1.359 d (Re_d)^{1/4} \tag{4.45}$$

Since the flow regime is closer to the laminar regime, is this flow region chosen to calculate the entrance length. This entrance length is equal to around 1.7m, which is more than twice the length of the pipe, 0.75m. So, the flow is either in an entrance regime of a laminar flow or in a turbulent flow.

The Nusselt number for the laminar flow regime in the entrance length of the pipe is equal to (Ansys, 2020)

$$Nu_{d,lam} = 1.86 * \left(\frac{Re_D * Pr}{\frac{L}{d_{tube,in}}}\right)^{1/3} = \frac{h_{conv,lam} d}{k} \tag{4.46}$$

The Nusselt number for the turbulent flow regime in a pipe is equal to (Ansys, 2020)

$$Nu_{d,turb} = 0.023 * Re^{0.8} Pr^{0.4} = \frac{h_{conv,turb} d}{k} \tag{4.47}$$

A point of reference is the first outlet temperature of the HTF shown in the reference paper. What can be assumed, is that the pipe at the start will be equal to the salt temperature at the start, 330°C. From this assumption, the heat transfer coefficient at the start can be determined. Since the heat transfer due to conduction in the tube itself is a fixed value, the heat conduction through the salt and the convective heat transfer are the ones that are dependent. At first, all the salt is melted. Therefore, this heat transfer inside the salt, as explained before, is not limiting and therefore a small heat transfer resistance value is assumed. The increase in energy which is adopted by the heat transfer fluid, the air, should be equal to the heat transfer coefficient in combination with the log mean temperature difference. This results in the overall heat transfer coefficient for the first time step

$$h_{c,t=1} = \frac{\dot{m} c_{p,HTF} (T_{out} - T_{in})}{A_{heattransfer} \Delta T_{lm}} \tag{4.48}$$

The heat transfer surface area can be calculated according to the paper. The log mean temperature difference is calculated with the assumption that during that time step the tube will be equal to the salt temperature, 330 °c. The in- and outlet HTF temperatures can be read from Figure 4.27b and the $\dot{m}$ can also be calculated according to the volumetric flow of the HTF. This results in a h_c around 29 W/m^{2}K. This enables us to determine the factors below

$$h_{conv} = fraction * h_{conv,lam} + (1 - fraction) * h_{conv,turb} \tag{4.49}$$

This results in a fraction of 0.75.

However, in the different regions within the pipe, the flow will also be different. The heat transfer in the first region is more likely to be more turbulent than the last region in the pipe. Therefore, a gradient is implemented with as mean value the above conclusion of fraction 0.75. This means:

- Region 1: fraction turbulent is 0.9
- Region 2: fraction turbulent is 0.8
- Region 3: fraction turbulent is 0.7
- Region 4: fraction turbulent is 0.6

To be able to use this semi-empirical model, two ratios are kept constant: the aspect ratio (AR) and the Shell to Tube (StT) ratio. These are the following

$$AR = \frac{l_{pipe}}{d_{shell}} \tag{4.50}$$

$$ST = \frac{d_{shell}}{d_{tube,out}} \tag{4.51}$$

The d_{shell} is equal to the salt which belongs to that pipe, not the shell of the thermal energy storage itself. These factors are equal to, respectively 15.4 and 3.8. These are kept constant for every pipe within the storage. The scaling can thus by increasing the length, inner diameter and salt diameter in the same ratios.

The next step includes the determination of the different regimes of energy storage. There are three regimes. The first is the sensible energy above the melting temperature, the second is the phase change energy and the third is the sensible energy below the melting temperature. These are referred to as sensible 1, latent and sensible 2 regions. The energy which can be extracted from these regimes is equal to

$$Q_{sens1} = (T_{salt,max} - T_{salt,melt}) * c_{p,salt} * m_{\text{salt}} \tag{4.52}$$

$$Q_{lat} = m_{\text{salt}} * L \tag{4.53}$$

$$Q_{sens2} = (T_{salt,melt} - T_{HTF,in}) * c_{p,salt} * m_{\text{salt}} \tag{4.54}$$

The mass of the salt is given as 61kg within the article. The energy extracted from one segment of one tube is therefore equal to the above equations divided by 25 tubes and divided by four segments.

Thereafter, the iterations will be carried out within Matlab. This is set up as follows. For a fixed time step, e.g. one minute, the HTF outlet temperature will be determined by solving this equation with one unknown on both sides. The unknown is the HTF outlet temperature, HTF_{out}, denoted as x

$$\dot{m} * c_{p,air} * (x - HTF_{in}) = h_c * A_{heattransfer} * \Delta T_{lm} \tag{4.55}$$

This ΔT_{lm} is equal to

$$\Delta T_{lm} = \frac{(T_{salt} - T_{HTF,in}) - (T_{salt} - x)}{ln(T_{salt} - T_{HTF,in}) - ln(T_{salt} - x)} \tag{4.56}$$

The first segment has HTF inlet temperature of 225°C according to the reference paper. This HTF outlet temperature per segment will be the inlet temperature for the next segment.

This HTF outlet temperature determines the energy which is every second extracted from one segment of the tube with

$$\dot{Q}_{1segment} = \dot{m}_{onetube} * c_{p,air} * (T_{HTF,out} - T_{HTF,in}) + \text{heat losses} \tag{4.57}$$

The time steps are set to 1 minute. It is assumed that the salt temperature and heat transfer resistance are constant in that minute. The extracted energy per second, $\dot{Q}$ should be equated by 60 seconds. The losses to the environment are also kept constant during the discharge. This is due to the estimation that the salt at the outside shell wall will be almost constant since it will solidify last.

Then, the new temperatures of the salt, the energy extracted in each regime and the solidified salt thickness should be determined. This is split into three cases:

- Case 1: If the Q_{sens1} is still available (>0), a fraction of the energy extracted in that minute for that regime will be dedicated to the decrease in Q_{sens1}. The other fraction will be dedicated to the solidification, Q_{lat}. That a fraction is dedicated to the solidification even if there is still sensible energy left is due heat resistance in the salt. It is plausible that the liquid salt near the pipe will solidify even if the liquid salt near the shell will have sensible energy left.
- Case 2a: If the Q_{sens1} is <0 and the weight of the solidified salt is less than 50% of the maximum solidification, then all the energy will go to the solidification of the salt.
- Case 2b: If the Q_{sens1} is <0 and the weight of the solidified salt is more than 50% then again a fraction of the energy extracted every minute will go to reducing the Q_{sens1} even if there is still Q_{lat} available. This is done for the same reason as above in Case 1.

These fractions of energy extracted in Case 1 which goes to the solidification is 40% and thus 60% goes to the sensible heat. Within Case 2b, the same 60% goes to sensible heat. This fraction is noted as $f_{sens,1}$ and $f_{sens,2}$. f_{lat} is equal to 1-$f_{sens1/2}$. These fractions are selected, based on fitting the model on the experimental data, and are open to discussion.

The next step is determining the influence of the extracted energy for every regime.

- Regime Q_{sens1}: The energy which is absorbed by the HTF, every minute, is originating from a decrease in the temperature of the salt in liquid form. The new temperature is determined as:

$$T_{salt,new} = T_{salt,old} - \frac{Q_{extracted} * f_{sens,1}}{c_{p,salt,liq} * m_{onetube}} \tag{4.58}$$

- Regime Q_{lat}: Within this regime the energy absorbed by the HTF originated from the solidification. The increase in thickness is determined based on the thickness of the previous minute. For the first solidification, the thickness is equal to the tube radius. The increase in thickness is determined for every minute as follows:

$$\Delta m_{salt,solid} = \frac{Q_{extracted} * f_{lat}}{L_{salt}} \tag{4.59}$$

$$\Delta V_{salt,sol} = \Delta m_{salt,solid} / \rho_{salt,sol} \tag{4.60}$$

$$\Delta t_{salt,sol}(t) = \sqrt{\frac{(\Delta V_{salt,sol} + \pi(r_{salt,out}(t-1))^2 * L_{segment}}{\pi * L_{segment}}} - r_{salt,out}(t-1) \tag{4.61}$$

The new thickness of the salt is equal to

$$r_{salt,out} = \Delta th_{salt,sol} + r_{salt,out}(t-1) \tag{4.62}$$

- Regime Q_{sens2}: The energy which is absorbed by the HTF, every minute, is again originating from a decrease in temperature of the salt in solid form. The new temperature is determined as follows:

$$T_{salt,new} = T_{salt,old} - \frac{Q_{extracted} * f_{sens,2}}{c_{p,salt,sol} * m_{onetube}} \tag{4.63}$$

A small decrease in $c_{p,salt,liq}$ and $c_{p,salt,sol}$ is shown in paper, respectively 1655 J/kgK and 1600 J/kgK and are implemented in the model.

The total energy extracted for every minute is equal to the HTF temperature at the end of segment 4, which is the outlet, minus the inlet temperature multiplied by the mass flow and specific heat of air.

The last step is determining the heat transfer coefficient for the subsequent minute. The heat transfer coefficient that decreases is the $h_{cond,2}$. This is due to the increase in solid salt. The new $h_{cond,2}$ is equal to Equation 4.64 and will be implemented in 4.42 and the process will run for the next minute.

$$h_{cond2}(t) = \frac{k_{salt}}{(r_{salt,out}(t) - r_{tube})} \tag{4.64}$$

In order to create a figure similar to Figure 4.27, it is essential to ascertain both the outlet HTF of the last segment, segment 4, and the average salt temperature over all the segments for every minute. This results in the following Figure 4.28.
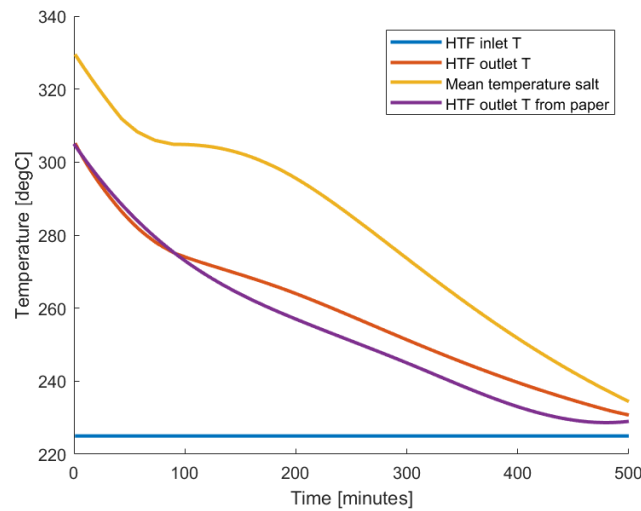
Figure 4.28: Temperature of the HTF outlet, HTF inlet, mean salt temperature, and HTF outlet from paper as function of time.

The HTF $T_{out,calculated}$ and $T_{HTF,out,real}$ show enough similarities to adopt this model for further research. Within the mean temperature of the salt in the model, the phase change is more visible than in the experimental data. This is the plateau around minutes 100-200. However, for the verification of the model, the focus is on the HTF outlet temperature since this is the most important parameter for discharging the storage.

To be able to generate results for the steam demand case which is discussed in this thesis, some input parameters need to be varied. First of all, the type of salt should be chosen. Thereafter, the maximum temperature deviation from the melting temperature of the salt, which represents the sensible heat at temperatures higher than the melting temperature, should be determined. This maximum temperature is partly a design choice but is also dependent on the maximum operating temperature of the salt.

Next, the variation of the following parameters should be implemented:

- Diameter of the tubes
- Length of the tubes
- Mass flow of the HTF
- Number of units in series

The diameter and the length of the tubes vary while respecting the AR and StT ratio. Thus a factor is implemented in the model which varies these all with the same proportions. However, the ability to put multiple tubes in series is also required. This is adjusted in the model by implementing a length factor, independent of the previous AR and StT ratio. This is a model simplification, increasing the length of the segments instead of increasing the number of segments. Lastly, the mass flow is also varied. For example, a design choice can be to increase the mass flow, with the consequence of a lower outlet temperature. This results in the following choices:

- Salt, including the melting temperature and thermophysical properties
- Type of HTF
- $T_{salt,max}$
- Dimensions, both the factor which respects the AR and StT ratio and the length factor which puts multiple tubes in series
- Mass flow of the HTF

Based on the choices made above, the energy extracted per tube can be determined. The final step in designing a system capable of generating the necessary power is determining the number of tubes. This is a result of the outcome of these equations in the following manner:

$$\text{Number of tubes} = \frac{\dot{Q}_{\text{required}}}{\dot{Q}_{\text{one tube,mean}}} \tag{4.65}$$

$$\text{Mean}(\dot{Q}_{\text{mean}}) = (\sum_{t=1}^{t=720} (T_{HTF,out} - T_{HTF,in}) * c_{p,HTF} * \dot{m})/720 \tag{4.66}$$

This $\dot{Q}_{\text{one tube, mean}}$ is a simplification of the reality on which the design is based. With this number of tubes, the heat transfer will in the beginning be too high and at the end too low. However, the mean heat transfer is achieved.

The amount of combinations of choices is enormous. Therefore, first, some goals and limits should be set in order to be able to make the right choices. The goal of the storage design is to minimize the volume of the storage. The limits are:

  • In order to prevent difficulties in the following heat transfer conversion step, e.g. the evaporator, the maximum temperature deviation of the HTF from the start to the end of the 12 hours is set to be 75°C.
  • The maximum factor used, which respects the AR and StT ratio, is 4. This is chosen based on the most used pipe diameters, which are a maximum of 50mm (Mills, 1992).

In order to assess the right combination of the parameters mentioned above, the following procedure is undertaken

  1. A salt is chosen
  2. A HTF is chosen
  3. The characteristics of the salt and HTF are collected
  4. The mass flow is varied
  5. The dimensions are varied
  6. A maximum temperature difference is set, 75°C as explained above
  7. The answer that is extracted from the calculations is the mean power which is transferred from the salt to the HTF within 12 hours per tube. With this value can the number of tubes, volume of storage and percentage of energy used with respect to energy available be calculated.

The number of tube calculations is explained above. The volume will be calculated as

$$V_{storage} = \text{Number of units} * V_{\text{one unit}} \tag{4.67}$$

The volume of one unit is based on the length and the diameter of one unit. The length is the original unit length multiplied by two factors, the factor that respects the AR and StT ratio and the length factor, which increases the length of a segment. The diameter is a multiplication of the original diameter by the factor that respects the AR and StT ratio. The diameter is the outer diameter, thus the tube plus the salt belonging to that tube.

The percentage of energy used compared the total energy available is determined as

$$\text{fraction}_{\text{used energy}} * 100\% = \frac{\dot{Q}_{\text{one tube,mean}} * 12h * 3600s}{m(Cp_{salt} * (T_{max} - T_{melt}) + L + Cp_{salt} * (T_{melt} - T_{HTF,in})} \tag{4.68}$$

The salt, which is implemented in the model is a commercially available salt (PCMProducts, n.d.). The melting temperature of this salt is approximately 500°C. This temperature is quite high for a phase change salt but is chosen based on the ability to generate steam in the evaporator. Higher temperatures will lead to better heat transfer. However, the corrosion at temperatures around 500°C can be more severe. In the future, another salt can also be chosen to perform the same analysis. Although on the website of the commercially available salts, the salt is denoted as H500, with no further specifications. It is expected that this salt is a combination of 33wt%NaCl and 67wt%CaCl$_2$. This is based on the thermophysical properties. For now, the HTF is chosen to be a thermal oil. However, common thermal oils such as Therminol 66, cannot operate at temperatures above 345°C. Therefore, a HTF with an even higher temperature range needs to be found. This is found to be Globaltherm Omnistore MS-600, which is able to operate to a temperature of 600°C (GlobalHeatTransfer, n.d.).

The thermophysical properties of the phase change salt and HTF can be found in Table 4.7.

	Density [kg/m^3]	Specific heat capacity [kJ/kgK]	Thermal conductivity [W/mK]	Viscosity [mPa s]	Maximum operating temperature [°C]	Phase change temperature [°C]
HTF	1835.6	1511.8	0.538	1.7764	600	-
Salt	2220	1.55	0.57	-	800	500

Table 4.7: Phase change salt unknown at which temperature, HTF at 400°C (GlobalHeatTransfer, n.d.) (PCMProducts, n.d.)

In order to explain the results of varying the dimensions, both size factor and length factor and the mass flow, first one of the optimal solutions is shown. Thereafter, varying the optimal results with corresponding outcomes will validate the optimum, shown in Figure 4.29.
One of the optimal solutions has as parameters:

- A constant size factor 2
- A combination of equal length and mass flow factor, for now, both 8 and 8

For example, if the length factor is chosen to be 9, the corresponding optimal mass flow factor equals 9.
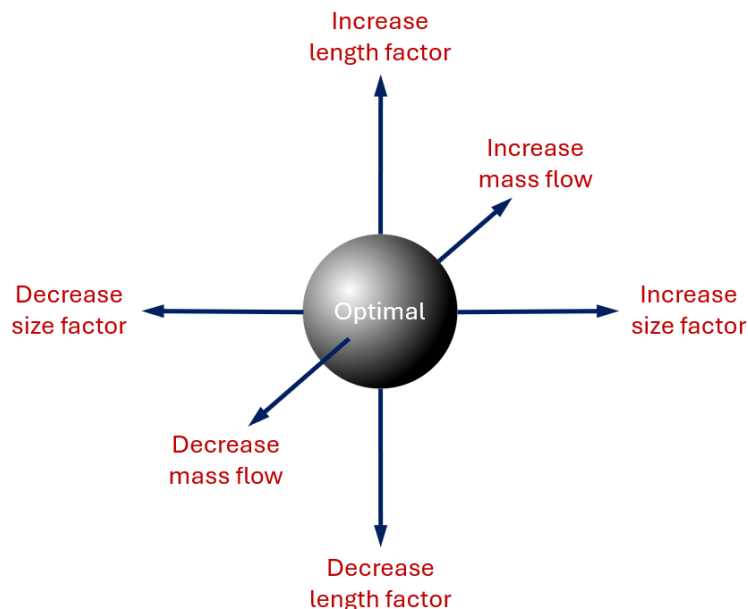
Figure 4.29: Visual representation of varying parameters in order to verify the optimal solution.

Variation of size factor with length and mass flow factor optimized
Changing the size factor from 2 to 4, with optimized length and mass flow based on trial and error, results in a decrease in the percentage of used energy and an increase in the volume of thermal energy storage (TES), both of which are undesired outcomes, shown in Figure 4.30. This is due to the low thermal conductivity of the salt, since the salt diameter belonging to a tube, scales along with the size factor. However, the low thermal conductivity inhibits the extraction of energy from this added salt. The size factor 1 does not give a viable solution based on the maximum temperature difference of the HTF exit temperature based on the first minute and all the subsequent minutes. Therefore is size factor 2 the optimal factor.
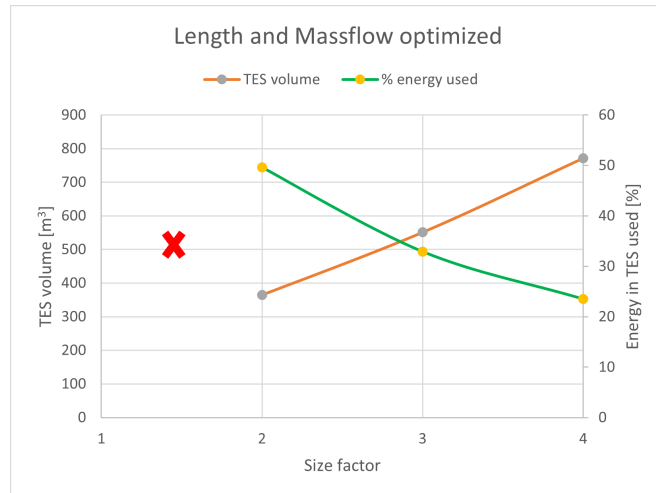
Figure 4.30: TES volume and energy percentage used as function of size factor

Variation of mass flow factor with size factor 2 and length factor 8
Next, with the size factor 2 and length factor 8, the mass flow factor is varied, shown in Figure 4.31$_l$. Decreasing the mass flow factor from 8 to 6 gives a higher number of tubes and is accompanied by a larger TES volume. This shows that for this range the heat transfer coefficient is capable of heating the HTF enough based on the requirements and decreasing the mass flow does have undesirable effects. However, increasing the mass flow factor to 9 or higher does not give a viable solution, based on the ΔT of 75K. Reducing the number of tubes and volume, increases the fraction of used energy, shown in Figure 4.31$_r$. Thus, with size factor 8 and length factor 8 is the mass flow factor 8 optimal.
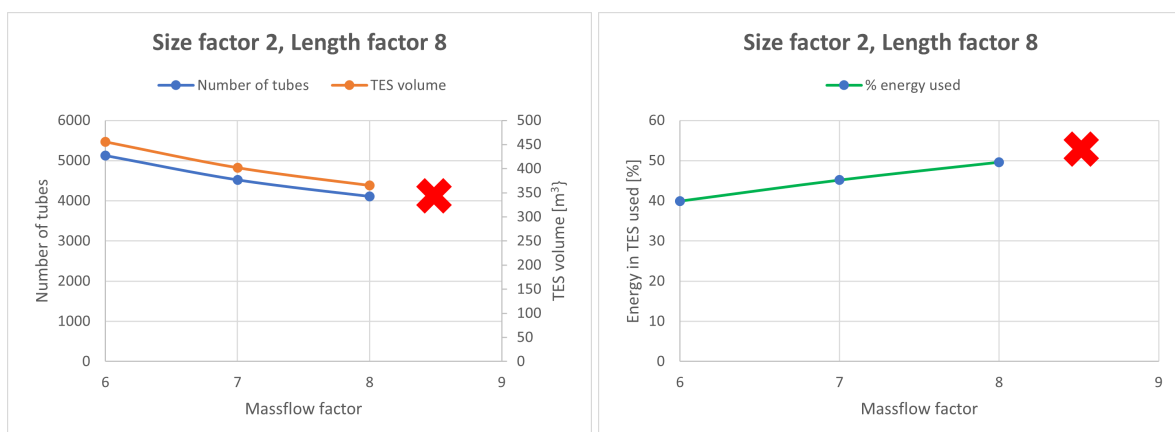
Figure 4.31: Number of tubes as function of mass flow factor for size factor 2 and length factor 8 (left). Energy percentage used as function of mass flow factor for size factor 2 and length factor 8 (right).

Variation of length factor with size factor 2 and mass flow factor 8

The following step is varying the length factor with the size factor 2 and mass flow factor 8 kept constant, shown in Figure 4.32. A length factor which is smaller than 8 will not results in a viable solution, based on the temperature limit of $\Delta T=75K$. This is due to the shorter time the HTF will be in the tube and this has as a result that it does not have enough time to extract the energy. Particularly when a smaller temperature difference between the salt and HTF occurs. Larger length factors only increase the TES volume and thus decrease the fraction of energy which is used. This shows that the mass flow could have been increased for an increase in length factor.
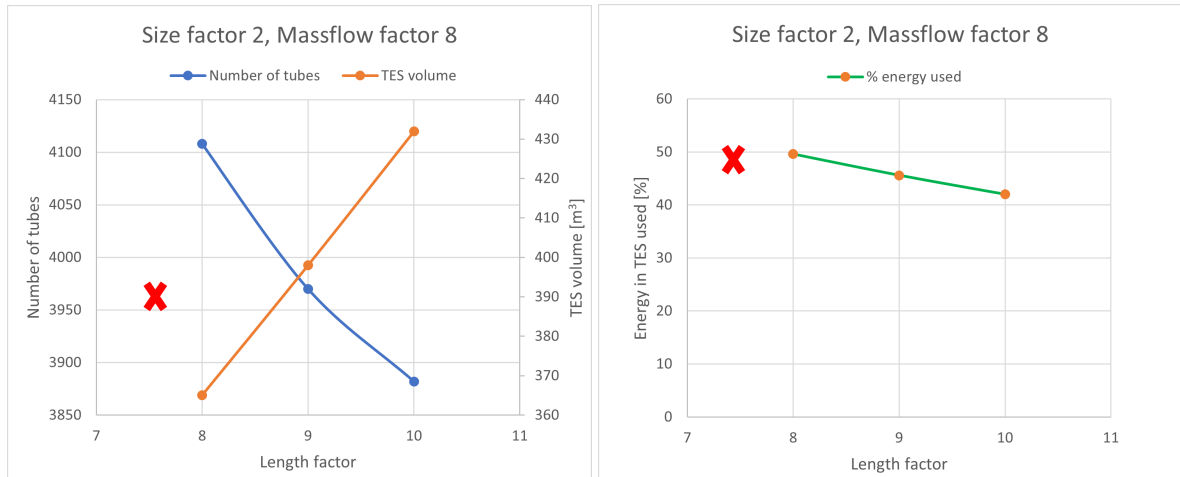
Figure 4.32: Number of tubes as function of length factor for size factor 2 and mass flow factor 8 (left). Energy percentage used as function of length factor for size factor 2 and mass flow factor 8 (right).

Variation of size factor with length factor 8 and mass flow factor 8

The starting point, was the optimal solution equal to size factor 2 and a combination of the same length and mass flow factor. The influence of increasing the size factor to 3 or 4 is shown in Figure 4.33. A drastic decrease in the fraction of energy used in the TES is seen due to the growth in size.
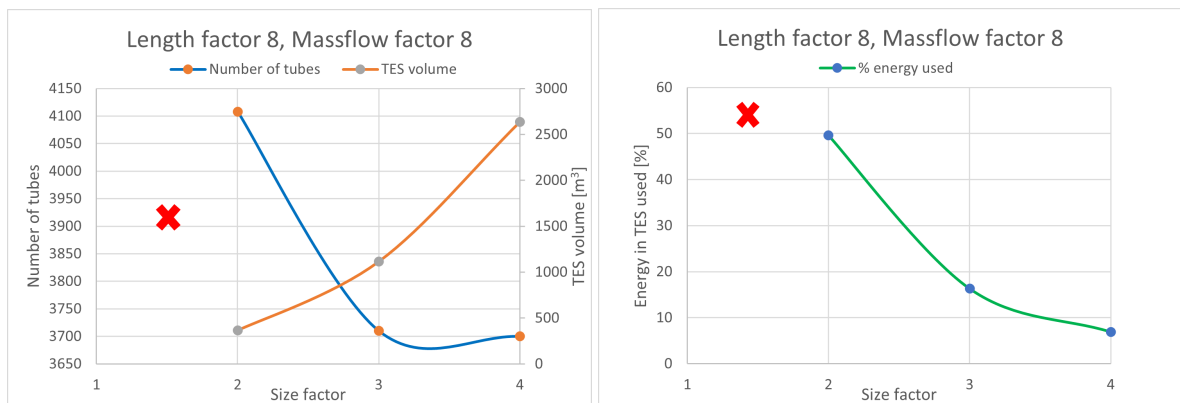
Figure 4.33: Number of tubes as function of size factor for length factor 8 and mass flow factor 8 (left). Energy percentage used as function of size factor at length factor 8 and mass flow factor 8 (right).

Equal variation of mass and length factor

Lastly, the fact that the mass flow and length factor should be equal, but can be varied is shown in Figure 4.34. For different length factors, with equal mass flow factors, it can be seen that the TES volume is equal. The number of tubes will decrease, however, the length will increase. In addition, the outlet temperature of the HTF for all these combinations is approximately the same.
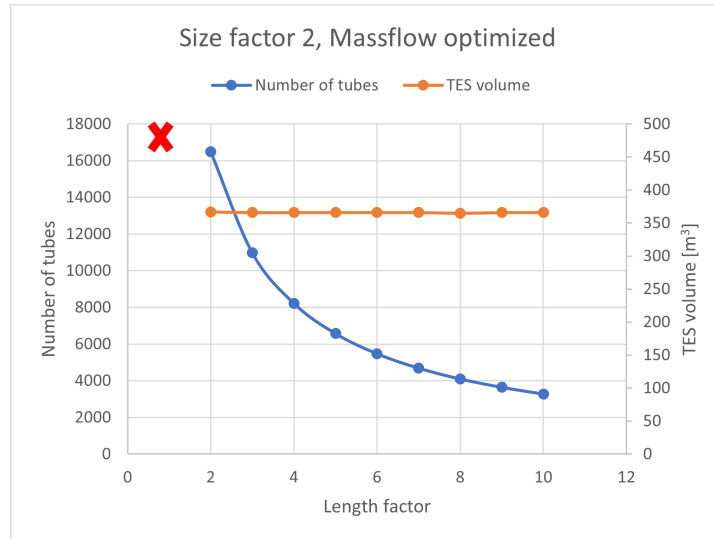
Figure 4.34: Number of tubes as function of length factor at size factor 2 and optimized mass flow factor.

The last conclusion is interesting since the TES can be varied based on the available space in, for example, the factory. Long tubes will give potential structural issues. Therefore, the length size is for now kept on 8 with accompanying mass flow factor 8.

The results of the Matlab simulations, with the optimal solution, are shown in Figure 4.35. With these outlet temperatures, the next step can be taken, which involves the evaporation of water into steam. However, in this thesis, this step is not executed. This is based on the fact that large scale testing to evaluate the above results should be conducted first.
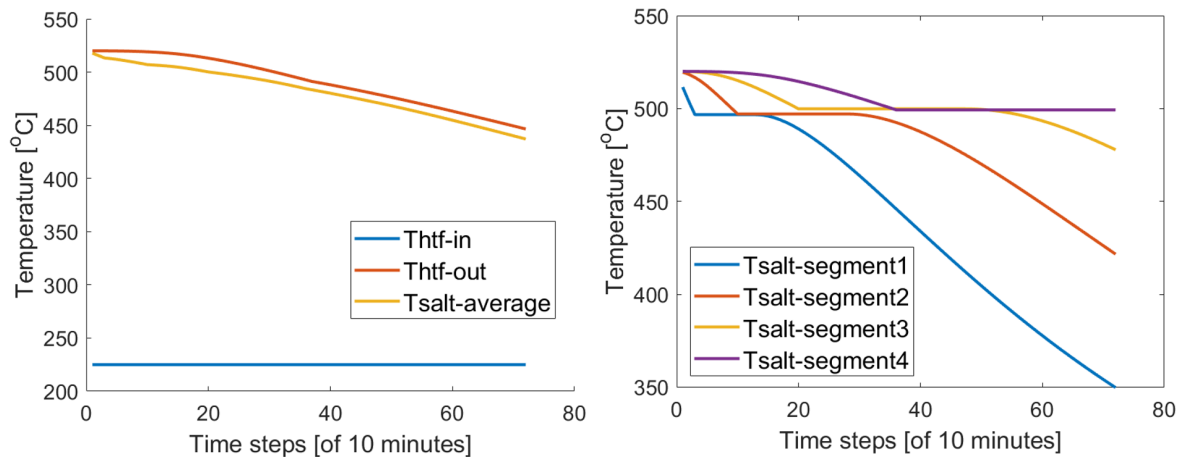
Figure 4.35: Matlab results. Temperature of HTF inlet, HTF outlet and mean PCM temperature as function of time (left). Salt temperature for segments 1-4 (right).

4.3.6. Dimensions and operating parameters

Stand alone energy supply

Large-scale latent heat thermal storage should consist of a multi-tube storage unit. However, Cieśliński and Fabrykiewicz (2023) stated that all the experimental results present in literature either contain a small number of tubes and a small amount of PCM. Therefore, this is based on the semi-empirical model. Additions to this model include the pressure drop and heat losses which will be explained below.

The pressure drop in a straight tube, according to the Darcy-Weisbach formula is equal to (Larock et al., 1999)

$$\Delta p = \frac{fL\rho v^2}{2d} \tag{4.69}$$

where f is the friction factor, dependent on the type of flow, and v is the velocity [m/s] of the fluid flow. When a volumetric flow is used in the equation this equals

$$\Delta p = \frac{8fL\rho \dot{V}^2}{\pi^2 d^5} \tag{4.70}$$

The friction factor for a laminar flow is equal to

$$f = \frac{64}{Re} \tag{4.71}$$

The power required to pump this flow is equal to

$$P = \dot{V} * \Delta p \tag{4.72}$$

The energy, for the amount of time is equal to

$$E = \int_{t_{begin}}^{t_{end}} \dot{V} * \Delta P dt \tag{4.73}$$

where $\dot{V}$ is the volumetric flow.

This results in a pressure drop over one tube in the order of $6*10^{-7}$ bar. For all the tubes, approximately 3600 tubes, this will result in negligible total pumping energy required to overcome this pressure drop.

The heat losses were first estimated with an insulation layer similar to the reference paper, 100 mm. However, this resulted in an outside temperature for the PCM storage system, below denoted as x, of 58°C. A device within a factory should have a temperature which you can touch on the outside. Therefore, a double insulation layer, 200 mm, is used. This resulted in a temperature of approximately 42°C. This results in losses of 69 kW. This insulation could be optimized further to obtain even lower temperatures of the outside insulation, but this is an estimation and there will be unavoidable losses.

Since the heat losses are incorporated in the semi-empirical model, the volumes are already correct and no addition based on the heat losses should be done.

This is obtained by solving the following equation

$$\frac{k_{ins}A(T_{shell,in} - x)}{d_{ins}} = 10A(x - T_{env}) + \epsilon\sigma A(x^4 - T_{amb}^4) \tag{4.74}$$

4.3.7. Conclusion dimensions
To conclude the dimensions and characteristics are as follows for the stand alone case:

- Stored energy 227 MWh
- Length 12 m
- Diameter 6.2 m
- Volume 369 m^3
- Mass approximately 766*10^3 kg without tube mass. With tube mass 802*10^3 kg (with SS310S, ρ 7890 kg/m^3).
- Effective storage density 213 kWh/m^3$_1$ 0.10 kWh/kg$_1$
- Heat loss in 12 hours 828 kWh
- Pump loss upon discharging in 12 hours is negligible

$_1$ Based on 12 hour steam demand (78.8 MWh)

The stored energy is calculated from a temperature of 25 to 520°C, which is 20°above the phase change temperature.

Peak shaving
It is expected that the phase change salt would work better in comparison to steel slag, regarding partial charging and discharging. This is caused by the low thermal conductivity of the salts. However, the model is based on data of complete charging and discharging. The model should first be validated with the use of experimental data. Therefore, no peak shaving results are presented in this thesis.

4.4. Molten salt

The structure of this section on molten salt will follow the same format as previous sections. Initially, there will be a brief explanation of molten salts. Subsequently, based on the literature in the respective section, a choice between a single or two-tank configuration will be made. Following this, key parameters will be identified, and their appropriate values will be determined in the section on key parameter values. The section will conclude with the dimensions and losses of the tank.

4.4.1. Explanation material

Within molten salts, the heat is stored as sensible heat in the liquid phase. Gabbrielli and Zamparelli (2009) state that this can be considered as the simplest and cheapest method. The storage of molten salts can be executed with a single or two-tank configuration. Opting for a single tank presents the advantage of a smaller volume and lower costs. However, it introduces additional challenges, such as possible instabilities within the thermocline region, which will be further explained later on. The main disadvantage of a two-tank storage is the price and volume of the tank. However, the storage of the hot and cold fluid in separate tanks results in a simpler system operation (Gabbrielli & Zamparelli, 2009). Furthermore, with a two-tank system, the temperature and thereby the power can be a constant in comparison to the thermocline tank where a drop in temperature can be expected upon discharging (Bauer et al., 2021).

Using molten salts has some advantages since molten salts are non-toxic, non-flammable, has high thermal stabilities and low vapour pressures. A low vapour pressure indicates that a substance has a limited tendency to transition into a vapour state at a specific temperature, reducing the need for pressurized storage tanks (Bauer et al., 2021).

Another configuration option for the molten salt tank involves choosing between a direct or indirect system. In a direct system, the molten salt serves as the storage material itself. Conversely, in an indirect system, the molten salt transfers thermal energy to another liquid storage material. This reduces the efficiency, since there will be a loss of thermal quality across the heat exchanger (Scott M. Flueckiger & Garimella, 2013). Hence, the preference and, consequently, the focal point of this research is directed towards utilizing a direct system.

González-Roubaud et al. (2017) presented the most commonly utilized molten salts along with their specifications. These, with the addition of L.-l. Zou et al. (2019) on thermal conductivity and operating temperature ranges, are displayed in Table 4.8.

	Solar salt	Hitec	Hitec XL
Composition [wt%]	60% $NaNO_3$ 40% KNO_3	7% $NaNO_3$ 53% KNO_3 40% $NaNO_2$	45% KNO_3 7% $NaNO_2$ 48% $Ca(NaNO_3)_2$
Melting point [°C]	220	142	120
Working temperature range [°C]	290-565	200-450	200-565
Specific heat [J/kg°C] @ 300 °C	1495	1560	1447
Density [kg/m^3] @ 300 °C	1899	1860	1992
Viscosity [cp] @ 300 °C	3.26	3.16	6.37
Thermal conductivity [W/mK] (Mean T)	0.52	0.35	0.655
Cost [$/kg]	1.30	1.93	1.66

Table 4.8: Most commercial used molten salts with properties (González-Roubaud et al., 2017) (L.-l. Zou et al., 2019).

Two main types of storage systems are identified, based on the energy collection method, both categorized under Concentrated Solar Power (CSP). These are the parabolic trough and central receiver (or tower) plants. The parabolic trough system comprises a modular solar field consisting of multiple rows of interconnected solar collectors. Each collector features a linear parabolic-shaped reflector that focuses solar radiation onto the parabola's focal point. Typically, a HTF, often thermal oil or molten salt, is heated in this process. In contrast, the central receiver system utilizes an array of solar reflectors to concentrate solar energy onto a central receiver tower, where a heat transfer fluid is then heated (Peiró et al., 2018). A parabolic dish is another form of the parabolic through collector and Linear Fresnel reflector is another form of the central receiver. All configurations are shown in Figure 4.36 for clarification. Within this section, as it falls outside the scope, no additional emphasis will be placed on the origin of the energy collection method.
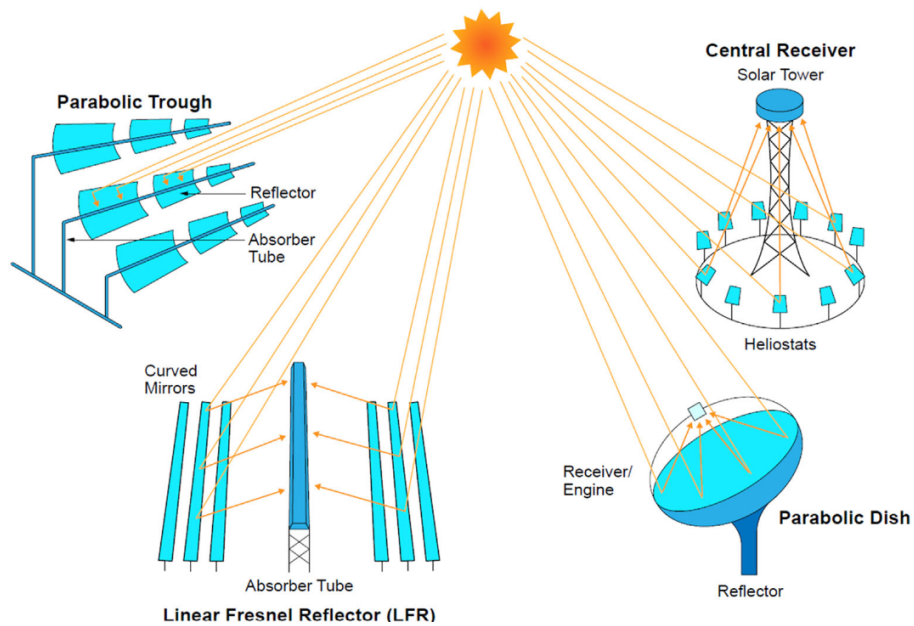
Figure 4.36: Four different concentration principles within CSP(Bhatnagar et al., 2022)

4.4.2. Literature

First, literature about deciding whether to choose a single or two-tank configuration is collected. A single tank consists of a thermocline region. Within this thermocline region, a thermal gradient along the axis of the tank is present. Thermal stratification would be perfect if the thermocline region had an infinitesimal thickness. In Figure 4.37a visual presentation of thermocline tank is presented. Within this thermocline tank often a packed bed of filler material is present, which makes the thermocline tank a dual-media storage system. This packed bed material, such as rocks, should be able to withstand the temperature of the fluid and be compatible with the fluid (Scott M. Flueckiger & Garimella, 2013).
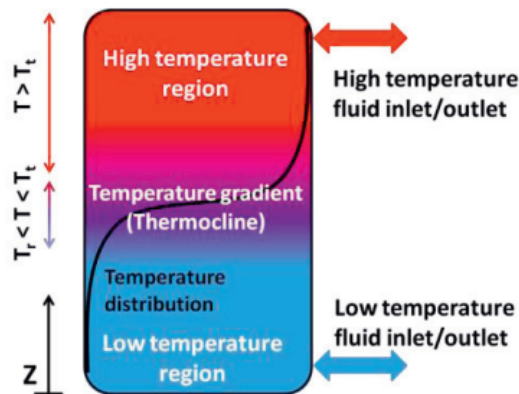
Figure 4.37: Thermocline storage tank temperature distribution example (Scott M. Flueckiger & Garimella, 2013).

The two-tank configuration is comprised of a hot and cold tank. To charge the tank, cold molten salt is heated by, for example, an electrical heater or heat exchanger. When the temperature of the hot tank is reached, the molten salt is stored in the hot tank. To extract the heat, the hot molten salt is pumped to a heat exchanger or other type of energy extraction method, and when cooled down, brought to the cold tank.

The study conducted by Angelini et al., 2014 involved a comparison of the performance between these two storage tank alternatives. This evaluation was carried out by substituting a two-tank configuration with a single thermocline tank and assessing it based on discharged energy. This resulted in a decrease of 33% in costs. However, also a reduction of 34% of the discharged energy was seen. This is due to the temperature decrease of the outlet molten salt when entering the thermocline. Since the configuration of Angelini et al. (2014) accepted only a small temperature drop for the use of the hot molten salt for the next processes, the molten salt was required to have a temperature above 545 °C. In contrast, in the two-tank configuration during discharge, the hot tank is maintained at 550°C, ensuring that 100% of the extracted energy aligns with the target temperature threshold of exceeding 545°C. In the case of this research of designing a thermal storage for the food industry, the strict target of temperature which needs to be above 545 °C is not applicable. So this does not yet exclude the single tank.

Scott M. Flueckiger and Garimella (2013) also concluded, based on literature, that the single thermocline tank is around two-thirds of the price of a two-tank storage. However, they also elaborated on the difficulties of dealing with the thermocline. Thermal stratification is inherently stable if only the density differences, and thereby the Buoyancy forces, are taken into account. This results in the warmer molten salt, with a lower density, on top and colder molten salt at the bottom. However, the viscous stability of the molten salt stratification is less clear. Similar to the density, does the viscosity decrease with higher temperatures. During charging, hot molten salts enter the tank and come in contact with the colder fluid. A negative phenomenon that can occur is viscous channelling. The fluid with the lower viscosity can penetrate the underlying cold molten salts by the formation of random channels or streams. This will enhance thermal diffusion and disturb thermal stratification.

To prevent this effect, the Buoyancy forces should exceed the mixing effect due to the viscosity differences. Qin et al. (2012) formulated a velocity of the fluid, based on the Darcy law formulation of fluid momentum transport. This critical fluid velocity is defined as

$$v_{crit} = gK \frac{\rho_{liq,c} - \rho_{liq,h}}{\mu_{liq,c} - \mu_{liq,h}} \tag{4.75}$$

With $liq,c/liq,h$ the liquid property of the hot and cold fluid.

Buoyancy forces can dampen viscous instabilities below this critical velocity. This process, as said before, is present during charging. During discharging is this viscous instability not present, since the hot molten salt will be extracted from the top.

Based on this instability factor and limitations, the storage configuration designed in this thesis will consist of a two-tank storage. This enhances the ease of use of the molten salt storage configuration.

Next, an example of a two-tank storage system found in the literature will be presented. However, detailed explanations, such as insulation options, will be discussed in the section on key parameter values.

Within literature, a lot of design considerations of a two-tank molten salt storage are optimized for the usage of parabolic through collector, i.e. CSP. This direct solar radiation can be converted into thermal power in two ways, according to the specific research of Gabbrielli and Zamparelli (2009): one option is to directly generate steam by heating high-pressure water, the other way is heating a thermal fluid. This thermal fluid can be used as the storage medium itself or the energy can be transferred to another storage medium.

Within this research, a two-tank configuration is chosen and the storage tank is optimized according to thermal, structural and economic aspects. This research is based on a location in Italy, where a 190,000 m^2 solar collection surface is available for this plant.

The energy storage requirement for this plant is 600 MWh, as outlined in the research, equivalent to 5500 tonnes of molten salts. It was stated that each tank should have the capacity to store the entire volume of molten salts, taking into account operational scenarios such as start-up and draining. Furthermore, both tanks need to possess the capability to store both cold and hot fluids. This operational scenario may arise in instances of shell failure or other circumstances where the rapid discharge of either the hot or cold tank becomes imperative. The proposed configuration is shown in Figure 4.38.
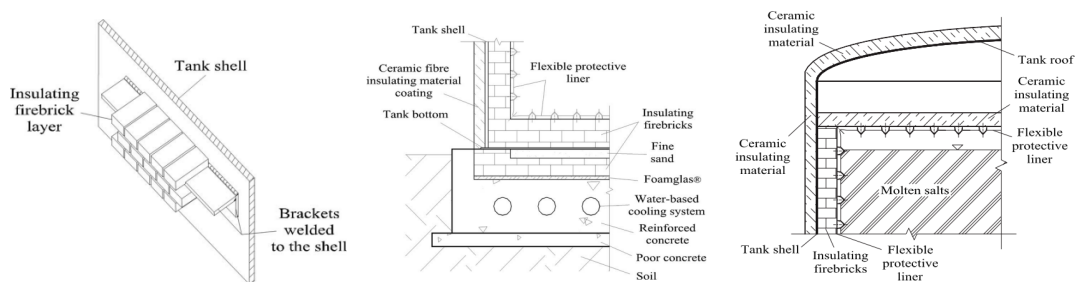
Figure 4.38: Molten storage. Left Insulating firebrick layer, middle storage-tank foundation and right storage tank roof construction (Gabbrielli & Zamparelli, 2009)

Within this research some findings are presented, such as the requirement of a suitable heating system, which ensures that the crystallization temperature of the molten salts will not be reached. Also, the concrete layer, shown in Figure 4.38 needs a cooling system to prevent reaching too high temperatures, lower than 90 °C. This cooling system is required, since concrete loses compressive strength at high temperatures (Mohamed Nazri et al., 2017).

The research of Gabbrielli and Zamparelli (2009) describes two options. One stainless steel tank and one internally insulated, with a firebrick layer, carbon steel tank to suppress the costs. Both tanks had a diameter of 22.4 m and a length of 11 m. The carbon steel tank resulted in lower costs, however, some technical problems concerning the withstanding of pressure differences were still unsolved.

In addition, from the research of a pilot plant based in Spain other lessons are learned. The start-up of the plant, which means the first heating of the storage, should be done progressively to avoid thermal stress within the container. Furthermore, this is also important to avoid HTF vapours and to avoid the presence of air. They also stated that, which was not expected by the authors, the heating of these salts could be done with the use of a simple immersion heater. The main problems they found were associated with leaks and salt solidification in cold points. Therefore, insulation is one of the key factors (Peiró et al., 2018).

4.4.3. Storage method and key parameters

The aim is to design, based on the previous sections, a two-tank molten salt storage with Hitec XL as storage material. Hitec XL is chosen since it has the widest operating range in combination with the highest thermal conductivity. Therefore, the compatibility of Hitec XL with the storage materials used in literature should be confirmed. Next, the differences between the hot and the cold tank should be determined.

Zaversky et al. (2013) elaborated on important tank parameters. First of all, the dimensions and the material of the tank itself. Another parameter is the height of the molten salt pump. This height defines the minimum level of molten salt in the tank. Also, the maximum molten and maximum salt level is a design choice.

Additional distinctions include variations in insulation and tank material selection. The primary challenge with a storage tank lies in heat loss, leading to potential crystallization. Therefore, there will be attention on the prediction of the heat losses.

Based on the literature section above, the hot and cold tank should be able to both handle the hot molten salt for safety reasons, two similar tanks will be designed.

In summary, the choices concerning the storage tanks are:

- Compatibility Hitec XL and thereby the material of the storage tank
- Dimensions tank
- Isolation
- Maximum filling and pump height

4.4.4. Value key parameters

Compatibility

The majority of research about the design of the storage tank does not specifically address Hitec XL as a molten salt; instead, other salts are commonly utilized in these studies. This is due to the comparatively later development of Hitec XL. However, almost all studies utilize stainless steel as material for the storage tank. Consequently, the interaction between Hitec XL and stainless steel becomes a notable focus of consideration. In the investigation conducted by Fernández et al. (2015), it was observed that Hitec XL exhibited reduced corrosion compared to solar salt when paired with various steel types. Notably, stainless steel subjected to tests at 390°C showed no corrosion during 2000 hours of testing, leading to the assumption of compatibility between stainless steel and Hitec XL in this particular application.

Dimensions tank

The choice for dimensions of the storage differs from those used for previous storage materials. In this specific type, as mentioned earlier, the emphasis is solely on storage within the tank, without the need to transfer heat to the HTF within the tank. Consequently, additional considerations come into play. These considerations encompass transportability, particularly adhering to specific regulations in the Netherlands governing maximum dimensions for road transport, which are as follows (RDW, 2015):

- Maximum length of 60 m
- Maximum height of 4.5 m
- Maximum width of 4.5 m

Focusing on finding the optimal aspect ratio did not lead to good results. Within the research of Prieto et al. (2016), an aspect ratio of 0.4 is used. However, this was simply based on enabling comparison to the commercial plant located in Spain. No other specific reason concerning storage efficiency was reported. Therefore, the maximum road dimensions will be leading and therefore a maximum diameter of 4.5 m, without insulation, is assumed.

What is noteworthy is that the commercial company Kyoto Group has optimized the storage tanks for molten salt by employing long, small tanks. This leads to the assumption that, in addition to the aforementioned advantages, it will also contribute to good efficiency.

Isolation and losses

The key parameters in designing this storage tank differ from previous designs, e.g. steel slag and phase change salts. This tank serves solely for storing molten salts, while the processes of heating them and transferring heat to generate steam occur externally. As a result, the primary focus lies in designing the storage tank with particular attention to minimizing heat losses.

A thermal loss, results in a temperature drop of the molten salt if no additional heating is applied. The temperature drop of the salt is dependent on the mass of the salt according to:

$$Q_{loss} = mc_p\Delta T \tag{4.76}$$

This implies that a greater degree of emptiness in the tank corresponds to a more substantial decrease in temperature (Wan et al., 2020). Major differences in temperature decrease can occur. For example in the research of Wan et al. (2020), the full tank weighs around 1380 tonnes. When a constant heat loss is present, the full tank decreases 3.62°C in comparison to 30.38°C for an almost empty tank.

Heat losses should be minimized and compensated to prevent the solidification of the molten salts.

According to Schulte-Fischedick et al. (2008), a uniform temperature distribution of the salt is anticipated within the storage tank. This is attributed to the phenomenon wherein the colder salt, situated at the tank's wall, experiences an increase in density, causing it to descend and attain its maximum velocity. Subsequently, it moves towards the central bottom of the tank, where its temperature begins to rise once more. This cyclic process facilitates effective mixing, allowing the salt to be considered ideally mixed.

There are some reports about the design of the storage tank, focusing on mechanical and thermal performances, with similar choices for storage materials within these reports. Prieto et al. (2016), Wan et al. (2020) and Zaversky et al. (2013) all used Solar Salt. The design of the storage tank in the three articles consists of a stainless steel cylindrical tank with isolation. This isolation differs in details:

- The use of a different tank material and isolation material for the roof
- The use of an air gap between the tank and the isolation material
- The use of an outer protection metal layer around the isolation

However, the major parts are similar and therefore the design considerations of Zaversky et al. (2013) is chosen as a starting point.

The set-up of Zaversky is the following Figure 4.39
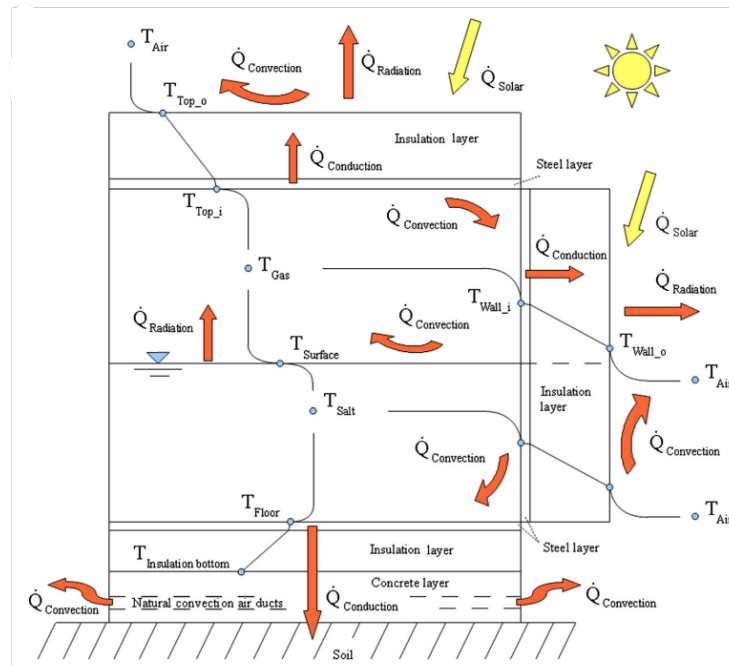
Figure 4.39: Molten salt storage tank thermal model scheme with heat flows and temperature distributions (Zaversky et al., 2013).

There is, in comparison to other research, no air gap between the tank and the isolation. Thermal stress evaluation will result in, as expected due to the high working temperatures, substantial thermal deformations. Therefore, a gap between the tank wall and thermal isolation is desirable (Wan et al., 2020). However, the approach of isolation based on mineral wool is assumed, which should also be able to withstand some thermal expansion (Zaversky et al., 2013).

Within the storage tank, natural convection is present between the molten salt and the storage tank. The heat transfer coefficient is a function of Prandtl and Grashoff. First, the natural convection between the molten salt and the vertical wall is presented in two equations. The first is valid if $10 < Gr*Pr < 10^8$ and the second is valid if $Gr > 10^9$ (Kreith & Manglik, 2016).

$$Nu = \frac{hL}{k} = 0.68 Pr^{1/2} \frac{Gr^{1/4}}{(0.952 + Pr)^{1/4}} \tag{4.77}$$

$$Nu = \frac{hL}{k} = 0.13(Gr * Pr)^{1/3} \tag{4.78}$$

Furthermore, natural convection between the molten salt and the bottom of the tank is present. The heat transfer coefficient is the following

$$Nu = \frac{hL}{k} = 0.27(Gr * Pr)^{1/4} \tag{4.79}$$

valid for $10^5 < Gr*Pr < 10^{10}$.

Finally, there is also natural convective heat transfer between the molten salt and the tank atmosphere. This is quantified according to the following relation

$$Nu = \frac{hL}{k} = 0.54(Gr * Pr)^{1/4} \tag{4.80}$$

$$Nu = \frac{hL}{k} = 0.15(Gr * Pr)^{1/3} \tag{4.81}$$

The first is valid for $10^5 < Gr*Pr < 10^7$ and the second for $10^7 < Gr*Pr < 10^{10}$.

Radiative heat transfer inside the tank is defined as follows. The molten salt is assumed to be a quasi-black body, with an emissivity of 0.95. The tank wall is, according to literature assumed to have an emissivity of 0.35. The Shape factor is based on the equation of Kreith and Manglik, 2016. However, this includes two different radii and in this case, the radii are the same for the two surfaces. Thus this equation will be

$$F_{1 \rightarrow 2} = \frac{1}{2r^2}(d_{1 \rightarrow 2}^2 + r^2 + r^2 - \sqrt{(d_{1 \rightarrow 2}^2 + r^2 + r^2)^2 - 4r^2 r^2}) \tag{4.82}$$

The outer wall surface heat transfer can be either natural convective or forced convective dominated. This is dependent on the following:

- $\frac{Gr}{Re^2}$ <0.7 is forced convection dominated
- $\frac{Gr}{Re^2}$ >1 is natural convection dominated

In natural convection dominated regimes, the equations above can be used. For forced convection on the side walls, this equation yields

$$Nu = \frac{hD}{k} = 0.3 + \frac{0.62Re^{1/2}Pr^{1/3}}{(1 + (0.4/pr)^{2/3})^{1/4}}(1 + (Re/282000)^{5/8})^{4/5} \tag{4.83}$$

valid if Re*Pr>0.2.

The forced convection on the roof gives

$$Nu = \frac{hL}{k} = 0.664Re^{1/2}Pr^{1/3} \tag{4.84}$$

$$Nu = \frac{hL}{k} = 0.037Re^{0.8}Pr^{1/3} \tag{4.85}$$

For the radiative heat transfer of the outer surface of the storage tank, Zaversky et al. (2013) considered both solar irradiation and long wave emitted radiation. Since the storage tank destination is not yet determined, the irradiation is neglected. Nevertheless, in future designs should irradiation also be taken into account since, according to Zaversky et al. (2013), the outer wall could reach temperatures up to 100°C originating from solar irradiation. The emitted radiation is based on

$$\dot{Q}_{radiation,roof} = A_{roof} * \sigma * \epsilon_{surface}(T_{surface}^4 - T_{sky}^4) \tag{4.86}$$

$$\dot{Q}_{radiation,wall} = A_{wall} * \sigma * \epsilon_{surface}(T_{surface}^4 - T_{air}^4) \tag{4.87}$$

with $\epsilon_{surface}$ 0.3.

Wan et al. (2020) stated that the heat transfer loss is a constant and 90 kW, this is built by losses via wetted parts, non-wetted parts and the bottom. The part of the heat transfer which is the largest, is dependent on the molten salt level of the tank. This is shown in Figure 4.40. SIDE represents the wetted part, CAP represents the non-wetted parts and BOTTOM represents the bottom part. To conclude, the modes of heat transfer are different within the tank, but the temperature of the wall, and therefore the heat losses, are almost constant and independent of the salt level. What furthermore can be concluded from this, is that radiation from the salt interface to the non-wetted inner wall plays a major role and therefore the roof should also be well insulated.
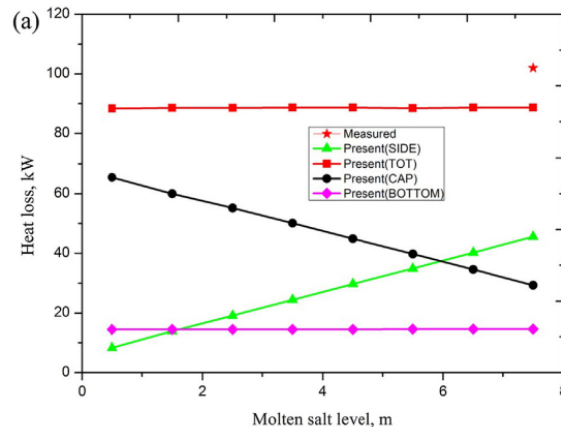
Figure 4.40: Heat losses molten as function of molten salt level (Wan et al., 2020).

Wan et al. (2020) showed a temperature distribution of the tank with an experimental validated numerical model, presented in Figure 4.41. What was concluded is that in the vertical direction, into the bottom, the temperatures exceed around 400°C if no cooling system is used. Therefore, multiple papers include a cooling system to keep the temperature of the tank foundation around 90°C and prevent temperatures that the materials cannot withstand. More specifically, a centre-to-outside cooling flow pattern should be used.
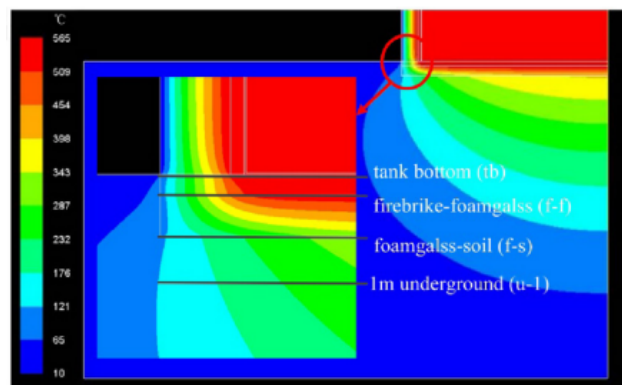
Figure 4.41: Temperature distribution for molten salt storage tank (Wan et al., 2020).

Based on the conclusion that the entire tank will have the same temperature and that thin insulation on the roof would result in greater losses, the decision was made to construct the entire tank with a uniform thickness of stainless steel and fully insulate it with 40 cm of mineral wool. This results in the following configuration in Figure 4.42.
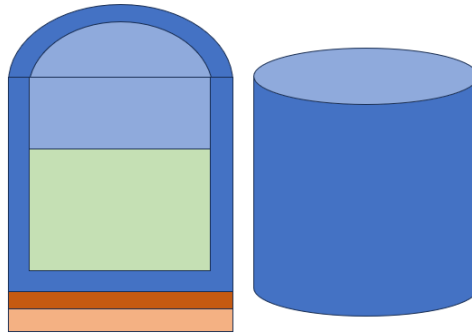
Figure 4.42: Tank configuration outline with salt (green), mineral wool isolation (blue), foam glass (orange), and air-cooeled concrete (light orange). Not specifically coloured are the 4 cm thick stainless steel tank and flat sheet metal on top of the mineral wool isolation.

With the following components:

- Tank is made of 4 cm thick stainless steel
- Wall and roof isolated with 40 cm thick mineral wool
- On top of the isolation a protective sheet of metal layer, this sheet is a weathered galvanized flat sheet metal
- The bottom is isolated with 40 cm foam glass isolation
- This isolation is followed by an air-cooled, concrete layer which will be at 90°C

The protective sheet layer will not be taken into account as a resistance for heat loss, since it is a thin layer with neglectable resistance. However, the emissivity of the sheet layer is taken into account. It should be noted that the irradiation is not taken into account since the location of the tank is not defined. However, the protective sheet layer radiation is also location dependent and this layer is taken into account. This is due to the minor effects of this layer. If the sheet metal layer is not applied, the emissivity of mineral wool should be used and this will be around 0.94, which is close to a black body.

With thermal conductivity for mineral wool and foam glass given as

$$k_{mineralwool} = 0.037 + 2*10^{-4}*(T - 273.15) \tag{4.88}$$

$$k_{foamglass} = 0.043 + 1.3*10^{-4}*(T - 273.15) \tag{4.89}$$

The other properties are 160 kg/m^3 for the density of mineral wool and 0.84 kJ/kgK for the heat capacity. For the foam glass, these are 7800 kg/m^3 and 0.49 kJ/kgK.

To verify if the order of magnitude of the losses is right, the results of the research of Zaversky et al. (2013) is presented below.

The results from the research of Zaversky et al. (2013) shown in Figure 4.43 shows in light grey the cold tank and in dark grey the hot tank. Furthermore, on the left a full tank is presented and on the right an empty tank. It should be noted that an empty tank is never really empty, since the pump within these tanks is not able to fully empty it. In all the configurations, the surface convective heat loss can be neglected. The main influences are the surface radiation heat losses. Furthermore, the lower the filling level, the radiation heat losses are more severe and lower convection heat losses are at the wetted inner wall.
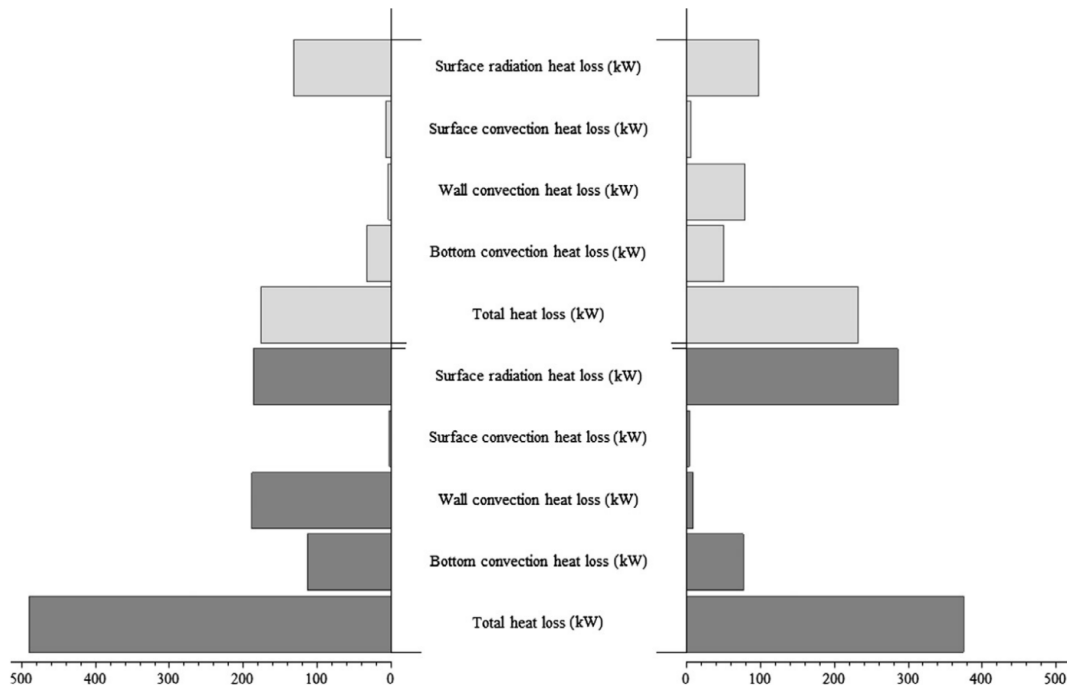
Figure 4.43: Heat losses molten salt for the cold tank (light grey) and hot tank (dark grey) both for full tank (left) and empty tank (right) (Zaversky et al., 2013).

Maximum and minimum filling

Regarding the maximum filling level, Zaversky et al. (2013) and Wan et al. (2020) both fill till 1m above the maximum, which results in filling to 13 and 7.4 meters respectively. However, Wan et al. (2020) performed a mechanical and thermal evaluation on different filling levels. They have shown that the stress has a linear relation with the filling level of the tank. The maximum stress for all filling levels is present in the bottom corner. They assumed a rigid foundation, which resulted in a total stress range of 100MPa, which requires extra attention since it can cause a fatigue problem. Furthermore, uniform settlement of the tank is required and some additional tank foundation stiffness requirements are presented.

However, for now, the filling levels of both papers are used to make the first design estimates. This will result in a filling level of 1m less than the maximum.

The minimum filling level is dependent on the height of the pump. This ranges in literature between 0.7 and 0.9 meters. The mean value of these is assumed. To conclude

- Maximum salt level: 1 m below maximum
- Minimum salt level: 0.8 m above tank foundation

4.4.5. Dimensions and operating parameters

The same approach as for the steel slag is applied here. This starts with a theoretical assumption of the amount of hot molten salt to be able to generate the required energy.

In Table 4.8 the thermophysical properties of different molten salts are shown which are from the research of González-Roubaud et al. (2017). Since the Hitec XL solar salt is chosen as molten salt based on the large operating range (200-565°C), a more in-depth search into these properties is done, for example, focusing on temperature dependence.

Hence, the study conducted by L.-l. Zou et al. (2019) is employed to illustrate the temperature dependence:

$$\rho_{HitecXL} = 2022744 - 9.43393 * 10^{-4} * T \tag{4.90}$$

$$Cp_{HitecXL} = 1.77878 - 7.55155 * 10^{-4}T \tag{4.91}$$

$$k_{HitecXL} = 3.83349 - 0.02857 * T + 8.07852 * 10^{-5} * T^2 - 7.24056 * 10^{-8} * T^3 \tag{4.92}$$

With T in °C.

What should be noted is that in the article of L.-l. Zou et al. (2019), the first 'T' within the equation of the thermal conductivity of the Hitec XL is missing. However, the assumption, based on unexpected values, is taken that this should be present in the equation. Furthermore, the ranges of input are between 250 and 500 degrees. Therefore, for the cold tank the values at 250 °C are assumed and for the hot tank, the values at 500°C are assumed.

With this information, the assumption of a steady state heat transfer problem is obtained with an inner wall temperature equal to the salt. The influence of the filling level on the heat losses is thereby neglected. The conduction via the tank wall and insulation should be equal to the radiation and convective heat losses within a steady state problem. With this information, a temperature, and therefore the heat losses, of the outer wall and roof can be obtained.

$$Q_{conduction} = Q_{radiation} + Q_{convection} \tag{4.93}$$

which is equal to the following equation:

$$\frac{1}{\frac{th_1}{k_1} + \frac{th_2}{k_2}} A(T_{wall,int} - T_{wall,ext}) = \sigma\epsilon_{surface}A(T_{wall,ext}^4 - T_{amb}^4) + hA(T_{wall,ext} - T_{amb}) \tag{4.94}$$

Within this equation only one unknown, the $T_{wall,ext}$ can be solved and thereby can the heat losses be determined.

Additionally, it is crucial to assess the heat losses occurring at the bottom, focusing on conductive heat transfer. It is assumed that the concrete foundation should not exceed 90 °C, which was also adopted by Zaversky et al. (2013) and Rodríguez et al. (2013). They stated that this is done by natural convective air cooling. However, an explicit model of this heat transfer is left aside and this approach is also adopted within this research.

Moreover, the consideration of solar irradiation is neglected at this stage, as the precise location of the tank has not been determined. Consequently, the presence or absence of solar irradiation on the tank remains uncertain. According to the findings of Zaversky et al. (2013), it is highlighted that the outer wall temperature can reach 100°C under irradiation. As a result, the results of the calculations which exclude this mode of heat transfer can be underestimated. Nevertheless, it is assumed that the ambient temperature remains constant at 25°C, which is a value notably high for the Netherlands and therefore can cause overestimation.

This results in a heat loss for the hot tank of 31.25kW and for the cold tank of 10.05kW. To be able to compare the values to the research of Zaversky et al. (2013) and Wan et al. (2020), the area of the salt tank of both tanks is calculated and the heat loss is divided by this area. Both tanks are larger than the tank in this research. The area for Wan et al. (2020) solely focused on the hot tank, so therefore only this value is shown. The first value is the calculated heat loss per area within this research. The results fall in the range of expectations.

- Hot tank at 565°C

    - 0.13 kW/m^2
    - 0.12 kW/m^2 (Zaversky et al., 2013)
    - 0.15 kW/m^2 (Wan et al., 2020)

- Cold tank at 220°C

    - 0.041 kW/m^2
    - 0.050 kW/m^2 (Zaversky et al., 2013) (at 290°C)

4.4.6. Conclusion dimensions
To conclude the dimensions and characteristics are as follows for the stand alone case:

- Stored energy 119 MWh
- Length 2 x 17.7 m
- Diameter 2 x 4.5 m
- Volume 2 x 281.2 m^3
- Mass 478*10^3 kg for both tanks
- Effective storage density 140 kWh/m^3$_1$ 0.16 kWh/kg$_1$
- Heat loss in 12 hours 516 kWh
- Pump loss upon discharging in 12 hours is negligible

$_1$ Based on 12 hour steam demand (78.8 MWh)

In this case, in comparison to steel slag and phase change salts, do the heat losses not result in a larger volume of thermal energy storage. This is since these heat losses should be compensated directly to prevent the solidification of the molten salts. Furthermore, it is designed to store energy for those 12 consecutive hours. Thus, the total mass is calculated by calculating the mass of the hot, full, tank in combination with the minimum level of salt in the cold tank. The pump losses for the storage itself are not present within this case.

And for the peak shaving case

- Stored energy 63.3 MWh
- Length 2 x 9.9 m
- Diameter 2 x 4.5 m
- Volume 2 x 157.2 m^3
- Mass 259*10^3 kg for both tanks
- Effective storage density 127 kWh/m^3$_2$ 0.15 kWh/kg$_2$
- Heat loss in 12 hours 312.8 kWh
- Pump loss upon discharging in 12 hours is negligible

$_2$ Based on 12 hour steam demand (40 MWh)

It should be noted that this is an addition to a constant boiler generation.

<div style="text-align: right; font-size: 3em;">5</div>

Steam generation

In this Chapter, the focus shifts to generating steam with the extracted energy originating from the thermal storage system. Initially, a distinction between fire- and water-tube boilers is delineated. These two boiler systems are well-known systems for the generation of steam within industry. Subsequently, the steam generator pathway is selected and the associated heat transfer equations are collected. Finally, the dimensions of the boilers are presented. This design encompasses the utilization of various HTFs at different temperatures. The first is hot air at 700°C and the second is molten salt at 565°C. For the latent storage, which encompasses the phase change salt, the steam generation is not included. This is due to the fact that the focus should first be on testing the assumptions regarding the large-scale phase change salt storage. When using thermal oil, the results will be closer to those obtained with molten salts rather than with air due to the density of thermal oil which is closer to the molten salt.

It should be noted that the steam generation, described in this Chapter, focuses on evaporating water at approximately 184°C (10 barg) to steam. However, the feed water, from the processes in the factory, is provided at approximately 104°C and 11 bar. This will be preheated with a part of the HTF, approximately 15%, and will be led to the steam drum. This 15% is calculated by dividing the energy required to heat the water by the total energy required to heat the water and evaporate the water, based on the enthalpy differences. This steam drum is at 11 bar and around 184°C. From there, it will be led to the evaporation step, described in this Chapter. This preheat step has two main advantages, the first is the prevention of salt precipitation from the feedwater by not evaporating 100% of the water. The second is the ability to store a portion of the steam by increasing the pressure in the steam drum.

5.1. Boiler choice

5.1.1. Boiler types

In the fundamentals of heat transfer during boiling, various modes of heat transfer exist. As mentioned, there are two primary types of boilers: the fire tube boiler and the water tube boiler. Fire tube boiler is, according to Towler and Sinnott (2022), known as pool boiling. Within pool boiling, a surface is submerged in a pool of liquid. The mechanism of heat transfer from this submerged surface is dependent on the temperature of the surface.

At low temperatures, only natural convection, which is caused by a density difference upon heating the water, at the liquid side is present as the mechanism of heat transfer. When the temperature of the surface is raised, boiling occurs. These vapour bubbles are formed at the surface and eventually break loose. The rising bubbles increase the heat transfer rate. This is called nucleate boiling. At higher temperature differences, this rate increases until a critical heat flux value is reached. The progression of this pattern is shown in Figure 5.1. After the critical flux, the heat transfer rate decreases drastically due to dry patches that occur on the surface due to vapour generation. When a higher temperature difference is present, the surface is fully blanketed with vapour. This induces the mechanism of heat transfer as conduction through the vapour film. When very high temperatures are reached, radiation augments the conduction, and heat flux is again increased.
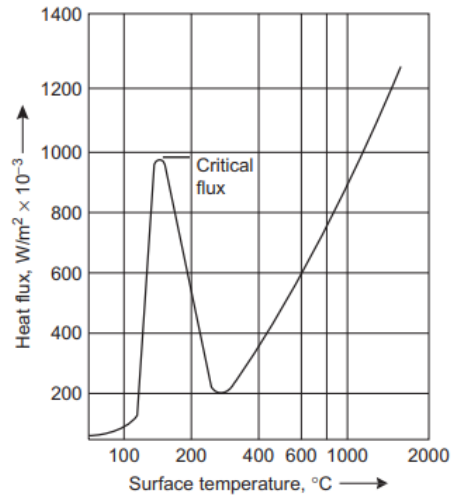
Figure 5.1: Representation of heat flux as a function of surface temperature (Towler & Sinnott, 2022)

The water tube boiler is referred to, according to Towler and Sinnott (2022), as convective boiling. In water tube boiling, heat transfer depends on the state of the fluid along the length of the tube. There are four possible flow regions within the tube, shown in Figure 5.2. These regions are described as:

- Single phase flow: within this region, the liquid is not boiling since it is below the boiling point. Heat is transferred by forced convection.
- Subcooled boiling: the liquid close to the wall reaches the boiling point and increases the rate of heat transfer. However, the bulk of the liquid is still in liquid state.
- Saturated boiling: within this region the bulk of the liquid reaches the boiling point and bulk boiling, similar to nucleate boiling, takes place. Within a long tube, the liquid will flow along the tube wall and the vapour flows in the central core. This is an annular flow pattern.
- Dry wall: this region occurs when a large fraction is vaporized. The wall is dried out. Heat transfer is due to convection and radiation to the vapour.
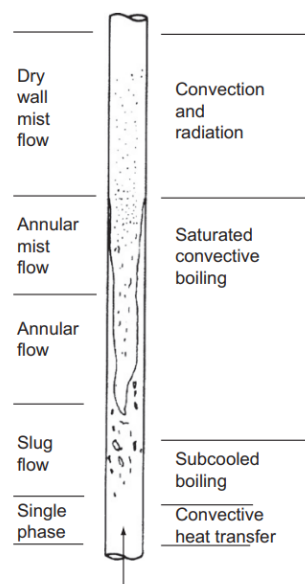
Figure 5.2: Water tube boiling phases (Towler & Sinnott, 2022)

According to Arcadis, the fire tube boiler is the most commonly utilized type within the food industry. Currently fueled by fossil fuels, these boilers are intended to be replaced by thermal energy storage systems.

The choice for the fire-tube boiler is probably based on the following arguments:

- Simple design and construction
- Ease of use, can handle fluctuations in steam demand easily
- Low operating and maintenance costs
- Cheaper than water tube boiler
- Based on Figure 5.3 from Babcock Wanson the fluctuating demand pattern with associated pressures the fire tube boilers should be the type of boiler (Wanson, n.d.)
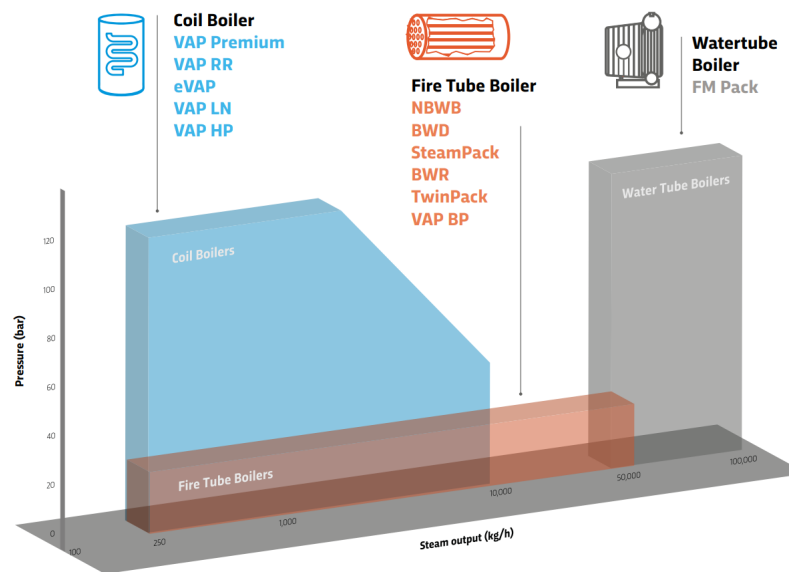
Figure 5.3: Babcock Wanson steam boiler range (Wanson, n.d.)

To evaluate if using a boiler, similar to a fire tube boiler with hot air or molten salt as HTF, is a viable option, the focus will be on the temperatures present in a fire tube boiler for the different sections. An example of a fire-tube boiler is shown in Figure 5.4. This fire tube boiler consists of three passes. The number of passes can be adjusted.
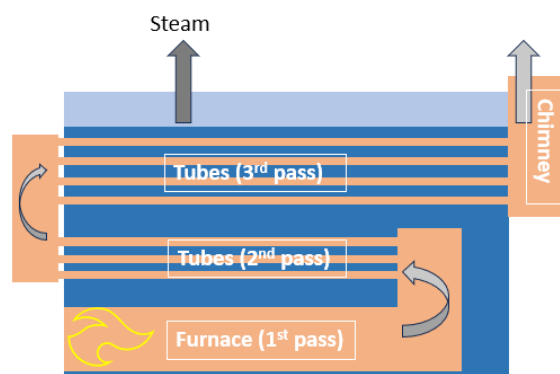
Figure 5.4: Visual representation of a fire-tube boiler with three passes

Within a conventional fire tube boiler two main sections are present, the radiation section and the convection section. The ration section is the section where the furnace is in. Within this section, the radiation heat transfer is, according to experimental validated numerical research of Rahmani (2014), responsible for 82.65% of the exchanged power in this section. Furthermore, the percentage of the radiation section in comparison with the total exchanged power in the fire tube boiler is 22.9%. This percentage is mainly due to the large heat transfer surface within the convection section in comparison to the radiation section.

In the combustion chamber, the temperatures of the hot gases are dependent on the oxygen-to-fuel ratio and the type of fuel. This temperature could reach 1900°C, shown in Figure 5.5. This profile encompasses a 4-pass fire tube boiler with a length of 5 m per pass. The operating pressure is higher and fluctuates from 0.689 bar to 20.68 bar. However, this did not influence the temperature profile largely (Rahmani, 2014).
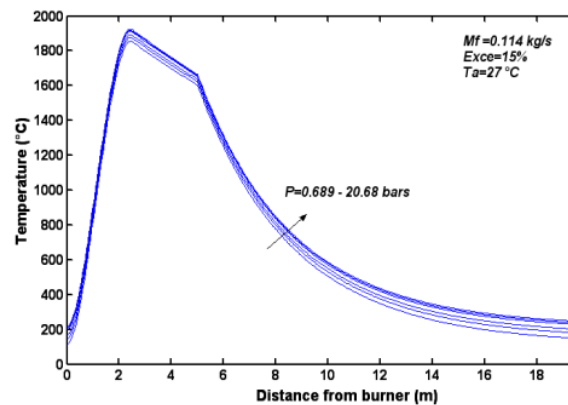
Figure 5.5: Temperature as a function of distance from the burner for different pressures (0.689-20.68 bar) (Rahmani, 2014)

What is noted is that these temperatures do not match the temperatures which are present within this study, 565-700°C. Therefore, further investigations into steam generation with air at temperatures around 700°C and from salt at 565°C are done.

Heat Recovery Steam generators (HRSG) are examined since these have familiar features regarding the HTF outlet temperature originating from steel slag. HRSG makes use of the heat from exhaust gases to generate steam. These exhaust gases are, for different processes, at different temperatures available. An example is exhaust gases from gas (combustion) turbine. These have temperatures of 480 to 600°C (A. Ahmed et al., 2018). HRSG, both horizontal and vertical, are present within industry. The evaporation part of an HRSG consists of tubes filled with water over which the exhaust gases will flow. This will evaporate the water. This could be simulated as a shell and tube heat exchanger.

For generating steam from molten salts, literature is mainly focused on transferring heat in a shell and tube heat exchanger where the molten salt is located in the shell. For example, Yuan et al. (2016) and Y. Zou et al. (2020), both use a shell and tube steam generator. The difference is the shape of the tubes, one uses U-shape tubes, and the other straight tubes. Additionally, the operating parameters, including the velocity of the molten salt, among other factors, differ between the two research studies. U-tubes are employed in shell and tube heat exchangers to accommodate thermal expansion and contraction while facilitating efficient heat transfer. To prevent the solidification of molten salts in the heat exchanger an electrical heat tracing system should be used to preheat pipes, vessels, and heat exchangers (Qian et al., 2017).

Based on the aforementioned steam generation pathways, which both resemble a shell and tube system, this approach will be adopted for the remainder of this Chapter. An U-tube configuration will be adopted, to avoid thermal stresses. The U-tube shell and tube steam generators will be designed with AspenEDR. The emphasis of the design will be on achieving the most cost-effective solution.

5.2. AspenEDR

As mentioned earlier, the design in AspenEDR will prioritize generating the most cost-effective solution. This is accomplished through an iterative process. Preceding this process, the characteristics of the substances involved in the steam generation process are put into AspenEDR. The properties of hot air and water can be implemented based on the databases available in the program. However, for molten salt, these properties must be manually implemented. This is based on findings from literature (L.-l. Zou et al., 2019).

The process will be based on the following steps, which represent an iterative process, shown in Figure 5.6:

1. The material of the shell and tubes is chosen
2. A typical pressure drop allowance will be adopted for each side
3. With this allowable pressure drop, the pinch temperature and tube diameter will both be varied within a chosen range
4. For the case with the lowest cost, based on the above steps, the pressure drop of both sides will be lowered to see the effects on the pumping power and costs
5. The lowest costs, for both CAPEX and pumping power, will be adopted as the design of choice
6. With this design of choice another iteration will be done for different pinch temperatures
7. Final design is selected
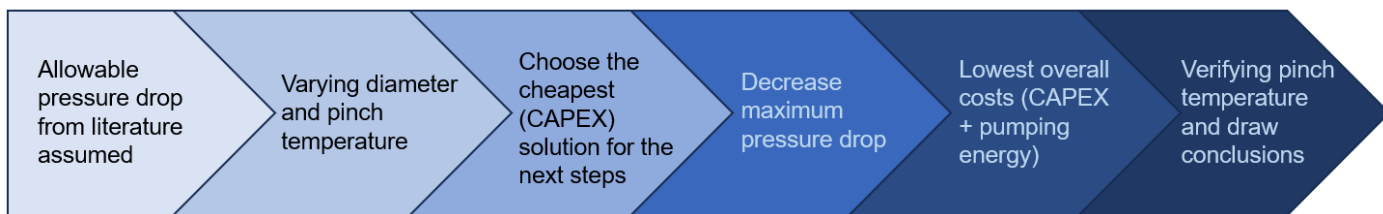
Figure 5.6: Representation of steps within AspenEDR

5.2.1. Results Steel slag

The first iterations were the following:

- The material used for the heat exchanger is carbon steel
- Maximum pressure drop liquid, tube side, is 0.5 bar (Towler & Sinnott, 2022)
- Maximum pressure drop vapour, shell side, is 0.5 x system gauge pressure and this is also around 0.5 bar (Towler & Sinnott, 2022)
- Pinch temperature ranging from 10 to 30°C
- Diameter of tubes ranging 20 to 38 mm

The results that are extracted are the price, shell-side pressure drop, tube-side pressure drop, and mass flow of the air for different pinch temperatures. The pressure drop in combination with the volume flow of the air results in the amount of Power that is required to run the discharging. The results are shown in Figure 5.7 and 5.8.
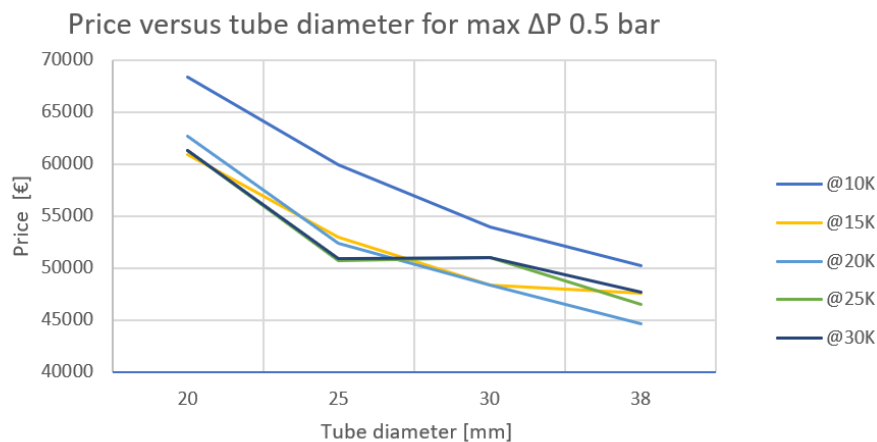
Figure 5.7: Price versus tube diameter with maximum △P 0.5 bar.
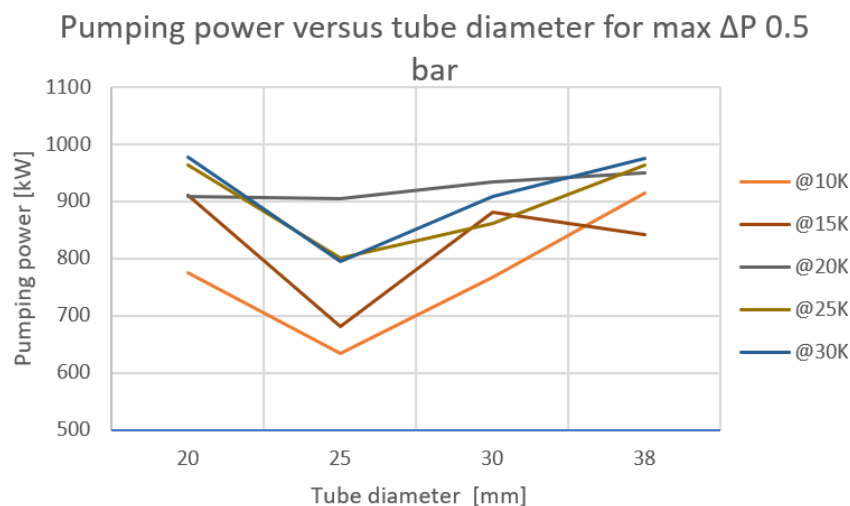
Figure 5.8: Pumping power versus tube diameter with maximum △P 0.5 bar.

The pressure drop on the tube side for every case was much lower than the shell side pressure drop. In combination with the lower volumetric flow, this can be neglected.

What is furthermore concluded from the Figures, is that the price decreases for larger tube diameters. The pumping power of the shell side is fluctuating but is high for all cases. Further investigation into decreasing the tolerance of the shell side pressure drop is done with the lowest value of the price, e.g. tube diameter 38mm and ΔT 20K. To make a good comparison, should the pumping costs also be included.

The pumping power costs are roughly estimated and are recorded for two years. The number of hours is based on 5 days a week, thus excluding the weekend and 90% of available time in operation to account for maintenance, for example. As the storage system needs to both charge and discharge, this calculation utilizes 50% of the remaining hours. Then the optimal case is chosen for which the following equation is minimized

$$\text{CAPEX} + 2 * \frac{5}{7} * \frac{1}{2} * 8760 * 90\% * €_{1kWh} * kW_{shellside} \tag{5.1}$$

The price is estimated to be around 0.1€/kWh (Tarieven, 2024). This resulted in the following Table 5.1.

Max SS ΔP allowance [bar]	ΔP SS [bar]	Price k[€]	Pumping power [kW]	Total price [k€]
0.5	0.49	45	950	579
0.4	0.36	47	695	439
0.3	0.28	51	546	358
0.2	0.18	67	341	260
0.1	0.06	93	118	160
0.05	0.04	900	78	944

Table 5.1: Influence of maximum allowable shell side (SS) pressure drop on price of the heat exchanger and pumping power

This shows that there is an optimum around the maximum allowable pressure drop of 0.1 bar. First, it will be evaluated if even larger tube diameters than the standard available in AspenEDR will give better results. If this is not the case, the choice of pinch temperature in combination with the maximum allowable pressure drop, around 0.1 bar, will be evaluated.

The evaluation of even larger tube diameters is shown in Figure 5.9. It is observed that the price first flattens and then increases slightly for larger diameters. Therefore, tubes with 38 mm diameter are adopted for the rest of this part.
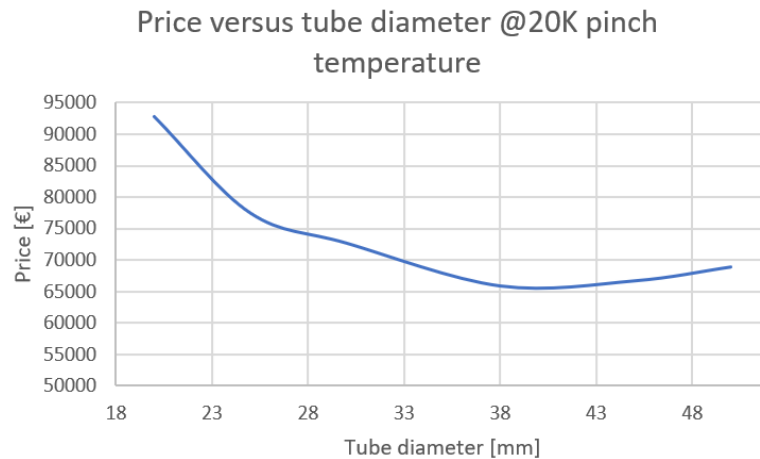
Figure 5.9: Evaluation of larger tube diameter on price at pinch temperature of 20K

Next, the other possible pinch temperatures should be evaluated for these pressure drop tolerances, to see if the assumption to go for the pinch temperature of 20K is correct. This resulted in Table 5.2

| Max ΔP | Pinch 10K | | | Pinch 15K | | | Pinch 20K | | |
	HEX [k€]	Power [kW]	Total [k€]	HEX [k€]	Power [kW]	Total [k€]	HEX [k€]	Power [kW]	Total [k€]
0.2	67	328	251	75	347	270	67	341	260
0.1	98	187	203	97	158	185	93	119	160
0.05	193	88	242	N.C.$_1$	N.C.$_1$	N.C.$_1$	900	77	944

| Max ΔP | Pinch 25K | | | Pinch 30K | | |
	HEX [k€]	Power [kW]	Total [k€]	HEX [k€]	Power [kW]	Total [k€]
0.2	69	350	266	67	349	263
0.1	96	106	156	93	121	161
0.05	1151	74	1193	900	79	945

Table 5.2: Fluctuating the allowable pressure drop for different pinch temperatures with as results price for heat exchanger (HEX), power, and total price including pumping costs. $_1$, not converged.

What could be noted from Table 5.2 is that for pinch temperature between 20-30K in combination with a maximum allowable pressure drop of 0.1 bar, the prices are the lowest and between 156-161 k€. The lowest pumping power, based on these three options, is for now chosen as a decision maker. This results in the, for now, optimal case of

- ΔT 25K
- Pressure drop shell side 0.055 bar
- Pressure drop tube side 0.054 bar
- Pumping power shell side 106 kW
- CAPEX 96 k€
- Energy cost for 2 years 60 k€

The TEMA sheet can be found in the Appendix B.

5.2.2. Results Molten salts

Regarding the heat transfer from molten salt to water in order to evaporate, the following iterations are conducted:

- The material used for the heat exchanger is stainless steel 316L (Y. Zou et al., 2020)
- Maximum pressure drop liquid, tube side, is 0.5 bar (Towler & Sinnott, 2022)
- Maximum pressure drop liquid, shell side, is 0.5 bar (Towler & Sinnott, 2022)
- Pinch temperature ranging from 15 to 30°C
- Diameter of tubes ranging 13 to 20 mm

The pinch temperature range is smaller than in the previous case due to the possibility of the solidification of the salts in the shell. Although a heat trace system is required which prevents the solidification of the molten salts, still a safe margin is taken. The results are again the price, shell-side pressure drop, tube-side pressure drop, and mass flow of the molten salt. The results are shown in Figure 5.10.
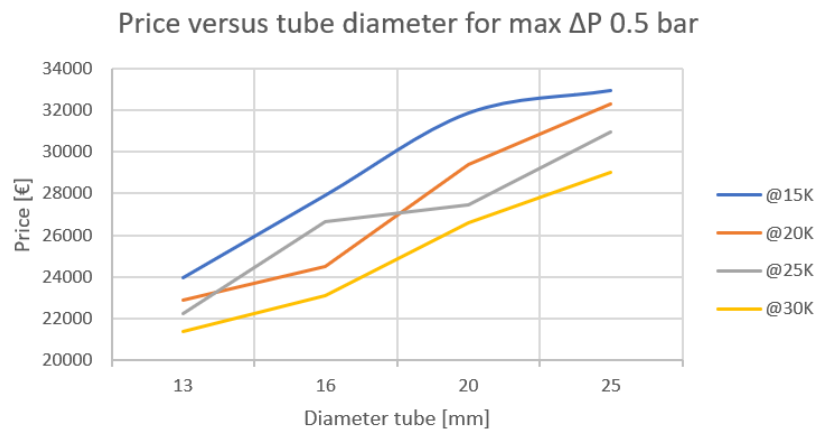
Figure 5.10: Price versus tube diameter for maximum ΔP 0.5 bar when using molten salts

For the molten salt, the pressure drop is less of an influence on the pumping energy since the volumetric flow on the shell side is lower due to the different heat transfer fluid. Molten salt has a higher heat capacity and density. The volumetric flow is therefore in the order of $5*10^3$ times smaller. Thus, decreasing the pressure drop will not greatly influence the pumping energy.

What is observed is that smaller tubes lead to lower prices of the heat U-type heat exchanger. In this case, even smaller tubes than the suggested smallest tubes in AspenEDR, 13 mm, are attempted. However, what is noted for the case of pinch temperature 25K, shown in Figure 5.11, is that even smaller tubes lead again to higher prices. Thus, the next iterations will be done for tubes with 13 mm diameter.
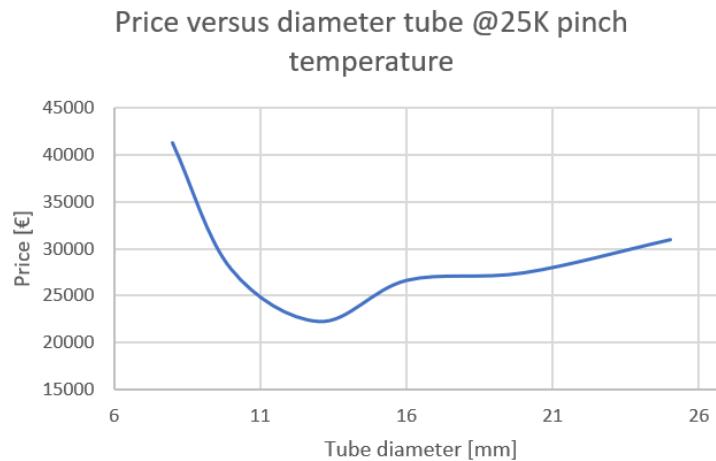
Figure 5.11: Evaluation of smaller tube diameter influence on price within molten salts

When the pressure drop, and resulting pumping power, are included in the total costs for two years, this will result in Equation 5.2. Both shell and tube side pressure drop are included since they almost contribute equally. The number of hours are based on the same assumptions in Equation 5.1.

$$\text{CAPEX} + 2 * \frac{5}{7} * \frac{1}{2} * 8760 * 90\% * \text{\EUR}_{1kWh} * (kW_{tubeside} + kW_{shellside}) \tag{5.2}$$

However, it is seen that the influence of the pressure drop on the total cost is negligible since it will be in the order of a few hundred euro for two years. Therefore it will not influence the choice.

In addition, some iterations focus on the influence of the allowable pressure drop on the price of the heat exchanger itself. This resulted, in general, in an increase in price when the boundaries on maximum allowable pressure drop were stricter. This leads to the fact that fluctuating the pressure drop first, followed by changing the pinch temperature would not lead to better results.

This results in the choice of the heat exchanger based on the lowest price in Figure 5.11. However, a closer look results that the prices of 13 mm tubes for all pinch temperatures are almost similar. Therefore, the pinch temperature of 25K is chosen, to have a safe margin. Thus, for now, the optimal case of molten salt to steam is

- ΔT 25K
- Pressure drop shell side 0.09397 bar
- Pressure drop tube side 0.38297 bar
- Pumping power both sides together 0.18 kW
- CAPEX 22 k€
- Energy costs for 2 years are negligible

The TEMA sheet can be found in the Appendix B.

What should be noted is that an electrical heating system is required within this HEX to prevent the solidification of the molten salts.

Also, the two steam-generating shell and tube devices are designed on an outlet temperature of 185°C. This leads to 100% evaporation. However, it should be evaluated if 100% evaporation does not lead to salt precipitation from the feed water. It is observed that, for example, 97% evaporation leads to almost similar results.

6

Results and conclusions Thermal storage

6.1. Results storage sizes

First for the stand-alone cases for all three materials:

	Steel slag	Phase change salt	Molten salt
Stored energy [MWh]	117	227	119
Volume [m^3]	343	369	560
Length [m]	12.0	12.0	17.7 (2x)
Diameter [m]	6.0	6.2	4.5m (2x)
Mass [kg]	$741*10^3$	$802*10^3$	$478*10^3$
HTF	Air	Thermal oil	Molten salt
Heat loss in 12 hours [MWh]	0.4	0.8	0.5
Pump loss in 12 hours [MWh]	3.6	Negligible	Negligible
Price storage material [$/kg]	0.08 [1]	0.024 [2]	1.19-1.66 [34]
HTF price [$/kg]	-	≈ 3-5 [5]	-

Table 6.1: Stand alone results

[1] (Ortega-Fernández et al., 2015), [2] (Q. Li et al., 2019), [3](Jacob et al., 2019), [4] (Bhatnagar et al., 2022), [5] from literature study.

Followed by the peak shaving results for solely molten salt:

	Molten salt
Stored energy [MWh]	63
Volume [m^3]	314
Length [m]	9.9
Diameter [m]	4.5
Mass [kg]	$259*10^3$
HTF	Molten salt
Heat loss in 12 hours [MWh]	0.3
Pump loss in 12 hours [MWh]	Negligible

Table 6.2: Peak shaving results

For the steam generation section the results are the following:

	Steel slag	Molten salt
Pinch temperature [K]	25	25
CAPEX [k€]	96	22
ΔP shell side [bar]	0.055	0.094
ΔP tube side [bar]	0.054	0.383
Pumping Power [kW]	106	0.2
Estimated pumping energy cost/year [k€]	60	$\approx$0
Tube material	Carbon steel	Stainless steel

Table 6.3: Results steam generation

6.2. Comparison to literature

6.2.1. Storage densities

The total stored energy is calculated by the energy contained in the storage, when fully charged, with respect to storage at 25°C. This is chosen to provide insights into the energy which cannot be used since every storage solution is based on the same steam demand. However, the useful energy densities are calculated by the required energy for the steam demand divided by the mass or volume.

For the slag material two main discrepancies regarding the energy densities compared to literature are present which cause a difference. The first is the range of thermal properties of the slag material and the second is the definition of a charged storage. As said before, the tolerances of the temperature drop of the HTF outlet temperature upon charging and discharging is an important factor regarding the energy in the storage when 'fully' charged or discharged.

In the research of (Calderón-Vásquez et al., 2021), the energy density is defined as the energy stored at the end of a charging period. However, the temperatures used for charging (650°C), and as a consequence the final temperature (630°C) of the packed bed, was lower. In addition, the strict tolerances of HTF outlet temperature during charging led to a partly charged, approximately half full, storage. This leads to the storage densities of 0.09-0.13MWh/m^3 which is much lower than the 0.23MWh/m^3 calculated in this thesis. The energy density of (Ortega et al., 2017), 0.23MWh/m^3 is the same as in this thesis. The 0.23MWh/m^3, from the reference paper, has a temperature tolerance of 100°C.

Focusing on latent storage, it is not logical to evaluate the storage energy densities in the literature. This is based on the following reasons. First of all, the choice of salt is a main influencing factor and differs per research. The second is that the cases present in the literature mainly focus on a single tube or small configurations to evaluate or improve charging or discharging performance. Thus, this combination leads to that there is no literature to which the calculated numbers can be compared.

For molten salt, the energy density is calculated as the useful energy contained in the hot and cold tank. When comparing the results of molten salt with literature, the two main differences lay within the used temperature tolerances and thermal properties of the molten salts in combination with the definition of energy density. For example, Bhatnagar et al. (2022) defined the maximum operating temperature between 480-505°C in combination with a 15% lower salt density and a 20% lower thermal conductivity. This thermal conductivity does not determine the energy density of the tank but it does play a role within charging and discharging rates. Other researchers use, in contrast, even better thermal properties than those used in this research. The second is the definition of energy density. Some researchers define it in the same manner, the energy which it can release in the specific operating range. This results in, for Giaconia et al. (2021), approximately in 700 MJ/m^3 which is lower than the result in this thesis of approximately 1000 MJ/m^3. This could be due to the lower heat capacity (20%) used in that research in combination with the temperature range 200-550°C instead of 200-565°C.

What should be noted is that 100% of the tank content, besides the height of the pump which hinders complete emptying of the tank, could be used to generate steam (Angelini et al., 2014). This is a consequence of not choosing a thermocline tank. Therefore, in principle, when using the same thermal properties regarding the salt in combination with the same energy density definition, this should match the values of energy density in this research.

6.2.2. Heat transfer coefficients U-tube HEX

The heat transfer performance of a U-tube molten steam generator also needs to be compared to the literature. Y. Zou et al. (2020) performed an experimental study on U-tube steam generators. An overall heat transfer coefficient of 181.7 W/m^{2}K is reported. This is much lower than the overall heat transfer coefficient reported in this thesis, 865 W/m^{2}K. The expected cause lies within the low heat transfer coefficient on the steam side, 252 W/m^{2}K, within the reference paper. This heat transfer coefficient of boiling water is lower than the expected heat transfer coefficient for boiling water or steam. However, this could be based on exceeding the critical flux in the reference paper, as can be seen in Figure 5.1. This induces dry regions and reduces the heat transfer coefficient. Other research, which focuses on molten salt steam generation reports values of 400-610 W/m^{2}K for the overall heat transfer coefficient which is already much closer to the calculated value in this thesis (Yuan et al., 2016). This research includes straight, single-pass tubes. The highest heat transfer coefficient is obtained for the highest mass flow, 1.8 m^3/h. This is equal to 0.15 m/s. The velocity of the, in this thesis, designed molten salt steam generator is 0.19 m/s. It is expected that the differences between 610 W/m^{2}K and 865 W/m^{2}K are based on three things. The first is the use of a different salt, where the reference paper among other thermal properties has a lower thermal conductivity. The second is the lower velocity of the salt, which negative impact on the overall heat transfer coefficient (Yuan et al., 2016). The third is the, in the reference paper mentioned, negative effects of superheating the tubes (Yuan et al., 2016). This is based on the similar cause mentioned above, exceeding the critical flux. When the pressure on the tube side rises, the saturation temperature correspondingly increases, leading to a reduction in superheating. In contrast to the reference paper, where the pressure is 2 bar, this thesis operates at 11 bar, potentially resulting in an enhanced overall heat transfer coefficient.

The heat transfer performance of the shell and tube evaporator with air as HTF, extracted from AspenEDR, has an overall heat transfer coefficient of 160 W/m^{2}K. A direct comparison could not be found in the literature. Compared to an HRSG, overall heat transfer coefficients are found ranging from 30-70 W/m^{2}K (H. Gao et al., 2022). Therefore, a closer look into the overall heat transfer coefficient is taken. At first, the 160W/m^{2}K seemed quite high for a heat transfer coefficient where air is involved. This is because air generally has a heat transfer coefficient between 10-100W/m^{2}K. Therefore, a comparison of the shell side heat transfer coefficient based on the Kern method is done ("Shell-and-Tube Heat Exchangers", 2019). AspenEDR gives a shell side heat transfer coefficient of approximately 190 W/m^{2}K. Kern's method leads to a heat transfer coefficient of the shell side of approximately 140 W/m^{2}K.

$$h_o = \frac{0.36k_s}{D_e}Re_s^{0.55}Pr^{1/3} \qquad (6.1)$$

With D_e is the equivalent diameter and this is for triangular pitch equal to

$$D_e = \frac{4\left(\frac{P_T^2\sqrt{3})}{4} - \frac{\pi*d_o^2}{8}\right)}{\frac{\pi d_o}{2}} \qquad (6.2)$$

However, this difference can be partly caused by averaging the Prandtl and Reynold numbers in the calculations. The inlet and outlet Prandtl and Reynolds numbers are extracted from AspenEDR. The Reynolds or Prandtl numbers are not specifically linear throughout the HEX thus this can cause some inaccuracies. However, it is still a higher value than expected.

6.3. Conclusions Thermal storage

What can be concluded, based on the results above, is the following. Steel slag is a solution which offers, despite being a sensible storage where the storage material temperature decreases, an almost constant HTF outlet temperature which is a desired outcome. The main problem within steel slag is the HTF, used in literature, which is air. Steel slag shows compatibility with other HTFs, according to the literature. However, no practical application of steel slag in combination with, for example, thermal oil is found in the literature. The discharge with air as HTF shows, besides pumping losses for the thermal storage itself, also considerable pumping losses within the evaporation step of water to steam. An advantage of using air as HTF is the low costs of the HTF itself.

Molten salt storage necessitates the largest volume due to the requirement of two tanks for storage. However, it shows the highest flexibility in partly charging and discharging in comparison to the other two storage options, resulting in the possibility of peak shaving storage. Another advantage is that the discharging temperature is constant, at the temperature of the hot molten salt tank, which is desirable for the steam generation step. Disadvantages are, besides the large volume, the relatively high cost of the storage material in combination with the measures that need to be taken to handle molten salts. These are the addition of a heat tracing system and the use of higher-grade steels to prevent corrosion.

Phase change salt resulted in almost the lowest storage volume in combination with the highest amount of energy which is stored. This last matter shows great potential for this storage type. The stored energy is a measure of the energy present in the storage. In this case, a lot of the stored energy cannot be used since the HTF outlet temperature decreases at a too high rate. This is mainly caused by the low thermal conductivity within the phase change salts. However, this large amount of energy present in the storage means that there is a large potential to decrease the storage volume when more of the energy is efficiently used. Another advantage of this storage type is the ability to use any HTF which is compatible with the tube material. This enables efficient generation of steam at the evaporation step. However, similar to molten salt storage should caution be taken based on the corrosion effects of the phase change salts. The price of the salt is lower in comparison to the molten salt. However, a disadvantage can be the price of the HTF which is required for the discharge. Nevertheless, the use of phase change salt is still not market-ready based on poor discharging performance.

Therefore, the next part of this thesis focuses on improving market readiness by increasing the thermal conductivity of this storage option, which shows great potential for implementation within the food industry.

In the next phase of this report, the goal is to improve the thermal conductivity of phase change salts to make it a more interesting solution within industrial applications.

This part is subdivided into distinct sections with the following layout. Initially, a general introduction to thermal conductivity is presented. Within this section, thermal conductivity improvement methods are also presented. From there a specific improvement method will be chosen and further investigations will be executed. The results are evaluated at the end.

7

Thermal conductivity

In this Chapter, thermal conductivity, in general, and focused on phase change salts, will be discussed. Phase change salts are characterized by low thermal conductivity. The low thermal conductivity hinders the heat transfer to or from the heat transfer fluid and thus slows down the charging or discharging rates. This represents a primary factor impeding their commercial deployment. Several methods to improve thermal conductivity can be found in the literature. For instance, the addition of fins to increase the heat transfer area or the addition of nanoparticles in the salts. After the definition of thermal conductivity, these improvement methods will be discussed.

7.1. Definition

Thermal conductivity, denoted as k, κ or λ, is an intrinsic property of a material and is defined as the rate of heat transfer through a unit cross-section area when a perpendicular temperature gradient is present (Tritt, 2005). Within this research, the notation, k, is chosen. Thermal conductivity can range from 0.015 W/mK to 3000 W/mK at room temperature for respectively aerogels to single layer graphene (D. Zhao et al., 2016). The thermal conductivity of a material is usually the highest in the solid state and the lowest in the gaseous phase (Palacios et al., 2019). The typical thermal conductivities are shown in Figure 7.1. Thermal conductivity varies with temperature and can be directional dependent (D. Zhao et al., 2016). The reciprocal of thermal conductivity is thermal resistivity.
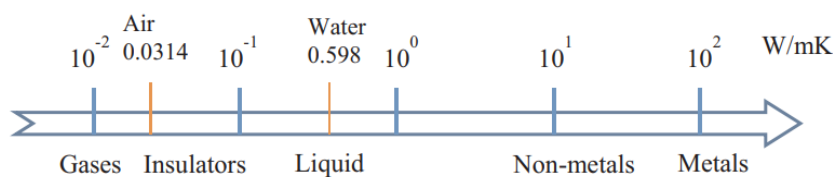
Figure 7.1: General thermal conductivity range (Palacios et al., 2019)

The thermal conductivity of a material, when assuming a material is isotropic and homogeneous, for a given unidirectional heat flow, is calculated according to Fourier's law (Palacios et al., 2019):

$$Q = -kA\frac{dT}{dx} \tag{7.1}$$

Even though Fourier is represented as a scalar, its general form is that of a second-rank tensor. However, this is only required in cases where the material is anisotropic.

According to Palacios et al. (2019) thermal conductivity influencing factors are chemical composition, temperature, porosity, grain size and direction of the heat current:

- Temperature
  The temperature dependence is different for metals and non-metals. For metals, the thermal conductivity is primarily dependent on the free electrons. According to the Wiedemann-Franz law, thermal conductivity is approximately proportional to the temperature multiplied by the electrical conductivity within metals. In pure metals, this electrical conductivity reduces with increasing temperature and therefore the thermal conductivity is rather constant (Yi et al., 2020). For non-metals the thermal conductivity is mainly dependent on lattice vibrations, phonons. In general, an increase in temperature enhances the thermal conductivity, until a maximum value is reached. From that point, the thermal conductivity remains constant in a small temperature range. When exceeding that temperature range, a sharp reduction is present until it reaches a minimum. This minimum is close to the melting point. The temperature influence on the thermal conductivity is different for solids, liquids and gases. Without delving deeper into the distinctions between liquids and solids, in broad terms, the thermal conductivity of gases is positively influenced by temperature, while that of liquids typically decreases with rising temperatures.

- Density
  The density or changes of density within a material greatly affect the thermal conductivity. Changes in density are particularly present when a phase change or reaction occurs. The density of a material as well as its porosity will define the bulk density of the material. Porosity reduces the bulk density and therefore reduces the ability of heat conduction inside the material. Voids and air trapped reduce the heat conduction.

- Grain size and porosity
  Smaller grain sizes result in more grain boundaries. These grain boundaries result in lower thermal conductivity since these are obstacles for the conduction of heat. An increase in porosity results in, as concluded before, a lower thermal conductivity.

- Crystal structure
  A cubic crystal structure results in an independence of orientation regarding the thermal conductivity. Anisotropy of the crystal structure affects the thermal conductivity. Whenever anisotropy is present in the material, the direction of the heat current plays an important role in the thermal conductivity.

- Chemical composition
  In general, materials with a simpler chemical composition and molecular structure have higher thermal conductivities. This is because impurities strongly affect the thermal conductivity.

7.2. Thermal conductivity enhancement

As mentioned above, various thermal conductivity enhancement methods are present in the literature. These enhancement methods can be divided into two main classifications: increasing the heat transfer surface area and increasing the phase change salt thermal conductivity. Increasing the heat transfer surface area is most often achieved with the addition of fins or encapsulating the PCMs. For thermal conductivity enhancement, porous media or nanomaterials additives are used. According to S. Zhang et al. (2023), one of the most efficient techniques for increasing the thermal conductivity within PCMs is making use of a finned tube. S. Zhang et al. (2023) reviewed the use of fins in phase change materials, including various configurations. These include annular, helical, longitudinal, topology-optimized and multiple-finned tubes. The findings are summarized below. The appearance of these finned tubes is illustrated in Figure 7.2.:

- Annular fins showed, especially in vertical shell-and-tube configurations, better performance when compared to porous media and nanoparticle additives. However, the performance is a trade-off between reducing natural convection and enhancing heat diffusion. This can be optimized by choosing the optimum fin geometry and pitch size. A disadvantage of using annular fins is the large stress on annular fins caused by the volume expansion of the PCM.
- Helical fins showed better heat transfer enhancement compared to conventional fins. This enhancement is based on the presence of natural convection and the formation of vorticities in combination with the high conductivity of the fins. However, literature is limited regarding helical fins in combination with PCM and further research is required.
- Longitudinal fins within literature are mainly focused on 2D studies. Therefore, additional research into the 3D-heat transfer enhancement should be performed. Furthermore, an extension into the solidification process of PCM in combination with PCMs should be done since most literature focuses solely on the melting process.
- Topology-optimized fins suffer from the same problem as longitudinal fins, with the focus on 2D-optimized fin structure. Furthermore, another limitation regarding these fins is their manufacturability. These fin types cannot be manufactured using conventional techniques.
- Multiple finned-tube expectations cannot be obtained from an extension of single-tube results according to literature. Therefore, research into the fin design within this configuration and a simplified method to design large scale shell and tube-based storage systems is required.
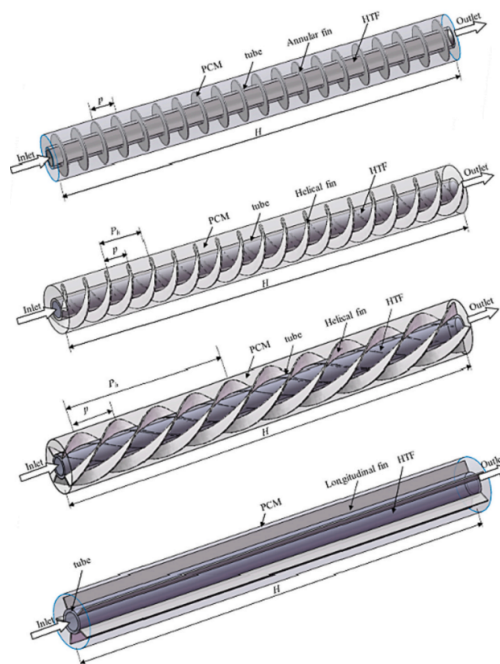
Figure 7.2: From top to bottom: annular, double helical, triple helical and longitudinal (S. Zhang et al., 2023)

Other heat transfer enhancement techniques according to the review of thermal conductivity enhancement methods from Qureshi et al. (2018), include porous media, nanomaterial additives, expanded graphite and encapsulation of the PCM. The main findings with respect to these techniques are:

- Addition of nanoparticles effectiveness is based on the shape, size, aspect ratio and concentration. Carbon-based nanoparticles showed, in comparison to metal-based nanoparticles, better performance. This is due to better dispersion and lower densities. Challenges regarding the use of nanoparticles include non-uniform dispersion and aggregation.
- Metallic foams have a positive impact on the thermal conductivity of the PCM. The porosity of the foam is of greater importance than the pore size. Metallic foams can enhance the thermal conductivity of the PCMs better in comparison to nanoparticles.
- Expanded graphite is a composite PCM which increases the thermal conductivity. The composite PCMs are prepared by impregnating the liquid PCM in the expanded graphite. The influence depends on mass fraction, aspect ratio, surface area, packing density and thickness.
- Encapsulation of the PCM influences the thermal conductivity and the lifetime, by preventing direct contact with the environment, of the PCM both in a positive manner. Furthermore, the problems regarding phase separation and leakage are diminished by making use of encapsulation.

What should be noted is that enhancement methods to increase the charging/discharging rates mentioned above, such as fins and additives, have a negative impact on the system energy density and can suppress the presence of natural convection (Ebadi et al., 2018). Furthermore, the added materials and fabrication techniques increase the cost of the thermal storage system considerably. Hence, these techniques are still only present in lab-scale prototyping and testing (Sodhi et al., 2021). Thus, increasing the commercial deployment, a readily available in combination with a cheap material is desired.

Opolot et al. (2023) performed research into the field of using a readily available, low-cost, stainless steel wire mesh as a periodic structure to increase the thermal conductivity of the configurations and thereby the discharge performance. This low-cost wire mesh is shown in Figure 7.3.
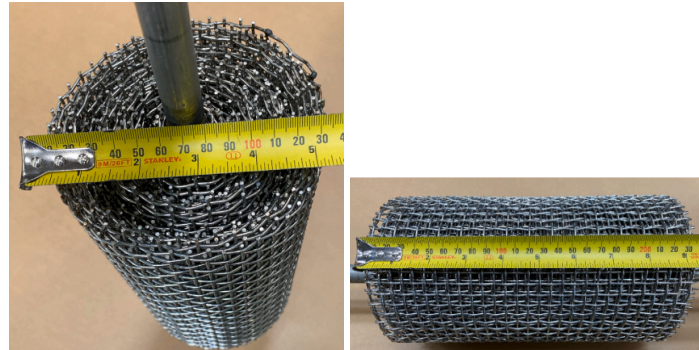
Figure 7.3: Rolled mesh inserted in PCM (Opolot et al., 2023)

This low-cost wire mesh is based on the idea of implementing a highly conductive wire net with periodic structure into the phase change salt. This periodic structure is based on the idea of metal or graphite foam inserts. With foam inserts, the porosity and thermal conductivity of the ligaments are crucial parameters. Lower porosity results in better heat transfer performance but has as a detrimental effect the reduced energy storage density. Besides the porosity, the pore density of the periodic structure can also be optimized. This is dependent on the type of material used for the wire net. This effect, for different materials, has been imitated by numerically investigating the heat transfer performance of a schematic, shown in Figure 7.4_l, with as computational grid Figure 7.4_r.
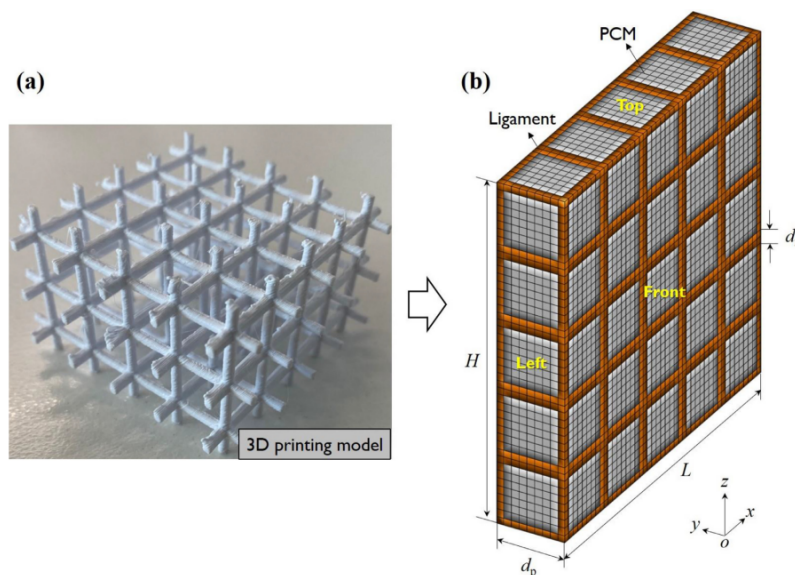
Figure 7.4: 3D-printed representation of periodic structure inserted in PCM (left). Computational grid of 3D-printed representation (right) (C. Zhao et al., 2021).

In general, the critical cell density increases as the thermal conductivity of the ligaments increases, when assessing the same porosity. This is due to the fact that within ligaments with lower thermal conductivity, the natural convection which will be suppressed by higher cell densities, cannot be ignored since it still contributes considerably.

What should be noted is that using a wire mesh as a periodic structure, shown in Figure 7.3, has the disadvantage of thermal contact resistance in the radial direction. This can be optimized by either brazing and/or spot welding to be able to make a network of ligaments. An overall improvement, even with stainless steel as low thermal conductive material, of the overall cycle performance of 10% is observed. The tests have been carried out with an eutectic PCM, 41.69wt% Na_2CO_3, 33.1wt% KCl and 25.21wt% NaCl with a thermal conductivity of 0.6 in solid state and 0.5 in liquid state. Stainless steel, in salt conditions at the temperatures of this storage system, eventually is prone to corrosion (Opolot et al., 2023).

More specifically, the influence of the mesh is as follows. In both cases, with and without the periodic structure, the salt completely melts. The impact of the periodic structure on charging becomes evident in the initial phases of melting. This is plausibly caused by the heightened conduction facilitated by the periodic structure. In this initial stage, the material remains solid, and conduction serves as the primary heat transfer mechanism. No enhancement is observed during the phase transition. However, the increase is once again noted after the completion of the phase transition. A decrease from 2.7h to 2h is observed, which is a decrease of around 25%.

For the discharging, which is conduction dominated as explained in Chapter 4, the periodic structure contributes positively to the discharging rate. However, it is additionally stated that in the early stage of heat rejection, convection is the dominant heat transfer mechanism. The periodic structure hinders the convection and thereby in the early stage no major increase in performance is observed. In the phase change section, an increase is observed due to the periodic structure resulting in finishing the solidification at an earlier stage. Thereafter, in the solid state sensible region also an improvement is observed.

However, when watching closer, a different decrease in discharging time is observed for different locations in the tank. In the axial direction, with a vertical tank, the decrease is respectively from the downside thermocouple to the centre thermocouple 15, 10 and 8%. Thus the periodic structure increases the melting rate in the bottom of the tank more due to conduction. For the radial direction, only a small increase of 5% is observed. This small increase is accommodated to the thermal contact resistance in the radial direction. There is a resistance to heat conduction in the radial direction compared to the axial direction.

The overall cycle performance registers a 10% increase. The reduction in natural convection during charging, a potential concern associated with the use of a periodic structure, does not pose an obstacle, as the overall performance is enhanced. Thus, despite the low thermal conductivity of stainless steel coupled with the diminished impact of natural convection, an improvement in the discharging rate has already been noted.

The use of stainless steel within this research is, according to the authors, validated based on the fact that this research is performed within the area of high temperature storage (>700°C). This excludes the possibility of using aluminum, due to melting temperature between 400 and 700°C and the loss of mechanical properties of Copper at higher temperatures. They stated that the use of graphite is the best alternative within this operating temperature range.

Another interesting conclusion based on the, experimentally validated, numerical model is that with the periodic structure enhanced PCM, an increase in heat transfer fluid velocity does decrease the discharging time. They stated that based on the required discharging time the appropriate discharging fluid flow rate should be chosen.

Disadvantages of the structure, as it is now presented in the paper, are among other things the poor corrosion resistance, the not-perfectly to the tube braised mesh and the thermal contact resistance in the radial direction from mesh layer to mesh layer. However, the low-cost and already promising results, show the value in enhancing this structure. Therefore, the focus will be on delving into this periodic structure and investigating potential improvements.

To further improve this periodic structure, some suggestions are presented within this paper. These include creating perfect contact between the periodic structure and the heat transfer pipe through welding or additive manufacturing and adding a thin layer of a non-corrosive material, such as graphite, onto the periodic structure to enhance corrosion resistance. As mentioned before in the same research, adding graphite could also enhance the overall effective thermal conductivity. This graphite layer will come at a cost. However, based on the fact that the periodic structure without a graphite layer costs approximately only $300 which is a low price compared to other solutions such as graphite foam, $10,000, this can still be a cheap and powerful solution. These prices are determined for a small-scale test setup.

In addition, concerning the reduction in natural convection, C. Zhao et al. (2021) demonstrated that as the thermal conductivity of a periodic structure rises, the impact of natural convection becomes less significant since the conduction will be dominant. It is important to note that this study was based on periodic structures that were not coiled but rather consisted of interconnected ligaments.

In addition, if the coating is corrosion resistant, in this case, a graphite coating, this enables the usage of a different mesh material. In the Table below, different thermal conductivity values are presented for different steels. Carbon steels are cheap and have a high thermal conductivity and are therefore chosen as mesh material.

	Thermal conductivity [W/mK]
Steel - Carbon 0.5%	54
Steel - Carbon 1%	43
Steel - Carbon 1.5%	36
Steel - Chrome 1%	61
Steel - Chrome 5%	40
Steel - Chrome 10%	31
Steel - Chrome 15% Nickel 10%	19
Steel - Chrome 20% Nickel 15%	15.1
Steel - Hastelloy B	10
Steel - Hastelloy C	8.7
Steel - Nickel 10%	26
Steel - Nickel 20%	19
Steel - Nickel 40%	10
Steel - Nickel 60%	19
Steel - Nickel 80% Chrome 15%	17
Steel - Nickel 40% Chrome 15%	11.6
Steel - Manganese 1%	50
Steel - Stainless Type 304	14.4
Steel - Stainless type 347	14.3
Steel - Tungsten 1%	66

Table 7.1: Thermal conductivity of steels measured at 20°C (Engineeringtoolbox, 2023)

Some research into the field of graphite addition onto a periodic structure is already executed numerically within a phase change salt application (HEDH & Hooman, 2023). Both for a graphite foam and a periodic structure which is coated with graphite. A periodic structure of solely graphite increased the thermal conductivity of the whole configuration from 0.8, which represents the thermal conductivity for solely PCM, to 3.87 for the combination of graphite and PCM. Thus although graphite has a higher thermal conductivity than 3.87, the effective thermal conductivity of the combination equals 3.87 For the stainless steel coated graphite, layers of graphite are applied to see the influence. The maximum layer thickness is equal to the thickness of the bars of the periodic structure. Thus the ratio coating to bar is 1. The effective thermal conductivity was eventually 3.21, which is equal to 83% of enhancement due to the foam made of solely graphite. This phenomenon is shown in Figure 7.5. It resulted in a bigger tank due to the periodic structure, but the melting time decreased by an order of magnitude.
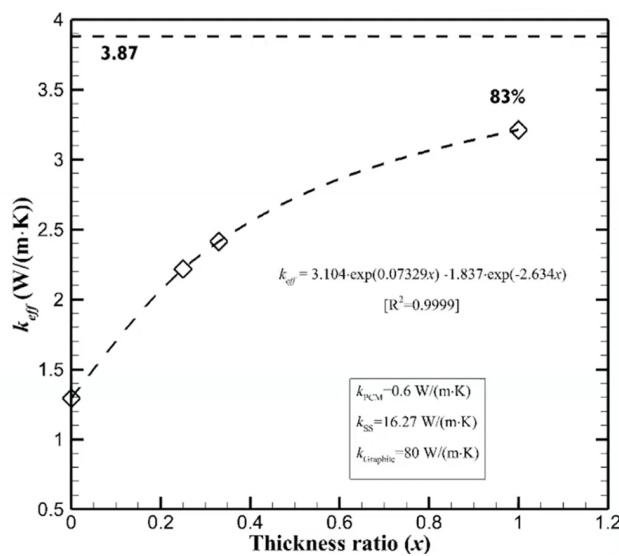
Figure 7.5: Effective thermal conductivity as a function of thickness ratio

In conclusion, Figure 7.6 shows the pathway to the idea of coating a carbon steel mesh with a graphite coating. The first step was expensive foams with good results. This is followed by mimicking this foam with a periodic structure. Graphite coatings onto these periodic structures were the next step with again promising results. To be able to have a cheap readily available solution, the rolled mesh seemed a possible solution. The next step, executed in this thesis, is improving this mesh in two ways. The first is prevention against corrosion with a graphite coating. The second is enabling the use of carbon steel basis mesh structure and thereby increasing the thermal conductivity as well as evaluating the increase due to the graphite coating itself.
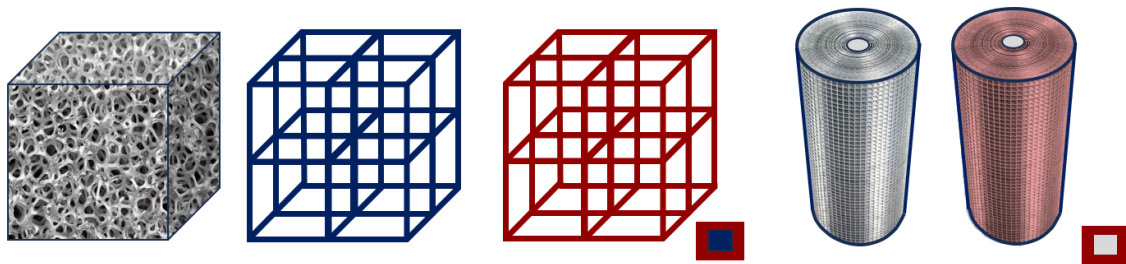
Figure 7.6: From left to right expensive graphite foam, periodic structure, graphite coated periodic structure (in red graphite coating and blue stainless steel), stainless steel wire mesh, graphite coated carbon steel wire mesh (in red graphite coating and grey carbon steel).

Based on the above findings, the focus for this part of the research will be on finding an optimal coating technique and coating material in order to enhance the periodic structure by decreasing the corrosion potential and assess the influence on the thermal conductivity through measurements.

8
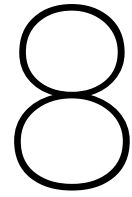
Corrosion

Continuing on the previous chapter, where a thermal conductivity improvement method based on a periodic structure is suggested, a new challenge arises. This challenge involves the corrosion of carbon steel in contact with salts, a concern that will be explored further below. To find a possible corrosion resistance solution, this Chapter has the following structure. It begins with a general explanation of corrosion. This is followed by a more in-depth review of corrosion based on salts as thermal energy storage material in contact with carbon steel. The chosen corrosion resistance strategy in this research is the application of a coating, although alternative corrosion inhibitor options will also be discussed. Thereafter, a literature review will be presented based on different coating material options. Finally, a coating material will be selected to conclude this Chapter.

8.1. General explanation corrosion

Corrosion is defined as the progressive degradation of materials, usually metals, caused by chemical or electrochemical reactions occurring between the materials and their surrounding environment. Corrosion leads to the deterioration of properties exhibited by materials and structures, such as their mechanical strength, appearance and permeability to liquids and gases. Due to the diffusion-controlled nature of corrosion, it primarily occurs on exposed surfaces.

Corrosion is driven by the thermodynamic principle of Gibbs free energy. The Gibbs free energy (ΔG) represents the energy available for a chemical reaction to occur. In the context of corrosion, a negative ΔG indicates a thermodynamically favourable reaction and signifies the tendency for a metal to corrode. This reaction converts metals into more stable compounds: metal oxides, metal sulfides or metal hydroxides. However, it is important to note that ΔG is not a direct measure of the corrosion rate but rather indicates the potential for corrosion to occur. A positive ΔG indicates no thermodynamic driving force for corrosion. The relationship between ΔG, the number of electrons involved in the reaction, n [-], and the electrode potential, E [J], is given by the equation

$$\Delta G = -nFE \tag{8.1}$$

where F represents Faraday's constant.

Corrosion can be divided into general and localized corrosion. General corrosion refers to the uniform deterioration of the entire surface of a metal material, resulting in a gradual and consistent thinning of the metal. This form of corrosion typically progresses slowly and is generally less severe than localized corrosion. Localized corrosion occurs primarily in specific areas of metal containers, while the majority of the remaining surface remains uncorroded. Detecting signs of localized corrosion can be challenging, as the exterior of the metal may still appear intact despite significant perforation occurring internally. Consequently, localized corrosion poses a greater threat to the integrity of the metal compared to general corrosion. Various types of localized corrosion include pitting, crevice corrosion, intergranular corrosion, transgranular corrosion, and selective corrosion, shown in Figure 8.1 (Connor, 2020).
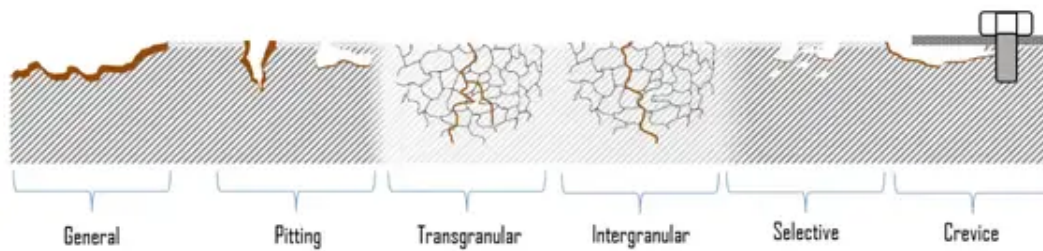
Figure 8.1: Forms of corrosion (Connor, 2020)

To conclude, some of the major drawbacks of corrosion are (Maaß, 2011),

- A reduction in metal thickness leads to a decline in mechanical strength, potentially resulting in structural failure or breakdown
- Mechanical damage to components and the introduction of added complexity to equipment
- The loss of essential surface properties in metallic components
- There is a risk of perforation of vessels and pipes and fluid contamination

Figure 8.2 is used as a guide for corrosion weight loss in industry.

mg/cm^{2}yr	Recommendation
>1000	Completely destroyed within days
100–999	Not recommended for service greater than a month
50–99	Not recommended for service greater than 1 yr
10–49	Caution recommended, based on the specific application
0.3–9.9	Recommended for long term service
<0.2	Recommended for long term service; no corrosion, other than as a result of surface cleaning, was evidenced

Figure 8.2: Corrosion rates and associated recommendations (Sastri et al., 2007)

8.2. Corrosion of phase change salts in carbon steel

Corrosion effects on the surface of the storage container are observed when salts are employed as either phase change material or as a sensible storage option in configurations documented in the literature. Most of the literature about corrosion in thermal energy storage is based on the storage material of molten salts instead of salts such as PCM. It affects the life of the container and thereby the performance of the whole storage system. Therefore, in the practical application of using salts as sensible or latent storage, is the compatibility between storage material and salts a key problem and a relevant research area (M. Liu et al., 2023). Literature about the corrosion prediction of solar salt in combination with the storage material of molten salt tanks has been under investigation for a considerable period.

Despite the existence of corrosion data for salts from the chemical industry, there is a lack of corrosion data specifically related to the use of these salts as PCMs. This is primarily because when these salts are utilized as PCMs, they are often employed in a non-aqueous state, which means without being in a water solution (Moreno et al., 2014). The absence of an aqueous environment for the salts in PCM applications generally reduces the likelihood of corrosion. However, PCMs employed for energy storage have a relatively challenging nature of their corrosion mechanism, compounded by the dynamic environment characterized by alternating hot and cold conditions (Hua et al., 2022).

Before proceeding, it is crucial to grasp the distinction between hydrated salts and salts in an aqueous solution, as previously discussed. Hydrated salts incorporate water molecules within their crystalline structure, unlike salts in an aqueous solution, where the salt molecules are dissolved in the water. In essence, hydrated salts possess water molecules as an integral part of their chemical structure, whereas salts in an aqueous solution have their molecules dispersed in water without forming a direct chemical bond between water and salt. However, when a salt hydrate is melted, which happens in molten salt or in phase change salts, some water molecules escape. This results in molten hydrated salts, with fewer moles of water, and water.

The current literature exploration will now specifically target the combination of PCM or molten salts with carbon steel in the context of corrosion. Several articles on corrosion are present within literature. The first interesting article tests corrosion due to HitecXL. Within this article isothermal as well as cycling tests are present. Furthermore, HitecXL and hydrated HitecXL tests are executed. However, the hydrated HitecXL, containing $Ca(NO_3)_2*4H_2O$, tests were done with an Argon atmosphere. Argon is an inert atmosphere and therefore is it possible that a small amount of water is present.

- Hydrated HitecXL + carbon steel (A516Gr70), isothermal 310°C, 1500h, argon environment

  Iron oxides, corrosion, was formed in heamatite and magnetite phases. In some cases, a protective carbonate layer, $FeCO_3$, was formed which reduced the layer by 50%, from 1μm to 0.6μm. Nevertheless, cases where this layer remained attached were rare, and the estimated percentage of the surface covered by this layer was only 1%. The SEM, Scanning Electron Microscopic, images are shown in Figure 8.3. This will result in 8.8+/-0.6 μm/year

- HitecXL + carbon steel (A516Gr70), isothermal 310°C, 1500h, air environment

  Clear signs of oxidation, $CaCO_3$. However, no specific amount of μm is presented in the paper.

- HitecXL + carbon steel (A516Gr70), Cycling 300-500°C, 125 cycles over 500h, air environment

  The corrosion layer is around 3.5x thicker than the isothermal hydrated salt, 31.5+/-1.6μm/year. The rate of corrosion increase is dedicated to the higher temperature. The layer detachment is attributed to thermal cycling. The corrosion is shown in Figure 8.4
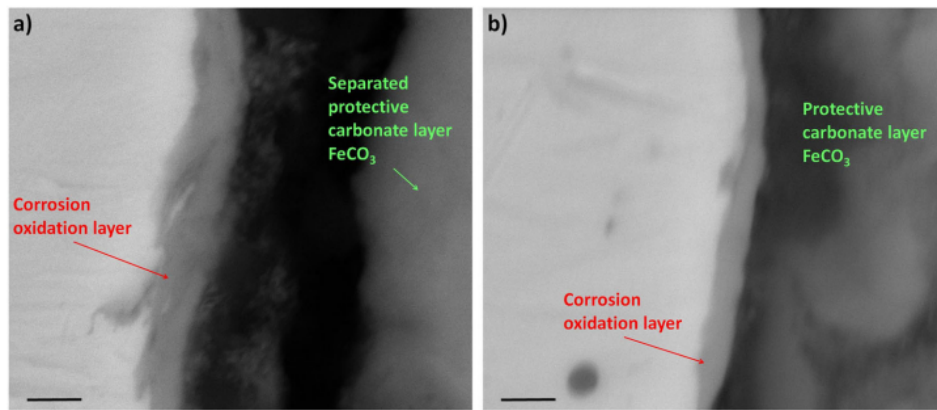
Figure 8.3: SEM images of carbon steel corrosion test, 1500h, with HitecXL*H_2O. a) Separated $FeCO_3$ layer. b) Attached $FeCO_3$ layer.(Grosu et al., 2018)
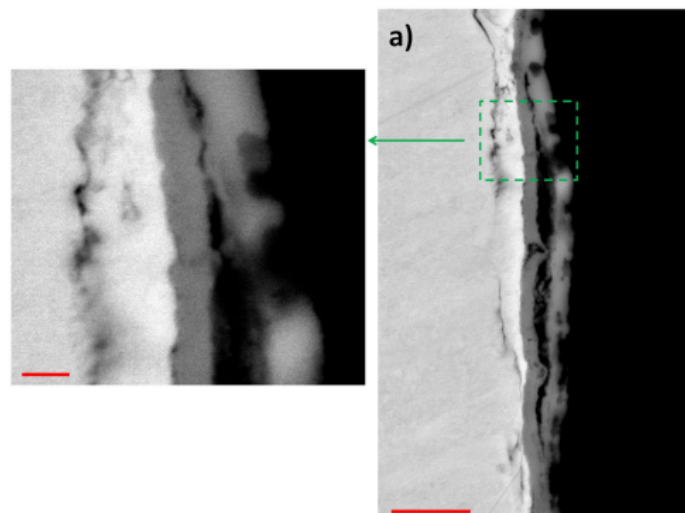
Figure 8.4: SEM images of carbon steel after 125 cycles ranging between 300-500°C (Grosu et al., 2018).

These iron oxides are, below the decomposition temperature of the salts, the main mechanism for construction materials to degrade. On the other hand, when the steel was in contact with Hitec XL also a protective layer, consisting of iron carbonate ($FeCO_3$), is present. The formation of the protective $FeCO_3$ layer inspired the researchers to explore the influence on graphite in two ways. The first is the addition of graphite within the salts, the second is the addition of a graphite coating on the carbon steel. When adding graphite, there will be a competitive reaction between the resistance layer which will consist of $CaCO_3$ and the formation of the iron oxides. These results will be discussed in the subsequent subsections.

This paper focuses on Hitec XL salt. However, it is concluded that Hitec XL, which consists of a $Ca(NO_3)_2$ group, is less corrosive compared to solar salt. Solar salt consists, as said before, of 60% $NaNO_3$ and 40% KNO_3. They conclude that this demonstrates the positive effect of the $Ca(NO_3)_2$ group. This does not instantly lead to the conclusion that every salt is corrosive to carbon steel. Nevertheless, it gives some perspective.

Other papers regarding the hydrated nitrates in contact with carbon steel are present and all have the same results, namely that almost all salt hydrates show, sometimes severe, corrosion when in contact with carbon steel. An interesting and worth mentioning research, is the research where low temperatures are present, below 100 °C. Results still indicated the severe corrosion for all the tested nitrate hydrates used as phase change materials, 11.9-33.3μm/cm^{2}yr, even at the relatively low temperatures except for one type, the magnesium nitrate tetrahydrate and calcium nitrate tetrahydrate mixture (1:1), $Mg(NO_3)_2$*$6H_2O$+$Ca(NO_3)_2$*$4H_2O$ (Danielik et al., 2016). The corrosion rate is according to 8.2 in the category "Caution recommended, based on specific application". They did not explicitly say which mechanism was on the basis of the corrosion inhibitance in this mixture. However, they overall concluded that using carbon steel in contact with nitrate hydrates can only be used with great caution. However, salt hydrates are often not the type of phase change salts at higher temperatures. Therefore, no further research into the salt hydrates will be executed.

Other worth-mentioning results are regarding the influence of the impurities on the corrosion rates within the commercially available alkali nitrates. A binary alkali nitrate mixture was tested at relatively low and isothermal temperatures of 316°C. The mixtures consist of $NaNO_3$+KNO_3. Two types of tests were done: one high purity mixture was made where impurities were added in different wt% and in the other tests commercially available salts, containing impurities, were tested. NaCl was added in the binary high-purity mixtures in order to have chloride ions as impurities without having other significant impurities. This was done till 1.3wt%, which is 30% higher than the highest expected level of impurities in commercial grades of salt. Other commercially available salts were also tested without the addition of NaCl, but they already had levels of impurities including chloride, perchlorate, sulfate, carbonate and nitrate. Results showed that the impurities had a relatively small effect on the corrosion of the carbon steel. Increasing the chloride impurities in steps of weight percentages did not show a clear increase in corrosion. There were, however, some differences within the different commercial salt mixtures. However, all the corrosion behaviors were modest and are around 5μm/year (Goods & Bradshaw, 2004). However, the temperatures were relatively low and isotherm.

Grosu et al. (2018) stated that it is evident that carbon steel, which is the economically most attractive storage material, cannot sustain the harsh conditions of molten salts at high temperatures. According to Vasu et al. (2017), this conclusion is supported, and it is affirmed that carbon steel is not a favorable option for prolonged exposure to various salts. Furthermore, the literature review of Grosu et al. (2018) concluded that, as expected, oxidation is the main mechanism for corrosion when the temperature of the salts is below the decomposition temperature.

For now, it is assumed that all the carbon steels will, to some extent, corrode under the cycling conditions of phase change salts in combination with air or some impurities when in contact with carbon steel. This is assumed based on the following. Isothermal Hitec XL shows corrosion at around 300°C. Cycling conditions revealed 3.5 times more corrosion in the same set-up. Hitec XL is not seen as the salt with the highest corrosive behaviour. Therefore, can be assumed that this is not an outlier. Corrosion was not specifically more severe upon impurities. However, these were under mild conditions in contrast to the more obvious conditions in expected application configurations. However, in the future, the corrosion tests should be done for more salts in different conditions when in contact with carbon steel to be able to substantiate this conclusion.

8.3. Corrosion resistance options

M. Liu et al. (2023) concluded that, based on experimental research, three approaches exist for the corrosion prevention of phase change materials: corrosion inhibitors, packaging and coating. The discussion on coating carbon steel will be addressed in the following subsections, as it represents the selected corrosion resistance option.

As for the other two methods, corrosion inhibitors and packaging, these are employed in various ways when there is contact between molten salts and carbon steel. Inhibitors are substances, either organic or inorganic, that diminish or entirely obstruct the corrosion of metals (Hua et al., 2022). Specifically, the use of corrosion inhibitors in a PCM salt solution, such as methionine and proline, has proven to be effective in preventing corrosion when carbon steel is exposed to a salt solution mixture. The methionine and proline act as anodic-type inhibitors. Anodic-type inhibitors refer to substances that primarily act on the anodic side of the corrosion reaction to impede or suppress the oxidation of the metal. These inhibitors form a protective layer on the metal surface, hindering the anodic dissolution process and mitigating the overall corrosive effects of salt exposure (Z. Zhang et al., 2016). Another combination, methionine and valine, as corrosion inhibitors in a salt solution also showed great potential when added at (1:1) weight percentage. Similar to the research into methionine and proline, the inhibitors acted as anode type inhibitors (Z. Zhang et al., 2018). Graphite is another type of corrosion inhibitor with good results. Graphite generates, as said before, a protective layer consisting of $FeCO_3$. It inhibits the corrosion layer at almost the whole surface. Graphite showed a decrease of more than 60% in corrosion rate in μm/year to 3.2+/-0.5. However, the addition of graphite into the salt creates a problem. The unconsumed graphite will thermally decompose at higher temperatures (>450°) (Grosu et al., 2018).

Packaging technology offers an effective solution to address the challenges posed by strong corrosion and low thermal conductivity. Packaging refers to the, for example, application of a shell on a PCM core. By utilizing appropriate packaging materials and techniques, the shortcomings of PCMs can be mitigated. Overall, the application of packaging technology in PCM systems offers a dual benefit of preventing corrosion and enhancing thermal conductivity. It ensures the reliability and performance of the PCM while also optimizing its thermal energy storage capabilities (Hua et al., 2022). The method of encapsulation has been examined in the literature review conducted prior to this research. Additional details can be obtained there.

8.4. Literature review graphite coatings for corrosion resistance in phase change salts

As stated in the conclusion of Chapter 7, enhancing thermal conductivity could be achieved by applying a graphite coating with a thickness equivalent to that of the periodic structure. Simultaneously, the coating's structure should possess corrosion resistance to safeguard the carbon steel structure. It is noteworthy that in the case of a stainless steel structure, the research on periodic structures also recommended the use of a corrosion-resistant coating.

Coating is a widely used anti-corrosion method that involves applying a protective layer onto metal surfaces to prevent direct contact. This method is considered the predominant approach for corrosion prevention. Within the realm of anti-corrosion techniques, the addition of coatings is recognized as a simple, quick and cost-effective method. Extensive production experience has demonstrated that coatings can significantly mitigate corrosion and effectively reduce economic losses (Hua et al., 2022).

Multiple researches present in literature confirm the corrosion resistance potential of a graphite coating in contact with salts.

The first paper continues to build on the observation of adding the graphite into HitecXL salt, 2wt%, which showed corrosion resistance potential by the formation of a protective layer of $CaCO_3$(Grosu et al., 2018). This phenomenon is explained in the previous subsection. However, the thermal degradation of the unconsumed graphite posed a challenge at elevated temperatures, leading to the suggestion that this might not be the optimal method for utilizing graphite. Therefore, they tested a graphite coating, commercially available. This spray graphite coating is bought from Kontakt Chemie and is available under the name Graphite 33. The weight of the graphite coating on the carbon steel is determined based on the difference between the weight of the sample with coating and without coating. This resulted in graphite per area of carbon steel of $5*10^{-3}$ g/cm^2, which corresponds to approximately 0.08wt% of graphite in the salt.

- Hydrated HitecXL + graphitized carbon steel (A516Gr70), isothermal 310°C, 1500h, argon environment

  Results showed an excellent surface coverage with $CaCO_3$ of 99.9%, based on SEM images. This coverage resulted in the absence of a corrosion layer and thereby confirms the protective behaviour. The disadvantage of thermal decomposition when directly adding the graphite to the salt is not present in this case. The salt in the new environment acts similar as pure HitecXL.

However, this isothermal Argon environment, which makes it possible to use hydrated salt, is not similar to the expected environment. Therefore the following, more challenging, test environment is also considered.

- HitecXL + carbon steel (A516Gr70), cycling 300-500°C, 125 cycles over 500h, air environment

  The graphitized carbon steel showed a clear protective $CaCO_3$ layer over the whole surface. X-ray diffraction (XRD), tests showed, however, the presence of some corrosion products in the form of two iron oxides. These are magnetite and haematite phases. However, a reduction of 3 times the corrosion rate with respect to the not graphitized carbon steel was shown. This reduced rate amounts to 11.4+/-1.2μm/year.

Gonzalez et al. (2019) had similar observations when considering the binary nitrate eutectic 51wt% $NaNO_3$+49wt% KNO_3. Tests were similar, i.e. first graphite was added to salt and afterwards, the graphite spray was used. However, they concluded in addition that the amount of sprayed graphite can be further optimized to have better protection.

The same type of graphite coating, Graphite 33, was used in similar research and also showed good results. In addition, the influence of the presence of nanoparticles with and without the coating was investigated. These nanoparticles have the function of enhancing the thermophysical properties of the salt. The heat capacity of the salt was enhanced by 20-30% for nitrate salts (HitecXL and solar salt) (S. F. Ahmed et al., 2017). This seemed promising. However, if the corrosion would be increased, the expected economic benefit would be suppressed. Therefore, tests are executed. What is noted at the start is that there are contradicting results present in literature regarding the influence of nanoparticles in nitrate salt on corrosion potential when in contact with carbon steel. This suggests that the effect is complex and depends on the base salt and conditions of the tests. The tests, with and without nanoparticles, were executed on as well graphitized as not graphitized carbon steel. They applied a quantity of 3 mg, which resulted in $5*10^{-3}$ mg/cm^2 of graphite per area of carbon steel and 0.05 wt% of the salt. The results are shown in Figure 8.5 and described below.

- HitecXL + carbon steel (A516Gr70), cycling 300-500°C, up to 500h, air environment

  A clear corrosion layer is observed. The corrosion rate between 100 and 500h is around 0.013 mm/year. This is an increase of 20% when compared to isothermal tests in previous research.

- HitecXL with SiO_2 nanoparticles + carbon steel (A516Gr70), cycling 300-500°C, up to 500h, air environment

  The SiO_2 nanoparticles increased the corrosive behaviour. XRD showed the presence of more iron oxides. The thickness is up to two times higher and the rate after 100h is more than three times higher, 0.041 mm/year. The nanoparticles are responsible for the loss of stability of the oxidation layer. This layer therefore detaches. This creates favourable conditions for subsequent oxidation.

- HitecXL + graphitized carbon steel (A516Gr70), cycling 300-500°C, up to 500h, air environment

  The graphitization provided, similar to the research of Grosu et al. (2018) a decrease in corrosion rate and thickness. The thickness is decreased by a factor two. The rate is decreased to 0.004 mm/year between 100 and 500h. This is a decrease of more than a factor of three.

- HitecXL with SiO_2 nanoparticles + graphitized carbon steel (A516Gr70), cycling 300-500°C, up to 500h, air environment

  The protective $CaCO_3$ is hardly detectable and strongly inhomogeneous. Numerous crystals of $CaCO_3$ were identified in the salt following the test in comparison to the nanoparticle-free salt where rarely found in the salt. This shows that the nanoparticles prevent the growth of the protective layer on the carbon surface. The corrosion rate is 0.035 mm/year. This is an increase of a factor of nine compared to the graphitized carbon steel without the nanoparticles present in the salt.
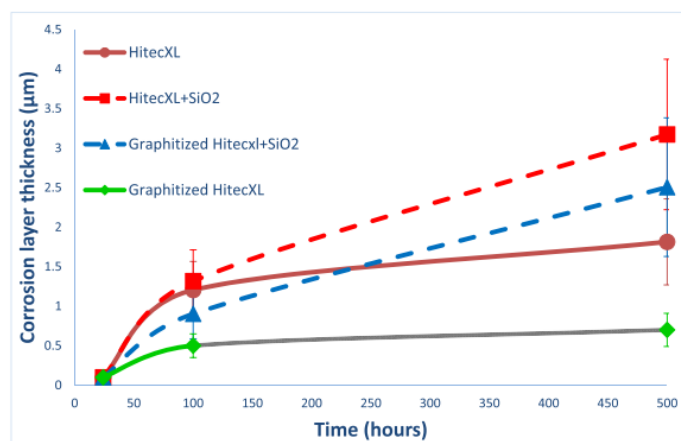
Figure 8.5: Corrosion layer thickness as function of time for HitecXL, HitecXL+SiO$_2$, Graphitized HitecXL+SiO$_2$, and Graphitized HitecXL (Piquot et al., 2019).

The influence of SiO$_2$ particles can be attributed to two main mechanisms. The first is the presence of trapped air bubbles in the interparticle porosity raises the local concentration of oxygen, promoting the oxidation of carbon steel. The second is the reaction and integration of nanoparticles into the corrosion layer also contribute to this process.

Above-mentioned observations suggest that while graphitization exhibits good performance in the absence of nanoparticles in HitecXL under cycling conditions, it is less effective when faced with corrosion attacks in the presence of nanoparticles. This lack of effectiveness may stem from a competitive reaction with silica nanoparticles, impeding the formation of a proper protective layer of CaCO$_3$. Furthermore, the introduction of nanoparticles into the corrosion layer could adversely affect the stability of the protective layer, leading to detachment during thermal cycling. The obtained results highlight the substantial impact of nanoparticles doping on the corrosive nature of molten nitrate salt.

However, the stability of this graphite coating should also be tested. In particular the concern of the solubility of CaCO$_3$ into the salt. Carbonates are namely, in general, soluble in molten salts. Grosu et al. (2018) performed these tests on all the above-mentioned test environments. First with a test on thermophysical properties before and after the test. These properties included heat capacity, melting temperature and enthalpy of melting. All showed no differences before and after testing, indicating no significant change in salt composition. Next, Fourier-Transform Infrared Spectroscopy (FTIR) spectra are made. There was limited dissolution visible of CaCO$_3$. Furthermore, no detectable traces of iron were observed within the salt. Lastly, a solubility experiment was performed. During one month, pure CaCO$_3$ was immersed into the salt at 310°C. This was in the form of pellets. It is observed that the pellets did not show, or very limited, dissolution into the salt. For now, this shows the good stability of the coating. However, it is suggested to perform longer tests. Another suggestion is to add small amounts of CaCO$_3$ into the salt up to the saturation concentration to decrease the already limited dissolution. This is named Le Chatelier principle (Grosu et al., 2018).

Another aspect is that the inclusion of graphite on the carbon steel surface offers an advantage in terms of reducing the surface energy, as evidenced by the contact angle images of the molten salt presented in the research of (Grosu et al., 2018) and shown below in Figure 8.6. This characteristic proves advantageous for molten salt pumping in challenging conditions, as it decreases frictional dissipation in laminar flow near the walls and decreases the stress on the carbonate layer, thereby extending its lifespan. Further validation of this approach is needed through additional dynamic tests.

Figure 8.6: Liquid salt drop at 310°C on the non-graphitized surface (left) and graphitized surface (right) (Grosu et al., 2018).

To conclude, the assumption of corrosion resistance of a graphite coating is based on the above conclusions within this subsection. However, these coatings are present in very thin layers, of approximately 20μm. To be able to reach the t/d=1, as mentioned in the research of HEDH and Hooman (2023), when the thickness is 2 mm, approximately 100 layers of Graphit 33 coatings are required. Hence, research will be conducted across various application areas to evaluate these coatings, ideally of greater thickness, for the specified application. To identify new application areas, an explanation of graphite is provided first.

<div style="text-align: right; font-size: 3em;">9</div>

Graphite coating

The depicted structure, as illustrated in Figure 9.1, serves as a framework to identify an appropriate coating containing graphite. Graphite itself, which is a starting point, is elaborated upon first. Thereafter, attention shifts towards exploring its utilization in various application domains. Following this, the discussion delves into the utilization of graphite in conjunction with thermal conductivity enhancement. The exploration of potential application areas results in the selection of coating options. Subsequently, the criteria for the desired coating are outlined, resulting in combination with the options in the final choice of coating composition and application method.
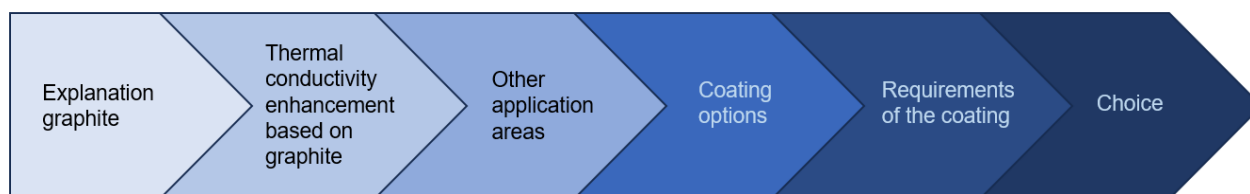
Figure 9.1: Structure of this Chapter to find suitable graphite coating.

9.1. Graphite

Graphite is one of the three forms of carbon. The other forms are diamond and fullerenes. Graphite has a two-dimensional crystal structure, in contrast to the three-dimensional structure of diamond. There are covalent and metallic bonds within each layer. These layers are stacked in an AB sequence and these layers are linked by van der Waal interaction. Van der Waal interactions are known as weak interactions. The different carbon layers within graphite are known as graphene layers (Chung, 2002). The visual representation of the graphite structure is shown in Figure 9.2.

Graphite is an anisotropic material, due to these different layers. Within the layers, graphite is known as a good thermal and electrical conductor. This is the result of the metallic bonding within the layers. However, due to the weak van der Waal interactions between the layers, graphite is a poor thermal and electrical conductor perpendicular to the layers. The weak interaction between the layers makes that the layers can slide with respect to one another. This makes graphite a good lubricant. Another consequence of the anisotropy of graphite is the ability of graphite to allow reactants to reside between the graphene layers and undergo chemical reactions there. These reactants, known as Graphite Intercalation Compounds (GIC), enable a modification to the properties of the graphite. For example, a higher electrical conductivity since higher charge transfer is possible between the CIG and graphite (Chung, 2002).
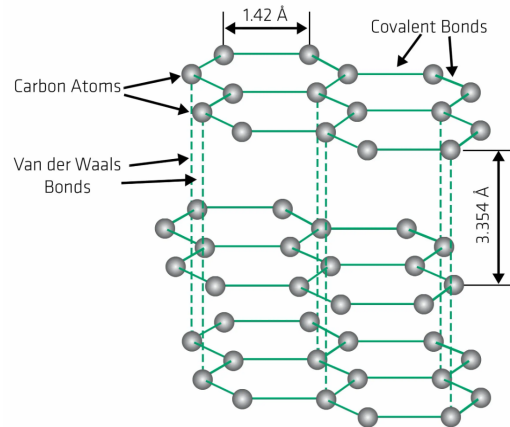
Figure 9.2: Graphite structure (Gomez, 2022)

Two types of graphite, used in most of the studies, are natural single crystal graphite or pyrolytic graphite. The first one is obtained from calcite stones and are flakes ranging between 1-2 mm in diameter. The second one is synthetic graphite with similar properties. Pyrolytic graphite is synthesised by cracking a carbonaceous gas on a graphite substrate at temperatures higher than 2000°C. This is followed by a crystallite alignment improvement treatment, pressing 300-500 kg/cm^2 at 2800-3000°C. A more advanced form of pyrolytic graphite is highly-oriented pyrolytic graphite, which is obtained by annealing the pyrolytic graphite at 3400-3500°C under light load (Chung, 2002).

The thermal conductivity of graphite has, as said before, an isotropic character. This can be observed in Figure 9.3. It is measured along the basal planes and hexagonal axis. The basal planes are denoted as K_a, and the conductivity along the hexagonal axis is represented by K_c. Thus, the components of the conductivity tensor are $K_{xx}=K_{yy} = K_a$, and $K_{zz} = K_c$ (Alofi & Srivastava, 2013). At room temperature, the thermal conductivity for the c-axis of graphite is around 2 W/mK. For the basal plane, it is 2195 W/mK and for graphene 3541 W/mK.
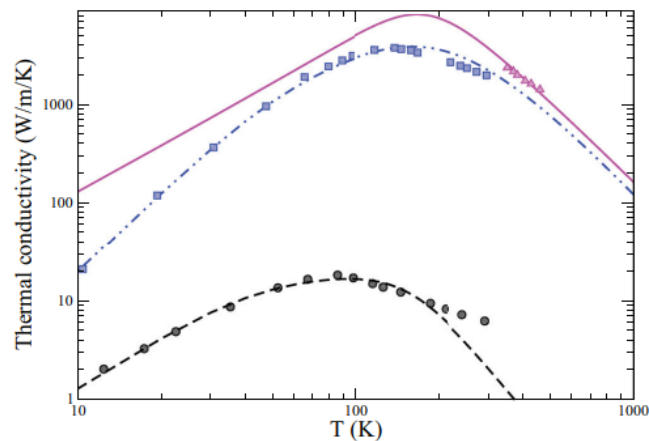
Figure 9.3: Thermal conductivity graphite and graphene both theoretical and experimental. Graphene theoretical (purple line), graphene experimental (purple triangular), graphite basal plane (blue line), experimental graphite basal plane (blue squares), graphite c axis (black line), experimental graphite c axis (black dots) (Alofi & Srivastava, 2013)

9.2. Application areas

Graphite, both in natural and synthetic form, is used at a large scale. In 2022, 1.3 million metric tons, is produced. This is an increase of 15% with respect to the previous year. Some of the main application areas are (Statista, n.d.):

- Pencils
- Lubricants
- Lithium-ion batteries
- Refractories
- Graphene technology

The mentioned application areas are widely recognized; however, as the graphite coating in this thesis aims to improve both thermal conductivity and corrosion resistance, a literature review is conducted at first to investigate whether thermal conductivity enhancement has already been achieved through the application of a graphite layer or coating. A review which contains information regarding the application of carbon materials, including graphite, in solar thermal storage is available (Badenhorst, 2019). The focus of this research is mainly on increasing the thermal conductivity of PCM by the addition of graphite in the PCM. Two other findings, which focus on applying a layer containing graphite to increase the thermal conductivity, are presented below.

Within thermal energy storage, graphite is found within the shell of the paraffin core. This shell consists of graphite nanoparticles embedded in melamine-formaldehyde (MF). This is prepared by an in-site poly-condensation process. Eventually, a microencapsulated phase change slurry is prepared by encapsulating the PCM with the MF/graphite shell followed by dispersing these in conventional HTFs. The process is summarized in Figure 9.4. This results in a new heat transfer fluid with twice the storage capacity compared to the previous one. The thermal conductivity of paraffin in MF/graphite dispersed slurries is higher than without the graphite (J. Liu et al., 2017).
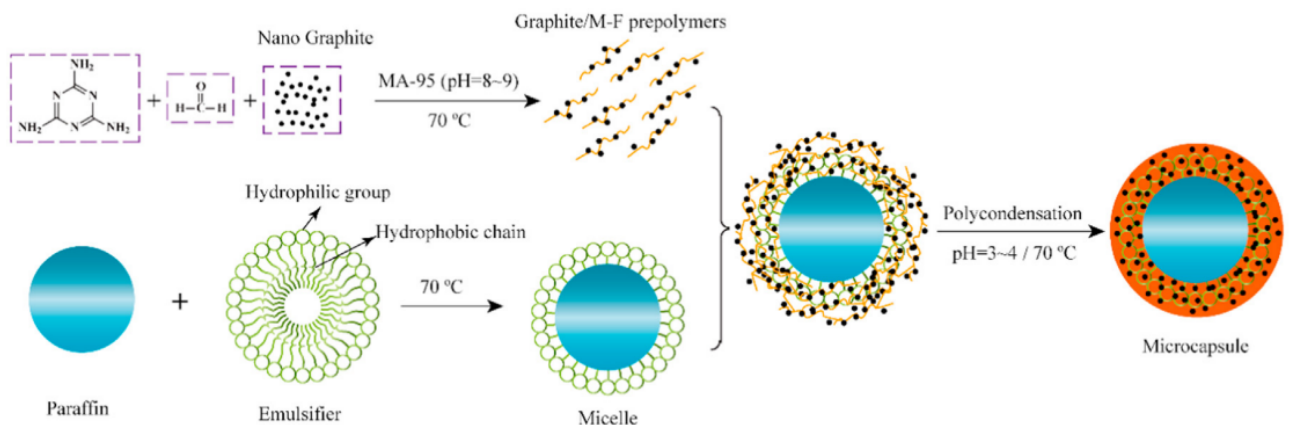
Figure 9.4: Process of preparing paraffin with graphite nanoparticles embedded in melamine-formaldehyde (J. Liu et al., 2017).

Yu et al. (2015) uses a graphite coating in order to enhance the thermal conductivity in a polyacrylonitrile-based (PAN-based) carbon fiber reinforced plastic (CFRP) composite laminates in order to generate a material with high strength, stiffness, low thermal expansivity and high thermal conductivity. They used highly oriented graphite films. The combination gives highly oriented graphite films carbon fiber-reinforced plastics (HOGF-CFRP) composite laminates. The HOGF is applied with an acrylate adhesive of 10μm. The in-plane and out-of-plane thermal conductivities are summarized in Figure 9.5 and 9.6. The T700 and M55J are different PAN-based carbon fibers. Figure 9.5 shows first an increase and then a decrease in in-plane thermal conductivity for higher volume fractions of HOGF. This is due to the application method for this configuration. The different layers of HOGF, chosen as 25μm, are applied beneath, for every layer, a 10μm thick layer of adhesive. Eventually, the number of layers thus

decreases the in-plane thermal conductivity. The main reason for this phenomenon is that the out-of-plane heat transfer path is obstructed. This out-of-plane heat transfer coefficient is in this research an input for determining the in-plane thermal conductivity with the use of a two-dimensional heat transient heat conduction model. This obstruction is due to the interfacial layers of acrylate adhesive.

Nevertheless, the thermal conductivity, both in-plane and out-plane, does increase for a single layer with increasing thickness, shown in Figure 9.6. The in-plane thermal conductivity is increased, at its maximum, 14.1 times the in-plane thermal conductivity without the coating.
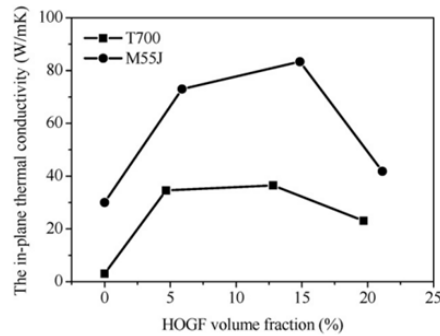
Figure 9.5: The in-plane thermal conductivity as a function of the increase of the volume fraction by increasing number of layers
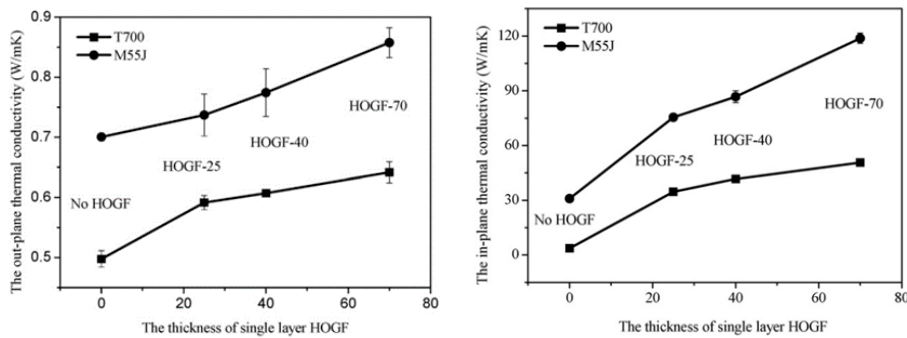
Figure 9.6: The out-plane (left) and in-plane (right) thermal conductivity as a function of the increase in thickness of single layers

It is concluded that increasing the in-plane thermal conductivity by increasing the volume fraction, while making use of multiple layers of graphite coating with an adhesive beneath, is not feasible due to the excessive low conductive acrylate adhesive. Nevertheless, applying thicker single layers does show an increase in thermal conductivity.

In the quest for applications aiming to improve thermal conductivity through graphite coatings, it is pertinent to explore potential applications related to enhancing electrical conductivity. This is justified by the similarity in mechanisms, involving the movement of electrons, which underscores the potential for dual improvement in both thermal and electrical conductivity. The investigation into such dual-enhancement applications broadens the scope for innovative uses of graphite coatings in diverse technological domains.

This results in the findings of coating compositions and application methods, which mainly focus on increasing electrical conductivity, in the following three fields:

- Bipolar plate in fuel cells
- Graphite screen printing electrodes
- Lithium-ion batteries

Regarding the electrical conductivity improvement, a graphite coating application area is within fuel cells. The bipolar plate requires high electrical conductivity, corrosion resistance, mechanical strength, gas impermeability, and light and low-cost material. According to W.-L. Wang et al. (2012), is pure graphite, which was first used, brittle and had a lack of mechanical strength and could therefore not be used as a single material bipolar plate. Consequently, stainless steel was investigated as an alternative material for the bipolar plate. Although stainless steel at first seemed corrosion resistant, a point of concern is the passive oxide film layer on the stainless steel. This layer protects from corrosion. However, it also affects the contact resistance between the bipolar plate and electrode leading to power degradation. Therefore, a graphite coating is assessed in this research. The stainless steel type used in this research is 316L. The binder used was a polymer binder combined with carbon fibre to increase the electrical conductivity. A graphical representation can be seen in Figure 9.7. The graphite sheet was made by expanded graphite (EG) flakes. Expanded graphite is a type of graphite that has been processed to increase its volume and create a three-dimensional structure with high porosity. The binder layer was 40μm and the graphite layer 130μm and showed, even after 2000h, low corrosion current.
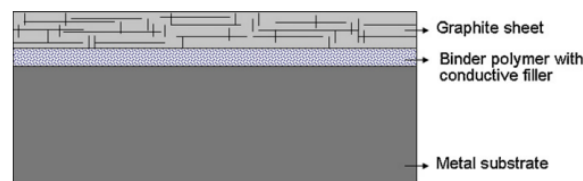
Figure 9.7: Metal surface with graphite sheet with as binder a polymer with conductive filler (W.-L. Wang et al., 2012).

Graphite screen-printing electrodes are an application which requires the binding of a carbon-based material on a substrate. These screen-printing electrodes are utilized for detecting or stimulating electrical signals in various applications such as biosensors, electrochemical sensors, and electronic devices. Within this screen-printing approach, a conductive composite material is obtained by mixing carbon particles and a binder (H. M. Mohamed, 2016). The binder is responsible for the adhesion on the substrate.

Multiple materials are tested as binder and solvent. Paper has emerged as an advantageous platform as a substrate. A possible binder is silicone glue. The conductive ink, prepared by mixing, consists of 70% graphite powder and 30% silicone glue. The content of graphite powder higher than 70% showed brittleness, which made them inappropriate to use. Silicone glue is a material with high viscosity and adhesion on porous materials and no electrical conductivity. Graphite has, in contrast to silicon, high electric conductivity. The process is shown in Figure 9.8. The thickness of the screen printed tracks was 102.3 +/- 14.3μm and the charge transfer resistance was 218.3 +/- 30.7Ω (Castro et al., 2023).
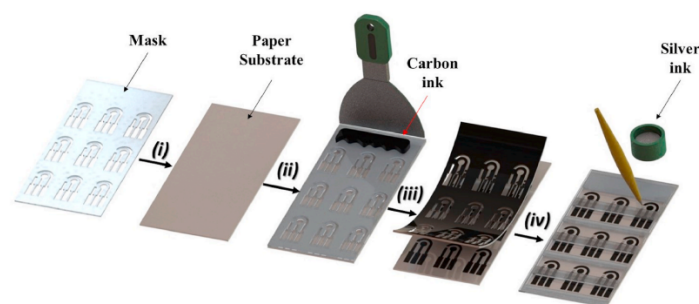
Figure 9.8: Example screen printing electrode (H. M. Mohamed, 2016).

Another research area where graphite coatings are used is within Lithium-ion batteries. Graphite is used in Lithium-ion batteries due to its ability to intercalate Lithium ions during charging cycles, providing a stable and reversible electrode material for energy storage. This graphite enhances, with

respect to previously used soft and hard carbons, the full-cell energy density. During discharging, the intercalated Lithium ions are released and taken back to the cathode. Graphite offers a high electrical conductivity, facilitating efficient electron transfer within the battery. Some of the latest type of research is focused on the binder distribution within the coating, the influence of calendering on the porosity, and introducing silicon(oxide) to the graphite to enhance the energy density (Asenbauer et al., 2020).

Gandert et al. (2023) focused on the thermal conductivity of the graphite anode in Lithium-ion batteries. They stated that this is important since till now the focus is solely on electrochemical behavior. However, the thermal behavior is of great importance on the ageing of the battery. Ageing is accelerated by a large temperature gradient perpendicular to the electrode. In order to prevent this temperature gradient should the thermal conductivity be optimized. Within this research, the focus is on the influence of calendering. This will be discussed in more detail at a later stage of this thesis.

Applying a thin layer of graphite poses a challenge due to the typically loose structure of carbonaceous thin layers, rendering them inadequate as a barrier layer against acidic solutions (W.-L. Wang et al., 2012). Therefore, a binder is required. This binder is, for example within Lithium-ion batteries, responsible for cohesion as well as adhesion to the current collector. Within these batteries, the binders are considered electrochemical inactive and therefore should the percentage be as low as possible. Regarding the thermal conductive coating are the binders a thermal resistance (Müller et al., 2017). Therefore it is expected that within the application of this research, the percentage should also be minimized.

9.3. Graphite coating options and choice

Based on the above information, the following can be concluded. First of all, graphite is already used within thermal energy storage materials as a thermal conductivity enhancer in different forms, but not commonly used as a thermal conductive layer. Focusing on thermal conductivity improvement by adding a layer of graphite, two examples are presented. While exploring other application areas, more conclusions could be taken. Based on the example of highly oriented graphite films can be concluded that using multiple layers with a binder beneath could negatively impact the thermal conductivity in comparison to thick layers. When focusing on improving electrical conductivity, while making use of graphite, multiple application areas are observed. What was furthermore learned is that adding a high wt% graphite can lead to a brittle material. On the other hand, the binder, even when not applied as an adhesive layer but spread within the coating, has a negative effect on the electrical and thermal conductivity.

To be able to choose the right coating composition in combination with an application method, some objectives are established. The first objective is finding a coating that binds on carbon steel, the second is finding a coating that is able to be applied in relatively thick layers, $\approx$0.5 mm.

This leads to the following conclusions:

- Materials with an adhesive layer instead of a binder distributed in the graphite coating are excluded
- The base material in the reference paper should be a metal
- It should be evaluated if adding layers in the order of 0.5 mm could be possible

This resulted in the choice for the graphite coating based on the research of Müller et al. (2017). This is due to the base material, copper, in combination with the binder, PVDF, distributed throughout the coating, and the addition of layers up to 400μm.

<div align="right">

10

</div>

<div align="right">

Hypothesis

</div>

10.1. Hypothesis thermal conductivity

In Chapter 7 the outcome is presented of previous research which led to the tests of graphite-coated carbon steel samples.

Based on those promising conclusions of various configurations, the more simplified low-cost periodic structure of a rolled mesh is developed. The uncoated stainless steel mesh resulted in, as explained before, already a 10% improvement of the overall cycle performance. Within the periodic structure, the thermal contact resistance is only present from the inner tube to the periodic structure. This graphite-coated material resulted in an effective thermal conductivity of the whole storage as high as 83% when compared to a graphite foam. It is expected that the thermal contact resistance between the layers will prevent achieving this 83%. A coated mesh will not behave similarly to the results of a numerical model, similar to the periodic structure with interconnected rods, due to the thermal contact resistance between different layers of the mesh.

Thermal contact resistance is the phenomenon that represents the resistance to heat flow between two materials, or in this case two layers of the same material, at their contact interface. It arises due to imperfections, microscopic roughness, or air inclusions on the surfaces of the materials (Ishizaki et al., 2020). Thermal contact resistance can, for example, be lowered by flattening the surfaces, brazing the two materials or applying compressive forces (Fiedler et al., 2014).

If two surfaces are perfectly smooth, no energy can be stored in the infinite small amount of material between these surfaces. This results in the requirement, according to the first law of thermodynamics, in

$$\dot{Q}_1 = \dot{Q}_2 \tag{10.1}$$

if a closed system is present between surfaces 1 and 2. This results, with the use of Fourier's law, in the requirement of

$$T_1 = T_2 \tag{10.2}$$

However, this situation is not realistic since all surfaces have some degree of roughness and heat conduction will be dependent on the spots of contact.

The thermal contact resistance of a surface is usually expressed in terms of an interfacial conductance, as h_i in W/m^{2}K, and is described as

$$\dot{Q} = h_i A(T_1 - T_2) \tag{10.3}$$

The contact resistance exhibits dependency on the applied pressure sustaining the contact. Contact resistance data is sparse in literature and is often unreliable. Some typical interfacial conductances are, with large ranges, present within literature (Mills, 1992).

The pathways within Figure 10.1$_l$, represent the interconnected rods with, at the position indicated with the arrow, the heat transfer pathways. In the mesh illustrated in Figure 10.1$_r$, the pathways within each layer, both tangentially and axially, remain effective conduits for heat transfer. However, the introduction of thermal contact resistance becomes significant in the radial direction, indicated by the dotted line.

Within this thesis tests will be performed to evaluate the thermal conductivity in the tangential direction from one layer to another layer.
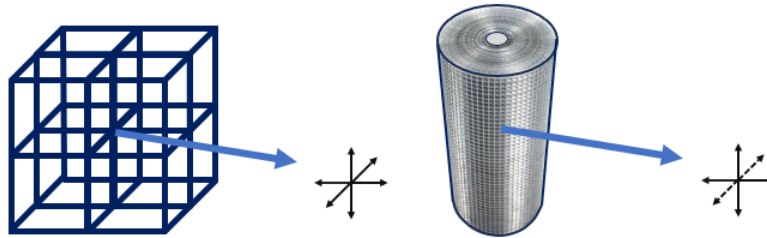
Figure 10.1: Difference of heat transfer pathway. Periodic structure (left). Rolled mesh (right).

When looking at the mesh in a horizontal cross-section, one layer will be similar to Figure 10.2$_l$. The coating will be applied before rolled up, this will result in a cross-section similar to Figure 10.2$_r$.
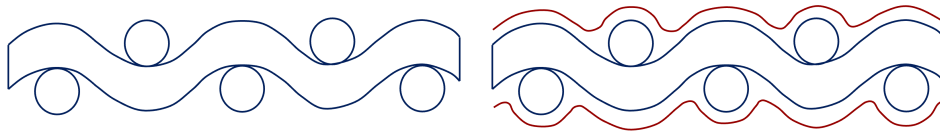
Figure 10.2: Uncoated cross-section of the mesh (left). Coated cross-section of the mesh (right).

Obtaining measurements to assess the impact of the coating is challenging using a structure similar to Figure 10.2b. Hence, for the time being, it is presumed that a coated flat sample will exhibit behaviour similar to a single layer, as depicted in Figure 10.3. Heat transfer is assessed from top to bottom, or vice versa. This will result in the resistance model explained below.
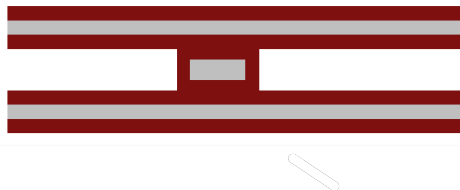
Figure 10.3: Cross section of flattened mesh.

10.2. Resistance model

The resistance model, shown in Figure 10.4, shows the visual representation of the hypothesis. The total resistance has as unit K/W. This resistance model is composed of the following resistances:

- R_{1a}: Thermal resistance of graphite coating
- R_{1b}: Thermal resistance of graphite coating, different thickness than R_{1a}
- R_2: Thermal resistance of carbon steel
- R_3: Thermal contact resistance from graphite coating to next layer
- R_4: Thermal contact resistance from graphite coating to carbon steel
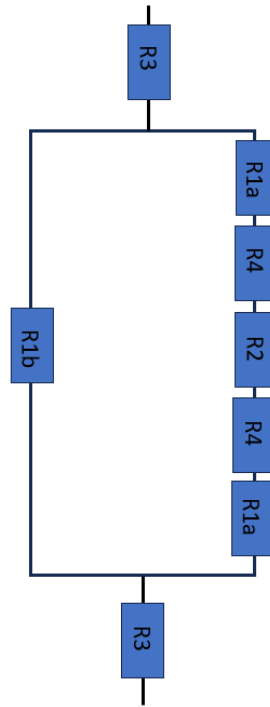
Figure 10.4: Representation of resistance model.

Some resistances are connected in parallel while others are in series. There exist three parallel pathways. Two of them are the pathways which are only through the graphite coating. The other one is the pathway which is through the coating as well as the carbon steel.

The sum of the resistances is equal to

$$R_{tot} = R_3 + R_{middle} + R_3 \tag{10.4}$$

where R_{middle} represents the pathway in the middle of the pathways in parallel. This R_{middle} is equal to

$$\frac{1}{R_{middle}} = \frac{1}{R_{1b}} + \frac{1}{R_{1a} + R_4 + R_2 + R_4 + R_{1a}} \tag{10.5}$$

Since resistances in series are equal to the sum of the resistance. Resistances in parallel are equal to the following equation, where R_x and R_y are examples of resistances

$$\frac{1}{R_{xy}} = \frac{1}{R_x} + \frac{1}{R_y} \tag{10.6}$$

In total this results in the following equation for the resistance

$$R_{tot} = 2R_3 + \frac{1}{\frac{1}{R_{1b}} + \frac{1}{2R_{1a} + 2R_4 + R_2}} \tag{10.7}$$

Thermal resistance due to conduction, R_1 and R_2 are equal to

$$R_{1,2} = \frac{th_{1,2}}{k_{1,2}A_{1,2}} \tag{10.8}$$

t is the thickness of the layer, A is the surface area and k, the thermal conductivity of the material.

The thermal contact resistance is equal to

$$R_{3,4} = \frac{1}{h_{c,3,4}A_{3,4}} \tag{10.9}$$

where h_c is the thermal contact resistance and A the surface area.

To formulate a hypothesis regarding the measurements, hypotheses for each individual resistance must be established. Based on the different samples the area and thicknesses can be filled in, in to extract the expected results.

First, the thermal conductivity of both materials is described followed by the two thermal contact resistances.

10.2.1. Thermal conductivity graphite coating

In the research on which coating with graphite is based, the thermal conductivity is approximately 80 W/mK. This is shown in Figure 7.5. Graphite is an anisotropic material, however, due to the powder form which will be used in the coating more isotropic behaviour is expected. When the anisotropy is not taken into account Oehler (2021) reports values between 130 and 142 W/mK, at 25°C, based on three references. The presence of binder and solvent materials is expected to slightly reduce the thermal conductivity. Determining the precise value for the coating alone is challenging; nonetheless, an approximate value of 80 W/mK is anticipated to be accurate.

For the use of a graphite coating in Lithium-ion batteries, other results are present regarding the thermal conductivity. However, these are measured over the whole configuration and are not based on the graphite coatings themselves. These take into account the thermal contact resistance. The results are explained at a later stage. What should be noted is the extremely thin layers compared to this thesis: $\approx 10\mu$m copper base layer with $\approx 70\mu$m coating. This 70μm is the uncompressed thickness.

The porosity of the coating influences the thermal conductivity of the coating. Gandert et al. (2023) evaluated the influence of the porosity on the thermal conductivity of an anode stack with graphite layers on it. These anode stacks are used in Lithium-ion battery electrodes. Lithium-ion batteries are usually important for their electrical conductivity. However, the properties of specific heat capacity, density and thermal conductivity play a huge role in the ageing process of the batteries. If large temperature gradients are present perpendicular to the electrode, caused by weak thermophysical properties, ageing accelerates.

This porosity is reduced by the use of a calendering machine. Calendering is a form of a compaction process. Compaction involves processes in which, usually by mechanical forces, gases are removed and density increases. In case of a graphite coating, calendaring can also increase the adherence to a surface. This process is shown in Figure 10.5.
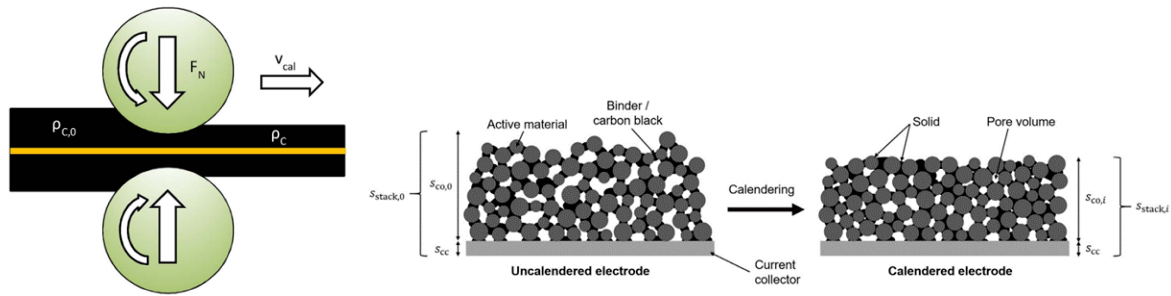
Figure 10.5: Calendering graphical representation (left). Influence calendering on microstructure (right) (Müller et al., 2017).

The results of calendering on the thermal conductivity are shown in Figure 10.6. First, a decrease in the thermal conductivity followed by an increase is seen. Furthermore, the same pattern is observed for the adhesion strength between the layers. This suggests that the thermal conductivity is impacted by the contact resistance. The decrease at first is expected due to the shear forces due to calendering, which impairs the connection of the coating and current collector. The increase is due to, at higher pressures, line loads which are high enough to interlock the coating onto the current collector.
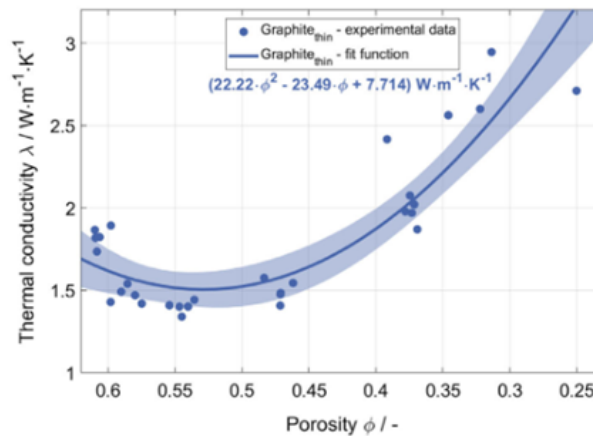
Figure 10.6: Thermal conductivity as function of porosity (Gandert et al., 2023).

Furthermore, when the loads are too high other structural changes occur. It can result in particle breakage and penetration of the coating into the current collector. It also might entail a partial delamination of the coating.

10.2.2. Thermal conductivity carbon steel
The thermal conductivity of the carbon steel is the one which is known well. This is the base material. The thermal conductivity of carbon steel is in the order of 30-60 W/mK depending on the specific type. The thermal resistance is dependent on the thickness of the material.

10.2.3. Thermal contact resistance coating to carbon steel

The thermal contact resistance of the coating to the carbon steel is approximately the same as from copper to the coating mentioned above. The overall values of the thermal conductivity of the whole configuration, 80.3μm thick, without any calendering, is equal to approximately 1.7 W/mK, shown in Figure 10.6. Together with the estimated conductivity of the copper and the graphite coating, it is possible to determine the thermal contact resistance. The total resistance, $\frac{th}{kA}$ with the 1.7 W/mK and thickness and area given in Gandert et al. (2023), should be equal to the resistances across the layers plus the thermal contact resistance

$$\frac{th_1}{k_1 A} + \frac{1}{h_{c,graphitecopper}} + \frac{th_2}{k_2 A} = \frac{th_3}{k_3 A} \tag{10.10}$$

where 1,2 and 3 are respectively the thickness of the graphite coating, the thickness of the copper and the total thickness of the combination of both. If both sides are divided by A and thermal conductivity values put in the equation the equation can be solved. The thermal conductivities are respectively 80, 360 and 1.7 W/mK for 1,2 and 3. This results in a thermal contact resistance of approximately 21,500 W/m^{2}K. This rough estimate of the thermal contact resistance is in the same range as literature (X. Li et al., 2016).

10.2.4. Thermal contact resistance layer to layer

The thermal contact resistance from layer to layer represents in reality graphite on graphite. Predicting this value is not reliable since it will depend on a lot of parameters. For example, the force with which the mesh will be rolled up. Therefore, for now, there will not be a comprehensive analysis of this thermal contact resistance. This is also because the measurements will be for one layer. However, according to literature graphite film on graphite film exhibits similar behaviour as graphite film on another specimen under the same conditions (X. Li et al., 2016). In this thesis, if required, an appropriate value of the thermal conductivity will be chosen, dependent on the measurement method.

10.2.5. Dot on the horizon

For now, the coating will be applied in order to assess the thermal conductivity from one layer to another layer. However, when the coating is applied when the mesh is rolled already, a behaviour more similar to an interconnected structure. Within the study of Opolot et al. (2023), a model was used which is based on an interconnected tetradecahedron periodic structure to be able to predict the effective thermal conductivity of the system (Mesalhy et al., 2005). The periodic structure, denoted by $_{ps}$ influences based on the following equation

$$k_{eff} = \frac{[k_{pcm} + \pi(\sqrt{\frac{1-\epsilon}{3\pi}} - \frac{1-\epsilon}{3\pi}(k_{ps} - k_{pcm})][k_{pcm} + \frac{1-\epsilon}{3}(k_{ps} - k_{pcm})]}{k_{pcm} + [\frac{4}{3}\sqrt{\frac{1-\epsilon}{3\pi}}(1-\epsilon) + \pi\sqrt{\frac{1-\epsilon}{3\pi}} - (1-\epsilon)](k_{ps} - k_{pcm})} \tag{10.11}$$

With ϵ the porosity of the periodic structure, k$_{pcm,ps}$ the thermal conductivity of the periodic structure and original phase change material.

This could provide an estimation of the overall improvement based on the effective thermal conductivity. However, it should be known that this structure will not be similar to an interconnected tetradecahedron periodic structure based on the thermal contact resistance between the layers.

11

Sample production

Following the conclusions drawn in the previous Chapter, the focus will now be directed towards the application of this graphite coating. Initially, the specific type of carbon steel will be determined. Subsequently, the elements of the graphite coating will be discussed. Thereafter an exploration of various coating methodologies documented in literature is executed. Based on the requirements of the coating, an appropriate application technique will be selected. The initial testing phase, aimed at determining the thickness of a single layer will then be outlined, succeeded by a proposed strategy for applying the coating onto the carbon steel to fabricate samples. Furthermore, challenges associated with the application of this coating will be addressed, accompanied by potential solutions. Finally, the outcome of the coated samples is presented.

11.1. Mesh material

In the study conducted by Opolot et al. (2023), a mesh material made of stainless steel, SS304, was employed. However, for this research, carbon steel is the material of choice. Although various types of carbon steel are commercially accessible, the specific variant is not important at this stage and could be optimized in further research. Consequently, a company was contacted that is able to supply customized samples to ascertain the precise type of carbon steel utilized within that company. Choosing this type of carbon steel ensures the option of generating the sample in a shape that will be required for a specific measurement technique.

The company is Tummers Plaatbewerking and the specific type of carbon steel is S235JR. The characteristics of this carbon steel are:

- Thermal conductivity 40-50 W/mK
- Specific heat capacity 0.460-0.480 kJ/kgK at temperatures 50-100°C
- Density 7800 kg/m^3

Next, the graphite coating, according to the reference paper will be mixed in the lab to evaluate the behavior and choose a strategy to coat the samples.

11.2. Graphite coating components

The coating, based on the research of Müller et al. (2017), is made of the following components:

- Graphite in powder form
  $<20\mu$m, synthetic
- Carbon black as conductive additive
  C-NERGY SUPER C65
- N-Methylpyrrolidone (NMP)
- Polyvinylidene fluoride (PVDF)
  Powder, Average M_w=534,000

The graphite, NMP, and PVDF are available at Sigma-Aaldrich. The carbon black conductive is available at Nanografi.

This coating is prepared in the reference paper with the following procedure:

1. The artificial graphite and carbon conductive black were dry-mixed
2. The binder solution was added step-wise with the use of a laboratory dissolver mixture
3. The final solid slurry content was 47.5wt%
4. The slurry was homogenized and degassed

In the original application of the research on which the mixture is based, the application method is a doctor blade coater. The dried coating composition in the reference paper is as follows:

- 92 wt% Graphite
- 2.8 wt% Carbon black
- 5.2 wt% PVDF

Based on these final compositions in combination with the knowledge that the solvent will evaporate upon drying the coating, the original proportions of the fluid content can be determined.

Additionally, the process for preparing the binder, NMP, and PVDF, solution was not outlined in the referenced paper. After contacting the author, it was revealed that the following method was employed:

1. A dissolver mixer operating at 2000 rpm for 1 hour was utilized to prepare a 10 wt% PVDF solution.
2. The solution is not utilized until the following day to ensure the complete dissolution of all materials.

It should be noted that if a magnetic stirrer is used, the dissolution process may take approximately 24 hours, according to the author.

PVDF and NMP are both required. PVDF is the binder and NMP is the solvent. However, it should be evaluated if the carbon black additive is required within the application of this coating.

Carbon black is a particle with a high surface area at sub-micron scale. The particle is roughly spherical shape. These spherical shape particles are fused in aggregates. An example of the application of carbon black is as filler in elastomers. Herein, is the carbon black added to modify the mechanical, electrical, and optical properties. Carbon black is identified based on the specific surface area and structure (Pantea et al., 2003). This structure is based on the degree of aggregation.

The electrical conductivity of carbon black is a well-known property. However, when assessing the thermal conductivity, there is no direct influence found regarding the addition of carbon black conductive. A research area where the thermal conductivity as well as the electrical conductivity is of great importance is within the area of bipolar plates. In the research of Greenwood et al. (2013) are carbon black, graphite, and magnetite mixed with a thermoplastic polymer tested on their electrical and thermal conductivity. The polyethylene is present to decrease the weight and increase the mechanical strength. Together this material is known as a high-density polyethylene (HDPE). The making of these HDPEs is done with either compression molding or injection molding.

The findings indicate that when incorporating graphite, an augmentation in thermal conductivity is observed with an increase in weight percentage. The highest wt% corresponds to the highest thermal conductivity. Notably, an immediate boost in thermal conductivity is noted after introducing the initial wt%. This outcome aligns with expectations.

In contrast, carbon black yields different results. Firstly, generating HDPE with a wt% exceeding 32% using carbon black proved impractical due to brittleness. However, this limitation did not apply to injection molding. Additionally, the rise in thermal conductivity with carbon black is significantly lower compared to graphite. Moreover, only compression molding exhibited an immediate response upon the addition of graphite, while injection molding showed a slower response.

These results prompted the execution of simple tests to assess the impact on the mixture's structure. When incorporating conductive carbon black, the mixture exhibited visually a steep increase in viscosity. Further tests with increased NMP revealed still a greater presence of visible grains compared to cases without carbon black conductive. Considering the assured increase in thermal conductivity with higher graphite content and the observed drawbacks with carbon black, the decision was made to exclude carbon black conductive as a component for the graphite coating. In future research can the influences of adding carbon black conductive on the thermal conductivity be evaluated.

11.3. Coating application methods

Different coating techniques are present in the literature. A comprehensive overview of these most-used coating techniques can be found in Appendix B In addition, below two coating techniques are described. The first is the used technique in the reference paper, the doctor blade technique and the second is the technique that will be used in this thesis, dip coating.

11.3.1. Doctor blade

Doctor blade, also known as tape casting, is used to produce thin films. In this process, a slurry is applied to a surface by moving the doctor blade with a constant velocity. The slurry spreads and a thin sheet is formed. Within the separation lab of the Process and Energy department of the TU Delft a manual doctor blade is available, shown in Figure 11.1a. The thickness of the layer can be controlled by the doctor blade by increasing or decreasing the gap between the doctor blade and the substrate. However, the wetting behavior is also dependent on the viscosity of the fluid and the coating speed (Berni et al., 2004). The process of the doctor blade method is shown in Figure 11.1b.
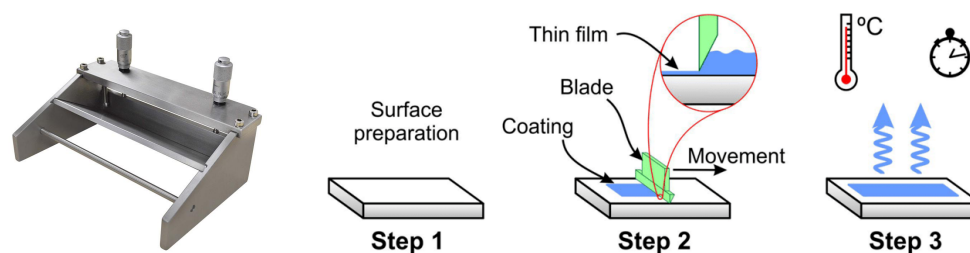
Figure 11.1: Doctor blade (Frederichi et al., 2021)

Since the mesh material shown in Figure 7.3 is not a flat surface, the doctor blade method is not applicable. In this thesis the tests are conducted with flat surfaces so it could be still possible to conduct the tests with this application method. However, the available doctor blade was uneven. Together with the inability of coating the mesh, this excluded this method. The most simple technique which is capable of coating object with a complex shape is dip coating. This coating technique is available at the Process and Energy department of the TU Delft.

11.3.2. Dip coating

The apparatus available at Mechanical Engineering Faculty, made by Ossila.

Figure 11.2: Dip coater (Ossila, n.d.)

In the dip coating apparatus, two types of parameters need to be configured: distance and time parameters. The time parameters encompass choices related to immersion, withdrawal, and drying times. Collectively, these parameters are:

- Coating length
- Substrate position
- Solution height
- Dip speed
- Dwell time
- Initial and final speed of withdrawal
- Dry time

The important parameter regarding the thickness of the coating is the speed of the withdrawal. These are split into the initial and final speed. However, these are set equal and treated as one. The relation between the speed of withdrawal and the thickness of the coating is, as said before, within the viscous regime (Griffin & O'Kane, 2024):

$$h = c(\frac{\mu u}{\rho g})^{1/2} \tag{11.1}$$

With u the withdrawal speed, and c a constant which is around 0.8 for Newtonian fluids. This viscous regime occurs for high velocities and viscous solutions.

If the withdrawal speed is not high enough to let the above approximation be valid, then the surface tension comes into play and this is called the drainage regime. The thickness of the layer will then be approximated as

$$h = c\frac{(\mu u)^{(2/3)}}{\gamma_{LV}^{1/6}(\rho g)^{1/2}} \tag{11.2}$$

Where γ_{LV} is the surface tension. This modification of the previous equation is known as the Landau-Levich equation.

When the speed is reduced to lower than 0.1 mm/s the third and last regime occurs, the capillary regime. In this regime is not the wet film thickness considered, but the dry film thickness.

This results in the following approximation

$$h_{dry} = \frac{kE}{Lu} \tag{11.3}$$

$$k = \frac{cM}{\epsilon\rho} \tag{11.4}$$

where E is the evaporation rate, L the width of the coated film, u again the withdrawal speed, and k the material proportion constant. M represents the molar weight of the solute, c the concentration of solute in solution, and ϵ the porosity of the deposited film.

The minimum and maximum speed of immersion and withdrawal are respectively 0.01 and 50 mm/s. The density can be defined according to the weight percentages of the solution. However, the viscosity is not so easy to predict. Therefore, different withdrawal speeds will first be tested in order to see if the thickness of the coating shows a relation with the speed.

11.4. Thickness coating

To be able to determine the thickness of the coating it is, as said before, dependent on the viscosity of the coating. After mixing the components in the ratios of the reference paper, it soon became clear that using these ratios in combination with dip coating would not give smooth thin layers. Therefore, the mixture should be diluted with the solvent. All the other components are kept at the same ratio since the solvent will evaporate and it is desired to have the original ratios. The amount of dilution influences the viscosity which has subsequently influence on the coating thickness. Therefore, some tests are executed with different amounts of dilution.

The first tests regarding the coating thicknesses were performed with square samples. These tests are focused on the first layer of the coating deposited on the carbon steel. The viscosities resulted, for any withdrawal velocity, in an uneven distribution of the coating.

Thereafter, the evaluation of the extremities of the withdrawal velocities are tested for different dilutions. Lower withdrawal velocities resulted in a more even distribution for the dilutions, which were in the order of adding 2-2.5 times the original amount of NMP. This original amount is 10.28gr NMP. This amount is the added NMP, not the NMP in the binder solution. Lower dilutions resulted for every withdrawal speed, tested in the extremes, in an uneven distribution. Higher dilutions lead to thinner layers and more even layers.

Thus, till now it is known that the lower withdrawal speeds resulted in more even layers of the coating. Furthermore, the dilution should be in the order of 2-2.5 times the original amount of added NMP. Now, tests will be done at 0.1-2 mm/s.

Four samples were tested with the following characteristics:

- 2x dilution + withdrawal speed 0.1mm/s (A)
- 2x dilution + withdrawal speed 2mm/s (B)
- 2.5x dilution + withdrawal speed 0.1mm/s (C)
- 2.5x dilution + withdrawal speed 2mm/s (D)

The measurement of the coating thickness is first attempted with the use of microscopic images. However, the size of the samples resulted in the impossibility of generating an image of the whole sample length (approximately 50x40x4mm). Thus, multiple images of one sample needed to be taken. The reproducibility and thus the correctness of these images was not good. Therefore, an electronic caliper was used. The measurements were done at three spots of the coating: the bare steel, on the bottom where the coating is applied, and on the top where the coating is applied to evaluate the gradient of the coating.
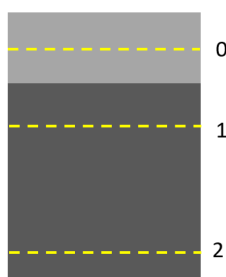
Figure 11.3: Sample (light gray) with coating (dark gray) and indication location of thickness measurement (yellow dashed line).

The results were the following, from left to right positions 0, 1, and 2:

- A: 4.30mm 4.64mm 4.96mm
- B: 4.30mm 4.59mm 4.99mm
- C: 4.30mm 4.41mm 4.42mm
- D: 4.30mm 4.40mm 4.60mm

Besides, these layers are quite thin, the only layer that shows the lowest gradient and thus the most even coating is sample C. This sample production method is therefore chosen to be the sample production method of choice: 2.5x the dilution and withdrawal velocity 0.1mm/s. The density results in approximately 1366kg/m^3 for the slurry.

According to the withdrawal velocity of 0.1mm/s the regime of the flow is in between the drainage regime and the capillary regime. For both equations, with the information now available, it is not possible to convert it back to the expectation of the viscosity of the slurry. This is due to the unknown surface tension or the unknown evaporation rate.

When applying the next layers, much thicker coating layers were obtained. However, the thickness of this layer was fluctuating significantly. Therefore, it is chosen to keep the same composition of the slurry for every coating layer and the different layers obtained will be measured and determined if another layer is required.

11.5. Drying

Within the research of Müller et al. (2017), special attention is on the drying rates of the coating which influence the binder distribution. Binders, within the field of lithium-ion batteries, are responsible for cohesion between the particles and adhesion to the, within this case, current collector. The binders are considered electrochemically inactive (Müller et al., 2017). Within this research, the binders are not responsible for the thermal conductivity within the coating, and therefore the binder distribution is also of importance.

In general, binder-containing particulate coatings suffer from binder migration. Binder migration means that a higher concentration of the binder is present at the surface and a lower concentration in other regions. The main reason for this phenomenon, within battery electrodes, is too high drying rates (Hagiwara et al., 2014). This uneven binder distribution can, besides electrochemically inactiveness at the surface, lead to reduced adhesion strength. Drying rates were modified by changing the temperature and fan speed of a convective impingement dryer (Müller et al., 2017).

The conclusions of the research showed that the drying rates should be as slow as possible from a binder migration point of view. However, from a technical and economical point of view, faster drying is preferred. The research of Müller et al. (2017) was not able to decide on a reasonable compromise and required more data to do this.

The drying rates were dependent on the temperature and fan speed. However, no information is presented based on the fan speed. What is given, are the drying rates for different temperatures. When putting these values in a graph, an almost linear trend is present. When choosing the lowest drying rates, e.g. 0.5g/m^{2}s, a 1mm thick sample with the size of 40mm by 50 mm, with the density of the binder of 1020 kg/m^3, leads to a drying time of 34 minutes. This is according to the following equation:

$$\text{Drying time in minutes} = \frac{\text{Length*Width*Thickness} * \rho * 1000}{\text{Length*Width*Drying rate} * 60} \tag{11.5}$$
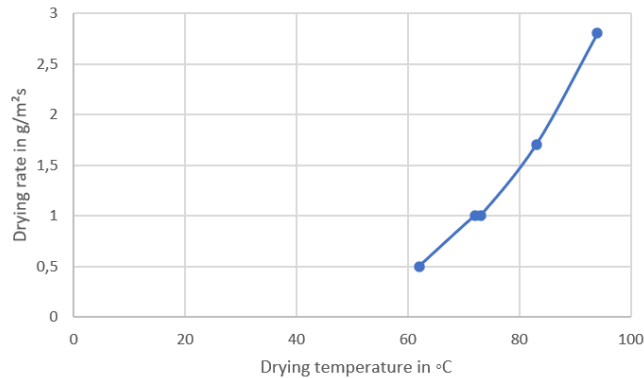
Figure 11.4: Drying rates (Müller et al., 2017)

However, what is obtained from the experiments is that drying times required were longer for the production of these samples. This is probably due to the higher dilution of the slurry preparation. To ensure the drying, the samples were dried per layer overnight in an oven at 70°C before depositing the next layer. It should be evaluated in the future how this influences the binder distribution.

11.6. Calendering

When using calendering, multiple changes occur within the microstructure of the coating itself and the adhesion strength of the coating onto the carbon steel. This was discussed in detail in Chapter 10. However, within the department of Mechanical Engineering, it turned out that there was not a calendering machine available which is similar to the ones explained in Chapter 10. The one that seemed similar turned out to be a rolling mill. A simple test with a hydraulic press caused the delamination of the coating. Therefore, the calendering process is not used within this thesis.

11.7. Commercially available coating

The other, commercially available, graphite coating is applied (spray coated). The coating, available from Kontakt Chemie, is defined as the Graphite 33 spray. Within the article, the thickness was determined by comparing the weights before and after the spray coating. Within the experiment in the article, approximately 3mg which corresponds to 5*10^{-3}mg/cm^2 was deposited onto the carbon steel (Piquot et al., 2019). This was a very thin layer of approximately 20μm.

11.8. Potential challenges

Fluoropolymer polyvinylidene difluoride (PVDF) is an organic binder. This binder is valued for its inertness, both thermal and chemical. Furthermore, it has excellent mechanical properties. Its molecule structure is shown in Figure 11.5. Fluoropolymers, in general, consist of a carbon backbone chain. This chain has multiple connected C-F bonds. These C-F bonds are the strongest possible single bonds to carbon. This is due to the electronegativity of the fluorine atom.
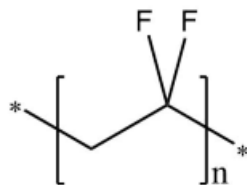
Polyvinylidene difluoride
(PVDF)

Figure 11.5: PVDF

However, this above-mentioned inertness has as a disadvantage that it is difficult to process. PVDF will not solve in many standard organic solvents. Known solvents of PVDF can be found in Marshall et al. (2021).

A disadvantage for the usage of this binder in the thermal storage application is the low melting temperature of 158-200°C. Substitutes for this binder, still part of the fluoropolymers, could for example be (Teng, 2012) (Marshall et al., 2021):

- Polytetrafluoroehtylene (PTFE) with a melting temperature of 317-345°C
- Polychlorotrifluoroethylene (PCTFE) with a melting temperature of 210°C
- Copolymer of fluorinated ethylene and propylene (FEP) with melting temperature 260-282°C
- Copolymer of tetrafluoroethylene and perfluoropropylvinylether (PFA) with melting temperature 302-310°C
- Copolymer of ethylene and tetrafluoroethylene (ETFE) with melting temperature 254-279°C
- Copolymer of ethylene and chlorotrifluoroethylene (ECTFE) with melting temperature 235-245°C

If even higher temperatures are encountered, inorganic binders may offer a viable solution. Nevertheless, careful consideration must be given to the potential thermal degradation of the binder.

Furthermore, as demonstrated by Müller et al. (2017) in the paper, a graphite coating exhibits a certain degree of porosity. The article highlights that this porosity has been reduced through the application of calendering. An important consideration is the impact of porosity on corrosion.

Open porosity and pinholes create a direct pathway between the corrosive environment and the substrate. This can result in rapid localized corrosion and pitting corrosion (Creus et al., 2000). Specific to graphite, literature shows attempts to decrease the porosity of a ceramic coating by reducing the size of the graphite grains which is added to this coating. The smaller sizes of the graphite could be settled in the pores of the coating. This gave a denser coating and showed better corrosion resistance (Lv et al., 2009).

11.9. Conclusion of coating composition and application method

The samples were prepared with the following procedure to samples with various thicknesses, up to a coating thickness equal to the bare sample thickness.

1. The PVDF will before usage be dried for 48h to decrease the ability of moisture being present in the PVDF.

2. The PVDF and NMP mixture is prepared with 10 wt% PVDF. This mixture is stirred overnight for at least 24 hours to completely dissolve the PVDF. This is done by making use of a magnetic stirrer.

3. The graphite is put in a beaker glass

4. The NMP, excluding the NMP present in the binder solution, is added and stirred

5. The binder solution is added to the graphite

6. Again the solution is stirred

7. One sample is coated with the commercially available spray coating and dried overnight. All the other samples can neglect this step.

8. The samples dipped into the slurry and withdrawn with a speed of 0.1 mm/s

9. The samples are dried overnight in the opposite direction to the dipping direction in an oven at 70°C

10. If required the process is repeated the next day with a new slurry

12

Measurement technique

Within this section, the experimental setup is presented. These experiments are executed to see how the thermal conductivity of carbon steel changes by applying a graphite coating.

12.1. Measurement equipment

In Appendix D, different thermal conductivity measurement methods can be found. Due to limited options at the TU Delft, a first attempt is done with the available device at Mechanical Engineering. This device is shown in Figure 12.1.

1 Measuring Point Switch	11 Thermometer (2x)
2 Master Switch	12 Overflow
3 Voltmeter	13 Regulation Valve for the Flow Rate
4 Ammeter	14 Specimens
5 Adjusting Transformer	15 Heater
6 Heater Switch (ON)	16 Cooler
7 Tank for Constant Water Pressure	17 Dewar Vessel
8 Inlet Valve	18 Clamping Device
9 Electric Heater Connection	19 Plates for Hindering Convection
10 Thermocouple Sockets (4x)	

Figure 12.1: Measurement device available at TU Delft.

In this device, the specimen is placed with a heater positioned on top. This heater can be regulated by the adjusting transformer to determine the power. The voltage and current can be read from the voltmeter and ammeter. At the bottom, named the cooler in the Figure, flows water. The water flow is regulated by a valve. This flowing water extracts the heat at the bottom of the specimen in order to have a constant temperature at the bottom. This will increase the temperature of this water. The increase in temperature of the water can be read from the two thermometers, both before the water passes the specimen and after the water has passed the specimen. The device has two copper cylinders provided with it. The copper cylinders are equipped with small apertures at both the top and bottom, providing locations for the placement of thermocouples. A schematic is shown in Figure 12.2. The thermocouples measure the temperatures at both ends of both cylinders. In this Figure also the energy distribution is shown. The differences between the energy supplied by the heater and the energy extracted at the bottom by increasing the water temperature are losses. These losses originate from radiation, convection, conduction, and thermal contact resistance.
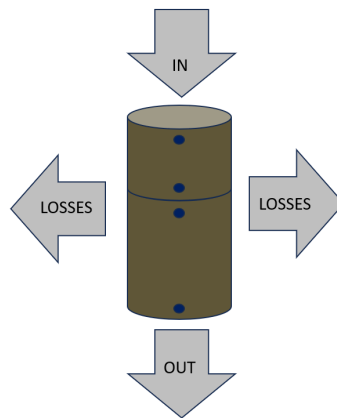
Figure 12.2: Global heat transfer balance across copper test sample.

In an ideal situation is the system in steady-state with at the top a constant hot temperature and at the bottom a constant cold temperature and is the energy input equal to the energy extracted at the bottom. The thermal conductivities of both cylinders can be determined based on the measured temperatures due to the four thermocouples and the distance between the thermocouples. Furthermore with the use of these two cylinders also a determination of the thermal contact resistance can be made.

To determine the thermal conductivity of the samples created in this thesis, will these samples be placed between the two copper samples with known thermal conductivity.

However, based on the first tests, with solely copper cylinders, it became clear that the device is not working as it should. Losses were around 70% and even the use of a vacuum shield did not decrease this considerably. Furthermore, by testing multiple times also different results were obtained for the thermal conductivity of the copper itself. Based on these losses in combination with the non-reproducibility of the results, is this measurement method excluded.

Hitherto, no other applicable measurement device is found at the TU Delft. Hence, there was a need to explore the possibility of engaging an external organization to conduct measurements on the samples.

After exploring various measurement companies, Linseis, a commercial company, was found. This company has previously performed tests for a thesis research. The measurement method was a Laser Flash Analyzer (LFA). Linseis required sample sizes which were either an approximate diameter of 25 mm. The LFA measurement method can be found in the appendix in more detail. The samples were selected to have a diameter of 23 mm to accommodate space for coating on the sides. However, after some time the University of Padova also gave a viable solution to measure the thermal conductivity with the Hot Disc Method, also known as the Transient Plane Source (TPS) method. Again, a brief explanation can be found in the Appendix.

To choose the direction, the two measurement techniques are compared. Within the LFA method, the specific heat capacity of the material should be determined at first. Furthermore, the density of the material is required. For the transient plane source, no additional measurements are required. The density of the coating cannot be determined with high accuracy. This is due to the evaporation of the solvent in combination with the unknown porosity of the coating. The specific heat capacity of the coating will be measured at Linseis for solely the coating, but again determining the specific heat capacity of the carbon steel in combination with the coating for all the samples will unavoidably lead to losses in accuracy. In addition, should the note be given that the tests in total were expensive, approximately €1800.

The combination of the price and uncertainty of the measurement method led to the choice of measuring the University of Padova. Because of time limitations, the decision has been made not to create new sample sizes. It should be noted that these sample sizes were not the perfect sample sizes for the measurements within the TPS. In addition to the brief explanation in the Appendix, a more extensive explanation of the TPS will be provided below.

12.1.1. Transient plane source method

The TPS is known for its wide range of thermal conductivity values (0.05-500W/mK) that could be measured in combination with short measurement times in comparison to steady-state methods. Within the TPS method, two identical samples are required. These are placed on top of each other with the sensor, shown in Figure 12.3a, in between. All the other surfaces of the sample are thermally insulated. This sensor acts also as electrical resistive heater. It consists of a bifilar spiral pattern in combination with a supporting material, in the case of Figure 12.3 it is Kapton (Ahadi et al., 2016). Kapton is a thermoplastic polymer primarily used for its exceptional heat resistance and insulating properties. The samples are heated by Joule heating. Through resistance thermometry, the temperature rise in the sensor is accurately monitored by recording the increase in the resistance of the metal sensor over time. By analyzing the temperature rise, can the thermal properties of the sample be determined (Zheng et al., 2020).

(a) (b)
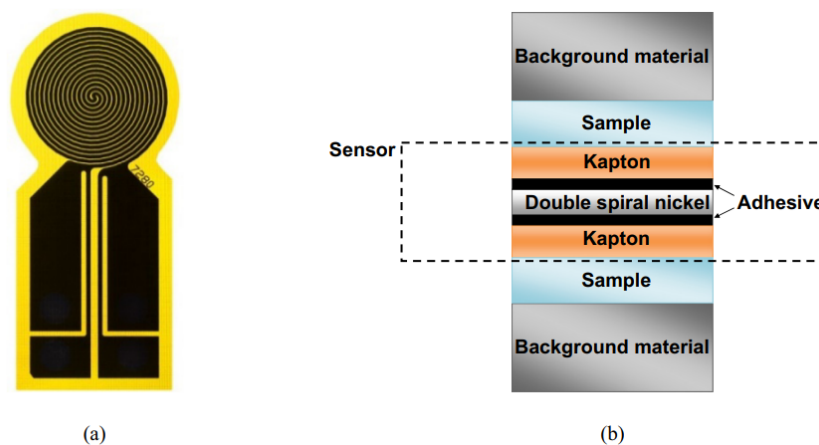
Figure 12.3: TPS sensor (left) and schematic of test column (in this case thin film test) (right)(Ahadi et al., 2016)

The thermal conductivity is determined based on the recorded temperature and electrical resistance, this can be found in the Appendix D.

The effective thermal conductivity conducted from the measurement includes (Ahadi et al., 2016):

- Bulk thermal resistance of the sample
- Thermal contact resistance between sample and sensory
- Thermal contact resistance between the adhesive and Kapton layer
- Thermal contact resistance between adhesive and double spiral nickel
- Thermal contact resistance between sample and background material (if present)

The behaviour inside the sample is neglected and the sample is treated as a whole. This exclusion represents, for example, the thermal contact resistance from coating to carbon steel. What should be noted is that there is literature present that modifies the TPS measurement, for thin films, in order to exclude the thermal contact resistance (Ahadi et al., 2016).

13

Results coating

13.1. Sample results

First, the coated carbon steel samples are shown. The uncoated samples had the dimensions shown in Figure 13.1.
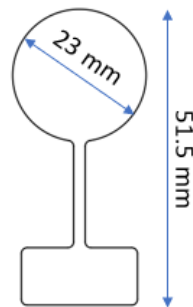
Figure 13.1: Sample size. The thickness of the sample is 2mm.

The coated samples are shown in Figure 13.2.
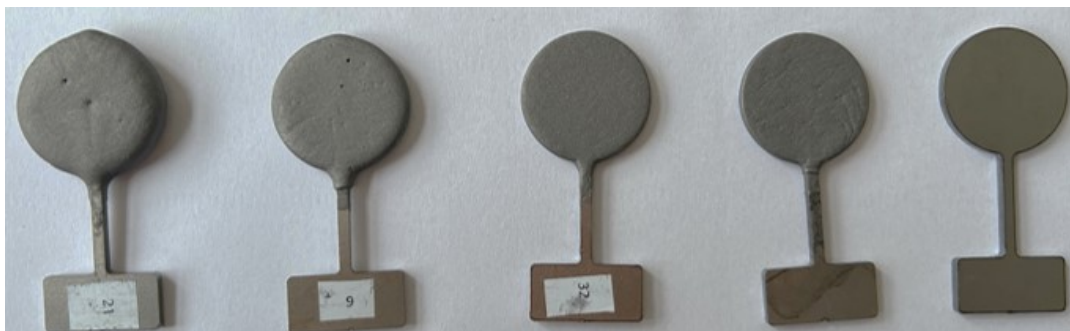
Figure 13.2: Coated samples. From left to right: 4 layers, 3 layers, 2 layers, 2 layers+commercial coating and bare sample.

	Bare sample	2 layers	3 layers	4 layers	2 layers*
Thickness [mm]	1.98	2.53	3.75	6.40	2.30
Weight [mg]	10146	10340	10550	11320	10170

Table 13.1: Thickness and weight samples where the *represents the two-layer coating with commercial spray coating beneath.

What is noted, based on the results of Table 13.1 is that the thickness and weight of the 2 layers*, which is the commercial coating with on top two layers of homemade graphite coating, is thinner and lighter than solely two layers. Thus, it can be concluded that the coating the homemade graphite coating on top of the commercial coating shows less binding.

13.2. Thermal conductivity improvement

Unfortunately, due to the not perfectly smooth surface of the samples, measurements could not be conducted with the use of the TPS method. Therefore, no experimental results are obtained. However, based on the resistance model from Chapter 10, the thermal resistances are calculated, shown in Figure 13.3. It is assumed that the thermal resistance from layer to layer for both coated carbon steel as well as stainless steel is the same. The three lines indicate the following:

- Reference 1, is the thermal resistance based on stainless steel with a sample thickness of 2 mm and diameter of 23 mm and is thus constant.
- Reference 2, is the thermal resistance based on stainless steel which increases its size and diameter at the same rate of the coated samples.
- Coated material, is the thermal resistance based on the, with graphite coated, carbon steel calculated with the resistance model.
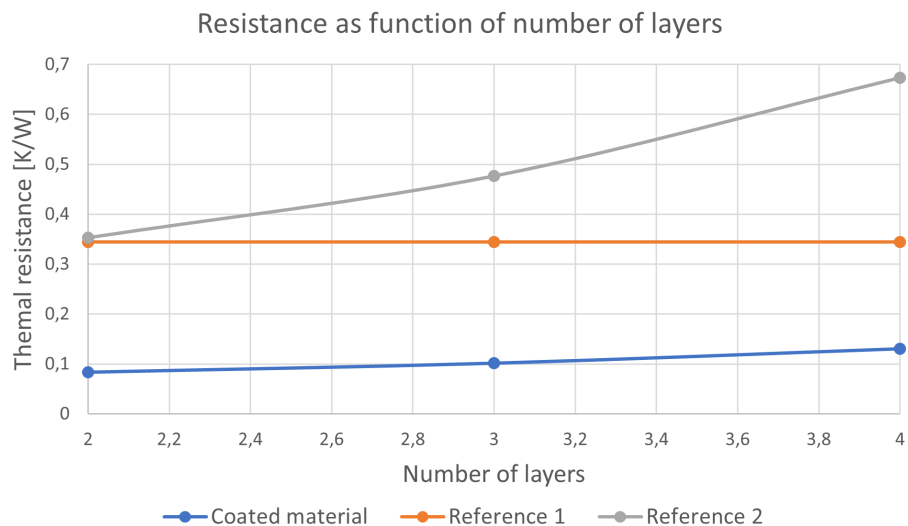
Figure 13.3: Thermal resistance as a function of the number of coating layers (2-4) for the coated sample, reference 1 and reference 2.

The reason why both reference 1 and reference 2 are shown in Figure 13.3 is to see the difference between the thermal resistance of the coated material with a 2 mm sample as well as with a sample which is the same thickness. By comparing the coated sample to Reference 2 can the decrease in thermal resistance be extracted when the coated sample, in total, reduces its size and thereby equal sizes are obtained, i.e. the graphite coating takes the place in of part of the base carbon steel material.

A slight increase in thermal resistance is observed with increasing number of layers. However, when comparing to reference 2, the differences are becoming larger, which is positive, for more layers. This indicates more gain in heat transfer in comparison to the stainless steel sample with similar sizes.

13.3. Coating surface roughness

An attempt is made to reveal the surface structure and roughness of the coating. This is done with the microscope available at the separation lab at the TU Delft.

First, the thickest sample (4 layers), is the 10x magnification and the 40x magnification shown in Figure 13.4. To be able to define the surface roughness with microscopic images, the focus first needs to be on the top of the surface roughness followed by focusing on the bottom. The working distance for focusing on an object is namely constant while using the same lens. Although Figure 13.4 shows an area scan, which encompasses multiple separate pictures, for a single scan no clear distinction could be made between top and bottom. This was only clearly visible for a sample with a single layer of graphite. An example of the focus on the top and bottom is shown in Figure 13.5. For four measurements, this resulted in a range of 5.4μm to 13μm.
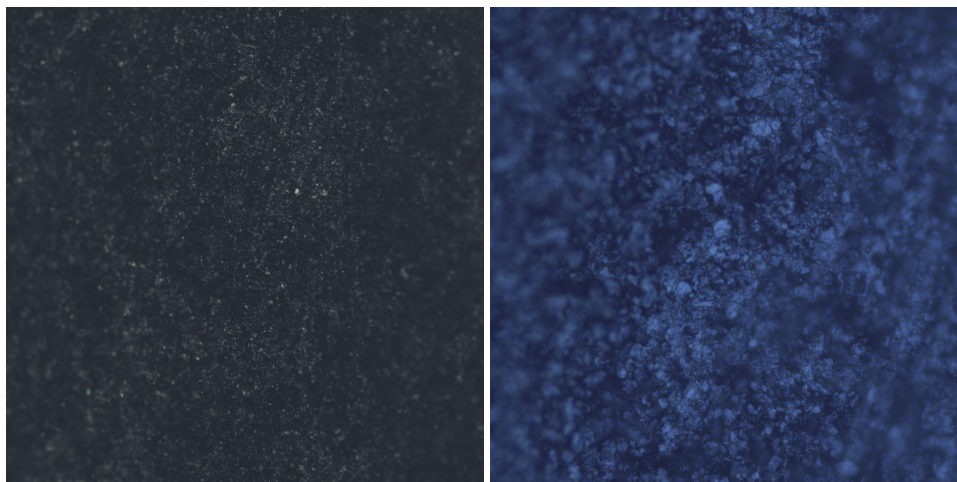
Figure 13.4: Microscopic image of coating (4 layers) with 10x magnification (left) and 40x magnification (right).
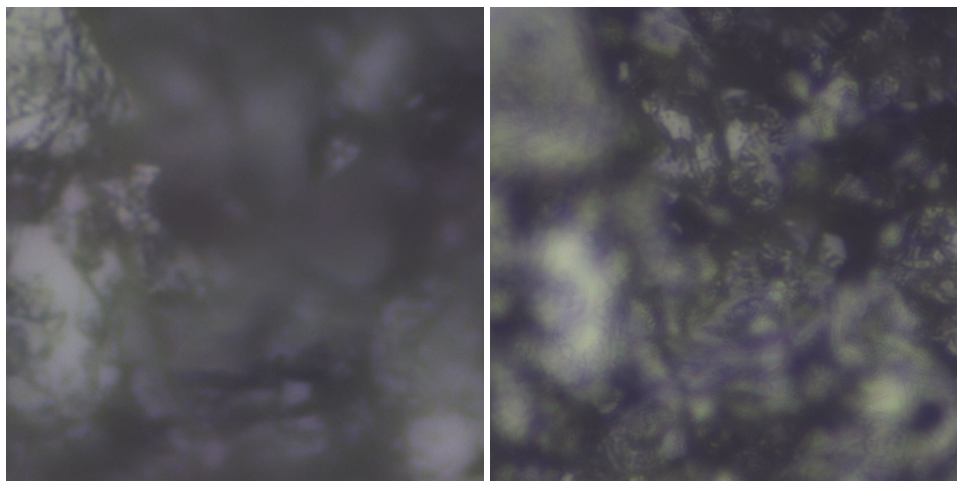
Figure 13.5: First focus at -22340.4 μm (left). Last focus at -22353.4 μm (right). Both with the same focus distance.

The cause of the difficulties of measuring the roughness for the four-layer coating, could be:

- Better total coverage when compared to a single layer, thus less contrast could be observed.
- The unevenness of the sample increases per layer of coating. Thus it had a gradient from itself when compared to the single-layer sample. This could influence the measurement.

Furthermore, this is a very qualitative measurement since it is not known what is specifically observed in the measurement. In future research, other surface roughness measurements could give better results. These measurements should be executed with a sample that is coated on one side to exclude the effect of the unevenness of the other side. For example, the use of a contact profilometer. However, it should be evaluated if the coating is hard enough for this measurement. If not, the contact profilometer would damage the coating and not give accurate results. Other options could be the use of a non-contact, optical profilometer, or the use of other measurement techniques based on optical interferometry (Y. Wang et al., 2017).

14
Conclusions

"How might thermal energy storage be implemented within the food industry?"

The research question will be addressed by answering the corresponding sub-questions.

What is the typical steam demand profile observed in the food industry? And how could thermal energy storage be applied?

In the food industry, steam demand typically exhibits significant fluctuations attributable to batch processes. The steam demand pressure ranges between 4 to 20 bar, depending on the application. To analyze this fluctuating pattern, an average week is considered. Two categories of energy storage systems are examined. The first entails a stand-alone thermal energy storage (TES) capable of continuously supplying steam for a chosen number of hours. In this study, a stand-alone energy source for 12 hours is analysed. To design such a storage system, the 12 consecutive hours with the highest steam demand during the average week, are selected, resulting in a storage capacity of approximately 80 MWh. This capacity is based on the enthalpy difference of the product, steam at 11 bar, and the feed water. The second type of storage system focuses on peak shaving. Storage is intended to accommodate the peaks in steam demand by discharging the storage with as goal, decreasing the standard steam generating equipment, the boiler. Initially, the mean steam demand for the average week is evaluated. This average value serves as the baseline for steam generation originating from the boiler available. When assuming a start capacity, the fill level of the storage, the cumulative sum of surpluses and deficits results in a storage requirement of approximately 40 MWh based on the average week. However, it is important to note that when extrapolating this approach to annual data, the storage requirement increases to 120 MWh due to inadequate alternation between surpluses and deficits. However, the value determined for the average week, 40 MWh, is assumed to represent the energy capacity of the peak shaving TES system within this thesis.

Which thermal storage materials show promise for integration within the food industry?

Preceding this thesis, a comprehensive review of the literature was conducted to examine thermal energy storage materials capable of generating steam pressures ranging from 4 to 20 bar. Materials were screened based on their discharge temperature, which must be sufficient to produce steam at the highest pressure, approximately 212°C. Three primary, suitable, categories emerged: liquid sensible, solid sensible, and phase change materials. Although phase change material (PCM) storage is comparatively less mature than solid and liquid sensible storage systems, this thesis continues to explore this material due to its potential advantages. In consultation with Arcadis, one material from each category was chosen to assess its potential. This analysis identified slag, a waste product of industrial processes, as a viable candidate from the solid sensible materials. Molten salt, was identified from the liquid sensible category. Phase change salts, while relatively underdeveloped, were considered as latent storage material, due to their phase change temperature range.

Which storage method is most relevant for each material, and what are the corresponding key parameters?

The design focus is predominantly on the discharging aspect for the storage materials. This emphasis is dictated by the scope outlined by Arcadis, which directs the research toward energy storage and its conversion into steam. Consequently, the question of what the energy source is for charging the storage, is excluded. As a result, addressing the intermittency of charging energy is not feasible.

Steel slag is a material that is a waste product from industry. The size of the slag can be adjusted. In literature, the slag is often employed as thermal energy storage material in a packed bed system. This system shows compatibility with multiple heat transfer fluids (HTFs), however, experimental validated results were focused on air as HTF. Therefore, a packed bed with air as HTF is chosen for further analysis. Parameters that determine the effectiveness of this storage are the maximum temperature of the slag at the end of the charging, the tolerance of the HTF outlet temperature, the aspect ratio of the storage tank, the diameter of the pebbles, and the fluid velocity of the HTF.

For phase change salts, various energy storage options are found in the literature. The most well-known, and therefore adopted, is the shell and tube configuration where the salt is located in the shell. Various HTFs can be used in the tubes. The parameters determining the efficiency are the type of phase change salt, the type of HTF, the choice for horizontal or vertical storage, the diameter and length of the shell and tube, the number of tubes, the mass flow rate of the HTF, and inlet temperature of the HTF.

Molten salt's most relevant storage solution is a two-tank storage, one cold and one hot tank, where the salt itself is used as HTF for the subsequent processes. Both tanks should, for safety reasons, be able to store all the salt. Thus, two identical tanks should be designed. Since the tanks solely act as storage and no heat transfer to the HTF exists in this configuration, the main focus needs to be on quantifying and minimizing the thermal losses. These losses should be compensated to prevent the solidification of the salt.

To what dimensions does this lead for thermal energy storage systems?

After analyzing the values for the key parameters, based on literature focusing on parametrization, the thermal slag results in a storage for the stand-alone case, of approximately 340 m^3 and 740*10^3 kg. Analyzing the peak shaving case in more detail showed that for the steel slag, this type of storage is not applicable. This is due to the decrease in efficiency when the storage is not completely charged or discharged in combination with the absence of a clear pattern in the steam demand.

For the phase change salt shell and tube configuration, limited and inflexible experimental research is found on the discharging performance of large-scale storage. Therefore, a semi-empirical model is built. This model is based on experimental research of a small-scale multi-tube shell and tube storage. In the model, the salt, the HTF, the sizes of both the tubes and total storage, and the mass flows can be adjusted to generate predictions on the HTF outlet temperature. This, together with the mass flow determines the discharging power of the system. The salt used in this thesis is a commercially available salt which changes phase at 500°C. The HTF is a high temperature thermal oil. This results in, for the stand-alone case, a storage of approximately 369 m^3 and a mass of 802*10^3 kg. For the peak shaving, experimental results regarding the alternating partly charging and discharging should first be tested in the model before conclusions can be drawn.

The volume of the two-tank molten salt storage is, for both tanks, 560 m^3. The salt weight for both tanks together is 478*10^3 kg. For the peak shaving case, this results in a total volume of 314 m^3 and a salt weight of 259*10^3 kg.

How is the discharged energy converted into steam for the respective materials?

Initial design estimations for the HTF exiting the thermal storage to evaporate water at 11 bar have been conducted for slag and molten salt with the use of an iterative process. For phase change salt, validation of outcomes from the semi-empirical model is deemed necessary before proceeding with similar analyses. The design focuses on identifying the most cost-effective shell and tube evaporators, with the HTF on the shell side. For the air originating from the steel slag storage, the optimization process involved balancing pumping power against the CAPEX. This optimization resulted in a CAPEX of approximately k€96, along with pumping energy costs total around k€60 per year. In contrast, for molten salt, pumping costs were significantly lower, with CAPEX being the primary cost factor. The minimum CAPEX was identified at approximately k€22, accompanied by negligible pumping costs.

What approaches can be adopted to accelerate the market readiness of phase change salts?

As previously mentioned, phase change salt currently lags, in comparison to sensible storage, in its application as thermal energy storage, primarily attributed to its low thermal conductivity, which limits its discharge power. To address this limitation and explore cost-effective thermal conductivity enhancement methods, a rolled mesh made of stainless steel has been identified. This mesh is implemented at the shell side, where the phase change salt is located in a shell and tube heat exchanger. The readily available mesh in combination with the low price could contribute to the market readiness of the phase change salts in comparison to more expensive thermal conductivity enhancement methods such as metal or graphite foams. However, the stainless steel mesh in the phase change salt was eventually prone to corrosion and has limited thermal conductivity. To further improve this enhancement technique, tests regarding the use of a graphite coating are undertaken. The graphite coating is based on another application area, Lithium-ion batteries, where a graphite layer enables the intercalation of Lithium ions between the different graphite layers and is modified for the use in thermal storage systems. A graphite coating holds the potential to improve the viability of carbon steel as a mesh material by potentially reducing corrosion, which is proven for other graphite coatings. Carbon steel has approximately a 3-4 times higher thermal conductivity compared to stainless steel which could increase the effect of the mesh on the heat transfer performance of the phase change storage. Additionally, the high thermal conductivity of the graphite coating itself could contribute to the heat transfer of the total system by enhancing the heat transfer within each mesh layer.

What are the effects of implementing these potential improvements?

The effect of the graphite coating regarding the decrease in thermal resistance is based on a thermal resistance model from mesh layer to mesh layer in the radial direction. For different layer thicknesses (0.28-2.21 mm), coated on 2 mm carbon steel, the results are compared to two reference materials. The first is a stainless steel sample with a constant thickness of 2 mm and the second is a stainless steel sample with a thickness equal to the coated sample, thus also increasing in thickness. The decreases in thermal resistance ranges respectively between 2.6-4.1 and 4.2-5.2. However, no experimental measurements could be conducted to verify the expected results.

15

Discussion and Recommendations

For the first chapters, where the thermal storage and steam generating systems are designed, the discussion is mainly focused on the fact that the design was based on literature and not on experiments. This leads to inflexibility of the design. It would have been more correct to make a design, which is experimentally validated. However, due to time constraints in combination with the lack of a test set-up, this was not possible. Furthermore, the focus was on the configuration of thermal storage, for the three materials, with the highest grade of research, so the most well-known storage technique. However, other storage solutions could have provided other results.

In this thesis, determining the storage size, in MWh, was based on an average week steam demand. When the method was extrapolated for the annual data, this did result in much larger storage sizes. This is caused by the absence of a clear pattern in steam demand. In further research the extrapolation to the annual steam demand should be explored with, for example, a back up boiler or multiple thermal storages.

The utilization of literature findings was necessary as said before. For instance, regarding steel slag, the heating process typically extends to a temperature of 700°C in literature, although temperatures up to 1000°C are feasible when combined with air. Nonetheless, such elevated temperatures might require adjustments in unconventional storage materials. Conducting tests to evaluate the impact of these factors on the results obtained from the literature regarding steel slag storage could be useful. Additionally, an assumption was made for slag storage that approximately 12.5% of the tank is unable to discharge or charge based on the discharging strategy. However, it is imperative to assess the accuracy of this assumption, particularly when considering specific application scenarios where the tolerance of the HTF outlet is larger. Moreover, given that steel slag has demonstrated compatibility with various HTFs, it is worthwhile to explore the storage design possibilities utilizing these alternative HTFs.

In the domain of phase change salts, a prospective area for future advancement involves establishing a standardized method for measuring the properties of these salts. The values for these properties, for example the specific heat capacity, are now in a widespread range present in literature.

For the semi-empirical model, based on the phase change salt experimental research, it should be noted that the key parameters do not correspond to the optimal values as found in literature. This could be explored in future research. Furthermore, the model is manually adjusted based on two variables. These variables are the fraction of energy that goes to solidification and to cooling for each solidification phase and the degree of turbulence in the tubes along the length of the tubes. This resulted in the HTF outlet temperature pattern which is comparable to the reference paper. However, the mean salt temperature showed a slightly different pattern. In the model, the solidification at a constant temperature could be observed in comparison to the reference paper where an almost linear decrease in mean temperature of the salt is present. This could be caused by the simplification of the model and could be optimized in future research.

Another assumption that could generate other results is the tolerance of the HTF outlet temperature. Other tolerances could result in different feasible storage dimensions, based on the semi-empirical model. Furthermore, it should be assessed what the influence of scaling the results for a single tube to multiple tubes with larger size is on the outcomes in practice. This should be done by large-scale testing.

Regarding the molten salts, assumptions have been made regarding the temperatures of the hot and cold tank. These are assumed to be within the limits of the salt, i.e. 200 and 565°C. However, this cold tank value is a bit critical. The prevention of solidification will be of utmost importance around this temperature. Another reason to adjust this temperature is based on the outlet temperature of the molten salt from the steam generator, which will be hotter than 200°C. The higher temperature is expected to result in a small increase in thermal losses for the cold tank in combination with a larger volume of the two tanks. The last is causes by the lower temperature difference between the hot and cold tank.

Another choice, which could have been made differently, is how to handle heat losses for the three systems. For the steel slag and the phase change salts, the heat losses resulted in a larger volume of storage since these heat losses are chosen to be covered by the storage itself. However, for the molten salt, the choice is made differently. This is done since the heat losses of the molten salt should be compensated directly to prevent solidification of the molten salts. For the phase change salts, which could also solidify, this is of less importance since the system can handle solidified salts.

Regarding the evaporation section, the decision has been made to preheat the feed water (≈ 100°C to ≈ 180°C) for both slag storage and molten salt storage, directing it to a steam drum. From there, the water (≈ 180°C) is transferred to the shell and tube evaporator. Subsequently, the steam is returned to the steam drum where, if necessary, any remaining water in the steam could be separated using, for example, a cyclone. Alternatively, the water could be heated and evaporated in the same shell and tube evaporator, eliminating the need for the HTF bypass and steam drum. This aspect should be evaluated during the design of the storage solutions. Phase change salts are not discussed in this section since this storage design does not involve the evaporation process in this thesis.

Focus for further research should be on exploring different types of renewable energy sources and options, compatible with these thermal storage systems, to evaluate the actual potential op implementing thermal storage solutions in industry.

The subsequent discussion points refer to the part of this thesis where the coating is created and the results of this coating are obtained. This is divided into subjects.

Coating choice
The first discussion point, focused on the coating choice, is regarding the type of coating. This is a graphite coating, where calendering was eventually not used. The porosity of the original coating was known. However, some adjustments with respect to the reference coating are made. These include the dilution and coating composition adjustments with respect to the reference coating. Furthermore, the mixing is done by hand and magnetic stirrer in contrast to the laboratory immersion mixer. Furthermore, the degassing step is excluded. The effects of excluding this step are not known. The influences on the porosity of this coating are unknown and should be evaluated in future research. In addition, the influence of the porosity on the corrosion resistance potential of the coating should be evaluated.

The binder present in the coating of the reference paper, PVDF, cannot withstand high temperatures. The replacement of this binder is interesting for potential research. The effect of the new binder on the thermal conductivity as well as the binding to the carbon steel should be evaluated.

The combination of the discussion points mentioned above, the unknown corrosion resistance, the exclusion of components of the reference paper, and the binder which is not heat resistant, led to the question if another coating composition would have been better. However, it should be noted that this is the first step in finding a possible graphite coating to coat a mesh. Some first results regarding the thermal conductivity influence are required to be able to determine the next steps. Therefore, it was chosen to continue with this coating. Future research could be focused on finding other coatings or even high conductive corrosion resistance materials that do not require a coating.

Application of coating on carbon steel
The application of the coating could also be done with different application methods. Dip coating did not result in a perfect reproducible, smooth coating layer, even at low withdrawal velocities. The dilution could be further optimized or other coating techniques could be tested. The coating is now applied on a flat round plate. Further research should also focus on how to be able to dip coat a mesh, both on a small and large scale.

The next point of discussion is regarding the wt% of the binder in the coating across various layers. Future research should investigate whether maintaining uniform binder wt% across different layers is necessary. The distinction between the initial layer and subsequent layers lies in the surfaces they are intended to bind to, namely carbon steel or another layer of graphite coating. While some binder wt% is necessary in each layer to bind the graphite in the coating together, there is potential for optimization over the layers.

Calendering was, due to the lack of an available calendering machine, not done. By executing this step, three influences are found. The first is the already mentioned, possible influence on the corrosion resistance of the coating based on the porosity. The second is based on the influence of thermal conductivity due to calendering the coating. The third is regarding the binding to the carbon steel. It should be evaluated if the binding increases or decreases upon calendering. It is expected that it will increase based on the literature. However, what should be noted in general regarding calendering, is that if the coating is applied on a mesh, it is not possible to calender the coating due to the structure of the mesh.

In this thesis it is tried to determine the surface roughness of the coating that is applied on carbon steel, with the use of a microscope. However, difficulties were found in measuring the coating which is dipped multiple times. Therefore, only a single-layer coating on carbon steel is measured. Future research could improve these measurements by the use of either contact or non-contact surface profile measurement techniques.

Measurement method
External measurements of the thermal conductivity of the coating do not provide a complete insight of the methods employed or how the results are obtained. It is recommended for future research to use a measurement method that can be conducted by the researchers themselves. This would enable adjustments to the research approach during the study. For instance, intermediate measurements related to the drying temperature, under the assumption that binder distribution affects thermal conductivity, could have altered the coating application approach. Such adjustments could potentially elevate the results to a higher level.

Additional aspects discussed in the measurement method section revolve around the transient plane source (TPS) method. Firstly, the sample sizes were determined based on the Laser Flash analysis (LFA) technique and were comparatively small for measuring with TPS. Typically larger sample sizes are used for this TPS technique, available at the University of Padova. This discrepancy might introduce inaccuracies. Secondly, attention is drawn to the surface of the sample. Ideally, a flat surface is preferred within the TPS measurement method. Achieving this was unsuccessful when employing the dip coating technique. Consequently, this led to the inability of performing the measurements. Future research could be focused on generating larger samples with more flat surfaces in order to be able to measure with the TPS method.

Based on the measurement of the thickness in combination with the withdrawal speed of the dip coater, no conclusion regarding the viscosity of the coating could be found. However, if the coating finds an application in thermal energy storage, all the thermophysical properties, in addition to the viscosity, of the coating should be evaluated.

Based on the inability of measuring at the University of Padova, the expectations of the thermal conductivity are based on the resistance model. In this resistance model, multiple assumptions are made. The first is the assumption that the thickness of the graphite coating layer results in perfect contact in the resistance model and that the thickness of the coating is uniform on all surfaces. Another assumption is the thermal conductivity of the graphite coating. The focus for future research should be on quantifying the exact thermal conductivity of the graphite coating. Based on the similar estimation for the thermal conductivity of the graphite coating, the thermal contact resistance from coating to carbon steel is determined. Although this contact resistance from coating layer to carbon steel was in the range compared to literature and together with the fact that it will probably not reduce the heat transfer significantly, it could still be evaluated in future research. Furthermore, the thermal contact resistance from mesh layer to mesh layer should be determined.

Implementation of coated mesh
Regarding the implementation of the coated mesh two main discussion points are present: the coating stability and the heat transfer direction.

The coating stability should be evaluated in combination with phase change salts. The coating on the carbon steel did bind quite well at first sight. However, upon uniform compression by a hydraulic press, the coating did show delamination from the carbon steel. The phase change of a material is often accompanied by volume changes. These volume changes can result in some pressure on the coating. These are expected to be lower than the pressure from the hydraulic press, however, it should still be evaluated what are the influences of these volume changes on the stability of the coating and if methods, such as calendering, increase the binding.

Another focus for future research could be on the final ratios between of the graphite coating and carbon steel base material. Thicker coating layers, compared to similar dimensions of stainless steel, led to better results. However, this would occupy more space from the phase change salt. Therefore, an optimal thickness of the coating and base material, which together provide the highest thermal conductivity in combination with the required strength, should be evaluated in future research.

The direction of heat transfer is another point of discussion. The study is based on a rolled mesh, which has already demonstrated improvements in thermal storage performance. This suggests that enhancing this mesh through coating, and thereby allowing for the use of other base materials, could contribute to this solution. Numerical research also indicates that upon coating a thermally conductive coating on a periodic structure, significant improvements can be achieved by transferring heat through the coating. This implies a solution akin to a coated periodic structure rather than a rolled mesh. However, the mesh was chosen as a viable option due to its cost-effectiveness. Thus, this thesis investigates a mesh that is first coated and then rolled. Nevertheless, it is noted that there is potential to achieve a structure similar to the periodic structure by first rolling the mesh followed by coating it as a whole. Exploring the feasibility and effects of this approach, could be intriguing topics for future research. Furthermore, it may be worthwhile to initially assess the results of thermal conductivity overall improvement in discharging performance for the mesh.

References

Agyenim, F., Hewitt, N., Eames, P., & Smyth, M. (2010). A review of materials, heat transfer and phase change problem formulation for latent heat thermal energy storage systems. *Renewable and Sustainable Energy Reviews*, *14*(2), 615–628. https://doi.org/https://doi.org/10.1016/j.rser.2009.10.015

Ahadi, M., Andisheh-Tadbir, M., Tam, M., & Bahrami, M. (2016). An improved transient plane source method for measuring thermal conductivity of thin films: Deconvoluting thermal contact resistance. *International Journal of Heat and Mass Transfer*, *96*, 371–380. https://doi.org/https://doi.org/10.1016/j.ijheatmasstransfer.2016.01.037

Ahmed, A., Esmaeil, K. K., Irfan, M. A., & Al-Mufadi, F. A. (2018). Design methodology of heat recovery steam generator in electric utility for waste heat recovery. *International Journal of Low-Carbon Technologies*, *13*(4), 369–379. https://doi.org/10.1093/ijlct/cty045

Ahmed, S. F., Khalid, M., Rashmi, W., Chan, A., & Shahbaz, K. (2017). Recent progress in solar thermal energy storage using nanomaterials. *Renewable and Sustainable Energy Reviews*, *67*, 450–460. https://doi.org/https://doi.org/10.1016/j.rser.2016.09.034

Al-Ajlan, S. A. (2006). Measurements of thermal properties of insulation materials by using transient plane source technique. *Applied Thermal Engineering*, *26*(17), 2184–2191. https://doi.org/https://doi.org/10.1016/j.applthermaleng.2006.04.006

Alofi, A., & Srivastava, G. (2013). Thermal conductivity of graphene and graphite. *Physical Review B*, *87*(11), 115421.

Angelini, G., Lucchini, A., & Manzolini, G. (2014). Comparison of thermocline molten salt storage performances to commercial two-tank configuration [Proceedings of the SolarPACES 2013 International Conference]. *Energy Procedia*, *49*, 694–704. https://doi.org/https://doi.org/10.1016/j.egypro.2014.03.075

Ansys. (2020). *Internal convection: Correlations and enhancements*. Retrieved December 24, 2020, from https://courses.ansys.com/wp-content/uploads/2021/02/S1-LT4-C3-L2-Handout-NT-v2.pdf

Asenbauer, J., Lisemann, T., Kuenzel, M., Kazzazi, A., Chen, Z., & Bresser, D. (2020). The success story of graphite as a lithium-ion anode material – fundamentals, remaining challenges, and recent developments including silicon (oxide) composites". *Sustainable Energy Fuels*, *4*, 5387–5416. https://doi.org/10.1039/D0SE00175A

Badenhorst, H. (2019). A review of the application of carbon materials in solar thermal energy storage [Thermal Energy Storage for Solar Applications]. *Solar Energy*, *192*, 35–68. https://doi.org/https://doi.org/10.1016/j.solener.2018.01.062

Bauer, T., Odenthal, C., & Bonk, A. (2021). Molten salt storage for power generation. *Chemie Ingenieur Technik*, *93*. https://doi.org/10.1002/cite.202000137

Beek, J. (1962). Design of packed catalytic reactors (T. B. Drew, J. W. Hoopes, & T. Vermeulen, Eds.). *3*, 203–271. https://doi.org/https://doi.org/10.1016/S0065-2377(08)60060-5

Bergman, T. (2011). *Fundamentals of heat and mass transfer*. Wiley. https://books.google.nl/books?id=vvyIoXEywMoC

Berni, A., Mennig, M., & Schmidt, H. (2004). Doctor blade. In M. A. Aegerter & M. Mennig (Eds.), *Sol-gel technologies for glass producers and users* (pp. 89–92). Springer US. https://doi.org/10.1007/978-0-387-88953-5_10

Bhatnagar, P., Siddiqui, S., Sreedhar, I., & Parameshwaran, R. (2022). Molten salts: Potential candidates for thermal energy storage applications. *International Journal of Energy Research*, *46*(13), 17755–17785. https://doi.org/https://doi.org/10.1002/er.8441

Broekman, M. (2023). Milieuhygienische kwaliteit ld-staalslakken. literatuurstudie. https://doi.org/10.21945/RIVM-2022-0180

Cabello Núñez, F., López Sanz, J., & Zaversky, F. (2019). Analysis of steel making slag pebbles as filler material for thermocline tanks in a hybrid thermal energy storage system. *Solar Energy*, *188*, 1221–1231. https://doi.org/https://doi.org/10.1016/j.solener.2019.07.036

Calderón-Vásquez, I., Segovia, V., Cardemil, J. M., & Barraza, R. (2021). Assessing the use of copper slags as thermal energy storage material for packed-bed systems. *Energy*, *227*, 120370. https://doi.org/https://doi.org/10.1016/j.energy.2021.120370

Castro, L. F., Silva-Neto, H. A., Sousa, L. R., de Araujo, W. R., & Coltro, W. K. (2023). Silicone glue-based graphite ink incorporated on paper platform as an affordable approach to construct stable electrochemical sensors. *Talanta*, *251*, 123812. https://doi.org/https://doi.org/10.1016/j.talanta.2022.123812

Cengel, Y., & Cimbala, J. (2013). Ebook: Fluid mechanics fundamentals and applications (si units). https://books.google.nl/books?id=LIZvEAAAQBAJ

Chung, D. (2002). Review graphite. *Journal of materials science*, *37*, 1475–1489.

Cieśliński, J. T., & Fabrykiewicz, M. (2023). Thermal energy storage with pcms in shell-and-tube units: A review. *Energies*, *16*(2). https://doi.org/10.3390/en16020936

Cohen, Y., & Metzner, A. (1981). Wall effects in laminar flow of fluids through packed beds. *AIChE Journal*, *27*(5), 705–715. https://doi.org/https://doi.org/10.1002/aic.690270502

Connor, N. (2020). What are forms of corrosion - Definition | Material properties. https://material-properties.org/what-is-forms-of-corrosion-definition/

Coquard, R., Coment, E., Flasquin, G., & Baillis, D. (2013). Analysis of the hot-disk technique applied to low-density insulating materials. *International Journal of Thermal Sciences*, *65*, 242–253. https://doi.org/https://doi.org/10.1016/j.ijthermalsci.2012.10.008

Creus, J., Mazille, H., & Idrissi, H. (2000). Porosity evaluation of protective coatings onto steel, through electrochemical techniques. *Surface and Coatings Technology*, *130*(2), 224–232. https://doi.org/https://doi.org/10.1016/S0257-8972(99)00659-3

Danielik, V., Šoška, P., Felgerová, K., & Zemanová, M. (2016). The corrosion of carbon steel in nitrate hydrates used as phase change materials. *Materials and Corrosion*, *68*, 416–422. https://doi.org/10.1002/maco.201609160

Defining a parameter study. (n.d.). https://anyscript.org/tutorials/Parameter_studies_and_optimization/lesson1.html

Ebadi, S., Tasnim, S. H., Aliabadi, A. A., & Mahmud, S. (2018). Melting of nano-pcm inside a cylindrical thermal energy storage system: Numerical study with experimental verification. *Energy Conversion and Management*, *166*, 241–259. https://doi.org/https://doi.org/10.1016/j.enconman.2018.04.016

Engineeringtoolbox. (2023). Metals, metallic elements and alloys - thermal conductivities. https://www.engineeringtoolbox.com/thermal-conductivity-metals-d_858.html

Fang, Y., Xu, H., Miao, Y., Bai, Z., Niu, J., & Deng, S. (2020). Experimental study of storage capacity and discharging rate of latent heat thermal energy storage units. *Applied Energy*, *275*, 115325. https://doi.org/https://doi.org/10.1016/j.apenergy.2020.115325

Fauchais, P. (2004). Understanding plasma spraying. *Journal of Physics D: Applied Physics*, *37*(9), R86. https://doi.org/10.1088/0022-3727/37/9/R02

Fernández, A., Galleguillos, H., Fuentealba, E., & Pérez, F. (2015). Corrosion of stainless steels and low-cr steel in molten ca(no3)2–nano3–kno3 eutectic salt for direct energy storage in csp plants. *Solar Energy Materials and Solar Cells*, *141*, 7–13. https://doi.org/https://doi.org/10.1016/j.solmat.2015.05.004

Fiedler, T., White, N., Dahari, M., & Hooman, K. (2014). On the electrical and thermal contact resistance of metal foam. *International Journal of Heat and Mass Transfer*, *72*, 565–571. https://doi.org/https://doi.org/10.1016/j.ijheatmasstransfer.2014.01.045

Fotovvati, B., Namdari, N., & Dehghanghadikolaei, A. (2019). On coating techniques for surface protection: A review. *Journal of Manufacturing and Materials Processing*, *3*(1). https://doi.org/10.3390/jmmp3010028

Frederichi, D., Scaliante, M., & Bergamasco, R. (2021). Structured photocatalytic systems: Photocatalytic coatings on low-cost structures for treatment of water contaminated with micropollutants—a short review. *Environmental Science and Pollution Research*, *28*. https://doi.org/10.1007/s11356-020-10022-9

Gabbrielli, R., & Zamparelli, C. (2009). Optimal design of a molten salt thermal storage tank for parabolic trough solar power plants. *Journal of Solar Energy Engineering*, *131*(4), 041001. https://doi.org/10.1115/1.3197585

Gandert, J. C., Müller, M., Paarmann, S., Queisser, O., & Wetzel, T. (2023). Effective thermal conductivity of lithium-ion battery electrodes in dependence on the degree of calendering. *Energy Technology*, *11*(8), 2300259. https://doi.org/https://doi.org/10.1002/ente.202300259

Gao, H., Zhang, Y., Liu, Y., Wang, Y., Sun, P., Ma, Y., Gu, Z., & Yu, W. (2022). Numerical simulation of heat transfer performance of different heat exchange tubes in heat recovery steam generator. *Process Safety and Environmental Protection*, *163*, 506–512. https://doi.org/https://doi.org/10.1016/j.psep.2022.05.045

Gao, W., Zhou, W., Lyu, X., Liu, X., Su, H., Li, C., & Wang, H. (2023). Comprehensive utilization of steel slag: A review. *Powder Technology*, *422*, 118449. https://doi.org/https://doi.org/10.1016/j.powtec.2023.118449

Gedzevicius, I., Valiulis, & Algirdas. (2006). Analysis of wire arc spraying process variables on coatings properties. *Journal of Materials Processing Technology*, *175*, 206–211. https://doi.org/10.1016/j.jmatprotec.2005.04.019

Giaconia, A., Tizzonia, A. C., Sau, S., Corsaro, N., Mansi, E., Spadoni, A., & Delise, T. (2021). Assessment and perspectives of heat transfer fluids for csp applications. *Energies*, *14*(22). https://doi.org/10.3390/en14227486

GlobalHeatTransfer. (n.d.). Globaltherm Omnistore MS-600. https://globalhtf.com/temperatures/globaltherm-omnistore/

Gomez, R. (2022). About Graphite - Graphite products. https://superiorgraphite.com/innovation/about-graphite/

Gonzalez, M., Nithiyanantham, U., Carbó-Argibay, E., Bondarchuk, O., Grosu, Y., & Faik, A. (2019). Graphitization as efficient inhibitor of the carbon steel corrosion by molten binary nitrate salt for thermal energy storage at concentrated solar power. *Solar Energy Materials and Solar Cells*, *203*, 110172. https://doi.org/https://doi.org/10.1016/j.solmat.2019.110172

González-Roubaud, E., Pérez-Osorio, D., & Prieto, C. (2017). Review of commercial thermal energy storage in concentrated solar power plants: Steam vs. molten salts. *Renewable and Sustainable Energy Reviews*, *80*, 133–148. https://doi.org/https://doi.org/10.1016/j.rser.2017.05.084

Goods, S., & Bradshaw, R. (2004). Corrosion of stainless steels and carbon steel by molten mixtures of commercial nitrate salts. *Journal of Materials Engineering and Performance*, *13*, 78–87. https://doi.org/10.1361/10599490417542

Government. (2019). Climate Agreement [https://www.government.nl/documents/reports/2019/06/28/climate-agreement].

Greenwood, P., Thring, R. H., & Chen, R. (2013). Conductive materials for polymeric bipolar plates: Electrical, thermal and mechanical properties of polyethylene-carbon black/graphite/magnetite blends. *Proceedings of the Institution of Mechanical Engineers, Part L: Journal of Materials: Design and Applications*, *227*(3), 226–242. https://doi.org/10.1177/1464420712454059

Griffin, J., & O'Kane, M. (2024). Dip Coating: Practical Guide to theory and troubleshooting. https://www.ossila.com/pages/dip-coating

Grosu, Y., Udayashankar, N., Zaki, A., & Faik, A. (2018). A simple method for the inhibition of the corrosion of carbon steel by molten nitrate salt for thermal storage in concentrating solar power applications. *npj Materials Degradation*, *2*. https://doi.org/10.1038/s41529-018-0055-0

Gutierrez, A., Miró, L., Gil, A., Rodríguez-Aseguinolaza, J., Barreneche, C., Calvet, N., Py, X., Inés Fernández, A., Grágeda, M., Ushak, S., & Cabeza, L. F. (2016). Advances in the valorization of waste and by-product materials as thermal energy storage (tes) materials. *Renewable and Sustainable Energy Reviews*, *59*, 763–783. https://doi.org/https://doi.org/10.1016/j.rser.2015.12.071

Hagiwara, H., Suszynski, W., & Francis, L. (2014). A raman spectroscopic method to find binder distribution in electrodes during drying. *Journal of Coatings Technology and Research*, *11*. https://doi.org/10.1007/s11998-013-9509-z

Han, G.-S., Ding, H.-S., Huang, Y., Tong, L.-G., & Ding, Y.-L. (2017). A comparative study on the performances of different shell-and-tube type latent heat thermal energy storage units including the effects of natural convection. *International Communications in Heat and Mass Transfer*, *88*, 228–235. https://doi.org/https://doi.org/10.1016/j.icheatmasstransfer.2017.09.009

Han, Z., Wickramaratne, C., Yogi Goswami, D., & Jotshi, C. (2022). Experimental study on operating characteristics of nitrate salt-based latent heat thermal energy storage unit. *Applied Thermal*

Engineering, *202*, 117846. https://doi.org/https://doi.org/10.1016/j.applthermaleng.2021. 117846

Hänchen, M., Brückner, S., & Steinfeld, A. (2011). High-temperature thermal storage using a packed bed of rocks – heat transfer analysis and experimental validation. *Applied Thermal Engineering*, *31*(10), 1798–1806. https://doi.org/https://doi.org/10.1016/j.applthermaleng.2010.10.034

HEDH & Hooman, K. (2023). High temperature thermal energy storage. https://hedhme.com/webinars/high-temperature-thermal-energy-storage/

Hua, W., Xu, X., Zhang, X., Yan, H., & Zhang, J. (2022). Progress in corrosion and anti-corrosion measures of phase change materials in thermal storage and management systems. *Journal of Energy Storage*, *56*, 105883. https://doi.org/https://doi.org/10.1016/j.est.2022.105883

Hwang, Y., Ahn, Y., Shin, H., Lee, C., Kim, G., Park, H., & Lee, J. (2006). Investigation on characteristics of thermal conductivity enhancement of nanofluids [Nano Korea 2004 Symposium on NT Challenge]. *Current Applied Physics*, *6*(6), 1068–1071. https://doi.org/https://doi.org/10.1016/j.cap.2005.07.021

IEA. (2022). Industry – Topics - IEA [https://www.iea.org/topics/industry].

Ishizaki, T., Igami, T., & Nagano, H. (2020). Measurement of local thermal contact resistance with a periodic heating method using microscale lock-in thermography. *Review of Scientific Instruments*, *91*(6), 064901. https://doi.org/10.1063/5.0002937

Jacob, R., Liu, M., Sun, Y., Belusko, M., & Bruno, F. (2019). Characterisation of promising phase change materials for high temperature thermal energy storage. *Journal of Energy Storage*, *24*, 100801. https://doi.org/https://doi.org/10.1016/j.est.2019.100801

Kenisarin, M. M. (2010). High-temperature phase change materials for thermal energy storage. *Renewable and Sustainable Energy Reviews*, *14*(3), 955–970. https://doi.org/https://doi.org/10.1016/j.rser.2009.11.011

Kreith, F., & Manglik, R. M. (2016). *Principles of heat transfer*. Cengage learning.

Larock, B., Jeppson, R., & Watters, G. (1999). *Hydraulics of pipeline systems*. CRC Press. https://books.google.nl/books?id=RAMX5xuXSrUC

Li, Q., Li, C., Du, Z., Jiang, F., & Ding, Y. (2019). A review of performance investigation and enhancement of shell and tube thermal energy storage device containing molten salt based phase change materials for medium and high temperature applications. *Applied Energy*, *255*, 113806. https://doi.org/https://doi.org/10.1016/j.apenergy.2019.113806

Li, X., Luo, R., Zhang, W., & Liao, H. (2016). Method for measuring thermal contact resistance of graphite thin film materials. *Measurement*, *93*, 202–207. https://doi.org/https://doi.org/10.1016/j.measurement.2016.07.015

Li, Y., Shi, C., Liu, J., Liu, E., Shao, J., Chen, Z., Dorantes-Gonzalez, D. J., & Hu, X. (2013). Improving the accuracy of the transient plane source method by correcting probe heat capacity and resistance influences. *Measurement Science and Technology*, *25*(1), 015006. https://doi.org/10.1088/0957-0233/25/1/015006

Lian, T.-W., Kondo, A., Akoshima, M., Abe, H., Ohmura, T., Tuan, W.-H., & Naito, M. (2016). Rapid thermal conductivity measurement of porous thermal insulation material by laser flash method [Special issue of the 5th Int'l Conf. on the Characterization and Control of Interfaces for High Quality Advanced Materials (ICCCI2015)]. *Advanced Powder Technology*, *27*(3), 882–885. https://doi.org/https://doi.org/10.1016/j.apt.2016.01.008

Liu, J., Chen, L., Fang, X., & Zhang, Z. (2017). Preparation of graphite nanoparticles-modified phase change microcapsules and their dispersed slurry for direct absorption solar collectors. *Solar Energy Materials and Solar Cells*, *159*, 159–166. https://doi.org/https://doi.org/10.1016/j.solmat.2016.09.020

Liu, M., Zhang, X., Ji, J., & Yan, H. (2023). Review of research progress on corrosion and anti-corrosion of phase change materials in thermal energy storage systems. *Journal of Energy Storage*, *63*, 107005. https://doi.org/https://doi.org/10.1016/j.est.2023.107005

Lv, G.-H., Chen, H., Gu, W.-C., Feng, W.-R., Li, L., Niu, E.-W., Zhang, X.-H., & Yang, S.-Z. (2009). Effects of graphite additives in electrolytes on the microstructure and corrosion resistance of alumina peo coatings. *Current Applied Physics*, *9*(2), 324–328. https://doi.org/https://doi.org/10.1016/j.cap.2008.03.001

Maaß, P. (2011). *Corrosion and corrosion protection*. Wiley Online Library.

Maeda, K., & Mizubayashi, H. (2006). Springer handbook of materials measurement methods. *Springer Handbook of Materials Measurement Methods, ISBN 978-3-540-20785-6. Springer-Verlag Berlin Heidelberg, 2006, p. 153*. https://doi.org/10.1007/978-3-642-16641-9_5

Marshall, J. E., Zhenova, A., Roberts, S., Petchey, T., Zhu, P., Dancer, C. E. J., McElroy, C. R., Kendrick, E., & Goodship, V. (2021). On the solubility and stability of polyvinylidene fluoride. *Polymers*, *13*(9). https://www.mdpi.com/2073-4360/13/9/1354

Mehta, D. S., Solanki, K., Rathod, M. K., & Banerjee, J. (2019). Thermal performance of shell and tube latent heat storage unit: Comparative assessment of horizontal and vertical orientation. *Journal of Energy Storage*, *23*, 344–362. https://doi.org/https://doi.org/10.1016/j.est.2019.03.007

Mesalhy, O., Lafdi, K., Elgafy, A., & Bowman, K. (2005). Numerical study for enhancing the thermal conductivity of phase change material (pcm) storage using high thermal conductivity porous matrix. *Energy Conversion and Management*, *46*(6), 847–867. https://doi.org/https://doi.org/10.1016/j.enconman.2004.06.010

Mills, A. F. (1992). *Heat transfer*. CRC Press.

Min, S., Blumm, J., & Lindemann, A. (2007). A new laser flash system for measurement of the thermophysical properties [6th KSTP Symposium]. *Thermochimica Acta*, *455*(1), 46–49. https://doi.org/https://doi.org/10.1016/j.tca.2006.11.026

Mohamed, H. M. (2016). Screen-printed disposable electrodes: Pharmaceutical applications and recent developments. *TrAC Trends in Analytical Chemistry*, *82*, 1–11. https://doi.org/https://doi.org/10.1016/j.trac.2016.02.010

Mohamed, S. A., Al-Sulaiman, F. A., Ibrahim, N. I., Zahir, M. H., Al-Ahmed, A., Saidur, R., Yılbaş, B., & Sahin, A. (2017). A review on current status and challenges of inorganic phase change materials for thermal energy storage systems. *Renewable and Sustainable Energy Reviews*, *70*, 1072–1089. https://doi.org/https://doi.org/10.1016/j.rser.2016.12.012

Mohamed Nazri, F., Shahidan, S., Baharuddin, N. K., Beddu, S., & Abu, B. (2017). Effects of heating durations on normal concrete residual properties: Compressive strength and mass loss. *IOP Conference Series: Materials Science and Engineering*, *271*, 012013. https://doi.org/10.1088/1757-899X/271/1/012013

Moreno, P., Miró, L., Solé, A., Barreneche, C., Solé, C., Martorell, I., & Cabeza, L. F. (2014). Corrosion of metal and metal alloy containers in contact with phase change materials (pcm) for potential heating and cooling applications. *Applied Energy*, *125*, 238–245. https://doi.org/https://doi.org/10.1016/j.apenergy.2014.03.022

Müller, M., Pfaffmann, L., Jaiser, S., Baunach, M., Trouillet, V., Scheiba, F., Scharfer, P., Schabel, W., & Bauer, W. (2017). Investigation of binder distribution in graphite anodes for lithium-ion batteries. *Journal of Power Sources*, *340*, 1–5. https://doi.org/https://doi.org/10.1016/j.jpowsour.2016.11.051

Oehler, D. (2021). *Bestimmung der thermischen transporteigenschaften poröser elektroden von lithium-ionen batterien*. Karlsruher Institut für Technologie. https://books.google.nl/books?id=tC9VEAAAQBAJ

Opolot, M., Zhao, C., Keane, P. F., Liu, M., Mancin, S., Bruno, F., & Hooman, K. (2023). Discharge performance of a high temperature phase change material with low-cost wire mesh. *Applied Thermal Engineering*, *223*, 120050. https://doi.org/https://doi.org/10.1016/j.applthermaleng.2023.120050

Ortega, I., Faik, A., Gil, A., Rodríguez-Aseguinolaza, J., & D'Aguanno, B. (2015). Thermo-physical properties of a steel-making by-product to be used as thermal energy storage material in a packed-bed system. *Energy Procedia*, *69*, 968–977. https://doi.org/10.1016/j.egypro.2015.03.180

Ortega, I., Loroño, I., Faik, A., Uriz, I., Rodríguez-Aseguinolaza, J., & D'Aguanno, B. (2017). Parametric analysis of a packed bed thermal energy storage system. *AIP Conference Proceedings*, *1850*, 080021. https://doi.org/10.1063/1.4984442

Ortega-Fernández, I., Nicolas Calvet, A. G., Rodríguez-Aseguinolaza, J., Faik, A., & D'Aguanno, B. (2015). Thermophysical characterization of a by-product from the steel industry to be used as a sustainable and low-cost thermal energy storage material. *Energy*, *89*, 601–609. https://doi.org/https://doi.org/10.1016/j.energy.2015.05.153

Ortega-Fernández, I., & Rodríguez-Aseguinolaza, J. (2019). Thermal energy storage for waste heat recovery in the steelworks: The case study of the reslag project. *Applied Energy*, *237*, 708–719. https://doi.org/https://doi.org/10.1016/j.apenergy.2019.01.007

Ossila. (n.d.). https://www.ossila.com/products/dip-coater.

Ostanek, J., Shah, K., & Jain, A. (2016). Measurement sensitivity analysis of the transient hot source technique applied to flat and cylindrical samples. *Journal of Thermal Science and Engineering Applications*, *9*. https://doi.org/10.1115/1.4034178

Palacios, A., Cong, L., Navarro, M., Ding, Y., & Barreneche, C. (2019). Thermal conductivity measurement techniques for characterizing thermal energy storage materials – a review. *Renewable and Sustainable Energy Reviews*, *108*, 32–52. https://doi.org/https://doi.org/10.1016/j.rser.2019.03.020

Pantea, D., Darmstadt, H., Kaliaguine, S., & Roy, C. (2003). Electrical conductivity of conductive carbon blacks: Influence of surface chemistry and topology. *Applied Surface Science*, *217*(1), 181–193. https://doi.org/https://doi.org/10.1016/S0169-4332(03)00550-6

Park, S. H., Park, Y. G., & Ha, M. Y. (2020). A numerical study on the effect of the number and arrangement of tubes on the melting performance of phase change material in a multi-tube latent thermal energy storage system. *Journal of Energy Storage*, *32*, 101780. https://doi.org/https://doi.org/10.1016/j.est.2020.101780

PCMProducts. (n.d.). PCM Products. https://www.pcmproducts.net/Phase_Change_Material_Products.htm

Peiró, G., Prieto, C., Gasia, J., Jové, A., Miró, L., & Cabeza, L. F. (2018). Two-tank molten salts thermal energy storage system for solar power plants at pilot plant scale: Lessons learnt and recommendations for its design, start-up and operation. *Renewable Energy*, *121*, 236–248. https://doi.org/https://doi.org/10.1016/j.renene.2018.01.026

Piquot, J., Nithiyanantham, U., Grosu, Y., & Faik, A. (2019). Spray-graphitization as a protection method against corrosion by molten nitrate salts and molten salts based nanofluids for thermal energy storage applications. *Solar Energy Materials and Solar Cells*, *200*, 110024. https://doi.org/https://doi.org/10.1016/j.solmat.2019.110024

Prieto, C., Miró, L., Peiró, G., Oró, E., Gil, A., & Cabeza, L. F. (2016). Temperature distribution and heat losses in molten salts tanks for csp plants. *Solar Energy*, *135*, 518–526. https://doi.org/https://doi.org/10.1016/j.solener.2016.06.030

Qian, J., Kong, Q.-L., Zhang, H.-W., Zhu, Z.-H., Huang, W.-G., & Li, W.-H. (2017). Experimental study for shell-and-tube molten salt heat exchangers. *Applied Thermal Engineering*, *124*, 616–623. https://doi.org/https://doi.org/10.1016/j.applthermaleng.2017.06.005

Qin, F. G., Yang, X., Ding, Z., Zuo, Y., Shao, Y., Jiang, R., & Yang, X. (2012). Thermocline stability criterions in single-tanks of molten salt thermal energy storage [Energy Solutions for a Sustainable World - Proceedings of the Third International Conference on Applied Energy, May 16-18, 2011 - Perugia, Italy]. *Applied Energy*, *97*, 816–821. https://doi.org/https://doi.org/10.1016/j.apenergy.2012.02.048

Qureshi, Z. A., Ali, H. M., & Khushnood, S. (2018). Recent advances on thermal conductivity enhancement of phase change materials for energy storage system: A review. *International Journal of Heat and Mass Transfer*, *127*, 838–856. https://doi.org/https://doi.org/10.1016/j.ijheatmasstransfer.2018.08.049

Rahmani, A. (2014). Numerical investigation of heat transfer in 4-pass fire-tube boiler. *American Journal of Chemical Engineering*, *2*, 65–70. https://doi.org/10.11648/j.ajche.20140205.12

RDW. (2015). wetten.nl - Regeling - Beleidsregel Ontheffingverlening exceptionele transporten RDW 2015 - BWBR0035903. https://wetten.overheid.nl/BWBR0035903/2015-01-01

Rodríguez, I., Pérez-Segarra, C., Lehmkuhl, O., & Oliva, A. (2013). Modular object-oriented methodology for the resolution of molten salt storage tanks for csp plants. *Applied Energy*, *109*, 402–414. https://doi.org/https://doi.org/10.1016/j.apenergy.2012.11.008

Rodríguez-García, M.-M., Herrador-Moreno, M., & Zarza Moya, E. (2014). Lessons learnt during the design, construction and start-up phase of a molten salt testing facility. *Applied Thermal Engineering*, *62*(2), 520–528. https://doi.org/https://doi.org/10.1016/j.applthermaleng.2013.09.040

Romao, C., Miller, K., Johnson, M., Zwanziger, J., Marinkovic, B., & White, M. (2014). Thermal, vibrational, and thermoelastic properties of y2mo3o12 and their relations to negative thermal expan-

sion. *Physical review. B, Condensed matter*, *90*, 024305. https://doi.org/10.1103/PhysRevB. 90.024305

Roslan, N. H., Ismail, M., Abdul-Majid, Z., Ghoreishiamiri, S., & Muhammad, B. (2016). Performance of steel slag and steel sludge in concrete. *Construction and Building Materials*, *104*, 16–24. https://doi.org/https://doi.org/10.1016/j.conbuildmat.2015.12.008

Sastri, V. S., Ghali, E. L., & Elboujdaini, M. (2007). *Corrosion prevention and protection: Practical solutions*. John Wiley; Sons, Ltd.

Schulte-Fischedick, J., Tamme, R., & Herrmann, U. (2008). Cfd analysis of the cool down behaviour of molten salt thermal storage systems. *Proceedings 2nd International Conference on Energy Sustainability*, *2*. https://doi.org/10.1115/ES2008-54101

Scott M. Flueckiger, Z. Y., & Garimella, S. V. (2013). Review of molten-salt thermocline tank modeling for solar thermal energy storage. *Heat Transfer Engineering*, *34*(10), 787–800. https://doi.org/ 10.1080/01457632.2012.746152

Scriven, L. (2011). Physics and applications of dip coating and spin coating. *MRS Proceedings*, *121*. https://doi.org/10.1557/PROC-121-717

Seddegh, S., Wang, X., Joybari, M. M., & Haghighat, F. (2017). Investigation of the effect of geometric and operating parameters on thermal behavior of vertical shell-and-tube latent heat energy storage systems. *Energy*, *137*, 69–82. https://doi.org/https://doi.org/10.1016/j.energy.2017.07. 014

Shell-and-tube heat exchangers. (2019). In *Kern's process heat transfer* (pp. 289–380). John Wiley; Sons, Ltd. https://doi.org/https://doi.org/10.1002/9781119364825.ch7

Singh, L., Chawla, V., & Grewal, J. (2012). A review on detonation gun sprayed coatings. *Journal of Minerals and Materials Characterization and Engineering*, *11*(03), 243. https://doi.org/10.4236/ jmmce.2012.113019

Sodhi, G. S., Vigneshwaran, K., & Muthukumar, P. (2021). Experimental investigations of high-temperature shell and multi-tube latent heat storage system. *Applied Thermal Engineering*, *198*, 117491. https://doi.org/https://doi.org/10.1016/j.applthermaleng.2021.117491

Statista. (n.d.). Global Graphite Production. https://www-statista-com.tudelft.idm.oclc.org/statistics/ 1005851/global-graphite-production/

Tao, Y., He, Y., & Qu, Z. (2012). Numerical study on performance of molten salt phase change thermal energy storage system with enhanced tubes. *Solar Energy*, *86*(5), 1155–1163. https://doi.org/ https://doi.org/10.1016/j.solener.2012.01.004

Tao, Y., Liu, Y., & He, Y.-L. (2017). Effects of pcm arrangement and natural convection on charging and discharging performance of shell-and-tube lhs unit. *International Journal of Heat and Mass Transfer*, *115*, 99–107. https://doi.org/https://doi.org/10.1016/j.ijheatmasstransfer.2017.07.098

Tao, Y.-B., Li, M.-J., He, Y.-L., & Tao, W.-Q. (2014). Effects of parameters on performance of high temperature molten salt latent heat storage unit [ASCHT2013]. *Applied Thermal Engineering*, *72*(1), 48–55. https://doi.org/https://doi.org/10.1016/j.applthermaleng.2014.01.038

Tarieven, E. E. (2024). Eerlijke energie tarieven - tot 52,8 procent lagere zakelijke energietarieven. https://eerlijkeenergietarieven.nl/

Teng, H. (2012). Overview of the development of the fluoropolymer industry. *Applied Sciences*, *2*(2), 496–512. https://doi.org/10.3390/app2020496

Thermal spraying techniques. (2008). John Wiley; Sons, Ltd. https://doi.org/https://doi.org/10.1002/ 9780470754085.ch3

Towler, G., & Sinnott, R. (2022). Chapter 19 - heat transfer equipment. In G. Towler & R. Sinnott (Eds.), *Chemical engineering design (third edition)* (Third Edition, pp. 823–951). Butterworth-Heinemann. https://doi.org/https://doi.org/10.1016/B978-0-12-821179-3.00019-4

Tritt, T. M. (2005). *Thermal conductivity: Theory, properties, and applications*. Springer Science & Business Media.

Trp, A., Lenic, K., & Frankovic, B. (2006). Analysis of the influence of operating conditions and geometric parameters on heat transfer in water-paraffin shell-and-tube latent thermal energy storage unit. *Applied Thermal Engineering*, *26*(16), 1830–1839. https://doi.org/https://doi.org/10.1016/j. applthermaleng.2006.02.004

V, S., M, R., Kumar, S., Tripathi, V., & Sharma, R. (2022). Study on developments in protection coating techniques for steel. *Advances in Materials Science and Engineering*, *2022*, 1–10. https://doi. org/10.1155/2022/2843043

Vasu, A., Hagos, F. Y., Noor, M. M., Mamat, R., Azmi, W. H., Abdullah, A. A., & Ibrahim, T. K. (2017). Corrosion effect of phase change materials in solar thermal energy storage application. *Renewable and Sustainable Energy Reviews*, *76*, 19–33. https://doi.org/https://doi.org/10.1016/j.rser.2017.03.018

Wakao, N., & Kaguei, S. (1983). Heat and mass transfer in packed beds. *AIChE Journal*, *29*(6), 1055–1055. https://doi.org/https://doi.org/10.1002/aic.690290627

Wan, Z., Wei, J., Qaisrani, M. A., Fang, J., & Tu, N. (2020). Evaluation on thermal and mechanical performance of the hot tank in the two-tank molten salt heat storage system. *Applied Thermal Engineering*, *167*, 114775. https://doi.org/https://doi.org/10.1016/j.applthermaleng.2019.114775

Wang, W.-L., He, S.-M., & Lan, C.-H. (2012). Protective graphite coating on metallic bipolar plates for pemfc applications. *Electrochimica Acta*, *62*, 30–35. https://doi.org/https://doi.org/10.1016/j.electacta.2011.11.026

Wang, Y., Xie, F., Ma, S., & Dong, L. (2017). Review of surface profile measurement techniques based on optical interferometry. *Optics and Lasers in Engineering*, *93*, 164–170. https://doi.org/https://doi.org/10.1016/j.optlaseng.2017.02.004

Wanson, B. (n.d.). Steam Solutions. https://r6n7c4f7.rocketcdn.me/wp-content/uploads/2022/04/Babcock_Wanson_Steam_Solution_Brochure_Oct_2021_web.pdf

Wei, G., Wang, G., Xu, C., Ju, X., Xing, L., Du, X., & Yang, Y. (2018). Selection principles and thermophysical properties of high temperature phase change materials for thermal energy storage: A review. *Renewable and Sustainable Energy Reviews*, *81*, 1771–1786. https://doi.org/https://doi.org/10.1016/j.rser.2017.05.271

Yi, H., Kim, J. Y., Gul, H. Z., Kang, S., Kim, G., Sim, E., Ji, H., Kim, J., Choi, Y. C., Kim, W. S., & Lim, S. C. (2020). Wiedemann-franz law of cu-coated carbon fiber. *Carbon*, *162*, 339–345. https://doi.org/https://doi.org/10.1016/j.carbon.2020.02.062

Yu, G.-C., Wu, L.-Z., & Feng, L.-J. (2015). Enhancing the thermal conductivity of carbon fiber reinforced polymer composite laminates by coating highly oriented graphite films. *Materials and Design*, *88*, 1063–1070. https://doi.org/https://doi.org/10.1016/j.matdes.2015.09.096

Yuan, Y., He, C., Lu, J., & Ding, J. (2016). Thermal performances of molten salt steam generator. *Applied Thermal Engineering*, *105*, 163–169. https://doi.org/https://doi.org/10.1016/j.applthermaleng.2016.03.080

Zaversky, F., García-Barberena, J., Sánchez, M., & Astrain, D. (2013). Transient molten salt two-tank thermal storage modeling for csp performance simulations. *Solar Energy*, *93*, 294–311. https://doi.org/https://doi.org/10.1016/j.solener.2013.02.034

Zawilski, B., Littleton, R. T., Pope, A., & Tritt, T. M. (1999). Parallel thermal conductance technique for measuring thermalconductivity of smaller thermoelectric materials. *Eigteenth International Conference on Themoelectrics*, 421–423. https://doi.org/10.1109/ICT.1999.843420

Zhang, P., Ma, F., & Xiao, X. (2016). Thermal energy storage and retrieval characteristics of a molten-salt latent heat thermal energy storage system. *Applied Energy*, *173*, 255–271. https://doi.org/https://doi.org/10.1016/j.apenergy.2016.04.012

Zhang, S., Mancin, S., & Pu, L. (2023). A review and prospective of fin design to improve heat transfer performance of latent thermal energy storage. *Journal of Energy Storage*, *62*, 106825. https://doi.org/https://doi.org/10.1016/j.est.2023.106825

Zhang, Z., Li, W., Zhang, W., Huang, X., Ruan, L., & Wu, L. (2018). Experimental, quantum chemical calculations and molecular dynamics (md) simulation studies of methionine and valine as corrosion inhibitors on carbon steel in phase change materials (pcms) solution. *Journal of Molecular Liquids*, *272*, 528–538. https://doi.org/https://doi.org/10.1016/j.molliq.2018.09.081

Zhang, Z., Tian, N., Zhang, W., Huang, X., Ruan, L., & Wu, L. (2016). Inhibition of carbon steel corrosion in phase-change-materials solution by methionine and proline. *Corrosion Science*, *111*, 675–689. https://doi.org/https://doi.org/10.1016/j.corsci.2016.06.005

Zhao, C., Opolot, M., Liu, M., Bruno, F., Mancin, S., Flewell-Smith, R., & Hooman, K. (2021). Simulations of melting performance enhancement for a pcm embedded in metal periodic structures. *International Journal of Heat and Mass Transfer*, *168*, 120853. https://doi.org/https://doi.org/10.1016/j.ijheatmasstransfer.2020.120853

Zhao, D., Qian, X., Gu, X., Jajja, S. A., & Yang, R. (2016). Measurement techniques for thermal conductivity and interfacial thermal conductance of bulk and thin film materials. *Journal of Electronic Packaging*, *138*(4), 040802. https://doi.org/10.1115/1.4034605

Zheng, Q., Kaur, S., Dames, C., & Prasher, R. S. (2020). Analysis and improvement of the hot disk transient plane source method for low thermal conductivity materials. *International Journal of Heat and Mass Transfer*, *151*, 119331. https://doi.org/https://doi.org/10.1016/j.ijheatmasstransfer.2020.119331

Zou, L.-l., Chen, X., Wu, Y.-t., Wang, X., & Ma, C.-f. (2019). Experimental study of thermophysical properties and thermal stability of quaternary nitrate molten salts for thermal energy storage. *Solar Energy Materials and Solar Cells*, *190*, 12–19. https://doi.org/https://doi.org/10.1016/j.solmat.2018.10.013

Zou, Y., Ding, J., Wang, W., Lee, D., & Lu, J. (2020). Heat transfer performance of u-tube molten salt steam generator. *International Journal of Heat and Mass Transfer*, *160*, 120200. https://doi.org/https://doi.org/10.1016/j.ijheatmasstransfer.2020.120200

<div align="right">

A

</div>
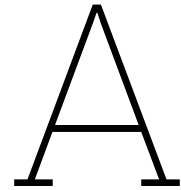
System description and flow sheet

A.1. Slag

A.1.1. Storage
Preparing the slag storage tank for the first charge and discharge is pretty self-explanatory. The tank should be filled with the slag. Thereafter should the tank be insulated.

A.1.2. Charging
The charging starts when there is energy, not specified in what form in this thesis, available. The ambient air, which is approximately 25°C at first needs to be heated to 700°C. This could be done by direct or indirect heating. For direct heating, with for example the use of concentrated solar power, hot air is directly generated. For indirect heating, with, for example, electricity generated by solar panels, this electricity will be converted into high temperature air with the use of a resistive heater or other equipment. The hot air, 700°C, will flow into the packed bed from top to bottom. This is accomplished by a fan which will be placed before the heating step. This enables the use of a low temperature, 25-200°C, fan. Then, the hot air will charge the packed bed and will leave the packed bed with temperatures around 200°C, this is equal to slag in the last part of the storage. This is due to the fact that the 'empty' storage tank is around 200°C. This air will be recycled and led back to the heating section. The charging will stop when the temperature of the HTF outlet rises till a value of 300°C. When the charging is completed, will these valves be closed.

A.1.3. Discharging
The discharging is done differently with respect to charging. For the start-up of the discharging will ambient air, at 25°C, be used. This will be heated to 700°C. The fan, which is required to generate the required velocity of the HTF, is placed at the entrance of the packed bed. This enables, again, the usage of a low, 25-200°C temperature fan. The discharging HTF will enter the packed bed at the bottom and leave at the top. Approximately 85% of the hot HTF will be led to the shell and tube evaporator. The other 15% will be used to preheat the process water from 100 to approximately 180°C in a pre-heater next to the steam generator. The HTF the steam generator at approximately 210°C and the pre-heater at approximately 200°C. These two will be mixed again and led to the bottom of the packed bed to be heated again to 700°C. The steam, which is in the design of the steam generator in AspenEDR 100% evaporated but in reality, could be around 97% evaporation, is led to a small steam drum. Here is the steam separated from the water, with the use of for example a cyclone separator, and can be used as process steam. The steam drum is kept at 11 barg. The water which is preheated to around 180°C will also be led to this steam drum. The water which enters the steam generator is extracted from this steam drum at 11 barg to the shell and tube evaporator. The discharging will stop when the HTF outlet temperature at the outlet of the packed bed will drop to around 600°C. Then, the valves will be closed and the packed bed will be, due to isolation kept at 200°C till the next charging step occurs.

A.1.4. Malfunctioning
In the event of a factory malfunction, for example, a failure in a valve, there is no cause for alarm concerning the storage tank. The air, which is used as HTF, could be exhausted and the tank could just cool down slowly. The steam generation should be done with a back-up boiler.

A.1.5. Notes
Besides the description of the choices, based on literature, regarding the design of the storage tank, two additional notes regarding should be kept in mind.

According to Ortega-Fernández and Rodríguez-Aseguinolaza (2019), where a tank of 3m^3 is used with different aspect ratios, is concluded that this relatively small tank length does not lead to variations in the void fraction between the lower and upper parts in the tank. However, since in this case, a larger tank is present, it should be evaluated what is the influence on the void fraction when scaling up.

The influence of flow channelling near the tank wall could, when the ratio between the tank diameter and particle diameter exceeds 30, be neglected. For smaller systems should these be taken into account (Cohen & Metzner, 1981).

A.2. Phase change salt
A.2.1. Storage
When the phase change salt storage is prepared, the salt is encapsulated in liquid form. This is due to two reasons. The first is that liquid salt ensures optimal heat storage capacity due to the absence of air gaps, which are present in salt powder, between the solid salt. The second reason is that this process also prevents high pressure, caused by the air in the salt powder, within the thermal energy storage units by encapsulating the phase change salt at elevated temperatures (P. Zhang et al., 2016). Thereafter should the tank be insulated.

A.2.2. Charging
The charging starts when there is energy, not specified in what form in this thesis, available. The thermal oil, which is approximately 200°C at first needs to be heated to a maximum of 600°C. The oil present in the charging area does, in principle not have to be refilled by the storage tank since it will recycle it in its own section. However, when there are some losses or for the start-up is the connection to the oil tank made. The oil is at the 'cold' part when the oil is around 200°C. The temperature maximum temperature of the thermal oil is dependent on the oil characteristics. The heating could be done by direct or indirect heating. For direct heating, with for example, the use of concentrated solar power, hot thermal oil is directly generated. For indirect heating, with, for example, electricity generated by solar panels, this electricity will be converted into high temperature thermal oil with the use of a resistive heater or other equipment. The oil at the outlet of the thermal storage, which, will differ in temperature based on the phase of the charging, will be recycled and heated again to charge the thermal storage further. Eventually, when the storage is charged, will the flow through the storage be stopped and come to a standstill by the valve depicted in the charging section of the phase change salt storage in the flow sheet.

A.2.3. Discharging
Discharging the storage will be conducted with the same thermal oil. The first oil which will go to the steam generation section will be the oil which is in the thermal storage (which came to a standstill). The next thermal oil will come from the thermal oil tank with the use of a pump. This tank will be around 200-225°C when entering the thermal storage. This thermal oil will, dependent on the start or end stage of the storage reach temperatures between 520-445°C when leaving the storage. Thereafter, will the steam generation be conducted. In this thesis, the steam generation process for latent storage is not elaborated upon. This decision is based on the need to verify the assumptions and calculations made thus far before delving into further specifics. From the steam generation will the oil be recycled back to the thermal oil tank by a pump and will the process continue. When the steam generation is not required anymore, the valve will stop the process. All the oil will come to a standstill.

A.2.4. Malfunctioning

In case of malfunctioning of a part of the steam generation process, can the thermal oil be stored in the thermal oil tank to not spill any oil. When there is a malfunction in the charging process, the oil can be led to the thermal oil tank via the steam generation process, since this part of the process is not directly linked to the thermal oil tank. This is due to the valve which is present. This can be opened towards to the heating the oil by the storage system for the steam generation or towards the heater to charge the storage itself. It cannot flow back through this valve. The steam generation, by malfunctioning, should be done with a back-up boiler.

A.3. Molten salt

A.3.1. Storage

Installing the molten salt storage is done by melting the salts. The first part at temperature around 200° and the second part at 565°C. This is according to Rodríguez-García et al. (2014) one of the largest logistical challenges. It will take more time expected. This is due to the imperfect contact between the different salts when they are delivered by the supplier. It is essential to ensure that all salts are completely melted and that there are no impurities or contaminants present, as these can reduce the efficiency of the system or cause damage to the equipment. The start-up of the plant, which means the first heating of the storage, should be done progressively to avoid thermal stress within the container. Furthermore, this is also important to avoid HTF vapours and to avoid the presence of air.

A.3.2. Charging

To charge the molten salt thermal storage will the molten salt from the cold tank be led to the heater. The temperature will be raised to the hot tank molten salt storage temperature, approximately 565°C. This could be done by direct or indirect heating. For direct heating, with for example the use of concentrated solar power, hot air is directly generated. For indirect heating, with, for example, electricity generated by solar panels, this electricity will be converted into high temperature air with the use of a resistive heater or other equipment. The pump will be positioned upstream of this heater to facilitate the utilization of a pump designed for lower temperatures.

A.3.3. Discharging

The discharge process of the thermal storage system will occur in the following manner. The hot molten salt will be led to the shell and tube evaporator by a pump. This pump should be able to handle the high temperatures. The water, originating from other processes, is pumped through the tubes and the molten salt through the shells. The water is originating from the steam drum. The feed of this steam drum, at 11 bar, is preheated by a bypass of the molten salt outlet from the hot tank ($\approx$ 15%). This steam drum is kept at approximately 180°C. The steam, generated in the shell and tube, is led to the steam drum. A cyclone, or other equipment, filters the last water in the steam and the steam is used in the processes. The cold molten salt is brought to the cold molten salt storage tank by making use of a pump.

A.3.4. Malfunctioning

To handle malfunctioning are both tanks able to withstand the high temperature salt and are both tanks able to handle the volume of the two tanks together.

A.3.5. Notes

It should be noted that an electrical heat tracing system should be installed in all pipes and equipment where the salt will pass through or stand still. This electrical heat tracing system preheats and maintains the temperature to prevent the solidification of the salt. It is thus kept at $\approx$200 °C. This will come at a cost of power consumption, namely between 67.3-114.2W/m for 2 inch pipes and between 202.3-679W/m for outer wall equipment (Rodríguez-García et al., 2014).

The other note is that the energy losses due to radiation, convection and conduction from the tanks are compensated immediately to prevent solidification. This is done by an electrical heater.

A.4. Flowsheets

The flowsheets of all the above described processes are provided in the Figures below. Figure A.1 displays the slag flowsheet. In respectively Figure A.2 and Figure A.3 are the charging and discharging processes presented of the slag thermal storage. Figure A.4 shows the phase change salt flow sheet, without the steam generation, as explained before. Figure A.5 shows the flowsheet of the molten salt storage.
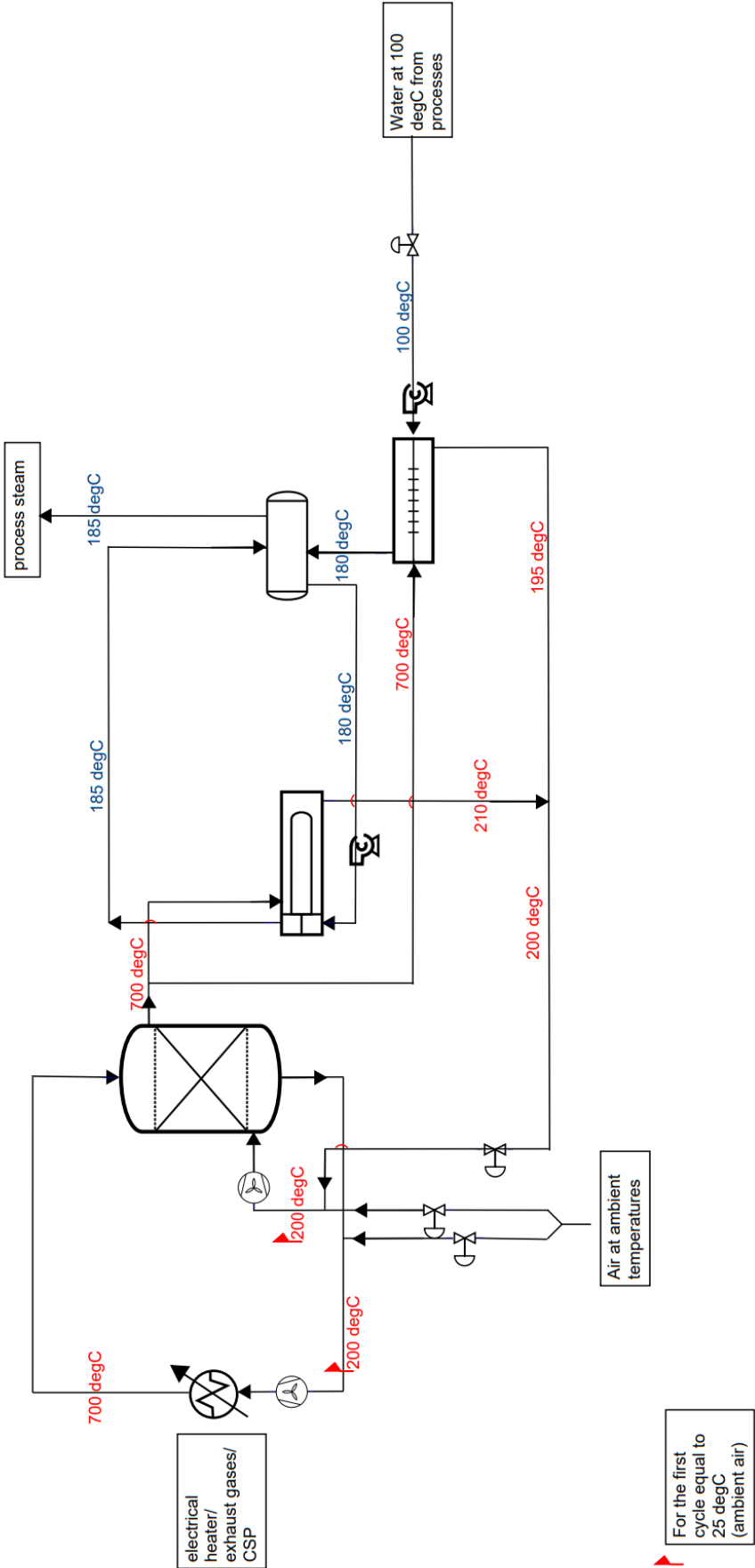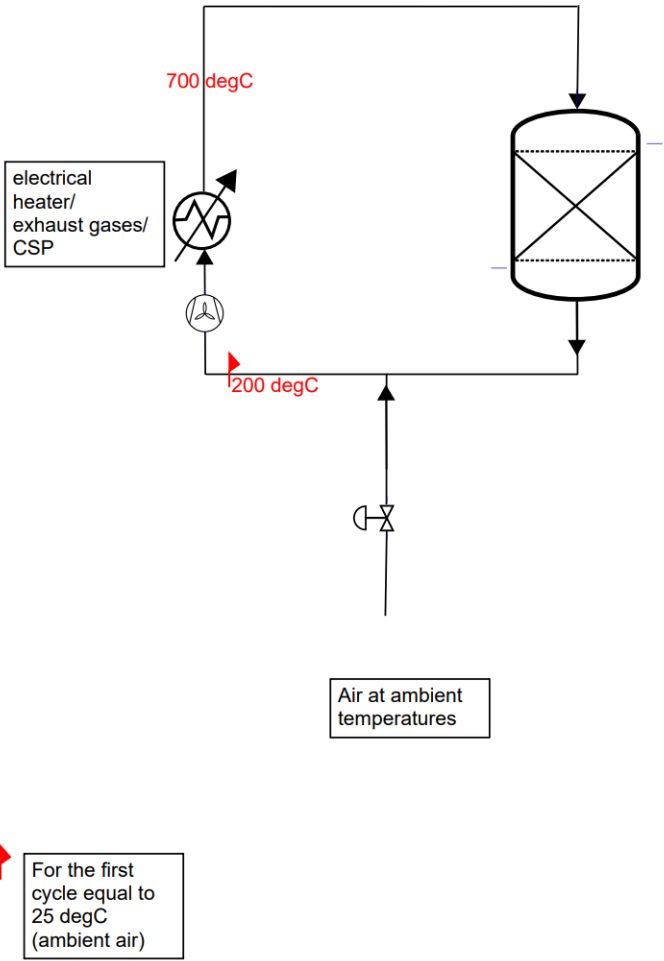
Figure A.1: Flowsheet slag total
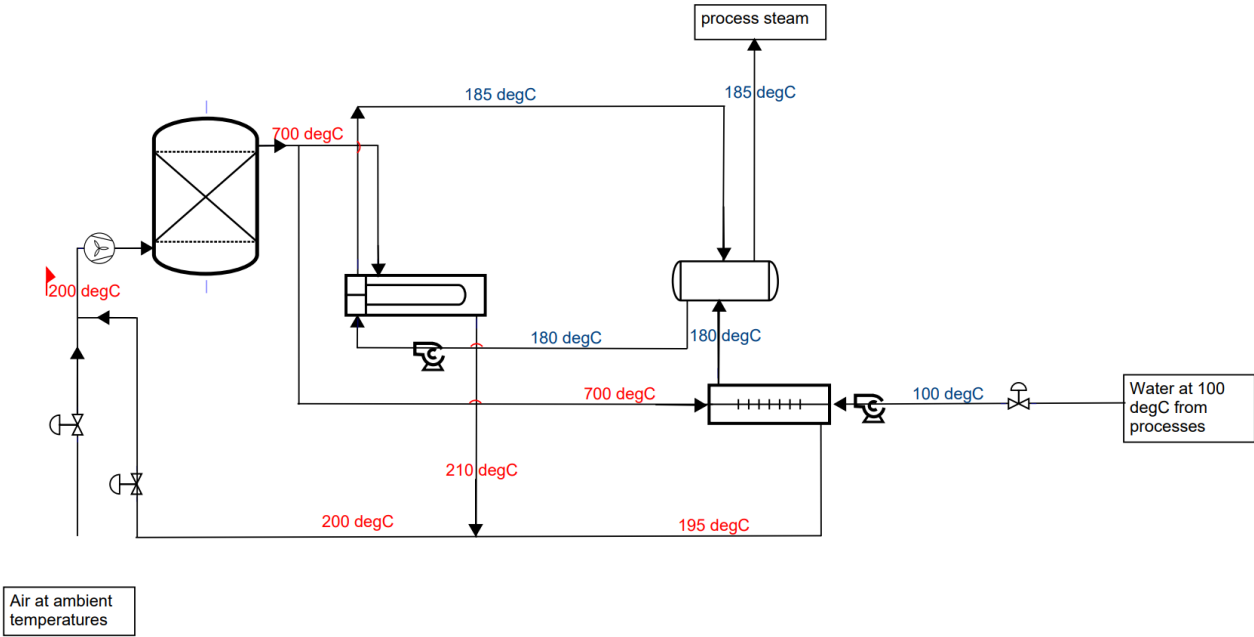
Figure A.2: Flowsheet slag charge

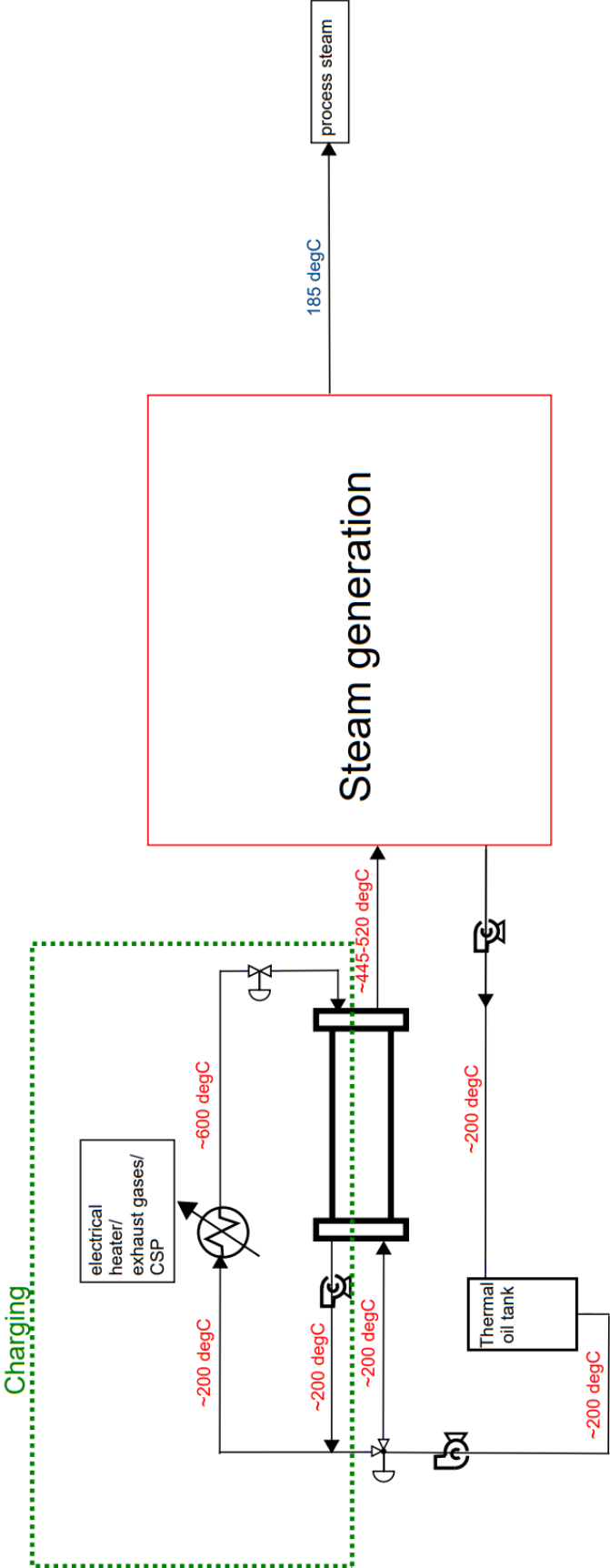**Figure A.3:** Flowsheet slag discharge

Figure A.4: Flowsheet phase change salt
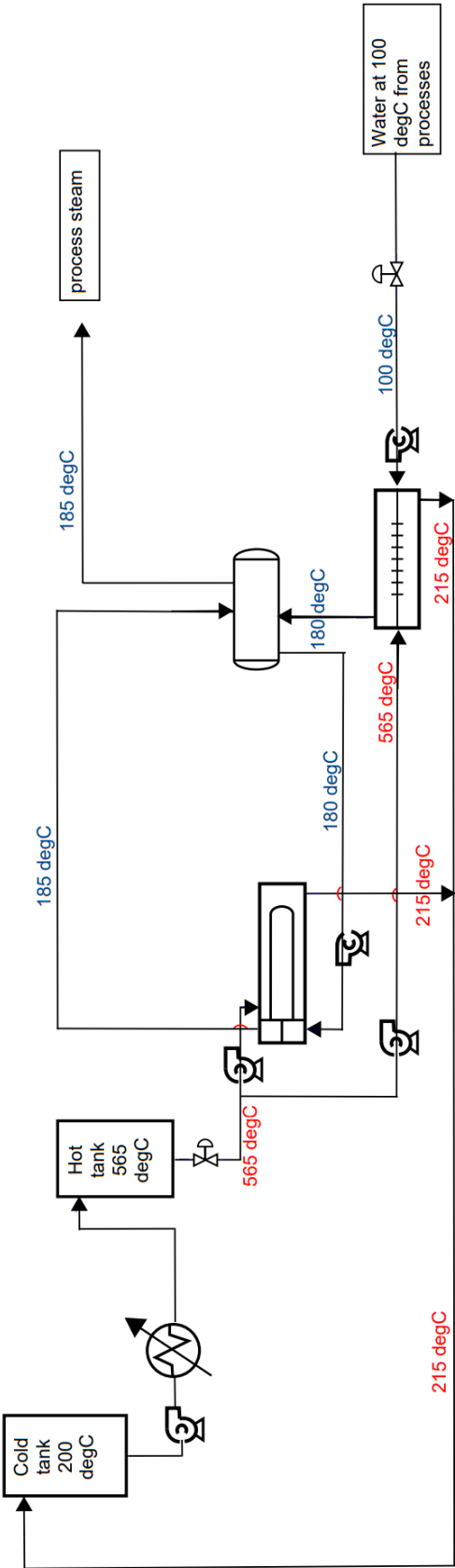
Figure A.5: Flowsheet molten salt

B

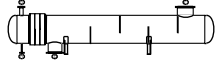## TEMA

TEMA Sheet

Heat Exchanger Specification Sheet

1	Company: TU Delft								
2	Location: Process and Energy								
3	Service of Unit:		Our Reference:						
4	Item No.:		Your Reference:						
5	Date:	Rev No.:	Job No.:						
6	Size: 737 - 3657,6 mm		Type: BEU Horizontal			Connected in: 4 parallel 1 series			
7	Surf/unit(eff.) 224,7 m²		Shells/unit 4			Surf/shell(eff.) 56,2 m²			
8	**PERFORMANCE OF ONE UNIT**								
9	Fluid allocation			Shell Side			Tube Side		
10	Fluid name			Air			Water		
11	Fluid quantity, Total		kg/s	10,6574			2,7967		
12	Vapor (In/Out)		kg/s	10,6574	10,6574		0	2,7967	
13	Liquid		kg/s	0	0		2,7967	0	
14	Noncondensable		kg/s	0	0		0	0	
15									
16	Temperature (In/Out)		°C	700	210		180	186,78	
17	Bubble / Dew point		°C	/	/		186,37 / 186,37	186,17 / 186,17	
18	Density Vapor/Liquid		kg/m³	0,54 /	1,04 /		/ 889,53	5,66 /	
19	Viscosity		mPa-s	0,0407 /	0,0251 /		/ 0,1644	0,0157 /	
20	Molecular wt, Vap			28,96	28,96			18,01	
21	Molecular wt, NC								
22	Specific heat		kJ/(kg-K)	1,136 /	1,027 /		/ 4,301	2,691 /	
23	Thermal conductivity		W/(m-K)	0,0684 /	0,0437 /		/ 0,6785	0,0346 /	
24	Latent heat		kJ/kg				1990,9	1991,7	
25	Pressure (abs)		bar	1,5	1,44539		11,5	11,44649	
26	Velocity (Mean/Max)		m/s	32,93 / 77,98			2,48 / 4,92		
27	Pressure drop, allow./calc.		bar	0,1	0,05461		0,5	0,05351	
28	Fouling resistance (min)		m²-K/W	0,0001			0,0002	0,00022 Ao based	
29	Heat exchanged 5645,6		kW			MTD (corrected) 167,86		°C	
30	Transfer rate, Service 149,7			Dirty 160,3		Clean 169,1		W/(m²-K)	
31	**CONSTRUCTION OF ONE SHELL**						**Sketch**		
32				Shell Side		Tube Side			
33	Design/Vacuum/test pressure	bar	3,44738 / /		13,10004/ /				
34	Design temperature / MDMT	°C	737,78 /		221,11 /				
35	Number passes per shell		1		4				
36	Corrosion allowance	mm	3,18		3,18				
37	Connections	In	mm	1 406,4 / -	1 19,05 / -				
38	Size/Rating	Out		1 355,6 / -	1 76,2 / -				
39	Nominal	Intermediate		/ -	/ -				
40	Tube #: 62 U's OD: 38 Tks. Average 2,11 mm Length: 3657,6 mm Pitch: 47,5 mm Tube pattern:30								
41	Tube type: Plain Insert:None Fin#: #/m Material:Carbon Steel								
42	Shell Carbon Steel ID 736,6 OD 755,65 mm				Shell cover Carbon Steel				
43	Channel or bonnet Carbon Steel				Channel cover -				
44	Tubesheet-stationary Carbon Steel -				Tubesheet-floating -				
45	Floating head cover -				Impingement protection None				
46	Baffle-cross Carbon Steel Type Single segmental Cut(%d) 40,54				Horiz Spacing: c/c 742,95 mm				
47	Baffle-long - Seal Type				Inlet 0 mm				
48	Supports-tube U-bend 0				Type				
49	Bypass seal Tube-tubesheet joint Expanded only (2 grooves)(App.A 'i')								
50	Expansion joint - Type None								
51	RhoV2-Inlet nozzle 952 Bundle entrance 2080 Bundle exit 137 kg/(m-s²)								
52	Gaskets - Shell side Flat Metal Jacket Fibe Tube side Flat Metal Jacket Fibe								
53	Floating head -								
54	Code requirements ASME Code Sec VIII Div 1 TEMA class R - refinery service								
55	Weight/Shell 2805,9 Filled with water 4751,1 Bundle 1435,5 kg								
56	Remarks								
57									
58									

Figure B.1: TEMA sheet air to steam

TEMA Sheet

Heat Exchanger Specification Sheet

1	Company: TU Delft								
2	Location: Process and Energy								
3	Service of Unit:		Our Reference:						
4	Item No.:		Your Reference:						
5	Date:	Rev No.:	Job No.:						
6	Size: 305 - 4876,8 mm		Type: BEU Horizontal			Connected in: 1 parallel		1 series	
7	Surf/unit(eff.) 49,2 m²			Shells/unit 1			Surf/shell(eff.) 49,2		m²
8	**PERFORMANCE OF ONE UNIT**								
9	Fluid allocation			Shell Side			Tube Side		
10	Fluid name			Molten salt			Water		
11	Fluid quantity, Total		kg/s	10,8666			2,7967		
12	Vapor (In/Out)		kg/s	0	0	0		2,7967	
13	Liquid		kg/s	10,8666	10,8666	2,7967		0	
14	Noncondensable		kg/s	0	0	0		0	
15									
16	Temperature (In/Out)		°C	565	215	180		185,03	
17	Bubble / Dew point		°C	/	/	186,32 / 186,32		184,39 / 184,39	
18	Density Vapor/Liquid		kg/m³	/ 1718	/ 2035	/ 888,34		5,46 /	
19	Viscosity		mPa-s	/ 6,317	/ 6,387	/ 0,1633		0,0156 /	
20	Molecular wt, Vap							18,01	
21	Molecular wt, NC								
22	Specific heat		kJ/(kg-K)	/ 1,354	/ 1,618	/ 4,304		2,684 /	
23	Thermal conductivity		W/(m-K)	/ 0,7	/ 0,6225	/ 0,6777		0,0343 /	
24	Latent heat		kJ/kg			1990,4		1997,1	
25	Pressure (abs)		bar	1,5	1,2764	11,5		11,01105	
26	Velocity (Mean/Max)		m/s	0,39 / 0,74		19,06 / 37,89			
27	Pressure drop, allow./calc.		bar	0,5	0,2236	0,5		0,48895	
28	Fouling resistance (min)		m²-K/W	0,0004		0,00018	0,0002	Ao based	
29	Heat exchanged 5641,4		kW			MTD (corrected)	133,19		°C
30	Transfer rate, Service 861,3			Dirty 865,7		Clean 1791,5			W/(m²-K)
31	**CONSTRUCTION OF ONE SHELL**						**Sketch**		
32				Shell Side		Tube Side			
33	Design/Vacuum/test pressure		bar	3,44738 / /		13,10004/ /			
34	Design temperature / MDMT		°C	604,44 /		221,11 /			
35	Number passes per shell			1		2			
36	Corrosion allowance		mm	0		0			
37	Connections	In	mm	1 88,9 /	-	1 38,1 /	-		
38	Size/Rating	Out		1 76,2 /	-	1 152,4 /	-		
39	Nominal	Intermediate		/	-	/	-		
40	Tube #: 122 U's OD: 13 Tks. Average 0,56 mm Length: 4876,8 mm Pitch: 16,25 mm Tube pattern:30								
41	Tube type: Plain Insert:None Fin#: #/m Material:SS 316L								
42	Shell SS 316L ID 315,93 OD 323,85 mm					Shell cover SS 316L			
43	Channel or bonnet SS 316L					Channel cover -			
44	Tubesheet-stationary SS 316L -					Tubesheet-floating -			
45	Floating head cover -					Impingement protection None			
46	Baffle-cross SS 316L Type Single segmental Cut(%d) 34,92 Horiz Spacing: c/c 158,75 mm								
47	Baffle-long - Seal Type					Inlet 0			mm
48	Supports-tube U-bend 0					Type			
49	Bypass seal Tube-tubesheet joint Expanded only (2 grooves)(App.A 'i')								
50	Expansion joint - Type None								
51	RhoV2-Inlet nozzle 1689 Bundle entrance 751 Bundle exit 411 kg/(m-s²)								
52	Gaskets - Shell side Flat Metal Jacket Fibe Tube side Flat Metal Jacket Fibe								
53	Floating head -								
54	Code requirements ASME Code Sec VIII Div 1 TEMA class R - refinery service								
55	Weight/Shell 607,6 Filled with water 1024,1 Bundle 274,3 kg								
56	Remarks								
57									
58									

Figure B.2: TEMA sheet molten salt to steam

Coating application methods

Physical and chemical vapor deposition

Physical Vapor Deposition (PVD), shown in Figure C.1a, is a coating method executed within a high vacuum environment. In this process, the coating material transitions into a vapour phase and subsequently condenses onto the targeted material, forming a thin film. The two primary PVD techniques are sputtering and evaporation. In general, the layers formed are thin. Therefore, often this is a multi-layered coating. In the evaporation process, the essential thermal energy required for the phase transition can be supplied by various units, including electron beams, heating wires, lasers, or molecular beams (Fotovvati et al., 2019).

Chemical Vapor Deposition (CVD) also requires a high vacuum. For this method, a chemical reaction, in gaseous phase, occurs which deposits a layer at the surface of the material. Heaters are required to generate a temperature which is high enough for the chemical reaction between the substrate and the vaporized materials. This process is shown in Figure C.1b (Fotovvati et al., 2019).
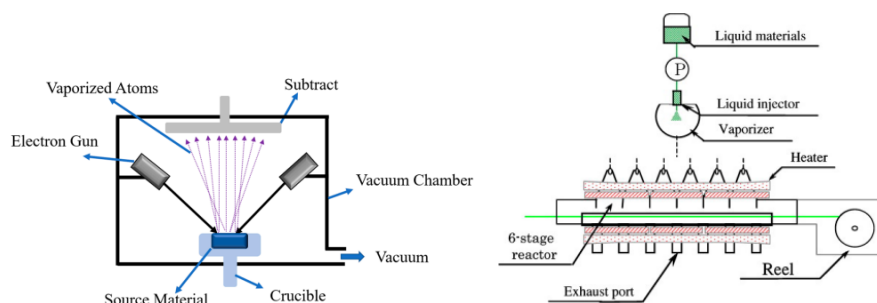

Figure C.1: a) PVD. b) CVD. (Fotovvati et al., 2019)

Dip coating

Dip coating, also known as immersion coating, is a liquid or liquid-like slurry which is deposited onto a rigid slab or cylinder. Other shapes are also optional, however uniform thickness of the coating is in those cases not always achieved. The coating process consists of five phases, shown in Figure C.2: immersion, start-up, deposition, drainage and evaporation. The initial three stages are obligatory in a sequential manner. The third and fourth stages happen simultaneously, while the ultimate stage, the fifth, unfolds throughout the entire process. The film thickness is determined by a competition among gravity, viscous force and surface tension. However, surface tension is often overshadowed in most cases, since the viscosity of the liquid and speed of the web are high enough to avoid a meniscus curvature.

However, surface tension cannot be neglected when the speed of the web or viscosity of the liquid are not high enough. This regime is referred to as the drainage regime.

The last regime, capillary regime, includes low speed of the web of approximately less than 0.1mm/s. Within this region the drying of the liquid plays an important role.
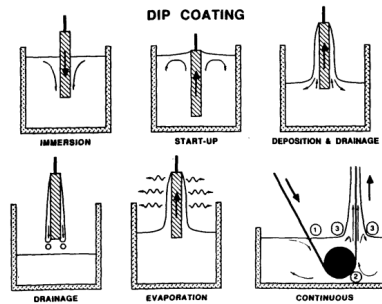

Figure C.2: Phases of dip coating (Scriven, 2011)

Spin coating

Spin coating is a batch process, with the outcome of a thin solidified coating on a flat disk, plate or curved bowl or lens. This process consists of four stages: deposition, spin-up, spin off and evaporation. The first three stages are conducted in this order and the last stage proceeds throughout the whole process. The thickness of the coating is dependent on the rotation-induced centrifugal force and the resisting viscous force. The thickness of the film is different over time, dependent on the initial deposit conditions, e.g. mildly uniform or severe uniform. However, over time all the initial conditions result in the same uniform coating, (Scriven, 2011)

$$h_{film}(t) = \frac{h_0}{\sqrt{1 + 4\rho\omega^2 h_0^2 t/3\mu}} \tag{C.1}$$

, where h_{film} is the film thickness [m], h_0 the initial film thickness [m], ρ the liquid density, ω is the angular velocity [s^{-1}], t is the time [s] and μ the viscosity [kg/ms].
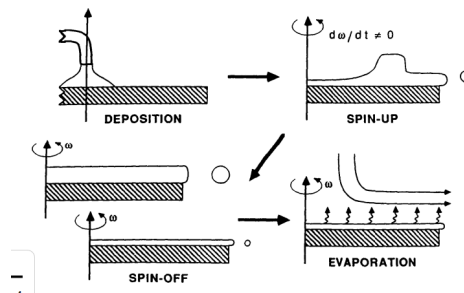

Figure C.3: Phases of pin coating (Scriven, 2011)

Sol-gel coating

Sol-gel coating is a method in which a solution called sol is made from calcium phosphorous precursors and ethanol/distilled water. This prepared mixture is heated to form a gel structure. Sol-gel is capable to enhance existing coating layers, since it has a liquid-permeating nature. Therefore, the coating can permeate through a seal porous coating or damaged layers. Dipping in the sol-gel medium, using a spray, or using a spin coating are often employed to deposit the medium on the material (Fotovvati et al., 2019).

Electrodeposition coating
Within this category of coatings, metallic ions are deposited on a substrate. This is established by a difference in potential between anode and cathode poles which causes a ion transfer. The common group of metals which is intensively studies is: Ni-P, Ni-P-W, Ni-P/Sn, Ag/Pd, Cu/Ag, Cu/Ni, Co/Ag, Co/Pt. However, the group is not limited to these metals. Two categories are present in Electrodeposition coatings: electrolytic deposition and electrophoretic deposition. Since this type of coating is limited to metals, the further research into this type is not executed(Fotovvati et al., 2019).

Thermal spray coating
Thermal spraying consists of a group of spraying techniques in which metallic or non-metallic material is deposited on a prepared substrate in molten or semi-molten state. A heat source heats the materials to this (semi-)molten state and sprays the coating with a high speed of a jet. Thickness of thermal spray coatings can range from 20μm to millimeters, this is significantly higher than electroplating, CVD or PVD. Different categories of thermal spray coating include plasma, detonation, high-velocity air and oxyfuel, flame and wire arc spraying (Fotovvati et al., 2019).

Flame spray
Flame spray coating, also known as powder flame process, is the mechanism in which powder particles are heated to near their melting point. Thereafter is this material welded with the steel substrate. This process utilizes a combustion flame to melt the feedstock material, typically in the form of wires or powders(V et al., 2022).

Plasma spraying
The to be deposited material is introduced into the plasma jet. Within the plasma or plasma jet, materials are (partially) melted with temperatures over 8000K at atmospheric pressure (*Thermal Spraying Techniques*, 2008). The (partially) melted materials are deposited onto the substrate, where they are flatten and solidify. The coating is being build out of layers of splats. Within 99% of the cases, the plasma spray is a direct current, instead of radio frequency, plasma spray (Fauchais, 2004).
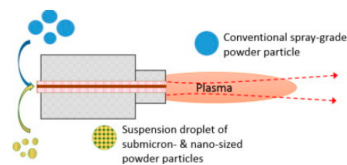

Figure C.4: Plasma spraying (Fotovvati et al., 2019)

Detonation gun spraying
To use detonation gun spraying, a precise measured quantity of coating is combined in the combustion chamber with a precise quantity of the combustion, consisting oxygen and acetylene, mixture. The gas mixture is ignited by a simple spark plug. This generates high pressure shock waves, called detonation waves, which propagate through the gas stream. The ratio of the combustion gases determines the temperature of the hot gas stream and the velocity of the shock wave, respectively up to 4000 °C and 3500 m/s. The hot gases heat the particles to the stage of plasticizing, which refers to only melting the skin of the particle, and accelerate the particles up to 1200 m/s. These particles form the coating and result in a dense and strong coating (Singh et al., 2012).
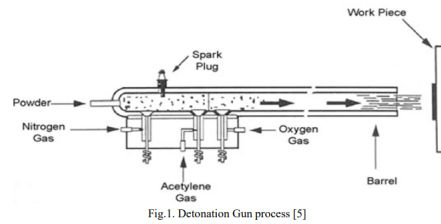
Fig.1. Detonation Gun process [5]

Figure C.5: Detonation gun spraying (Singh et al., 2012)

High velocity oxy- and air-fuel

For the high-velocity oxy-fuel coating, a fuel undergoes combustion with oxygen in gas or liquid phase. After combustion, coatings in the form of powder, are injected in this hot jet stream and are partially melted. This semi-solid mixture is deposited onto the substrate. The thickness of this coating can be up to millimeters(Fotovvati et al., 2019). HVAF also involves the combustion of fuel and oxygen, but the process is designed to achieve even higher particle velocities. HVAF typically uses higher gas pressures and lower combustion temperatures, resulting in higher particle velocities during the spraying process.

Arc wire spraying

Within this method, the to be deposited material is introduced, as two wires, into the plasma in the form of two consumable arc electrodes. These two wires are charged and between them an arc is generated. The heat, which is generated by the arc, melts the incoming wire. This is entrained in an air jet from the gun and deposited onto the substrate. Another form is the plasma transferred wire arc, where a single wire is used as feedstock. The wire is melted, atomized and propelled by a supersonic plasma jet. This plasma jet is formed between the wire and non-consumable electrode in the form of an arc (Gedzevicius et al., 2006). This is also depositing a metal and thus not interesting for our application.

Micro-arc oxidation

Micro-arc oxidation (MAO), also known as plasma electrolytic oxidation (PEO), is a surface treatment process that forms a protective and reinforced oxide coating on metal workpieces. By applying an electric voltage in an electrolyte bath, micro-arcs generate extremely high temperatures on the metal surface, leading to controlled oxidation and the formation of a porous ceramic oxide coating, this process is shown in Figure C.6 (Fotovvati et al., 2019).
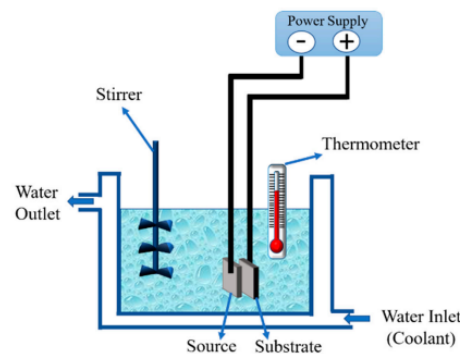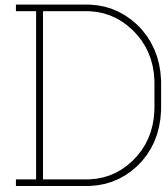

Figure C.6: Micro-arc oxidation (Fotovvati et al., 2019)

<div align="right">

D

</div>

Thermal conductivity measurements

It is imperative to consider that the thermal conductivity assessments will be conducted under low-temperature conditions. This makes certain application methodologies viable that may not be resilient to elevated temperatures.

In general, determining thermal conductivity and interfacial thermal conductance with an error margin of less than 5%, presents a highly challenging endeavor. The selection of an appropriate measurement technique to characterize thermal properties necessitates careful consideration based on the following factors:

- Thorough knowledge of the sample under investigation, including its geometry, size, and the method of material preparation.
- Comprehensive understanding of the fundamentals and procedures associated with the chosen testing technique, considering that certain techniques may be limited to specific sample geometries or a particular range of thermophysical properties.
- Profound awareness of potential sources of error that could impact the final results, such as convective and radiative heat losses.

Comprehensive understanding of the fundamentals and procedures associated with the chosen testing technique, considering that certain techniques may be limited to specific sample geometries or a particular range of thermophysical properties.

Making informed decisions based on these criteria is crucial for conducting accurate and reliable measurements of thermal properties in diverse materials and configurations (D. Zhao et al., 2016). To assess thermal conductivity, two distinct categories of methodologies are employed, namely, steady-state and transient state methods (Palacios et al., 2019).

Furthermore, in literature, a clear distinction is made between bulk materials and thin films. Thin films typically vary in thickness from several nanometers to several micrometres, and they can be adhered to a substrate, assembled as a multilayer stack, or exist as free-standing structures. The thermal conductivity of a thin film is reduced compared to its bulk, due to geometric constraints, when the thickness of the film is smaller than the mean free path of the heat carriers. The thermal conductivity of a thin film is, often, anisotropic and thickness-dependent. Furthermore, the preparation method as well as the substrate have great influence on the thermal conductivity (D. Zhao et al., 2016).

The variation in measurement technologies is attributed to the fact that bulk material techniques often prove impractical for measuring the temperature drop and heat flux across thin films due to their larger size. The smallest thermocouple beads typically have a diameter of approximately 25μm, which could exceed the thickness of certain films. As a result, specialized methods are required to accurately assess the thermal properties of thin films (D. Zhao et al., 2016).

For now it is assumed that the focus will not be on thin films in this thesis. This leads to the following, which are generally known, options presented below.

D.1. Steady state

Within steady-state measurements the thermal conductivity is determined by measuring the temperature difference under a steady-state heat flow. The slope of the power versus temperature gradient between both sides results in the thermal conductivity of the material. These steady-state methods are directly based on Fourier's law and measure the thermal conductivity directly. This method is well-suited for materials with low thermal conductivity and composites. However, steady-state methods necessitate relatively large sample sizes and longer testing duration compared to transient methods. Moreover, they entail certain drawbacks, including parasitic heat losses and contact resistance due to the implementation of temperature sensors (Tritt, 2005). On the positive side, steady-state methods offer the advantage of unidirectional heat flow over a larger area, making them suitable for measuring samples with anisotropic thermal conductivity and composites.

Guarded hot plate or absolute technique

The guarded hot plate method is, according to Palacios et al. (2019), one of most used and reliable techniques in order to measure thermal conductivity. Among the steady state method, it is the most accurate method. A solid sample, usually a rectangular or cylindrical shape, is placed between a hot and cold temperature controlled plates. The hot plate is heated by a inner heater, with known steady-state power input. Besides the guarded hot plate, thermal insulation is present to prevent heat losses and achieve heat transfer in an uni-axial direction. At the time the system reaches the steady state, the thermal conductivity can be calculated from Fourier's law with the measured temperature difference across the given length. The sensors can be thermocouples or thermistors. The thermal conductivity is according to D. Zhao et al., 2016:

$$k = \frac{QL}{A\Delta T} \tag{D.1}$$

where Q is the amount of heat [W], A cross-sectional area [m^2], L, distance [m] and ΔT temperature difference [K].

Within the guarded hot plate method, losses due to convection, conduction and radiation are minimized. However, in general, the losses should be less than 2% of the total heat flow through the sample.

Drawbacks of this technique include relative large test sample required, long test time, and only suitable for solid with relatively low thermal conductivity (D. Zhao et al., 2016)(Palacios et al., 2019).

Comparative cut bar technology

The above mentioned guarded hot plate method, is a direct technique. Since the heat flow through the sample is difficult to accurately determine, a material with known thermal conductivity can be the compared to the sample. This is called the comparative cut bar technology. A minimum of two sensors is applied on each bar. More samples can be used to determine the linearity of the temperature with respect to the distance along the sample. The amount of heat flow through the reference material is equal to the flow through the sample material. The thermal conductivity is as followsD. Zhao et al., 2016:

$$k_1 = k_2 \frac{A_2 \Delta T_2 L_1}{A_1 \Delta T_1 L_2} \tag{D.2}$$

where $_1$ is associated with the sample and $_2$ with the reference.

As advantage, compared to the direct method, the error associated with the measurement of the heat flow can be eliminated. Nevertheless, it is not considered easy to achieve uniform heat flow between the standard material and the test specimen.

Heat flow meter

The heat flow meter has similarities with respect to the guarded hot plate. Moreover, akin to the comparative bar technology, this is an comparative approach. However, the heat flow meter uses transducers to be able to measure the heat flux density through the material sample. With the measured heat flux during the heat transfer the thermal conductivity and thermal resistance can be calculated, again with Fourier's law. This method is suitable for low thermal conductivity materials (D. Zhao et al., 2016).

Radial heat flow method

To overcome radiative heat loss at higher temperature within the aforementioned techniques, in this method is the cylindrical sample heated internally. A steady state radial heat flow is established and according to the temperature difference, the thermal conductivity will be calculated according to equation D.3 (D. Zhao et al., 2016).

$$k = \frac{Q ln(r_2/r_1)}{2\pi H \Delta T} \tag{D.3}$$

where r_2 and r_1 are the radii where the two temperature sensors are applied, H is height of the sample and ΔT is the difference in temperature.

Parallel thermal conductance technique

Due to the challenges encountered in attaching thermocouples and heaters directly to small samples, which may result in increased heat losses and measurement errors, the parallel thermal conductance technique was developed. This method addresses to the specific needs of small samples and mitigate potential inaccuracies arising from the conventional approaches.

This technique involves conducting an initial thermal conductance measurement of the sample holder itself. This preliminary measurement determines the baseline or background thermal conduction and losses associated with the sample stage. Thereafter, the sample is attached and the thermal conductance of the system is measured. After subtraction, the thermal conductance, which is due to the sample, thermal contact and blackbody radation, is calculated. The contribution of the radiation is excluded by a third measurement within the same system. What should be noted, is that this technique measures the thermal conductance and the measurement of the area is required to determine the thermal conductivity. Therefore, inaccurate measurements of the dimensions can result in large errors (Zawilski et al., 1999).

D.2. Transient state

To surmount the limitations inherent in the aforementioned steady-state methods, which include issues like parasitic heat losses, contact resistance of temperature sensors, and long wait times to establish a steady-state temperature difference, a diverse array of transient techniques have been developed (D. Zhao et al., 2016).

Within a transient method, the heat is supplied in pulses or periodically. This results in transient or periodic temperature changes within the sample. With these methods, the thermal diffusivity is measured during the heating process. Thermal diffusivity measures the heat transfer rate. Thermal diffusivity is related to density and specific heat capacity as follows:

$$\alpha = \frac{k}{\rho c_p} \tag{D.4}$$

where α is the thermal diffusivity [m^2/s], k the thermal conductivity [W/mK], ρ the density [kg/m^3] and c_p the specific heat capacity [kJ/kgK] (Palacios et al., 2019).

Pulsed power technique

The pulsed power technique is a derivative of the above mentioned guarded hot plate method, also known as the absolute technique. The difference is the periodic electrical heating current, I(t). The sample, often rectangular or cylindrical, is placed in between a heat source and sink. The heat source can be either a constant-amplitude square wave or a sinusoid wave (Romao et al., 2014). The periodic electric current is applied, while the heat sink temperature slowly drifts and thereby a small temperature gradient ($\approx$ 0.3K) is generated. The result of thermal conductance is:

$$k = \frac{RI_0^2}{\Delta T_{pp}} tanh(\frac{K\tau}{2C})$$ (D.5)

where τ is the half period of the current, C the volumetric heat capacity, I_0 the amplitude of the current and R the thermal resistance.

Transient hot wire/hot strip method

With the use of the transient hot wire method, the thermal conductivity of non-electrical conductive materials can be measured. This method is commonly used for liquids. However, solids, gases, and slurries can also be measured with this technique. To measure the thermal conductivity, a heated wire is implemented in the sample. This wire is along the length considered as an ideally linear heat source with a uniform output. This wire is, besides a heat source, a temperature detector. The heat of the wire flows radially outwards to the sample. The slope of the temperature rise is proportional to the time-lapse (Palacios et al., 2019). The determination of the thermal conductivity is according to the following equation:

$$k = \frac{q}{4\pi(T_2 - T_1)} ln(\frac{t_2}{t_1})$$ (D.6)

where k is the thermal conductivity [W/mK], q is the heating power per unit length [W/m], T is the temperature of the wire [K] at heating time t [s] (Hwang et al., 2006).

However, the sample thickness of the hot wire method is comparable to the sensor thickness, e.g. thin film. Therefore, the needle probe variation is developed. This is able to measure the thermal conductivity in situ by inserting the probe in the test sample. Another method, transient plane source is developed and can, as well as the hot wire method, measure solid non-electrical conductive samples. The difference is the flat heat source in this technique. The thermal conductivity measurements are executed in one direction. Therefore, heterogeneous or anisotropic structures are not suitable for this technique.

Transient plane source method

Transient plane source is also known as the hot disc or Gustafsson probe method (Al-Ajlan, 2006). To measure the thermal conductivity, a set of rings is implemented as a planar heater between the sample. These rings are often made from Nickel and are reinforced by insulating gaps (Ahadi et al., 2016). While conducting the experiment, a small and consistent electric current is employed. The voltage generation of the sensor is in direct proportion to the temperature, according to Ohm's law (Y. Li et al., 2013) (Ostanek et al., 2016). The thermal conductivity is determined based on the recorded temperature and electrical resistance, according to:

$$k = \frac{P_0}{r\Delta T(\tau)\pi^{3/2}} D_s(\tau)$$ (D.7)

where P_0 is the power input [W], r is the radius of the largest ring [m], τ is the time (non-dimensional [-], ΔT is the temperature rise and D_s is the shape function of τ.

The non-dimensional time and shape function are, (Coquard et al., 2013)

$$\tau = \sqrt{\frac{t\alpha}{r^2}} \tag{D.8}$$

where t is the recorded time [s], α is the thermal diffusivity [m^2/s].

$$D_s(\tau) = \frac{1}{n^2(n+1)^2} \int_0^\tau \left(\frac{1}{s^2} \sum_{l=1}^n l \sum_{k=1}^n k * exp\left(-\frac{l^2+k^2}{4n^2s^2}\right) I_0\left(\frac{lk}{2n^2s^2}\right) \right) ds \tag{D.9}$$

where n is the number of heater circles [-], I_0 is the intensity of the radiance of the black body, and s is the integration variable.

The determination of the thermal conductivity is an iterative process where the diffusivity is approximated and the thermal conductivity is estimated from the slope.

Laser flash analysis technique

With the laser flash analysis technique the measurements determine the thermal diffusivity (Maeda & Mizubayashi, 2006). In combination with the specific heat, C$_p$ [kJ/kgK] and density, ρ [kg/m^3], this technique is able to determine the thermal conductivity:

$$k = \alpha \rho C_p \tag{D.10}$$

where α is the thermal diffusivity [cm^2/s].

The thermal diffusivity is calculated as follows,

$$\alpha = 0.1388 \frac{d^2}{t_{1/2}} \tag{D.11}$$

where d is the sample thickness [cm] and $t_{1/2}$ is the time when 50% of the maximum temperature increase is achieved (Lian et al., 2016).

The method is non-contact, non-destructive and has high accuracy (Min et al., 2007). With the use of a laser beam, a laser pulse is applied at the bottom of the sample. An infrared sensor is utilized to monitor the temperature rise at the top, facilitating the determination of the corresponding thermal diffusivity (D. Zhao et al., 2016).